



PROGRAMA DE DOCTORADO EN FÍSICA
DEPARTAMENTO DE FÍSICA APLICADA I ELECTROMAGNETISMO

Crystal growth of functional materials by using CSVS and MOCVD: The $A_{II}MnB_{VI}$ and II -oxides case

TESIS DOCTORAL PRESENTADA POR:

Oleksii Klymov

Y DIRIGIDA POR:

Dr. Vicente Muñoz Sanjosé

Dr. Denys Kurbatov

Valencia, Octubre de 2021

Vicente Munoz Sanjosé, Professor of Applied Physics at the University of Valencia, and Denys Kurbatov, Leading Researcher of the Electronics and Computer Technics Department of Sumy State University.

CERTIFY THAT:

The dissertation entitled "*Crystal growth of functional materials by using CSVS and MOCVD: The $AlMnB_{VI}$ and II-oxides case*" has been carried out under our advisory, by Oleksii Klymov, Graduate in the field of Electronic Equipment at the Sumy State University, and constitutes his thesis to obtain the degree of "Doctor por la Universidad de Valencia", in the frame of the "Programa de Doctorat en Física".

In compliance with the Spanish current legislation, the aforementioned PhD Thesis is presented to be evaluated.

Burjassot, 30/07/2021

VICENTE
MUÑOZ
SANJOSE -
NIF:19084088E

Firmado digitalmente
por VICENTE MUÑOZ
SANJOSE -
NIF:19084088E
Fecha: 2021.07.30
07:09:19 +02'00'



Dr. Vicente Munoz Sanjose

Dr. Denys Kurbatov

*To my family,
and particularly in memory of my father*

*When science reaches any summit, a vast prospect
of the further path to new heights opens up from it,
new roads open, along which science will go further.*

S. I. Vavilov

Acknowledgment

Preparing and writing a thesis is a journey full of learning, difficulties, memories, and emotions. This is a large volume of work, in the process of which we receive help and support from a large number of people. During the seven years of preparation, I met many people who accompanied me, directly or indirectly made this project possible, and to whom I would like to dedicate a few words of gratitude.

First of all, I must thank the director of this dissertation, Professor of the Universidad de Valencia Dr. Vicente Muñoz, for the scientific contributions and ideas that served as the basis for this study. Thank you for your concern, wise advice, and all the hours you spent teaching me and checking my work. I am grateful to you for giving me the opportunity to work in your scientific group and for your constant concern, not only about my thesis, but also about me and my family.

On the other hand, I want to thank my director from Sumy State University, Denys Kurbatov. Thank you for opening the world of semiconductor physics. Your help at the beginning of my scientific career was very valuable to me. You were ready to help me when I needed it, to give a hint when I was in difficulty, to push me to reach new heights. Thank you very much.

I am grateful to all my colleagues who are or have been part of our Crecycsem research group. Thanks to the wonderful teacher M. Carmen Martínez for her care and help not only with the analysis of diffraction and structural properties of the material but also for her advice and tips, which helped me a lot in this work. I also want to thank Saïd Agouram for his responsiveness, comments, and advises, as well as help in the research and interpretation of the results. Lluís Manel and Vicent Marín were my role models, from whom I learned a lot and who, and were always ready to lend me a helping hand, helping me to adapt to the new environment. Thanks to Ade Huerta, my unaltered partner at the "yellow fingers team", for spending a lot of time with me in the MOCVD lab and helping me with my Spanish when I asked for help. Javi Yeste has taught me how to use LaTeX and kept me company in our big office. I would like to thank Antonia Atencia for being our "second mother", supporting and caring for our research group.

Thanks to all the members of the Departamento de Física Aplicada y Electromagnetismo at the Universidad de Valencia. Diego Gómez and Juan Damas for their golden hands in helping

solve technical problems. Braulio García for his cheerful character. Seokmin Hong for Korean humor and collaborative sports activities. Anahí, Miguel, Marina, David, Martina, and others for fun lunchtime, after-work dinners, and Valencia visits.

Thanks to all the *SCSIE* (*Servei Central de Suport a la Investigació Experimental*) staff I have contacted for their support, training, and resources to carry out a structural study of the material of my work. In particular, I would like to thank the members of the microscopy section, especially Enrique, Tony, Pilar, and Rafa, for their help in managing the equipment. Alicia and Malva, powder X-ray Department, for quick feedback on the measurements that were used to make changes to optimize material growth parameters. Also to members of the secretariat department Antonio, Tony, Juanmi and others, which made it easier to work with our work with documents, and the cleaning ladies, who kept our office clean.

I am grateful to the members of the Department of Electronics and Computer Technology of Sumy State University. Thanks to Anatoliy Opanasyuk for his wisdom and advice during my studies. To the secretary of the department, Irina Golofost, who always extended her helping hand. Pavel Koval, who was my partner in the “Nanoelectronics materials” group, and together mastered the CSVS growth methodology. Volodymyr Kosyak and Maxym Kolesnyk, who shared their knowledge and experience of both working with thermal growth equipment in a vacuum and processing the obtained results. Oleksandr Dobrozhan and Taisiia Berestok for their help and spending time together on the internship. Andrii Voznyi and Yaroslav Znamenshchikov for their help, support and keeping my workplace and things in order after my move to Valencia.

In addition to my stay at the University of Valencia and Sumy State University, I was fortunate enough to work in two more places, to which I would like to express my special gratitude.

Professor Adrián Hierro from the Universidad Politécnica de Madrid for his guidance, advice, and help in the study of the spectral properties of materials and more. And also to members of his research group, in particular, Miguel Bajo for the friendliness and care, Julen Tamayo for support and collaboration, and Alejandro Kurtz for introducing me to the study of the electrical properties of the material. Thanks to everyone I spent my lunch breaks with, having fun talking.

Many thanks to Ana Cros and Nuria Garro from the scientific group *POEMAS* (*Processos optoelectrònics en materials avançats i superfícies*) of ICMUV for allowing me to become a member of your group for a while and opened the world of atomic microscopy, in particular KPFM. Thank you for your training, support, help in difficult times. Also Andre, Dominic, Ana, Giulia, Damián, Xavi, Sarah, Alberto, Alvaro, Marta, Rosa, Pablo, and others for a good time both during lunch break and activities after work.

Thanks to people not only in the scientific world. My flatmates Jordi, Manuela, Ali, Jorge, Costi, Vicente y Carlos, supported me after returning home, spent their free time with me, and

did not refuse help. Esther, my first Spanish friend, and Luis, a cheerful guy with a saxophone, with whom I spent the most time, shared sorrows and joy, discovered interesting places. You will always have a special place in my life.

Спасибі моїм друзям: Олегу, Андрію, Сергію і Юрію, що весь цей час тримали зі мною зв'язок, запитували як у мене справи, цікавилися як йде робота над дисертацією, вислуховували мене та підтримували коли це було необхідно.

Нарешті, я хочу подякувати моїй сім'ї, моїм дядям і тіткам, моїм двоюрідним братам і сестрам, племінникам, що вірили в мене і допомагали по мірі можливостей. Бабусі Олі, що навчила мене життєвим мудростям і наставляла на правильний шлях. Моїй улюбленій сестрі Анні за терпіння і все що вона зробила для мене. Велике спасибі моїм батькам за їх величезну підтримку, яка мала величезне значення. Тату, моїй найповажніший людині в світі, за всі ті жертви, які прийшлося принести заради мене. Мамі, за любов, турботу і переживання. Спасибі, що навчила мене, що не потрібно засмучуватися, що немає безвихідних ситуацій і необхідно докласти трохи більше зусиль для вирішення проблем і досягнення поставлених цілей.

I am grateful to you all from the bottom of my heart.

List of Acronyms

1D - One dimension
2D - Two dimension
3D - Three dimension
AFM - Atomic force microscopy
Arb. Units – arbitrary units
CPD - Contact potential difference
CSD - Coherent scattering domain
CSVs - Close space vapor sublimation
DEZn - Diethylzinc
DIPTe - Diisopropyl telluride
DMCd - Dimethylcadmium
DMS - Diluted magnetic semiconductors
EDX - Energy dispersive X-ray spectroscopy
FFT - Fast Fourier Transform
FWHM - Full width at half maximum
GB - Grain boundary
hkl - Miller indices
KPFM - Kelvin probe force microscopy
MFC - Mass Flow Controller
MOCVD - Metal Organic Chemical Vapor Deposition
MOVPE - Metal Organic Vapor Phase Epitaxy
NIR – Near infrared
PIXE - Particle Induced X-ray Emission
r.m.s. (rms) – Root-mean-square
RT - Room temperature
SAED - Selected area electron diffraction
Scm - Standard cubic centimeters per minute
SEM - Scanning electron microscopy
SE - Secondary electrons

SF - Staking fault
Slm - Standard liters per minute
SMSC - Semi-magnetic semiconductors
SPV - Surface photovoltage
TCO - Transparent Conductive Oxide
TEM - Transmittance Electron Microscopy
 T_e - Evaporation temperature
 T_s - Substrate temperature
t – Growth time
t-but - Tert-Butanol
XRD - X-Ray Diffraction
WH - Williamson-Hall plot
WZ – Wurtzite phase
ZB – Zinc blende phase

Contents

1	Introduction	3
2	Materials and growth technique	11
2.1	ZnO, CdO and ternary alloys	11
2.1.1	Zinc oxide (ZnO)	12
2.1.2	Cadmium Oxide (CdO)	14
2.1.3	Ternary compound of $CdZnO$	16
2.2	Cadmium telluride ($CdTe$)	18
2.3	$A_{II}MnB_{VI}$ chalcogenides	21
2.3.1	Zinc manganese telluride ($ZnMnTe$)	22
2.3.2	Zinc manganese sulfide ($ZnMnS$)	24
2.4	Metallorganic chemical vapor deposition technique	26
2.4.1	Metallorganic chemical vapor deposition system	26
2.4.2	Electronic system of MOCVD	31
2.4.3	Our working system	33
2.4.4	Precursors	35
2.4.5	Substrates	38
2.4.6	MOCVD growth parameters	40
2.5	Close-spaced vacuum sublimation technique (CSVs)	43
2.5.1	Close-spaced vacuum sublimation system	43
2.5.2	Temperature control system	48
2.5.3	Our working system	50
2.5.4	Substrates	51
2.5.5	CSVs growth parameters	53
3	Characterization techniques	55
3.1	Scanning Electron Microscopy (SEM)	55
3.1.1	The principle of the scanning electron microscope	57
3.1.2	Sample's preparations	59

3.1.3	Used equipment - Experimental set-up	60
3.2	Transmission Electron Microscopy (TEM)	62
3.2.1	Measurement technique	62
3.2.2	Sample's preparations	63
3.2.3	Used equipment - Experimental set-up	64
3.2.4	Energy Dispersive X-Ray Spectroscopy	65
3.3	Particle Induced X-ray Emission (PIXE)	67
3.3.1	Principle of PIXE (Particle Induced X-ray Emission)	67
3.3.2	Used equipment - Experimental set-up	70
3.4	X-Ray Diffraction (XRD)	71
3.4.1	X-ray diffraction	71
3.4.2	Basic principles	72
3.4.3	Coherent scattering size and microdeformation	74
3.4.4	Williamson-Hall plot	76
3.4.5	Density of dislocations	77
3.4.6	Pole figures	78
3.4.7	Vegard's law for ternary compounds	79
3.4.8	Used equipment - Experimental set-up	80
3.5	Optical transmission measurement	84
3.5.1	Basic principles	84
3.5.2	Used equipment- Experimental set-up	87
3.6	Kelvin probe force microscopy (KPFM)	90
3.6.1	KPFM operation mode: FM mode	92
3.6.2	Contact potential difference (CPD)	94
3.6.3	Surface photovoltage (SPV)	95
3.6.4	Used equipment- Experimental set-up	97
4	Growth and characterization of ZnO, CdO, CdZnO, CdTe and their heterostructures	99
4.1	Zinc oxide: morphological and structural study	99
4.1.1	SEM and XRD measurements	99
4.1.2	AFM studies	113
4.2	CdZnO: morphological and structural study	122
4.2.1	SEM and XRD measurements	122
4.2.2	Transmittance and absorption spectra	130
4.3	CdTe/CdO heterostructures	135
4.3.1	Structural characterization	135

4.3.2	Parameters for the growth of heterostructures	144
4.3.3	Electrical characterization	148
5	Effect of Mn alloying on structural and optical properties of ZnTe and ZnS thin films	151
5.1	Structural and morphological studies of $Zn_{1-x}Mn_xTe$ thin films	151
5.1.1	Morphological study	151
5.1.2	Lattice constant and Mn content	153
5.1.3	Out-plane orientation of films	157
5.1.4	In-Plane orientation of films	158
5.1.5	Coherent scattering domain and microdeformations	161
5.1.6	Crystallite size and density of dislocations	164
5.2	Structural and morphological properties of $Zn_{1-x}Mn_xS$ thin films	168
5.2.1	Morphological study	168
5.2.2	Lattice constant and Mn Content	169
5.2.3	Out-plane orientation of films	175
5.2.4	In-plane orientation of films	176
5.2.5	Coherent scattering domain and microdeformations	178
5.2.6	Density of dislocations and defects	180
5.3	Optical (spectral) studies	183
5.3.1	Transmittance and Reflectance (Band gap determination)	183
6	Summary and Conclusions	191
6.1	II-oxides, ternary compounds and heterostructures based on them.	192
6.1.1	ZnO studies	192
6.1.2	$Cd_{1-x}Zn_xO$ studies	193
6.1.3	CdTe/CdO heterostructures	195
6.2	$A_{II}MnB_{VI}$ materials	196
6.2.1	$Zn_{1-x}Mn_xTe$ studies	196
6.2.2	$Zn_{1-x}Mn_xS$ studies	198
6.2.3	Optical (spectral) studies	200
6.3	General conclusions	201
7	Resumen en español	207
	Bibliography	224

Part I

Chapter 1

Introduction

Motivation and Objectives

Motivation. Since its inception, humanity has gradually sought opportunities to invent tools for improving its living conditions. Beginning with the Stone Age and the control of fire, the first metals such as copper, bronze and iron were gradually subdued by humans. The invention of language and writing allowed to make a qualitatively big leap in the development of society. Knowledge has become possible to accumulate knowledge and pass it to future generations. For hundreds of years, humanity has been refining its tools, constantly experimenting and pushing different theories.

A new round of instrumental development was the great industrial revolution of the XVIII-XIX centuries, during which there was a mass transition from manual to machine work. The main consequence of the industrial revolution was industrialization - the transition from a predominantly agrarian economy to industrial production. This contributed to the invention of new equipment and devices, as well as the use of new types of energy. Technical achievements in electricity and magnetism and new advances in chemistry accelerated the development of humanity and added diversity in instrumentation. A recognized classic expertize of post-industrialism time, D. Bell, has identified 3 major technological revolutions [1]:

- The invention of the steam engine in the XVIII century;
- The scientific and technological achievements in the field of electricity and chemistry in the XIX century;
- The creation of computers in the XX century.

It is worth to note that, the rapid development of technology also requires a large amount of energy. Finding this energy and being able to minimize its consumption while improving efficiency has become a new challenge for scientists. In order to replace non-renewable resources such as coal, oil or gas, renewable sources from water, wind and solar radiation have gradually been used. This forces scientists to develop materials and structures based on them that can effectively transfer energy for its application.

In order to open new paths for technological applications now, at the beginning of the XXI century, there is an active search for materials that could be complementary of the pioneer semiconductors such as Silicon or Germanium. Thus, interest in the study of mono-, polycrystalline films and nanocrystals of different compounds has increased significantly, as for instance the ones from the $A_{II}B_{VI}$ family. The interest on this family is due to the enormous potential applications that they could have in different areas like anti-reflective, absorption and window layers of photovoltaic heterojunction [2, 3], tandem solar cells (SC) [4], base layers of photodetectors [5, 6], hard radiation detectors [7, 8], LEDs, gas sensors, pyro- and piezoelectronic devices [5, 6, 9], etc. The compounds of this family make possible to obtain materials with a band gap from a few hundredths of eV (from mercury chalcogenides) up to 3.72 eV (ZnS) or even more if we go to MgO based compounds.

Among all the variety of II-VI materials, there are 2 sets of semiconductors that have attracted particular interest due to their unique features. The first one includes oxides of group-12, elements like zinc and cadmium with a high transparency at the visible optical range. They have been widely studied for use in various electro-optical applications, among other, as Transparent Conductive Oxides (TCOs). The other set is formed by the diluted magnetic semiconductors (DMS) from the II-VI compounds that, in addition to the ordinary properties of a semiconductor, have enhanced magnetic properties. Improving the methods to obtain these interesting materials in a systematic and reproducible form and in-depth studies of each of them open the door to find new opportunities.

Since TCOs have good conductivity, they can be used as electrodes when the situation requires low resistance electrical contacts without blocking the light. This ability opens up great opportunities in the field of solar cells, plasmonic and other applications. The main requirements for TCOs to be used as contacts in a solar cell are: (i) a high conductivity enough to minimize resistive losses and (ii) minimal optical absorption over the wavelength range in which the solar cell absorber is responsive. Typically, as the conductivity of a TCO is increased, the NIR (near infrared) wavelength range transparency is reduced as a result of enhanced free charge carrier absorption. Thus, in the design of TCO materials, a trade-off is sought between these two properties.

Both Zinc Oxide (ZnO) and Cadmium Oxide (CdO) can be TCOs with their strengths and weaknesses. ZnO is a semiconductor of the II-VI material family, which has been devoted to a

large number of scientific works. ZnO thin films have direct band gap, high exciton energy, stable electrical and optical properties, good electron mobility at room temperature, and depending on the growth conditions and doping a high carrier concentration [10]. The oxygen vacancies and zinc interstitials make this material an n-type semiconductor. It is worth to note that reliable p-type doping of ZnO remains difficult. This problem originates from low solubility of p-type dopants and their compensation.

Some of the properties of CdO were described long ago [11, 12]. CdO has a small indirect band gap and a larger direct band gap [13]. CdO generally possesses large carrier concentrations that generate a pronounced Moss-Burstein (MB) effect which can considerably extend the optical band gap [14]. Doped CdO samples [15] have mobilities and conductivities which are an order of magnitude (or more) higher than the typical conductivities of the industry-standard TCOs. Undoped CdO thin films usually exhibit low resistivity due to native defects of oxygen vacancies and cadmium interstitials [16]. Thus production of high-quality CdO films is important in the development and improvement of TCO.

Ternary compounds are an option to modify the properties of binary structures, thereby expanding the range of application of the material. This results in changes in characteristics such as lattice parameters, band gap width, carrier mobility, or transmittance. The properties of ternary compounds are highly dependent on the materials as well as on the growth techniques. In particular, materials with different lattice parameters or different crystal phases (wurtzite or zincblende in the case of ZnO and CdO) are difficult to combine. Tensions and impurities due to low crystal quality result in low optoelectronic properties [17]. Thus an important point will be the optimization of crystal growth conditions to achieve a good crystalline quality and consequently better optoelectronic properties.

Obtaining ternary compounds of CdZnO allows changing the properties of the initial binary compounds, adjusting them at least potentially to the needs of modern materials engineering. However, CdO has the structure of rock salt, which is different from the structure of wurtzite ZnO. Therefore, a high concentration of zinc in the CdO host or Cd in the ZnO matrix is expected to lead to a phase mixing or phase coexistence.

Due to the difference between the effective ionic radius of Cd^{2+} (0.95 Å) and the ionic radius of Zn^{2+} (0.74 Å) [18], Zn ions can easily penetrate into the CdO crystal lattice and substitute Cd ions in their equivalent crystallographic position. The difference between the ionic radii (22 %) is more than the 15 % required for the formation of a solid substitution solution according to the Hume-Rothery rules [19]. The material properties will be affected by a large lattice mismatch between ZnO and CdO, which will cause internal stresses, deformations, lattice distortions, or defects in films. For these reasons, alloying one material with another is a complex task that requires the selection of the optimal growth conditions.

Thin films of $Zn_{1-x}Cd_xO$ alloys have been prepared by several physical and chemical deposition techniques such as spray pyrolysis [18], sol-gel [20], radio-frequency magnetron co-sputtering [21], pulsed laser deposition [22], atomic layer deposition [23], MOVPE [24], laser molecular beam epitaxy (LMBE) [25] and electrochemical deposition [26]. Although Cd^{2+} ions can easily replace Zn^{2+} in a crystallographic lattice, it has been shown that the thermodynamic solubility limit of Cd in ZnO is $\sim 2\%$ in thermal equilibrium condition [27]. Most authors claim [28–31] that, at a concentration of Zn $< 20\%$, the ternary compounds retain the cubic structure. Other authors assert that the wurtzite phase in CdZnO films appears at zinc concentration of $\sim 50 - 70\%$ [23, 24, 30]. When the content of Zn is in the range from 20 to 50 %, phase mixture will exist, which means the coexistence of the cubic phase of CdO and the hexagonal phase of ZnO in thin films of the ternary compound CdZnO. A typical scheme for the formation of different phases is shown in Figure 1.1. The existence of a two-phase region can be a hindrance to stable operation when micro- and optoelectronics devices are the goal.

Regarding Semi-magnetic semiconductors (SMSC), also called diluted magnetic semiconductors (DMS) these are semiconductor compounds II-VI, IV-VI and III-V, in which part of the non-magnetic cations are replaced by ions of a magnetic transition metal or rare earth metal, such as Mn, Fe, Co, Cr, Ni, Sm, Er, Dy, Gd [32]. Due to its properties, DMS combine elements of the physics of semiconductors and magnetism, which is a unique opportunity for research [33] and technology. Compared to classical semiconductor alloys, the random distribution of magnetic ions leads to the appearance and development of individual magnetic phases depending on the concentration of magnetic ions [32].

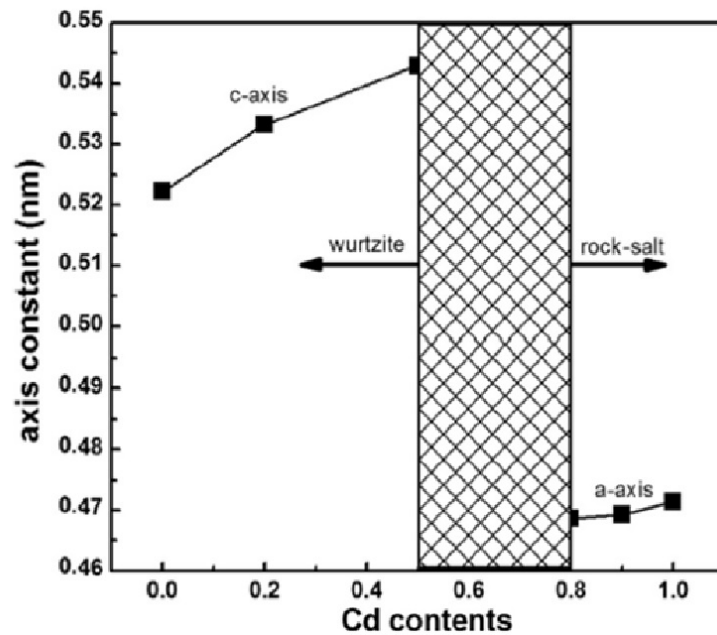


Figure 1.1: Crystalline phases formation depending on the Cd concentration [30].

Among alloying elements, the inclusion of Mn atoms in the II-VI lattice demonstrates phenomena such as negative magnetoresistance, giant Faraday rotation, and spin glass behavior. This element (Mn) may be part of different alloyed structures, but our attention will be drawn by the Mn alloy with thin films of ZnS and ZnTe, due to the wide band gaps and optical features of these binary compounds, some of which will be commented below. Changing the alloying parameter allows to change the spectral optical characteristics when applied in optoelectronics.

The optical properties of ZnTe are well known [34]. This compound is an interesting material for use in optoelectronics because it has high radiation efficiency. The synthesis of a ternary alloy based on it can offer a band gap adjustment for wider applications. In particular, the resulting compounds of semi-magnetic solid solutions $Zn_{1-x}Mn_xTe$ thin films present interesting photoluminescent, magnetic and magneto-optical features making possible to use these compounds for designing devices of micro- and optoelectronics, photovoltaics and spintronics [35,36]. The authors of reference [37] showed that the total photoluminescence intensity for a ternary sample with a content of 4.5 % Mn is approximately five times higher than for a pure ZnTe film. This means that the probability of nonradiative recombination processes will nonlinearly depend nonlinearly on the concentration and increases with increasing Mn content. In this case, the bonds for free light hole excitons in pure ZnTe are 12.7 meV, which is less than in ZnSe and ZnO, which are 21 meV and 60 meV at room temperature, respectively [37].

Like ZnMnTe, the ternary compound ZnMnS also belongs to DMS family. ZnS is a typical wide-gap (~ 3.8 eV) II-IV semiconductor material with a direct band gap. ZnS is chemically more stable and technologically more suitable than other semiconductor materials, so it is considered a promising host material for Mn^{2+} ions that can exhibit a broad emission peak. Manganese is usually used as a dopant in applications as displays, electronic devices, laser devices, as optical coatings, solid state solar window layers, optical sensors, photocatalysts, light sources, photocopy lamps, etc. [38–40].

Mn alloyed ZnS and ZnTe films have been fabricated by using different physical and chemical methods such as metal-organic vapor phase epitaxy (MOVPE) [41], molecular beam epitaxy [42], pulsed laser deposition [43], chemical bath deposition [44], radio frequency magnetron sputtering [45] and others. As substrate for obtaining nanocrystalline Mn alloyed thin films, it is possible to use different materials among them glass, silicon, or quartz [44].

Cadmium Telluride (CdTe) is another typical representative semiconductor of II-VI group. Due to its optoelectrical properties, it can be used like an n-type material in simple and cheap thin film CdS/CdTe solar cells [46,47]. The conductivity of CdTe can be changed depending on the growth conditions. CdTe grown under *Cd*-rich conditions is *n*-type due to the Fermi-level being pinned at or near the midgap by the compensating donor defect Cd_i^{+2} to meet equilibrium conditions. On the other hand, in the *Te*-rich limit, CdTe has *p*-type conductivity, since the Fermi energy is pinned close to the valence band maximum [48].

Over the past 40 years, the effectiveness of CdTe in solar cells field has increased significantly. Kodak in 1981 received CdTe cells with an efficiency of 8 % [49], and in February 2016, First Solar, the largest manufacturer of thin film technology CdTe, announced that it had reached a record 22.1 % conversion efficiency in its CdTe cells [50]. G. Kumar and K. Rao [46] made a comparison of CdTe with other semiconductor materials with optimum band gap energy in the range of 1.0-1.7 eV, to present power conversion efficiency as a function of semiconductor band gap.

Despite the wide range of use of CdTe as a semiconductor (wich will be briefly described in Section 2.2), the search for heterojunctions and compounds based on it continues. Heterojunctions CdTe/CdS and CdTe/CdSe have been well studied [51]. Nevertheless, heterostructures with TCOs, in particular the p-n heterojunction of CdTe/CdO has been less studied. Over the past 20 years, the problem of obtaining and studying the structure of CdTe/CdO was considered only in a few papers [52–54]. Complexity in the formation of this structure is due, between other factors, to the lattice mismatch between the lattice parameter of CdO (4,69 Å) and CdTe (6,49 Å). Another difficulty is the control of the preferential orientation of the layer when growing on the underlying one, in which the lattice parameter is mismatched, these difficulties makes the study of the CdTe/CdO heterostructure an attractive challenge for fundamental research.

Objectives. In the context of the above commented interest on the II-VI materials the main goal of this thesis is to study of crystal growth of some $A_{II}B_{VI}$ functional materials, determining the structural, optical and electrical properties, as well as surface morphology and the study of the influence of different growth parameters on the structural properties of the obtained materials.

Thus we will have carried out not only an in-depth study of growth but also the characterization of the studied materials. Obtaining films of binary and ternary compounds with good crystalline quality requires the choice of a suitable method and growth parameters, but to do that a correlation between growth conditions and properties must be established.

In order to a better understanding about the solubility limit and how the transition from one phase to a mixed one affects the structural properties of the CdZnO ternary compounds, we have conducted growth and characterization correlated studies of these films. Among other techniques of growth, the MOCVD method was chosen for this research. MOCVD is a technically complex and expensive method, but has great versatility and reproducibility, as well as easily scaled to production.

To obtain ZnMnTe and ZnMnS films, we have chosen the close space vacuum sublimation method (CSVs). Design features of this method allow obtaining films, under relatively well-controlled process in conditions close to thermodynamically equilibrium [55–57]. The simplicity and the low cost make possible to carry out a large number of experiments for a detailed analysis of compounds alloyed by Mn.

As in the case of CdZnO, in order to obtain the CdTe/CdO heterojunctions, the MOCVD method was used. The scarcity of information about this heterojunction increases interest in its research. Previously, our group had already analyzed these binary compounds of the heterostructure [58, 59], and these studies have been the starting point of our research.

I would like to comment that the two growth methods cover two approaches to the growth methodology: a more accurate, multiparameter-controlled system (MOCVD) and consequently expensive methodology, and one not too much expensive, and less parameter controlled as the CSVs without renouncing to offer good layers for some applications.

In accordance with the objectives, the following methods for the characterization of the samples have been used: AFM, scanning and transmittance electron microscopy, X-ray diffraction analysis, energy-dispersive X-ray spectroscopy, Particle Induced X-ray Emission (PIXE) and optical spectroscopy for transmittance, reflectance and absorption measurements.

Structure of the thesis

The work consists of six chapters, which include the introduction, main information, conclusions and the list of references. The thesis is posted on 255 pages, contains 128 figures and 25 tables. The list of used references contains 331 publications.

In **Chapter 1** motivation, object and subject of study of this thesis work are presented.

Chapter 2 shows a detailed description of the methods for obtaining films of $A_{II}MnB_{VI}$ chalcogenides and oxide-based film, as well as general information on the growth parameters and conditions for the growth of these materials.

Thereafter, in **Chapter 3**, the different characterization methods for the study of morphology, structural and substructural properties, electronic and optical features are described.

Oxides of $A_{II}B_{VI}$ group, ZnO and CdO in particular, and their heterostructure are presented in **Chapter 4**. In it, the influence on the morphology of films of growth temperature, deposition time, amount of precursors and used substrate is shown. The influence of Zinc concentration on the composition of films CdZnO is given. Also in this chapter the heterostructures based on CdTe/CdO will be analyzed.

In **Chapter 5** we present the structural properties of chalcogenides alloyed with Mn, in particular, ZnMnTe and ZnMnS. The morphology of the formed structures, the change in the lattice parameter and the final content of Mn in the deposited films are shown. The orientation of the films, the crystallite size and the density of dislocation will be described.

Finally, in **Chapter 6** we summarize the main conclusion resulting from this work.

The results obtained in the work have both a fundamental and an applied significance. The new information on the crystalline structure and substructure, the chemical composition, the film surface morphology, their optical characteristics, depending on the physical and technological growth conditions, should contribute to the development of materials based on the $A_{II}B_{VI}$ binary compounds.

Publications. The results of the thesis work are published in 8 articles, 7 of them indexed in the Scopus and WoS databases. They will be referenced at the end of the thesis in [Related articles](#).

Chapter 2

Materials and growth technique

This chapter is devoted to a brief description of the materials and crystal growth methods used in this thesis. In the first part of the chapter, we will consider the characteristics of the II-VI oxides (ZnO, CdO, CdZnO), and other II-VI materials like CdTe and ZnTe and ZnSe, these two last showing magnetic properties when alloyed with Manganese (ZnMnTe and ZnMnS). In the second part of the chapter, two methods for producing thin layers of these materials such as the chemical vapor deposition method MOVCD and the close space sublimation CSVS will be presented. The growth parameters and used substrates will be analysed.

It should be noted that, despite the fact that we will talk about the some of the properties of materials which justify the interest on them, our work has been focused mainly in terms of crystal growth and morphological and structural characterization.

2.1 ZnO, CdO and ternary alloys

Nowadays, probably the most widely used TCO in the industry is indium tin oxide (ITO). However, due to the fact that the primary metal of the film (indium) is expensive and not too much abundant, and the fragility and insufficient flexibility of the ITO layers, alternative materials are being investigated [60]. As alternative compounds, oxides like zinc oxide and cadmium oxide has been proposed, consequently in recent years they have played an important role in the field of TCO. In the first Subchapter 2.1, we briefly consider the physical properties of these oxides of the II-VI group and the ternary structure based on them. The main characteristics, production methods and problems inherent in these materials, which we have studied during our research, will be described.

2.1.1 Zinc oxide (ZnO)

Depending on the growth conditions, ZnO crystallizes in three forms: the hexagonal structure of the wurtzite, the cubic structure of zinc blende (sphalerite) and the cubic structure of rock salt. The wurtzite structure is the most stable under environmental conditions and therefore the most widespread [61]. In this structure, the atoms are far away to compensate for their repulsions. Thus, each zinc atom is surrounded by a tetrahedron of 4 oxygen atoms and vice versa, as can be seen in Figure 2.1. Zinc blende can be stabilized when ZnO is grown on substrates with a cubic lattice structure [62] and finally the structure of rock salt is obtained only at relatively high pressures of ~ 10 GPa [63].

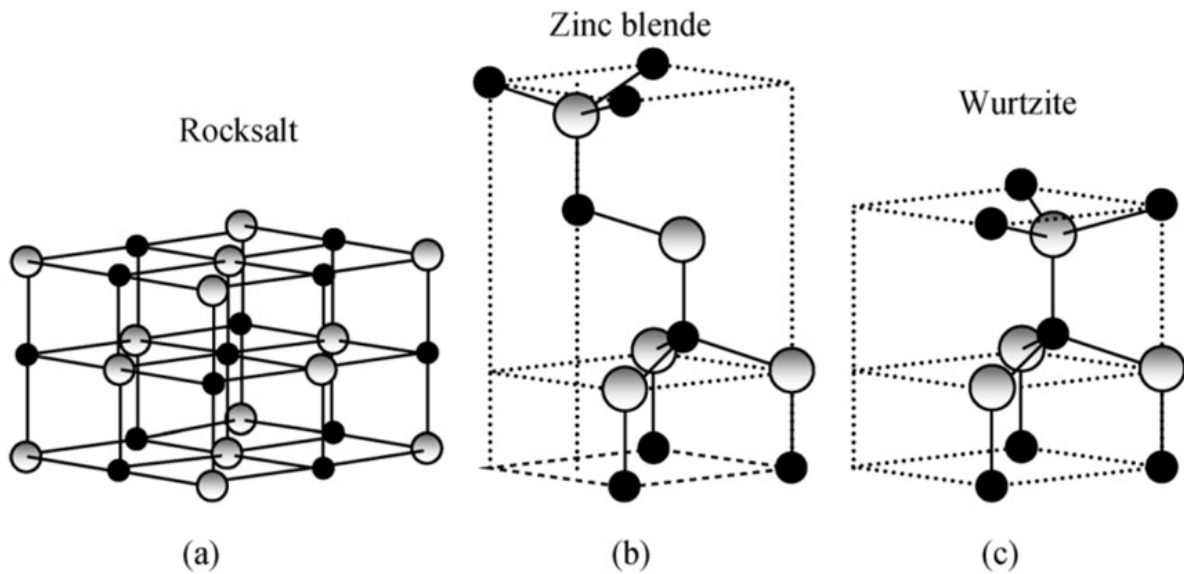


Figure 2.1: Stick-and-ball representation of ZnO crystal structures [64]:

(a) Cubic rocksalt, (b) cubic zinc blende, and (c) hexagonal wurtzite. Shaded grey and black spheres denote Zn and O atoms, respectively.

The lattice parameters at the wurtzite structure are $a \sim 3.250$ Å and $c \sim 5.205$ Å; and their ratio $c/a \sim 1.60$ is close to the ideal value for the hexagonal cell $c/a = 1.633$ [65]. ZnO has a predominantly ionic bond, as most of the II-VI compound semiconductors. Some physical characteristics of the material are shown in Table 2.1.

Although sapphire is one of the more suitable substrates for the growth of ZnO layers, high-quality ZnO crystalline layers can be obtained on different substrates [69]. Different growth methods have been used to obtain ZnO as spray pyrolysis (SP) [61], physical vapor transport (PVT), hydrothermal, chemical vapor deposition (CVD), molecular beam epitaxy (MBE), pulsed laser deposition (PLD), or chemical vapor deposition from the vapor phase of metal-organic precursors (MOCVD) [64].

Property	Values
Stable phase at 300 K	Wurtzite, P63mc
Lattice parameter a , Å	3.250 [66], 3.2495 [67]
Lattice parameter c , Å	5.205 [66], 5.2069 [67]
Density, $\text{g} \cdot \text{cm}^{-3}$	5.642 [66]
Melting temperature, $^{\circ}\text{C}$	1975 [67]
Energy band gap, eV	3.37 (at 300 K) [66, 67], 3.437 (at 4 K) [68]
Excitation binding energy, meV	60 (at 300 K) [66, 67]
Linear expansion coefficient α , $^{\circ}\text{C}^{-1}$	a_0 : 6.5×10^{-6} [67]
	c_0 : 3.0×10^{-6}

Table 2.1: Physical properties of Zinc Oxide (ZnO)

ZnO is a non-toxic and biocompatible material [70]. Due to the wide band gap ($E_g = 3.37$ eV), ZnO has a high optical absorption in the UV (320-400 nm) region. On the other hand, due to the high energy of the excitons (60 meV), it is possible an effective laser generation at room temperature (RT) [71, 72]. Combination of the ZnO optical, electrical and piezoelectric properties are used in piezoelectric devices [73], Li-ion batteries [74], light-emitting diodes (LEDs) [75, 76], gas sensors [76, 77], chemical sensors, biosensors, UV sensors or pH sensors [78].

ZnO is a material that can be grown in a wide variety of morphologies. Structures such as nanorods, nanowires, nanonails, nanobelts, nanorings, nanospirals and nanohelices have been synthesized and studied [79], in addition to the growth of bulk and layers.

Mostly, ZnO is a semiconductor of n-type conductivity due to excess of zinc atoms, which results in the presence of such inherent defects as oxygen vacancies (V_O) or zinc interstitials (I_{Zn}). The un-doped ZnO obtained by the chemical vapor deposition technique is characterized by a typical room temperature carrier concentration of $\sim 10^{16} \text{ cm}^{-3}$, that can be increased with doping by different elements up to 10^{21} cm^{-3} [80]. It was found that electron concentration changes from $5.9 \times 10^{17} \text{ cm}^{-3}$ to $4.0 \times 10^{19} \text{ cm}^{-3}$ resulted in a reduced mobility and carrier scattering time, as electron effective mass varied from $0.23 m_0$ to $0.26 m_0$ [81]. In addition, other common defects include zinc vacancies (V_{Zn}), oxygen interstitials (I_O), as shown in Figure 2.2. This scheme qualitatively represents the energy levels of intrinsic point defects in ZnO and energy transitions that can occur.

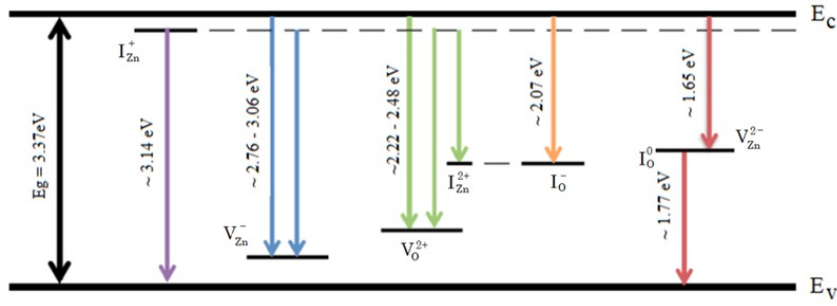


Figure 2.2: Schematic diagram showing possible radiative transitions in ZnO due to various defects, such as Zn and O interstitials, and vacancies [82]

In the wurtzite structure, the difference in electronegativity between Zn and O atoms, in combination with a low degree of symmetry, leads to spontaneous polarization in some crystallographic directions. From the point of view of obtaining thin ZnO layers with a flat surface morphology, nonpolar orientations become the best option. In this sense, nonpolar oriented ZnO obtained using MOCVD on R-sapphire are of particular interest. Moreover, the optimization of the growth parameters is very important in heteroepitaxy processes in order to obtain films without significant loss of crystalline quality.

2.1.2 Cadmium Oxide (*CdO*)

CdO crystallizes in the rock-salt structure consisting of a face centred cubic (*fcc*) lattice with a two atom basis, Cd at (0,0,0) and O at (1/2, 1/2, 1/2), with a lattice parameter $\sim 4.695 \text{ \AA}$ [83] as shown in Figure 2.3. The fundamental band gap of CdO is indirect at $\sim 0.84 \text{ eV}$ ($\sim 1480 \text{ nm}$) [84], and this is much too low for optical transparency (380 to 740 nm), therefore transmission of visible spectrum occurs at the CdO direct band gap of $\sim 2.28 \text{ eV}$ ($\sim 500\text{-}560 \text{ nm}$) [85]. Heavy carrier concentration leads to a Moss-Burshtein shift, which can increase the band gap to 3.25 eV ($\sim 380 \text{ nm}$) [86]. CdO has a high carrier concentration ($> 10^{21} \text{ cm}^{-3}$) [86, 87], which can also lead to a high conductivity. Table 2.2 shows some characteristics of the material.

Due to the characteristics listed above, CdO can be used as material for gas detectors [88,89], solar cells [90], photodetectors [91], and other photo-optical and optoelectronic devices [92–94].

There are many ways to obtain thin films and nanostructures of CdO. This wide range of processes includes MOCVD [83, 95], PLD [84], SP [96], thermal evaporation (TE) [97], PVT [92], radio frequency magnetron sputtering (RF) [93] etc. Different growth parameters will affect the structural properties of the material, leading to differences in optical and electrical characteristics.

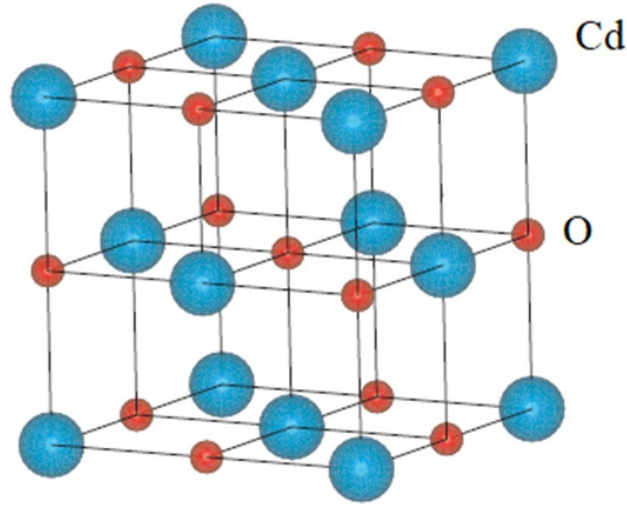


Figure 2.3: Crystal rocksalt structure of CdO [98].

Property	Values
Lattice parameter a , Å	4.695 [13, 83], 4.689 [85]
Density, $\text{g} \cdot \text{cm}^{-3}$	8.15 [13, 85]
Melting temperature, $^{\circ}\text{C}$	> 1500 [13, 85]
Indirect band gap, eV	0.84 [13, 85]
Direct band gap, eV	2.28 [85, 95]
Linear expansion coefficient α , $^{\circ}\text{C}^{-1}$	4×10^{-6} , at 27 ... 497 K [85]

Table 2.2: Physical properties of Cadmium Oxide (CdO)

Zúñiga-Pérez et al. [99] showed that the morphological and structural properties of the micrometric layers of CdO largely depend on the orientation of the substrates. The MOCVD method allowed to obtain [002] oriented CdO compounds on R-sapphire with high crystalline quality and flat layer morphology.

Despite the high number of articles devoted to CdO, there are few publications where the layers had good crystalline quality and thickness of the order of 100 nm or lesser, which could be used in some optical devices. In the works of A. Huerta-Barbera et al. [100, 101], CdO films on R-sapphire with a threshold thickness of the order 40 nm, below which island-shaped structures appear, were achieved. Using chemical etching to increase the density of inherent nucleation points on the substrate they managed to get very thin films with truly flat morphologies with thicknesses up to 20 nm. So we want to carry out an in-depth study of this well-known material in order to find the growth conditions at which the compounds has good crystalline quality and able to be used in various heterostructures, like CdTe/CdO.

2.1.3 Ternary compound of *CdZnO*

Due to the properties of ZnO and CdO they can be used in various fields. In addition, the synthesis of ternary compounds based on these binary semiconductors will further expand the scope of applications. Structures of ZnCdO (hexagonal Zn rich compound) will lead to a redshift of the band gap of ZnO and the ability to cover the visible light range. In the case of CdZnO (cubic Cd rich compound), the direct gap of CdO will be extended by the presence of Zn. In both cases, the properties of the resulting compound will depend on the content of the alloying element, but several problems will appear due to the difference in the cubic structure of CdO and wurtzite structure of ZnO, depending on this content.

Zn ions can enter into the CdO crystal structure in a substitutional position, and the Zn content will affect the structural, optical, and electrical properties of the material. Influence of the alloying element on optical characteristic was shown [102] in $Cd_{1-x}Zn_xO$ ($x \leq 10\%$) thin films prepared on glass substrates by the spray pyrolysis technique at $470^\circ C$. At higher concentrations ($20\% < x < 80\%$) the films presented a mixed structure of cubic and hexagonal phases. When the concentration of Cd increases from pure ZnO one can observe in addition to the variation of the film colour (from transparent to yellow), a variation in the average transmittance, which is about 60-70 %, which is lower compared to pure ZnO ($\sim 90\%$) [31]. On the contrary the introduction of more zinc in the CdO structures will increase the transmittance and the width of the band gap due to the blue shift of the edge of the bandwidth [18].

In CdZnO ternary compounds, depending on the Zn concentration, X-ray patterns associated with the (200) and (111) planes corresponding to the cubic crystal structure of pure CdO will gradually shift to higher angles and will be replaced by peaks related to the (100), (002) and (101) planes of hexagonal structure of ZnO [31, 103].

In reference [102] was showed that, under its experimental conditions, if the threshold of 3 % solubility of Zn in CdO films was exceeded, the intensity of XRD peaks decreased, which indicated a decrease in the crystallinity of the compound when defects appear in the crystal structure due to an excess of Zn inclusions in the lattice structure.

With a decrease in the concentration of Cd in the ternary compound CdZnO, the size of the crystalline grains usually decreases. Theoretically, an increase in grain size, thickness and packing density of the film should have a negative effect on the transmittance, which has an opposite dependence to them [104]. An increase in polycrystallinity when it is alloyed with an additional element will lead to unevenness in the lattice and therefore scattering and absorption increase and the transmittance must inevitably be reduced. Earlier, our research group showed [29] that at a low concentration of Zn ($Cd_{0.95}Zn_{0.05}O$) the mobility of compounds increases, with a gradual decrease at a higher concentration of Zn. The initial rise of mobility indicates the good crystalline quality of the CdZnO layers, but with increasing of Zn content into

the cubic crystals, they start to be oriented in different directions with further phase mixing of the cubic and wurtzite crystal structure. Degradation of electron mobility led to rise in the resistivity of CdZnO alloy. Along with growth of the Zn content, carrier concentration has upward trend that can be responding to the formation of intrinsic defects. At a certain concentration of zinc atoms, the oxygen vacancy (V_o) will begin to decrease, since the Zn^{2+} ions tend to form separate ZnO centers with O^{2-} , and, consequently, the resistivity begins to increase [18].

The growing method, growth time and temperature, substrate and other conditions of the synthesis of the compounds will affect the properties of the resulting films. The authors of ref. [20, 24, 105] showed that increasing the growth temperature, the Cd content in the CdZnO ternary compounds can decrease. A high growth temperature contributes to the formation of large crystal grains [23]. On the other hand thermal annealing (as 450 °C for SP or 300-600 °C for RF magnetron sputtering method), is an important way to improve the quality of crystals and the optical properties of thin films. In the papers [102, 106] it was presented that annealing can favor a better crystallinity of the material.

A simplified equation ($E_g = 3.36 - 0.063x$) for the band gap of the $w - Zn_{1-x}Cd_xO$ compound at 10 K, was proposed in [24]. A more complex expression for the optical band gap was presented in [22, 107]:

$$E_g^{CdZnO} = (1 - x)E_g^{Zn} + xE_g^{CdO} - bx(1 - x) \quad (2.1)$$

where, x is the Cd content, b is the bending parameter, and E_g^{CdO} and E_g^{ZnO} are the band gaps of the CdO (~ 2.28 eV) and ZnO (~ 3.37 eV), respectively. In their work Bakke et al. [23] gave approximate equations for the parameters of the crystal lattice for the wurtzite phase of CdZnO ternary compounds at a high concentration x of Zn ($x > 50$ %):

$$a_{hexagonal} = 3.58 - 0.33x; c_{hexagonal} = 5.85 - 0.54x \quad (2.2)$$

In recent years, there have been many publications devoted to CdZnO, but the overwhelming majority of the obtained compounds were polycrystalline. Most ternary structure studies focused on compounds rich in Zn with a wurtzite phase. A. Huerta-Barberá in her work [101] investigated the inclusion of cadmium in the hexagonal lattice of ZnO and Zinc into the cubic one of CdO. For the first case, the study of the structural parameters as a function of the growth temperature made possible to optimize the temperature at which is possible to introduce Cd more than 8.5 % into the hexagonal lattice. For $Cd_{1-x}Zn_xO$ compounds with different growth times and Zn content, a maximum Zn incorporation of 10.4 % into the cubic lattice was found at which a unique out-plane orientation [002] remains and for higher zinc concentrations the coexistence of phases appear. Also for 10.4 % of Zinc content a very low value of resistivity was shown, which is, not only a record value for this type of material, but also comparable to other

transparent conductive oxides that dominate the market today, opening up new possibilities for optoelectronics.

2.2 Cadmium telluride ($CdTe$)

$CdTe$ has a crystal structure of zinc blende [85]. This structure is formed by two intersecting face-centered cubic sublattices (one for Cd atoms and the other for Te atoms), with the unit cell shifted by $1/4$ along the $[111]$ direction between each other. Its common unit cell contains 8 atoms, 4 of Cd and 4 of Te . Atoms are located in such a way that around each atom there are four atoms of the other element that are located at equal distances from each other are located at the vertices of the tetrahedron with the center in the other element. The structure of $CdTe$ does not have a center of symmetry, as in the case of the structure of diamond, since the atoms that form the basis are different. The view of the $CdTe$ unit cell and the coordinate system are shown in Figure 2.4.

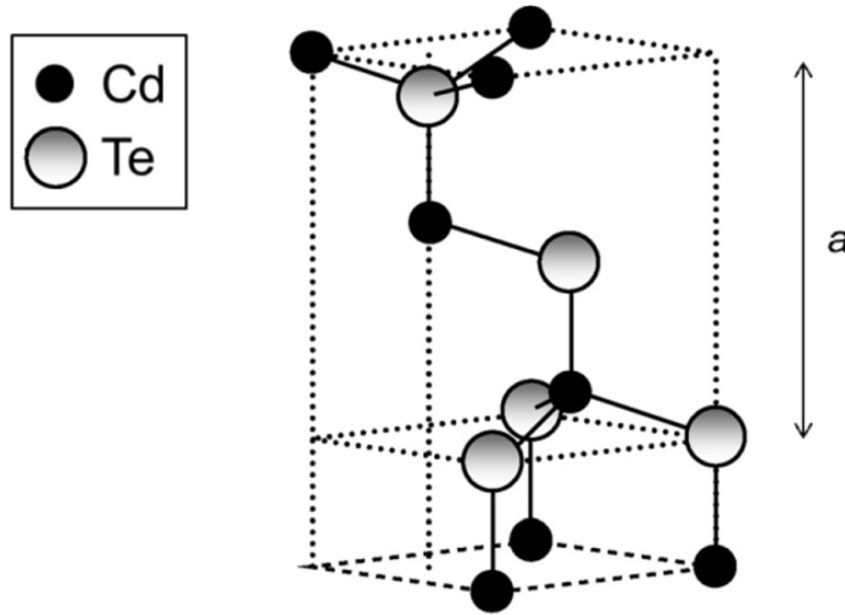


Figure 2.4: The unit cell of cubic zinc-blende crystal structure for $CdTe$. Dotted lines define the boundaries of the unit cell, and solid lines represent $Cd-Te$ bonds.

$CdTe$ is a direct-band-gap $E_g \sim 1.49$ eV material, which is close to the optimal band gap, theoretically established, for solar cells (1.28 eV) [108], and a high optical absorption coefficient ($> 5 \times 10^5 \text{ cm}^{-1}$) above the gap [109]. Some of the basic structural properties of $CdTe$ are listed in Table 2.3. Depending on the process of obtaining the material, some of the characteristics of $CdTe$ can vary, especially the electrical properties are very sensitive in respect to doping and presence of defects in the material.

2.2. Cadmium telluride (*CdTe*)

Property	Values
Lattice parameter a , Å	6.481 [59, 110], 6.46 [85]
Density, $\text{g} \cdot \text{cm}^{-3}$	5.85 [59], 5.87 (at 4K) [85]
Melting temperature, $^{\circ}\text{C}$	1092 [59, 85]
Energy band gap, eV	1.49 (1.606 at 4K) [59], 1.475 [85], 1.512 [110]
Linear expansion coefficient α , $^{\circ}\text{C}^{-1}$	$4.932 \times 10^{-6} + 1.165 \times 10^{-9}T + 1.428 \times 10^{-12}T^2$ at -253 ... +147 $^{\circ}\text{C}$ [85]

Table 2.3: Physical properties of Cadmium Telluride (CdTe)

CdTe provides a good performance over a wide temperature range and it is used as infrared optical material for optical windows and lenses [111]. Besides it can be used in various science fields, such as solar cells [112, 113], LED [47], [114], some biological application [115, 116], X-ray and gamma detectors [117]. CdTe can be alloyed with mercury to make infrared material detector (HgCdTe) [118]. CdTe, alloyed with a small amount of zinc (up to 20 %), is an excellent solid-state X-ray and gamma-ray detector (CdZnTe) [118, 119].

CdTe films can be obtained by different physical and chemical method, such as space sublimation [120], SP method [121], chemical bath deposition (CBD) [122], MOCVD [123], thermal evaporation [124], PLD [125, 126], sputtering [127], electrodeposition [128, 129] and others. CdTe is shown as a semiconductor of particular interest, both for its applications and for its capabilities, although the devices produced with it are below its theoretical characteristics and potentialities, often due to defects whose control, probably, has not been optimized in the growth process.

I. Mora-Seró in his work showed [59] that the polarity of the surface and the orientation of the substrate affect both the texture of the layer and the growth rate. Thus, the substrate orientation is of great importance in the growth of layers. The study showed that, GaAs can be adequated for the preparation of CdTe. Depending on the growth conditions one can grow CdTe with (111) or (100) orientation over (100) GaAs, while growth over (111) GaAs always gives (111) oriented CdTe by using MOCVD. Obtaining layers of one or another orientation on GaAs, as well as polycrystalline layers with grains with both orientations or even with different ones, will depend on the previous treatments to which the substrate is subjected.

Despite the wide variety of substrates (GaAs, Si, InP, InSb, sapphire, and others), as well as the possibility of creating heterostructures of the CdTe/CdS or CdTe/CdSe type, the search for alternative substrates and compounds for heterostructures continues. In [130] authors used bi-layer TCO structures CdO:Sn/SnO as substrate for the fabrication of CdS/CdTe solar cells that exhibited a conversion efficiency of 14.3 %. The TCO layers were deposited using MOCVD, and closed-space sublimation was used to prepare the semiconductor layers - CdS and CdTe.

Other authors [131] fabricated $Cd_{0.9}Zn_{0.1}S/CdTe$ photovoltaic device on substrates of different TCOs: fluorine doped tin oxide (FTO), ITO and CdO. The device layers on the CdO substrate delaminated but devices with 0.8 μm CdTe absorber layer were successfully made onto 240 nm thick CdS onto CdO and compared favourably with the silmlar device on ITO. Solving the growth problem, fabrication and optimization of $CdTe/CdO$ and $CdO/CdTe$ heterostructures could be of great interest for applications in short-wavelength optoelectronic devices, where CdO can be chosen as window material and CdTe as absorber for the fabrication of $n\text{-CdO}/p\text{-CdTe}$ heterojunction solar cells.

As a rule, ternary alloys formed by substituting Mn for the group II element in the $A_{II}B_{VI}$ lattice retain the crystal structure of the "parent" $A_{II}B_{VI}$ compound [134]. Exceptions to this rule are $Zn_{1-x}Mn_xS$ and $Zn_{1-x}Mn_xSe$, which exhibit the structure of the cubic $A_{II}B_{VI}$ host for low Mn content, but above a certain value of x show the wurtzite structure. In the case of $Zn_{1-x}Mn_xS$, the ZB structure is maintained at a Mn concentration of 10 % or less (Figure 2.5). A natural upper limit on the Mn mole fraction x in DMS is imposed by the fact that MnB_{VI} does not crystallize in the zinc blende or wurtzite structures [134].

Next we will consider some characteristics of $ZnMnTe$ and $ZnMnS$ compounds, as materials for potential use in modern electronics.

2.3.1 Zinc manganese telluride ($ZnMnTe$)

One of the most typical representatives of DMS is $Zn_{1-x}Mn_xTe$, which can be considered as mixed of crystalline systems between two zinc-blended materials, ZnTe and MnTe [135]. In this compound, Zn^{2+} ions are replaced by Mn^{2+} ions. The Figure 2.6 shows a primitive cell of ZnTe containing 32 atoms in equal proportion, where one of Zinc nodes is substituted by an Mn atom. The crystal ionic radius of Zn^{+2} is 0.88 Å, but Mn^{+2} is depends on the spin state, therefore can be 0.81 Å for the low spin state and 0.97 Å for the high spin state [136]. The increase in the Mn content will lead to an increase in the lattice parameter of the compound $Zn_{1-x}Mn_xTe$, in addition to an increase in the band gap, and the generation of a certain density of punctual defects of the vacancy and interstitial types which can disturb the lattice parameter. Vacancy and their more complex systems based on should, as a rule, decrease the lattice parameter, and atoms in interstitials positions should increase it [137].

In references [134, 138] it was shown that $Zn_{1-x}Mn_xTe$ exhibits the zinc blende (ZB) structure with the composition $x < 0.86$. In respect to the band gap, it changes from an energy band gap of 2.28 eV (ZnTe) to 2.9 eV (zincblende MnTe) [139]. when the Zn^{2+} ions are replaced by Mn^{2+} ions.

The authors of ref. [140] showed relation between the lattice constant and Mn content x measured by RBS and EDX for $Zn_{1-x}Mn_xTe$ epilayers, where with increasing Mn content the lattice parameter varied from 6.1037 to 6.3595 Å. The result is consistent with the Vegard's law, according to which the lattice parameter of a ternary alloy should be linearly proportional to the chemical composition.

The lattice constants perpendicular to the interface ($a \perp$) of the $Zn_{1-x}Mn_xTe$ layers grown on GaAs (100) were found by using the separation between the GaAs substrate (400) peak and the $Zn_{1-x}Mn_xTe$ (400) peak of double crystal rocking curves [141] and turned out to be equal:

$$a \perp (x) = 6.1056 + 0.2403x \quad (2.3)$$

Apart to spintronic applications, ZnMnTe compounds can be used in other fields where non-magnetic properties of the material can be useful. It was reported that ZnMnTe alloyed with O could be considered as a suitable material for photovoltaic [142] or thermoelectric [143] devices. On an other hand, ZnMnTe alloyed with Cr may be a good candidate for solid-state infrared lasers [144].

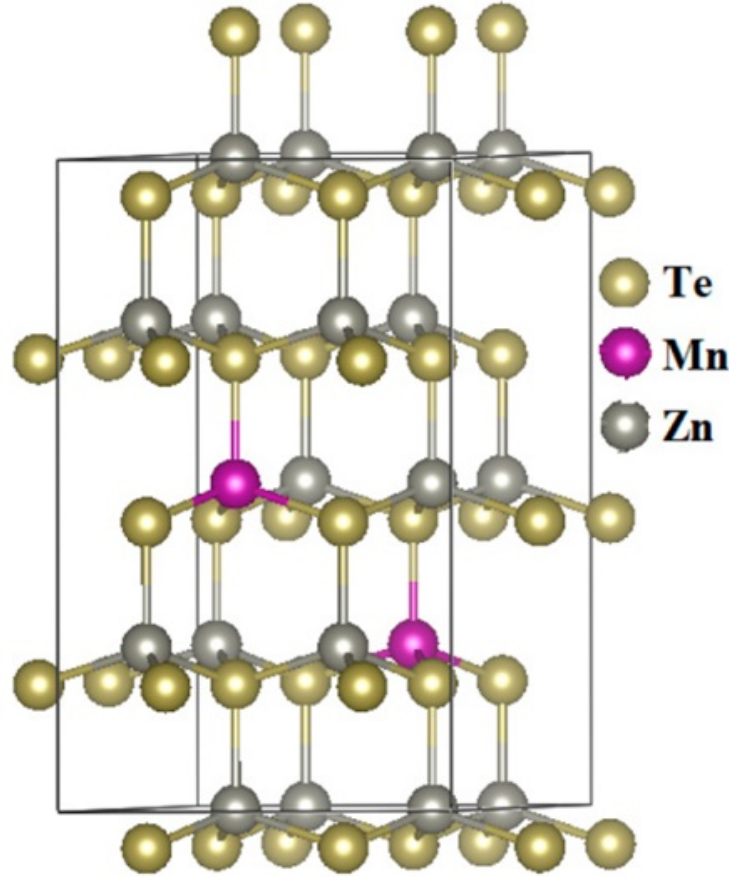


Figure 2.6: Representation and labeling of unit cell structure for $Zn_{1-x}Mn_xTe$ crystalline solid state [145]

There are many different methods for preparing ZnMnTe compounds, among which metal-organic vapor phase epitaxy (MOVPE) [41], molecular beam epitaxy [42], pulsed laser deposition [43], Bridgman method [146], hot-wall epitaxy [140], etc.

In some methods, a temperature of the order of 400 °C is required to obtain the $Zn_{1-x}Mn_xTe$ compound, but sometimes this value is higher. Thus, the temperature of the Bridgman furnace should be maintained at about 1000 °C and for low Mn concentrations, good quality large crystals of $Zn_{1-x}Mn_xTe$ can be grown, but with high contents of Mn the quality of the crystals is worse [134]. Taking into account the potential applications of this material, the use of relatively low-cost growth methods which could make possible to obtain films of good crystalline quality, is an interesting challenge.

2.3.2 Zinc manganese sulfide ($ZnMnS$)

Manganese alloyed zinc sulfide ($ZnMnS$) is a semiconductor with transparency in the UV-visible region. It is used as main material for thin film phosphors devices [45], cathode-ray tubes [147], antireflection coatings [148], light-emitting diodes [149], thin film electroluminescent displays [150], and photonic technologies [151]. Unit cell of pure ZnS with alloyed Mn atom at Zn -site is shown in Figure 2.7.

ZnS exists in two different crystal structures: cubic zinc blende and hexagonal wurtzite structure. In the cubic crystal structure of ZnS , the optical properties are isotropic. The crystal structure of the zinc blende is a face-centered cube with $a \sim 5.4093 \text{ \AA}$, belonging to the space group $F\bar{4}3m$. The transition from ZB to the wurtzite structure occurs at $1020 \text{ }^\circ C$. The hexagonal space group is now $C6mc$ with lattice parameters of $a \sim 3.811 \text{ \AA}$ and $c \sim 6.234 \text{ \AA}$ [152].

The α - MnS phase is a stable form of MnS . It has a rock salt structure with a lattice parameter $a \sim 5.2236 \text{ \AA}$. On the other hand, β - MnS is a metastable form that has a cubic zinc blende structure with $a \sim 5,600 \text{ \AA}$, while the γ - MnS phase is a metastable form with a hexagonal wurtzite structure with $a \sim 3,976 \text{ \AA}$ and $c \sim 6,432 \text{ \AA}$. Metastable forms can be stabilized by the formation of solid solutions with ZnS , in which Mn atoms are substitutional at some Zn sites.

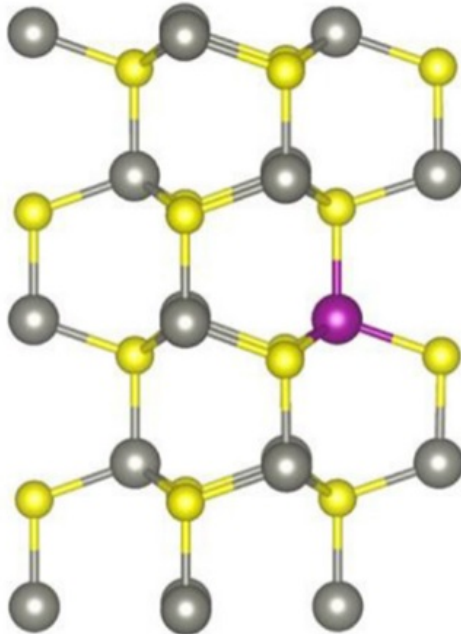


Figure 2.7: The relaxed wurtzite structures of ZnS alloyed with Mn . The gray, yellow and purple balls represent the Zn , S and Mn atoms, respectively. [153]

The lattice parameter of the films of the $Zn_{1-x}Mn_xS$ samples obtained at different levels of alloying, can be calculated using the equation for the determination of average distance of cations-cations (d_c) [154]:

$$d_c(Zn_{1-x}Mn_xS) = (3.8300 \pm 0.0005) + (0.1391 \pm 0.0010)x \quad (2.4)$$

providing a value of $d_c=3.843$ Å for $x=0.10$. The lattice parameters a and c for a wurtzite crystal are then obtained from the relations [154]:

$$a = d_c, c = \left(\frac{8}{3}\right)^{1/2}d_c \quad (2.5)$$

Mn alloyed ZnS thin films have been obtained by using different physical and chemical methods such as resistive thermal evaporation [38], chemical bath deposition [44], radio frequency magnetron sputtering [45], vapor phase [155], chemical co-precipitation [156], liquid-solid-solution (LSS) [157], molecular beam epitaxy [158], metal-organic chemical vapor deposition [159] and hydrothermal method [160]. As a substrate for obtaining nanocrystalline $ZnMnS$ thin films, it is possible to use different materials among them, glass, silicon, and quartz [44] are frequently applied.

It was shown in [160] that the crystal size of Mn^{2+} -alloyed ZnS nanoparticles synthesized by the hydrothermal method and treated at $90^\circ C$ were in the range $\sim 2.8 \pm 0.1$ nm and the size had no the apparent change with the content of Mn^{+2} ions from 1 % to 20 %. On the other hand, the crystal sizes of $ZnMnS$ (10 %) nanoparticles prepared by this method slight increase in the range $2.5 \sim 3.4$ nm when synthesis temperature rise from $70^\circ C$ to $110^\circ C$. Authors in reference [161] presented that an increase in the Mn concentration from 1 to 40 % leads to a gradual decrease in the lattice parameter from 5.402 to 5.316 Å. Moreover, as in the previous work, the particle size did not depend on the Mn content and it was in the range of 1.8 ± 0.2 nm. Therefore, obtaining high-quality compound films by low-cost methods is a promising way to produce switching devices, creation of buffer layers for photodetectors and sensors, resistors, transparent heating elements, electro-optical modulators, electromagnetic protective layers, optical coatings, window photoconverters, etc.

2.4 Metallorganic chemical vapor deposition technique

2.4.1 Metallorganic chemical vapor deposition system

Metal Organic Chemical Vapor Deposition (MOCVD), sometimes called Metal Organic Vapor Phase Epitaxy (MOVPE), is a method that is based on the gas-phase transfer of constitutive elements (usually in the form of the precursor) to a substrate where they will react. The deposition ultimately occurs through a chemical reaction on the surface of the substrate and usually leads to high-quality deposition of thin films under optimized growth conditions. This method is well suited for the production of layers with high-quality surface morphology and precise control of the thickness and uniformity used for different types of devices: lasers, LEDs, photocathodes, heterostructural bipolar transistors, thin-film transistors, transparent conducting oxides, photodetectors, and solar cells [80, 162, 163]. Although there may be some discussion in the name of the method, it is not significant. If MOVPE can be represented as epitaxial growth with a given relationship between layer and substrate structures, then MOCVD will have a more general meaning, which includes the growth of both epitaxial and non-epitaxial layers.

In this section, we briefly describe the MOCVD growth technique. The main processes occurring inside the MOCVD reactor will be considered, and the features of the system used during this work will be emphasized. Growth conditions that were used to grow ZnO, CdO, CdTe films and structures based on them will be presented.

Basic concepts of the growth process

Figure 2.8 is a diagram of the processes that occur inside the MOCVD reactor. The growth process takes place by introducing precursors into the main gas flow. Material grows at the reactor, where heated substrates are located. The precursor are driven by an incoming inert gas, usually H_2 , N_2 , He , or Ar . Although the use of hydrogen is not always the best choice since hydrogen can react with organic radicals. After entering the reactor, diffusion and convection processes take place; the precursors will pyrolise and reach at the surface of the substrates where adsorption will occur. As the precursor approaches to the substrate and it is broken (pyrolised), they can be adsorbed onto the surface of the substrate. Under adequate conditions, when there is an energetically favorable sites for the growth, chains of physical and chemical reactions can occur at the surface. The processes of adsorption, diffusion, chemical reactions and the introduction into the lattice leads to the formation of units of ZnO, CdO, CdTe or other materials, depending on the growth parameters. As a result, a growing film and a by-products are formed, which should be removed from the reactor in the main flow, to limit the effects on the further film growth process [58].

All processes that occur sequentially in the reactor can be listed as [164]:

1. Transport of precursors to the growth zone of the reactor.
2. Transfer of precursors from the main gas flow onto the substrate surface.
3. Adsorption of precursors on the surface of the substrate.
4. Superficial diffusion, chemical reactions including pyrolysis, nucleation and crystal formation.
5. Desorption by-products, unadsorbed or unreacted reagents.
6. Transfer of reaction by-products from the substrate surface into the main gas flow.
7. The exhaust of reaction-products outside the growth region.

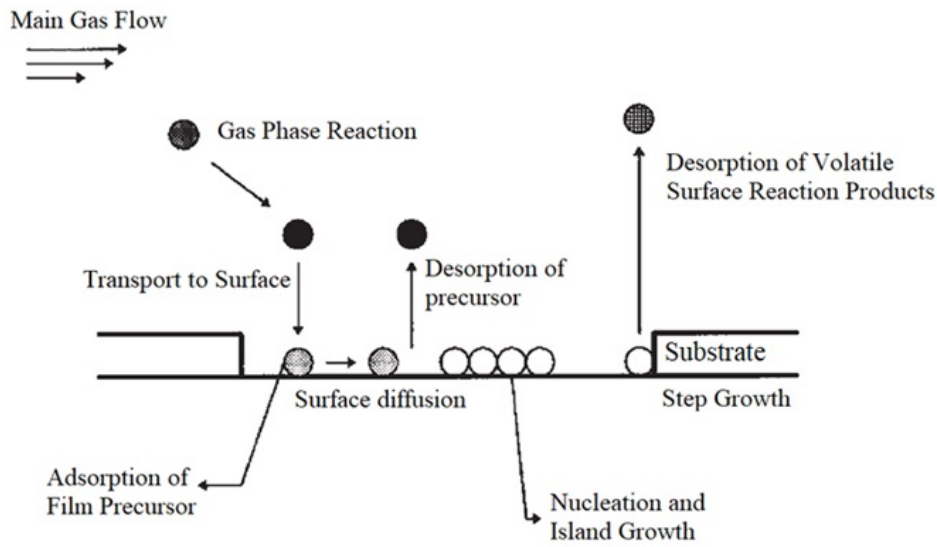


Figure 2.8: Precursor transport and reaction processes in the CVD system [165].

Since these steps are performed sequentially, the overall speed of the growth process will be determined by the speed of the slowest process. On the other hand, although the slowest process limits the speed, when a balance is reached, the crystal growth occurs in stationary conditions. Jones in his work [165] showed that the growth rate depends on the temperature of the substrate during the growth of the material (Figure 2.9).

At low temperatures, the surface processes take place slowly due to the speed of the surface reactions, which are sensitive to temperature; therefore, the growth process is kinetically limited by the surface reaction. This region is normally called the region of kinetic growth control and the growth rate increases exponentially with the rising of substrate temperature according to the Arrhenius equation [165]:

$$Growth_{rate} \propto \exp\left(-\frac{E_A}{RT}\right) \quad (2.6)$$

where E_A is the apparent activation energy, R is the gas constant and T is the temperature in Kelvin. Since the growth rate of the film is controlled by chemical kinetics, the uniform film thickness can be achieved by minimizing temperature fluctuations over the substrate surface. In this growth zone, the substrate is of great importance, since its nature and morphology largely affects the surface processes that limit the reaction.

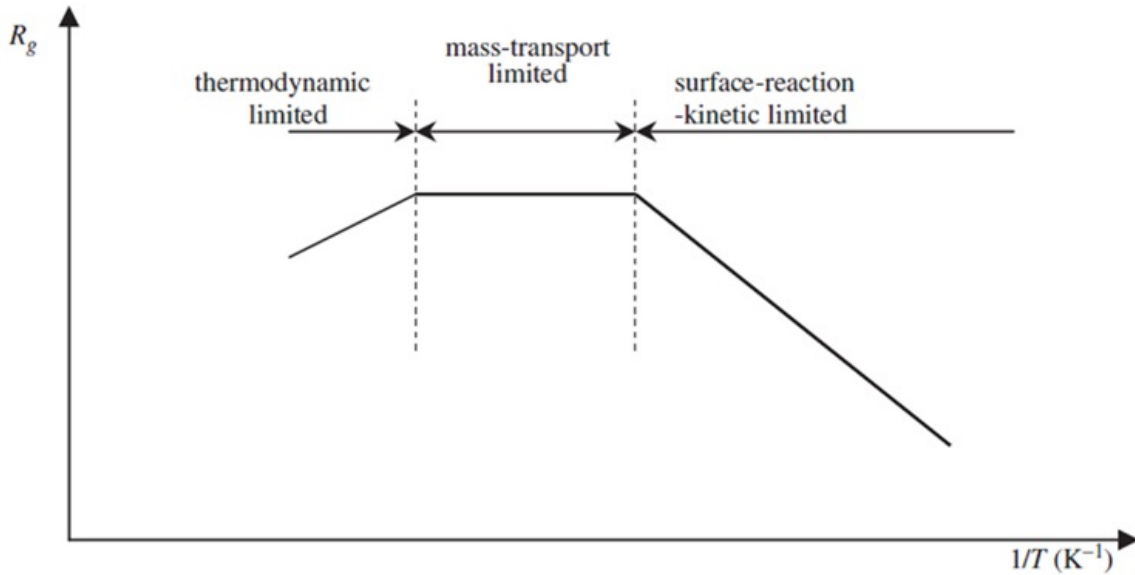


Figure 2.9: Plot of the normalized MOCVD growth rate as a function of growth temperature [165].

As the temperature increases, the dependence of the growth rate on temperature shifts to the diffusion-limited region, since the growth temperature increases the reaction rate exponentially, while the reaction rate of the diffusion process slows down until the diffusion process becomes limiting. The transition from one region to another occurs gradually. In this region, the growth rate changes relatively little with temperature and mainly depends on the process of gas-phase transfer to the substrate surface, therefore, in this region, hydrodynamic conditions play a decisive role in the growth rate [164].

In addition to these two regions, a third region is observed where the growth rate decreases with increasing temperature. This decrease can be associated with various phenomena that become energetically favorable at high temperatures, such as the formation of a "parasitic" homogeneous reaction, a decrease in the amount of reagents due to their deposition on the walls of the reactor, re-evaporation of material from the layer, or desorption of reagents from the solid surface. This region is called a zone limited by thermodynamic processes [164].

MOCVD System Description

For a successful crystal growth using the MOCVD method, it is necessary to use a complex experimental system that guarantees the quality of the material obtained and the safety of working with hazardous substances, such as metallorganic precursors. Therefore, the MOCVD system is not only the reactor where crystal growth reactions take place, but also a complex net of valves and pipelines that control the exhaust gases and precursors entering the reactor [166].

In our case thin films of materials of II-VI group were obtained in a horizontal quartz reactor (Quantax 226) of the VENT-RUN type. The MOCVD system consists of the reactor itself, the gas transfer system and the gas exhaust system. Figure 2.10 presents a simplified diagram of the MOCVD system of the Vent-Run type, gas transfer lines, evacuation path, location of the reactor and bubblers with metallorganic (MO) precursors. The flow of each of the lines is controlled by Mass Flow Controllers (MFC), which we will briefly describe in the next subsection.

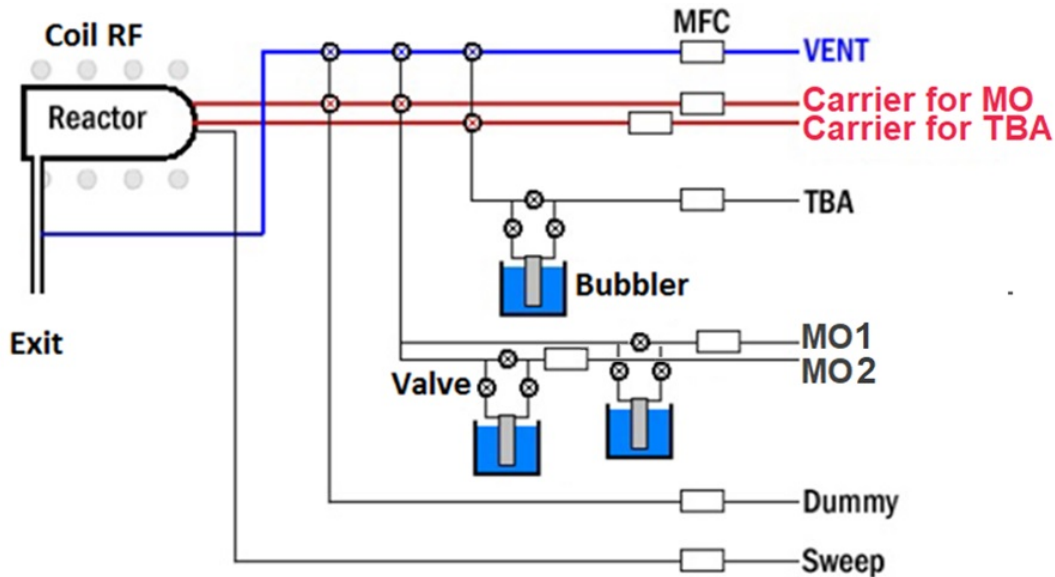


Figure 2.10: MOCVD horizontal cell configuration

At rest condition, the system is purged by Hydrogen with high purity, which due to its potential danger, must be outside in a well-ventilated area.

All processes during the experiment are controlled by console. The console controls the valves with compressed air that are closed or opened, depending on the growth step. Different carrier gases can be used depending on the objectives of the experiment. During system operation, the gas is distributed to two transport lines: *VENT* and *RUN*.

The *VENT* branch is sent directly to the exit of the system, without passing through the reactor, and is used as an auxiliary gas line for drive out the carrier gas and precursors that do

not have to pass through the reactor at some particular growth stage. In turn, with the help of the *RUN* branch, various flows inside the reactor are controlled. The step of the experiment defines which of the lines will be activated. To ensure stable operation of the system, it is necessary that the pressure in both lines be maintained at the same level, due to pressure compensation by other lines throughout the entire growth process. This allows avoiding the possible formation of vortices in the main gas flow or the appearance of reverse voids when redirecting the *Run-to-VENT* line or vice versa. For this purpose, an electronic regulator is used, which controls the branch output and the pressure in the branches, as well as two *SWEEP* and *DUMMY* compensating gas lines. The *SWEEP* line allows gas to directly enter the reactor through a side inlet to balance the flow in the reactor and helps to hold the precursors inside the reactor. *DUMMY* line is used in the steps before and after growth when we do not introduce precursors into the reactor. *DUMMY* line will always be displayed as the sum of the injection lines of the precursors involved in the growth and we can always keep the same amount of flow inside the reactor and avoid possible turbulence or vortices during the growth stage.

Figure 2.11 shows the appearance of the MOCVD system reactor used to grow the thin films presented in this thesis. The reactor has several inlets for the delivery of precursors and lines for stabilizing the gas flow. The top inlet is used for the intake of metal precursors and the bottom inlet for the entrance of the oxygen precursor. This prevents or reduces the interaction and preliminary reactions in the vapor phase in the internal lines. Precursors are located in special containers called Bubblers. The name is due to the fact that the carrier gas enters the container with the precursor through a tube and forms bubbles that are saturated with precursors vapors and then transported by the carrier gas to the outside. Bubbler's outlet lines are heated to temperatures above 50 °C to avoid possible condensation along them.

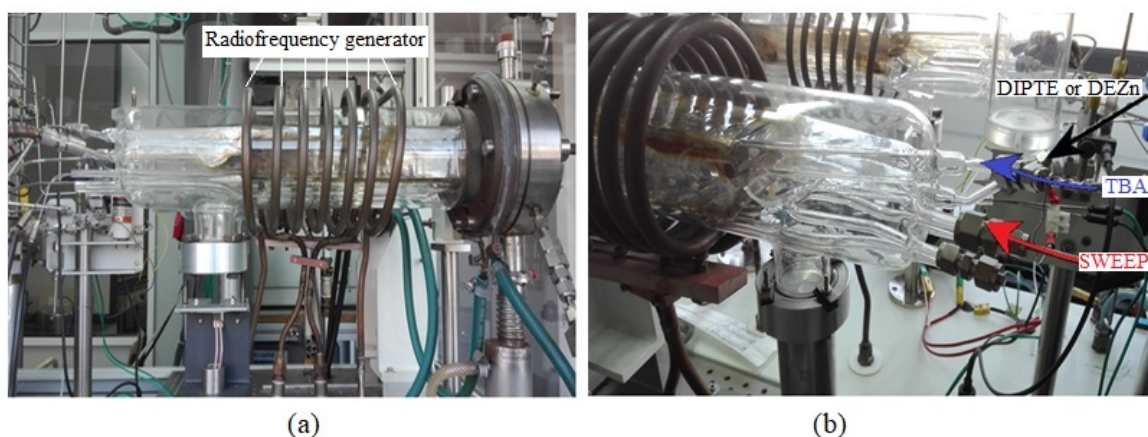


Figure 2.11: Side (a) and Rear (b) view of the reactor, with the designation of independent inputs.

Inside the reactor are two fundamental elements, such as the deflector and the susceptor. The deflector is a rectangular cover made of quartz, which is used to conduct the gas flow inside the reactor, while the susceptor is the element, constituted by graphite, which will heat the substrate to the desired growth temperature. Heating is provided by an external radiofrequency generator. The surface of the susceptor is coated with a layer of silicon carbide (SiC) to prevent any diffusion of impurities from the graphite, as well as the absorption of gas by graphite pores. The substrate holder is made of molybdenum, which, due to the high thermal conductivity, ensures uniform temperature at the substrate, which is controlled from the control panel using two K-type thermocouples. The distance between the thermocouples and the substrates and the corresponding temperature difference make necessary to pre-calibrate the temperature.

Finally, all gases, including those that have passed through the VENT line and which, therefore, have not passed through the reaction chamber, are collected in a common pipe under the reactor and removed to the atmosphere after passing through the appropriate filters.

2.4.2 Electronic system of MOCVD

The carrier gas, together with the precursor, enters to the reactor chamber to provide the formation of films of the necessary materials. The amount of flow entering the reactor is controlled with the help of valves called Mass Flow Controllers (MFC). The value is measured in units of *Volume/Time* and under standard pressure and temperature conditions the units are *sccm* (standard cubic centimeters per minute) or, in the case of main branches, *slm* (standard liters per minute). Mass flow controllers consist of a flow sensor, bypass, valve, and control circuit, as shown in Figure 2.12 [167].

MFC in working position directs the flow of gas from the bubbler to the reactor. A portion of the main carrier gas flow is introduced into the valve through the base. In the VENT position, the flow is directed to the external circuit connected to the gas outlet, which allows stabilizing the flow of precursors before transferring it to the reactor. To achieve optimum system performance, the pressure on the vent side and entrance side must be balanced.

During MFC operation, the gas flow is divided into two parts, so that one part passes through the sensor and the other through the bypass. The amount of gas that passes through the sensor is proportional to the total amount of gas, so by measuring it, we get an indicator of the total flow that passes through the MFC. The sensor consists of a capillary tube with two thermistors that surround it at the inlet and at the outlet. When the gas begins to flow into the sensor, a temperature difference occurs between the inlet and the outlet thermistors, thermal balance is lost and the temperature distribution of the sensor changes. This change causes the change in the resistance and it is measured as a change in a signal from 0 to 5 V. The signals at the input and output resistive elements are compared and the circuit acts on

the control valve, so the difference between these two signals is zero. This circuit in the form of a loop with feedback provides protection against changes in pressure and temperature in the environment and ensures stable operation. In other words, MFC always maintains the target value by opening or closing the valve. The difference in temperature created between the two elements depends on the mass flow and the specific density and heat capacity of the gas. The accuracy of the MFC we use in the MOCVD system is 1 % of the full scale.

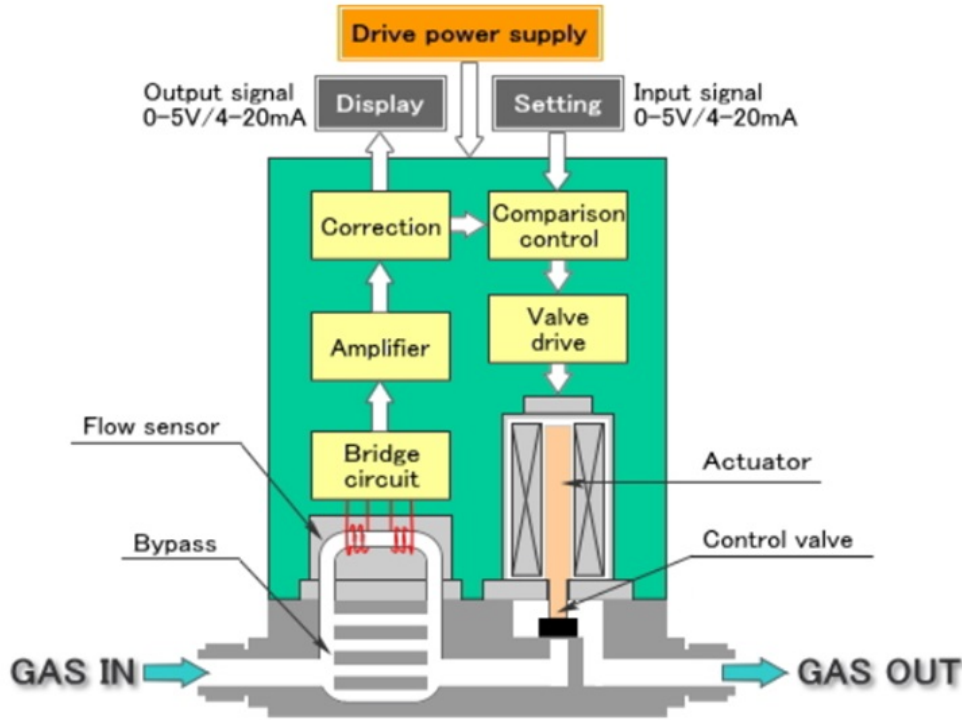


Figure 2.12: Structure of Mass Flow Controller [167]

Thermocouple-based MFCs typically use nitrogen as a reference for calibration. In the case using the other gases, their specific heat capacity and density may not match, what will affect the value of conversion factor (C.F) and the actual flow rate and can cause abnormal operation or abnormal flow. Table 2.4 shows the multipliers that should be applied to the MFC readings for the different gases used in the MOCVD processes.

Gas	N_2	He	H_2	O_2	Ar	Air
Conversion factor	1.0	1.4	1.0	0.993	1.4	1.0

Table 2.4: Conversion factor for MFC application for various gases [167].

2.4.3 Our working system

For optimal growth of layers of *II-VI* group materials, a modified MOCVD Quantax 226 system was used by our Crystal Growth group at the University of Valencia. The working system has two horizontal reactors of the Vent-Run type (Figure. 2.13), which work alternately to grow different materials. The system is controlled by a control panel (Figure 2.14), which regulates the transport lines, as well as the opening and closing of various system valves and the growth temperature. The transport lines connect the bubblers with the precursors to the reactor chamber. The bubblers themselves are located in thermostatted baths, where the required temperature is maintained depending on the task in hand (Figure 2.15).

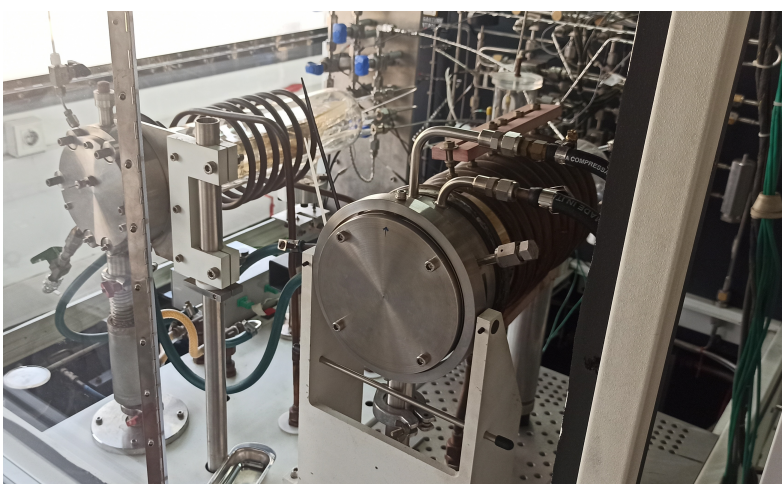


Figure 2.13: Photographs of the reactor cell cabine



Figure 2.14: Control panel of MOCVD Quantax 226 system

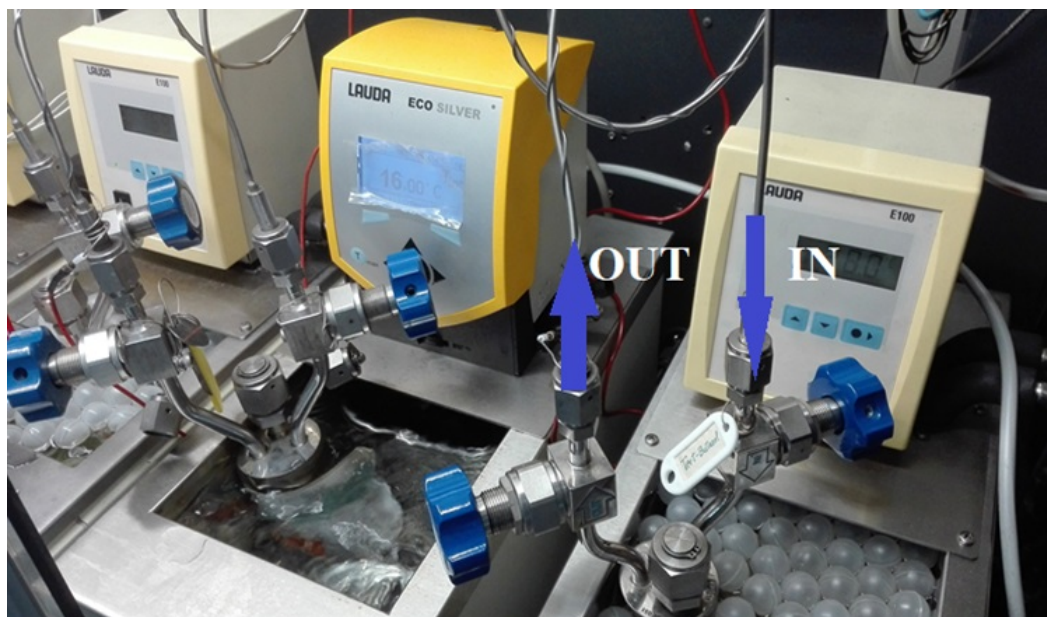


Figure 2.15: Photographs of thermostatic baths for precursor cooling

Figure 2.16 shows the components that are located inside of the reactor during the material growth. To prevent contamination during the formation of films, it is necessary to get rid of the residual deposition of the previous experiment. The precipitate formed after the experiment is removed using aqua regia (a mixture of hydrochloric and nitric acid $HCl : HNO_3$ in a volume ratio of 3:1) in a well-ventilated cabinet, after which each part is rinsed abundantly with ultrapure water. Finally, the pieces are dried for at least 12 hours to avoid the remaining moisture entering the reactor.

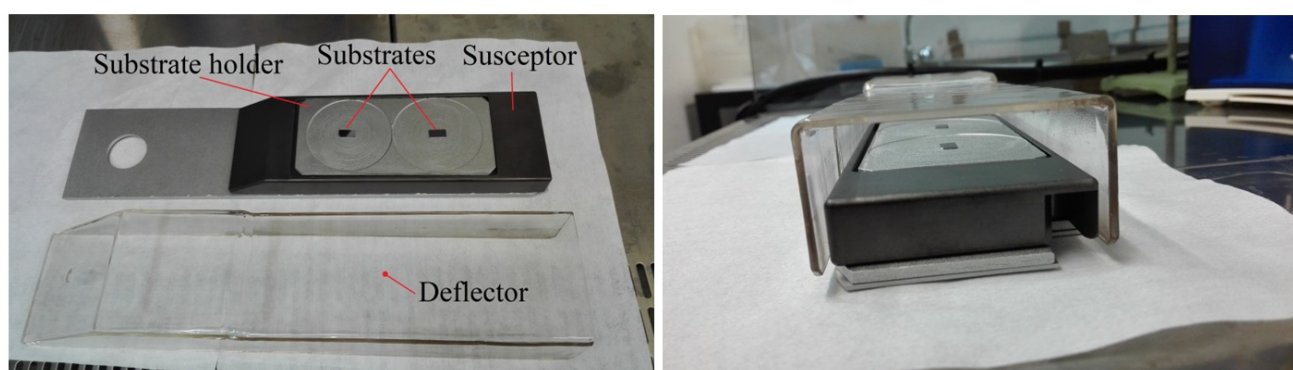


Figure 2.16: View of the pieces on which we place the substrate inside the reaction chamber

2.4.4 Precursors

The molecules used to grow the material in the MOCVD system are usually formed by atoms of groups II, III, V, or VI associated with one or more organic radicals and/or hydrogen. The most common designation used in MOCVD to designate precursors are *M*, *E*, *NP*, *IP*, *NB*, *IB*, *TB* and *A* to designate *methyl*, *ethyl*, *n-propyl*, *i-propyl* (or *isopropyl*), *n-butyl*, *isobutyl*, *tert-butyl* and *allyl* radicals. The chemical nature of these molecules allows their pyrolysis to be low at relatively high temperatures, releasing the atoms of interest and causing layer deposition, leaving various organic molecules as a residue [59]. There are different molecules of the same element, therefore, the choice of precursor must be made depending on the conditions specified in obtaining the desired material.

In the process of crystal growth, a very important parameter is the amount of material - precursor that is fed into the system. As we already described above, the precursor was introduced into the reactor of the system using a carrier gas. The carrier gas passes through a bubbler with the precursor (Figure 2.17) and blows and extract the molecular fractions of the required material through the transport tubes to the substrate surface in the reactor. Precursors may be present in both solid and liquid phases [168, 169]. To change the amount of material produced, it will be necessary to take into account different parameters as the temperature of the precursor, the pressure in the bubbler, and the flow of gas flowing inside it.

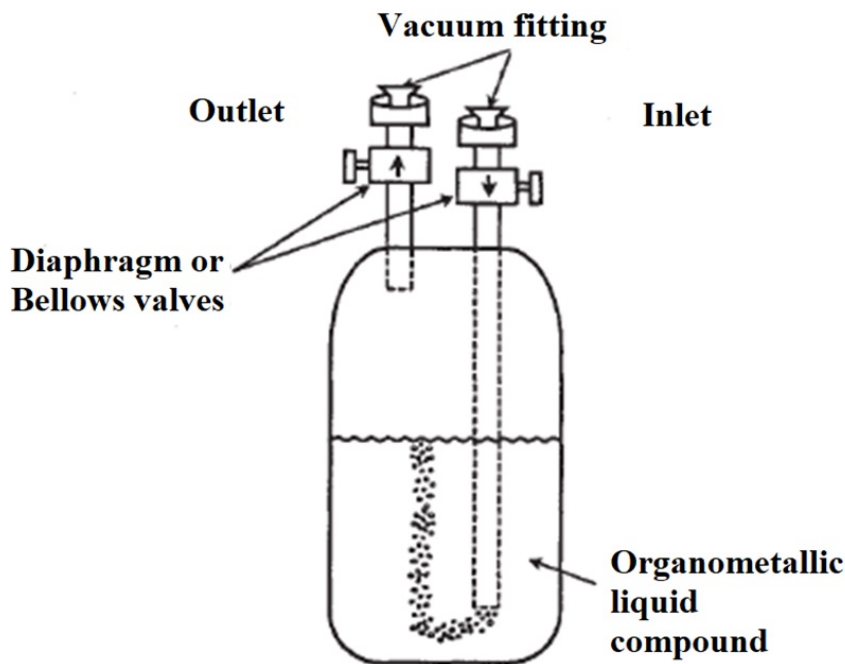


Figure 2.17: Bubbler for the precursors of MOCVD [168].

Chapter 2. Materials and growth technique

Let us use the work of R.J. Betsch [170], who carried out a parametric analysis of control in the MOCVD system. Suppose that the gases, we work with, follow the laws of an ideal gas. Thus, the gas inside the bubbler and the precursor vapor are in perfect balance:

$$\frac{N^{pre}}{N^{gas}} = \frac{P_{par}^{pre}}{P_{par}^{gas}} \quad (2.7)$$

where the variables N and P_{par} represent the number of moles and the partial pressure, respectively, superscripts *pre* and *gas* represent the metal precursor and the carrier gas, respectively. In this case, the pressure of the system, or more precisely, the pressure at the outlet of the bubbler (P_{bub}) is equal to the sum of the partial pressures of the carrier gas (P_{par}^{gas}) and the partial pressure of the precursor (P_{par}^{pre}). But since the pressure in the system is much greater than the partial pressure of the precursor ($P_{bub} \gg P_{par}^{pre}$), and, taking into account that we are in a situation of dynamic equilibrium, the expression will have the form:

$$N^{pre} = N^{gas} \cdot \frac{P_{vap}^{pre}}{P_{bub} - P_{par}^{pre}} = N^{gas} \cdot \frac{P_{vap}^{pre}}{P_{bub}} \quad (2.8)$$

where ($P_{vap}^{pre} = P_{par}^{pre}$) - since we are in a situation of dynamic equilibrium, that is, the gas mixture is saturated and, therefore, the precursor partial pressure is equal to its vapor pressure. If replace the number of moles by the amount of flow we need, the expression will be written as:

$$Flux_{(mol/time)}^{pre} = Flux_{(mol/time)}^{gas} \cdot \frac{P_{vap}^{pre}}{P_{bub}} \quad (2.9)$$

If we know how much carrier gas is supplied, its pressure and pressure in the bubbler with a precursor, we can calculate the number of moles of the precursor, which we extract per unit of time. Since control takes place with the help of MFC, which measures in sccm or slm, and taking into account that *1 mole* of ideal gas takes up *22.4 liters* under standard conditions, we have a direct relationship between measuring MFC and the number of moles per unit time in the carrier gas:

$$Flux_{(mol/min)}^{gas} = \frac{Flux_{(sccm)}^{gas}}{22400} \quad (2.10)$$

Substituting equation 2.9 into equation 2.10, we obtain an expression for calculating the number of moles per unit time for a precursor:

$$Flux_{(mol/min)}^{pre} = \frac{P_{vap}^{pre}}{P_{bub}} \cdot \frac{Flux_{(sccm)}^{gas}}{22400} \quad (2.11)$$

2.4. Metallorganic chemical vapor deposition technique

Metalorganic precursor		P at 298 K (Torr) LogP=B-A/T	Constans (A/B)	Melting point ($^{\circ}C$)	Boiling point ($^{\circ}C$)	Density (g/mL)	Molecular Weight(g/mol)
$(C_3H_7)_2Te$	Te	3,46	2309 / 8,288 [171]	N/A	49	1.365	213.778 [172]
$(C_2H_5)_2Zn$	Zn	8,53	2109 / 8,280 [165, 168]	-28	117	1.205	123.50 [173]
$(CH_3)_2Cd$	Cd	35,64	1850 / 7,764 [168]	-4,5	106	1.985	142.484 [174]
$(CH_3)_3COH$	O	56	2545 / 10,14 [101]	25	82	0.775	74.123 [175]

Table 2.5: Physical properties of precursors.

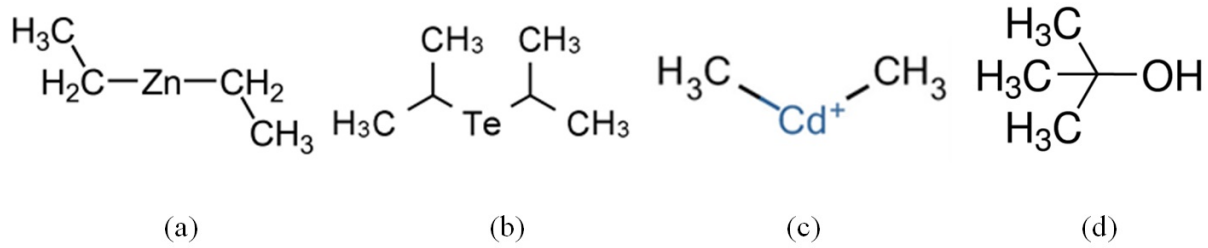


Figure 2.18: Precursors: (a) Diethylzinc ($DEZn$) [173], (b) Diisopropyl telluride ($DIPTe$) [176], (c) Dimethylcadmium ($DMCd$) [177] and (d) tert-Butanol ($t-butanol$) [178].

Table 2.5 presents the main parameters of the precursors that we applied in this work. We used Diethylzinc ($DEZn$), Diisopropyl telluride ($DIPTe$), Dimethylcadmium ($DMCd$) and tert-Butanol ($t-butanol$) as precursors for Tellurium, Zinc, Cadmium and Oxygen, respectively (Figure 2.18).

The vapor pressure of a material depends on the nature of the material and its temperature. Using the August equation [165, 168, 171], we can have an expression for each material:

$$\text{Log}_{10} \text{Pressure}(mmHg) = A - \frac{B}{T} \quad (2.12)$$

where A and B are two given constants for each material, and T is the temperature of the termobath with precursor's bubbler in Kelvin. The temperature control will determine the vapor pressure of the precursors, which will make possible to control the amount of the substance entering into the working chamber of the reactor.

To recalculate the pressure in Pascal, the equation will take the form:

$$\text{Pressure}(kPa) = \text{Pressure}(mmHg) \cdot \frac{101.325}{760} \quad (2.13)$$

where 101.335 is the standard atmospheric pressure in kilopascals, and 760 is the equivalent of atmospheric pressure in $mmHg$ ($Torr$) [179].

2.4.5 Substrates

During the films growth using MOCVD, the nature and surface state of the substrate is very important, because the layer nucleation depends on the arrangement of the surface atoms and their availability to be bound. Moreover, ideally, the substrate should be inert under growth conditions in order to avoid diffusion into the layer or reaction with the precursors.

The substrate will play the role of support for the thin layer of the obtained material. In the case when the grown material reproduces the crystal structure of the substrate we have epitaxial growth. The easiest way to induce epitaxial growth occurs on a substrate of the same material with a well-defined orientation at the face on which the layer will grow. But it is not always possible to find substrates of the same material for growing crystals with sufficient quality or affordable cost, so in many cases, it is necessary to choose alternative substrates that closely match, as fast as possible, the required conditions. This can affect the structure and orientation of the resulting layer of material that grows on it. In this case, we are talking about heteroepitaxy.

During heteroepitaxy, it is important that the lattice parameters of the substrate and the layer be as similar as possible. Achieving a certain critical thickness, so large that the layer is forced to relax to its lattice parameter, will lead to the creation of defects, such as dislocations. The coefficient of thermal expansion of the substrate and the layer should be as close as possible in order to avoid an additional introduction of defects during the cooling process after growth. Optimization of the growth process will minimize defects, which will increase the crystalline quality of the sample.

Using the previous experience with materials of the II-VI group [58, 180], sapphire and GaAs were used as substrates for the growth of materials under study in this thesis. Some parameters of the substrates are shown in Table 2.6. Thus, oxide films (ZnO and CdO) were prepared onto sapphire substrates [180]. This material has probably been the most commonly used substrate, not only for the growth of layers of these materials but also in obtaining nanostructures. Sapphire, or $\alpha-Al_2O_3$, is the only aluminum oxide thermodynamically stable at room pressure and temperature conditions, although there exists a polymorph phase $\gamma-Al_2O_3$.

Sapphire crystallizes on the corundum structure and, thus, presents rhombohedral symmetry (figure 2.19 a). To improve the sapphire surface, chemical polishing and/or chemical etching processes are carried out. Sapphire plates can be cut to a desired orientation with small miscuting (less than 0.5°) or others miscuting, and it can be commercially accesible polished for one or both sides. Sapphire has different natural planes, as the C , M , A or R - planes, which are used for the production of various materials, including oxygen sublattices with hexagonal symmetry (Figure 2.20).

2.4. Metallorganic chemical vapor deposition technique

Property	Sapphire	GaAs
Lattice parameter, a (Å)	4.758 [181], 4.763 [182]	5.6515 [183], 5.653 [184]
Lattice parameter, c (Å)	12.991 [181], 13.003 [182]	-
Density ($\text{g} \cdot \text{cm}^{-3}$)	3.98 [181], 3.99 [182]	5.3176 [183]
Melting temperature ($^{\circ}\text{C}$)	2040 [181], 2053 [182]	1.238 [183]
Band gap (eV)	9.5 [185]	1.441 [183], 1.43 [186]
Linear expansion coefficient α , $^{\circ}\text{C}^{-1}$	5.8×10^{-6} , at 20°C to 50°C [181]	5.39×10^{-6} , at 0 to 30°C [187]

Table 2.6: Physical properties of sapphire and GaAs

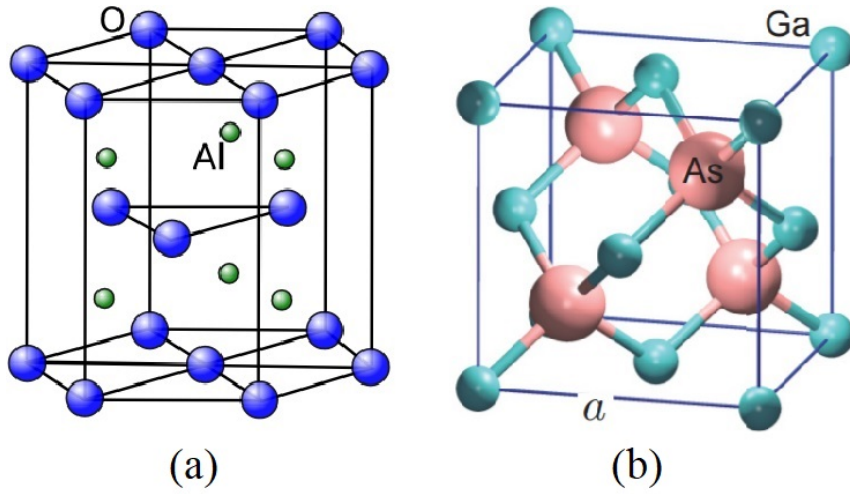


Figure 2.19: Crystal structure of (a) trigonal crystal of sapphire [188] and (b) *ZB* GaAs [189].

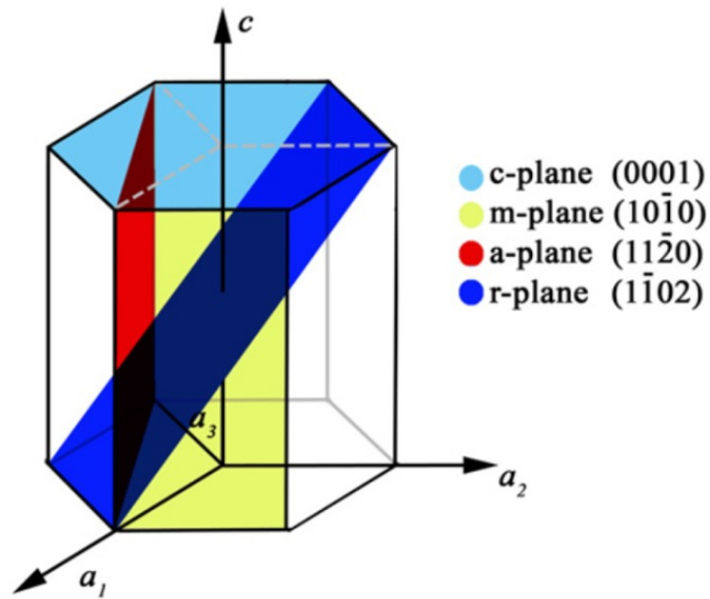


Figure 2.20: Sapphire crystal planes [190]

Chapter 2. Materials and growth technique

It have been shown [59] that a suitable substrate for *CdTe* is *GaAs* (figure 2.19 b). *GaAs* is the third semiconductor most widely used in industry after silicon and germanium. in our case, *GaAs* with a $(100) \pm 0.5^\circ$ orientation (from ATX) was used as a substrate with one of the faces polished with "epyready" quality, with a surface roughness of ~ 0.3 nm, which was measured using AFM. The substrates were supplied in the form of a two-inch "plate" with a thickness of 500 mm. These substrates, like sapphire, were cut to obtain smaller substrates that were used for the growth of *CdTe*, *CdO* films and the *CdTe/CdO* heterostructures.

2.4.6 MOCVD growth parameters

In order to obtain films with the desired characteristics, it will not be enough just to use a suitable substrate. Important factors to be taken into account during the growth of the layer are the susceptor temperature, the molar ratio and flow of precursors, the flow of the carrier gas, the reactor pressure and the growth time, in addition to the reactor design, chosen precursors, carrier gas, etc. Any change in them will affect the physical properties of the obtained films, in particular, their structural characteristics (crystal quality, lattice parameters, etc.) and their morphology. All of these changes will be measured using several characterization techniques, which will be discussed in the next chapter.

As described in Section 2.4.1, the separation into two branches of the injection lines of MO precursors (*DEZn*, *DMCd* or *DIPTe*) and oxygen precursor (*t-butanol*) helps to avoid or reduce parasitic reactions before the precursors arrive onto the substrate. The used growth conditions are shown in Tables 2.7 and 2.8. Mostly, high purity Nitrogen (6N) was the usual carrier gas, but sometimes Hydrogen or Helium were used. All films were grown at atmospheric pressure.

Parameter	ZnO	CdO	CdTe	CdZnO
	Values			
Fluxes (sccm) Carrier II	1900	1900	2800	1900 (2700) ²
Carrier VI	300	300	200	300 (426) ²
Dummy	200	150	50	250 (355) ²
Sweep	2000	2000	1250	2000 (2840) ³
Reactor preassure (Torr)	760			
Prec. Ratio (VI/II)	5.04	5.17	0.12-5.25 (10.5) ¹	5.10
Substrate temp. ($^\circ C$)	300-400	304	284-380	304
Growth time (min)	1-90	15	60 ²	3.75-15 ³
Substrate	R, M, A-sapph	R-sapph or CdTe	GaAs or CdO	R-sapph

Table 2.7: The growth parameters of *ZnO*, *CdO*, *CdTe* layers and structures based on them in the MOCVD

2.4. Metallorganic chemical vapor deposition technique

Precursor	Bath temp.($^{\circ}C$)	Preassure (Torr)	Carrier gas (sccm)	Precursor flux ($\mu\text{mol}/\text{min}$)
ZnO				
DEZn	16	760	5-35	2.85-19.91
tert-butanol	28		5-35	14.35-100.40
CdO				
DMCd	12	760	25	71.77
tert-butanol	28		12.5	13.87
CdTe				
DIPTe	15	760	25-475	1.16-52.54
DMCd	12		9 (4.5) ¹	9.99 (4.95) ¹
CdZnO				
DEZn	16	760	5	5 (7.71) ²
DMCd	12		20-96	10-48 (14.2) ²
tert-butanol	28		25-98	25-98 (35.5) ²

Table 2.8: Parameters of precursor fluxes during growth of ZnO, CdO, CdTe layers and structures based on them in the MOCVD system

1 - In the last experiments with Ratio(VI/II)=10.5, 2-step growth was made with 1 and 6 min for the steps, respectively, maintaining the DIPTE flow and decreasing the DMCd one.

2 - Due to the use of He as carrier gas, growth parameters like gas and precursor flow were changed (see Conversion factor in Table 2.4)

3 - In experiments with higher nominal Zn content, the growth time increased

To obtain *ZnO* thin films, we applied the previous experience of our scientific group [180]. From this experience, several changes in the values of precursor fluxes, growth temperature and time were tested to have a film with the lowest thickness and surface roughness. Sapphire with different orientations (see cut planes in Figure 2.20) was used, and a chemical treatment of the substrates in some experiments was carried out. Two different positions at the susceptor were used for placing there the substrates. The first position of the substrate holder is at a distance of 5.1 cm from the entrance to the cell, and the second is at 16.3 cm. The results of the experiments will be shown and analyzed in Chapter 4.1.

For the growth of *CdZnO* ternary compounds, *R*-sapphire, was the choice as substrate, because the ability of this cut plane to produce *CdO* films with good structural quality [100,191] and considering that the cubic phase of the ternary should be similarly matched as *CdO*. High purity Nitrogen (6N) was the carrier gas, but for the sample with high Zn content (20 %), Helium was applied too. In this case, the flow parameters were corrected taking into account the conversion factor (see Section 2.4.2).

As mentioned above, *GaAs* and *R*-sapphire were used as substrates for the growth of *CdTe* films and *CdTe/CdO* heterostructures. We used the data obtained in a previous work [59] as starting point to grow *CdTe* thin films. After finding the optimal parameters of the experiment, a growth series of *CdTe/CdO* and *CdO/CdTe* heterostructures were carried out. Since it was not possible to obtain monocrystalline films with a single orientation, before the beginning of *CdTe* films growth, the short time growth (2.5 min) with a reduced temperature (295 °C) was performed to create more nucleation points. Ultimately, the growth time was reduced and the ratio of precursors VI-II increased to 10.5. The results of the experiment and their analysis are given in Section 4.3.

2.5 Close-spaced vacuum sublimation technique (CSVs)

2.5.1 Close-spaced vacuum sublimation system

It is widely believed that the growth of bulk monocrystals from the vapour phase is of little practical importance due to the relatively low growth rates inherent at this method. Indeed, the growth rate of bulk single crystals from the vapour phase is usually equal to tens of $\mu\text{m}/\text{h}$. Nevertheless this method can be successfully used for growing thin films. The processes of growing layers from the vapour phase are very sensitive to changes in growth conditions and the composition of the feed phase. However, the influence of these factors is significantly smoothed out due to the low growth rates, which contribute to be near of the equilibrium growth conditions [192].

The advantages of growing crystals in a vacuum (10^{-5} - 10^{-6} Torr) with subsequent condensation on a substrate include the cleanliness of the conditions for obtained materials. Due to the fact that usually the reactions in the gas phase proceed at relatively low temperatures, a number of compounds that melt incongruently can be grown by using the vapor phase methods at temperatures significantly lower than the melting temperature.

Among the methods from the vapour phase there are the thermal evaporation methods. Despite the advantages of an vacuum thermal evaporation process, as simplicity, low cost, fast process, and others, this method has some disadvantages, among which we should note that:

- 1) it is difficult to strictly have the same conditions in different processes, as a result of which the chemical and phase composition from sample to sample can vary;
- 2) the films cannot be grown at high substrate temperatures, as a result of that they could consist of small crystallites of 0.02-1 μm in size and consequently have a carrier mobility 1-2 orders of magnitude lower than in monocrystals.

To reduce these shortcomings at the synthesis of films, it is possible to use thermal evaporation at short distances from the substrate which is called the close space vapour sublimation (CSVs), which offers some advantages. The method produces samples in which, after adequate selection of the growth conditions the composition of the growing crystal can be near to the composition of the source, and the vapour phase consists only of atoms or molecules that form the source and crystal.

In this section, we briefly describe the CSVs growth technique. The main processes occurring inside the working volume of chamber under vacuum will be considered, and the features of the system used during this work will be emphasized. Growth conditions that were used for growth of ZnMnTe and ZnMnS will be presented.

Basic concepts of the growth process

To obtain films in modern microelectronics, there are many mechanical, chemical and condensation methods. Among them, the growth of crystals from the vapour phase is considered one of the important methods for obtaining stoichiometric crystalline materials. Vapour phase deposition is convenient for large scale operations (from the coating of turbine blades to growing epitaxial layers of semiconductor materials), it can be used to coat irregular-shaped substrates, including growth on inside surfaces, and offers maximum control of materials properties such as thickness and composition. Another practical advantage is that it does not involve the contacting of the growing surface with a liquid or solid phase, thus avoiding numerous potential problems during and after the growth process [193].

Growth from vapour is the preferred phase transition to obtain thin layers, while the growth of bulk crystals from vapour is more likely an exception as before said, applicable only in case of unavoidability of other options [194]. The process of crystal growth from the vapour phase consists of the same steps as the crystallization process from the liquid phase: 1) supply of the crystallizing component to the growth surface (mass transfer processes); 2) surface diffusion (migration along the growth surface and the incorporation of atoms into the crystal); 3) diffusion in the crystal (migration in the crystal); 4) removal of crystallization heat from the growth surface (heat transfer processes).

From a technological point of view, the methods for growing crystals from the gaseous phase are divided into three large groups, differing in the way atoms are delivered from the source to the growing crystal [192]:

- 1) sublimation-condensation method;
- 2) chemical reactions of decomposition - reduction method;
- 3) chemical transport method.

In modern semiconductor technology some technological processes for producing single crystals from the vapor phase in systems with reduced pressure (in vacuum) are used. Mass transfer in vacuum includes the following three main stages:

- 1) transition of a substance from a condensed (solid) phase to a gaseous one;
- 2) transfer of this substance from the source to the substrate under a reduced overall gas pressure;
- 3) condensation of vapors of the substance on the substrate.

The transfer of a substance from a condensed phase to a gaseous phase is mainly carried out by thermal evaporation, which consists in heating the substance to a temperature where the energy of the surface atoms of the substance becomes higher than their binding energy with neighboring atoms, as a result of which they acquire the ability to be transferred to the vapor phase.

2.5. Close-spaced vacuum sublimation technique (CSVS)

Depending on the relationship between the mean free path of an atom or molecule in a vapor, l , and the distance from the vapor source to the substrate L , there are two main modes of mass transfer of the substance in vacuum. At $l \ll L$, the vapor from the surface of the evaporated substance moves in the form of a continuous flow, which is characteristic of chemical vapor deposition (CVD) methods. At $l \gg L$, the vapor moves from the evaporation surface in the form of molecular beam within which atoms or molecules propagate along straight paths, which is more characteristic of physical vapor deposition (PVD) methods. Consequently, PVD processes usually proceed under vacuum conditions to maintain the flow in the form of a beam, while CVD processes usually take place at atmospheric or only slightly reduced pressure ($10^5 \text{ Pa} \geq P \geq 10^2 \text{ Pa}$) [194].

The borders between the two classes of vapor phase growth techniques are not sharp. Even in the processes generally considered as typical physical vapor deposition processes, in most cases chemical reactions take place.

When growing from the vapour phase, it is customary to isolate diffusion and kinetic growth regime. If the limiting stage of the process is the supply of material to the growth surface, then this growth process is spoken of as going at diffusion regime. If the limiting stage is the processes of migration and incorporation of atoms onto the growing surface, then the growth process is governed by the kinetic. If the rates of supply of crystallized material and migration processes are comparable, then it can be said that the process proceeds in the transition regime.

It is customary to distinguish at least three simultaneously proceeding stages:

- 1) transfer of reacting substances to the interface - the reaction zone;
- 2) chemical interaction in the reaction zone;
- 3) removal of reaction products from the reaction zone. The overall speed of the process will be determined by the speed of the slowest (limiting) stage.

The main parameters affecting the equilibrium of chemical reactions are temperature, pressure and concentration of reacting substances. In practice, these parameters are usually used to shift the equilibrium in the desired direction, that is, to regulate the equilibrium degree of conversion in accordance with the law of mass action.

The **sublimation-condensation method** can be used to grow congruently evaporating semiconductor compounds and solid solutions based on them, the components of which have sufficiently high vapor pressures ($\approx 1 \text{ mmHg}$), as well as in cases where their growth by other methods is complicated or leads to crystal degradation. Growth by evaporation and subsequent condensation is used widely to make thin layers and bulk crystals, as for instance compounds of cadmium or zinc with sulfur, selenium, or tellurium [195].

Chemical reactions of decomposition - reduction method turns out to be very effective for growing single-crystal ingots of some compounds from the gaseous phase, the components of which have low vapor pressures at acceptable growth temperatures. The source consists of

gaseous molecules containing atoms of a crystallizing material. A crystal of a given composition is formed as a result of a chemical reaction proceeding on the substrate (or near it) and leading to the release of atoms of the crystallizing material.

The growth of crystals from the vapor phase by the **chemical transport method** is based on chemical reactions, the same as chemical reactions of decomposition - reduction method. Crystal growth occurs as a result of decomposition reactions of gaseous molecules. When a gaseous reagent X interacts with a solid, non-volatile substance A at certain temperatures and vapor pressures X , volatile compounds of different compositions can be formed. Under constant conditions, a certain state of equilibrium is established between them. If the temperature of the system will be changed, then the state of equilibrium will be violated and the composition of the mix components will change. By choosing the conditions under which the formation reaction of the volatile compound XA predominantly takes place in the source region, and its decomposition with the release of component A in the crystallization region, it is possible to provide conditions under which the transfer of A from the source to the growing surface and the growth of a crystal of substance A will occur [192].

As evaporation in the vacuum, CSVS method allows getting layers with a thickness of a few angstroms to several tens of microns. At the same time, uniformity and a maximum purity of the material are achieved, the film growth conditions are easily controlled and it is possible to use masks for the manufacture of layers of a given configuration. The use of a two-temperature control (evaporation (T_e) and substrate (T_s) temperature) allows a better control of the film growth process. A schematic representation of the working vacuum chamber for evaporation is shown in Figure 2.21. In some cases to prepare $A_{II}B_{VI}$ films two sources can be used. In this case, a three-temperature control method is used: a substrate (T_s) and 2 independent evaporators (T_e), one of which contains metal, and the other a chalcogenide. [55].

The quality of the deposited films (chemical composition, degree of structural perfection, electrical, optical properties) is determined by the evaporation processes of the initial material, the difference in vapor pressure of the components, the processes and conditions of condensation on the substrate, and the integrity of the layers is determined by the design feature of the evaporator.

The vacuum (1×10^{-1} to 1×10^{-7} Pa or 1×10^{-3} to 1×10^{-9} Torr) allows the growth process to be carried out at evaporator temperatures lower than when atmospheric pressure is used, in addition vacuum conditions significantly reduces the film contamination, but the low density of the material in the vapour phase leads to low growth rates.

The advantages of vapor growth methods can be summarized as follows [194]:

- Crystallization proceeds at temperatures much below the melting point.

2.5. Close-spaced vacuum sublimation technique (CSVS)

- Also "difficult" materials, which are complicated to be obtained by other methods (for example, owing to large differences in the segregation coefficients of the constituents of an alloy) can be synthesized.
- Mixed crystal composition and dopant concentration can be held constant or changed in almost any desired manner during growth.
- Generally, the source materials for the synthesis process can be provided with high purity.
- The thickness of crystalline layers to be deposited can be controlled with an accuracy of one atomic monolayer.
- The crystalline material generally shows good surface morphology, high purity, good crystallographic perfection and uniform layer thickness.

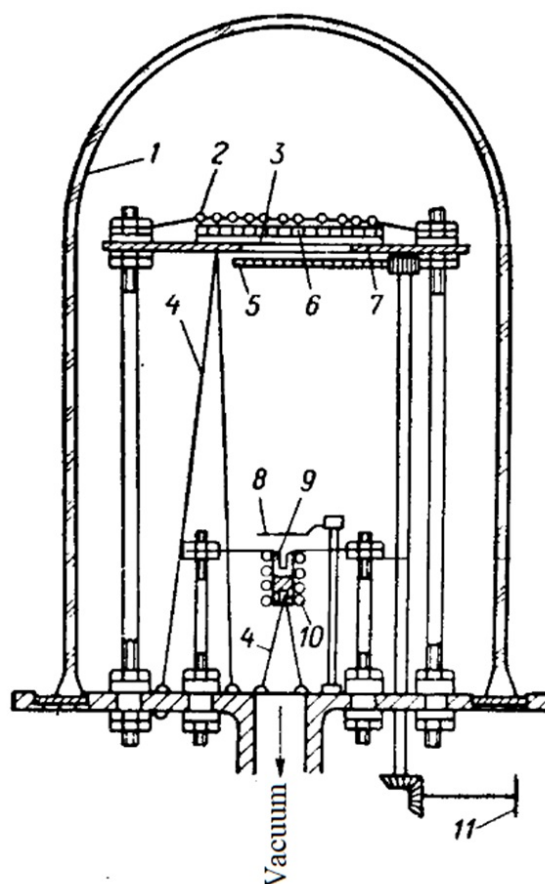


Figure 2.21: Schema of a vacuum chamber for condensation of a film by two-temperature method [55]:

1 - Glass or metal cap; 2 - Heating element for heating the substrate; 3 - substrate; 4 - thermocouples for measuring the temperature of the substrate; 5 - step shutter; 6 - quartz plate; 7 - support for a substrate and a heater; 8 - shutter; 9 - evaporator; 10 - tungsten or molybdenum spiral for heating the evaporator; 11- handle for moving the shutter 5.

Our CSVS system overview

The scheme of the original device for depositing thin films in the *CSVS* is shown in Figure 2.22. The main constructive element of the device is a ceramic monolithic cylinder (1), which forms a compartment for the evaporation of the semiconductor substance (2). At the bottom of the compartment there is an evaporator, made in the form of a thin tungsten tape (3). By adjusting the amount of current flowing through the tape, it is possible to change the evaporation temperature and, accordingly, the rate of evaporation of the films. The substrate (4) on which the layers of the three-component compounds are growing is secured to the holder (5) with the heating element (7). In the process of growing films, the substrate with the help of a manipulator was pressed to the *CSVS* sealing it. The substrate was fixed at a distance of about 25 mm from the evaporator. To reduce the condensation of the evaporating substance on the *CSVS* walls, they were heated by means of a heating element (8). The temperature of this heater was chosen in such a way that the condensation of the substance occurs only on the substrate (4). To monitor the temperature of the evaporator and the substrate, chromel-aluminium thermocouples (6, 10) were used, the signal from which comes to the multimeter, which determine the temperature. To prevent heat dispersion when heating the *CSVS*, the walls of the ceramic cylinder with the heating element was surrounded by an auxiliary metal screen (9), which separated the system from the rest of the vacuum chamber. In the process of evaporation of the material, the condensation volume is "locked", and the gases of the residual atmosphere do not get into the film.

The temperature of the evaporators, the walls and the substrate was controlled by chromel-alumel thermocouples $\ll\text{THA-50+1300}\gg$ (6, 10 in Figure 2.22). The signal from which was driven to ADC multimeters APPA-108N and UT70B.

2.5.2 Temperature control system

Stabilization of the temperature of the substrate, in other words, the temperature of deposition, plays a crucial role for obtaining samples with repeating characteristics. This is due to the fact that the size of the crystallites and the structure of the condensate is determined by the temperature of the substrate. At low temperatures, the size of the crystallites can be very small, with the increase in the temperature of the substrate, the size of crystallites increases. In case of homoepitaxy during the condensation on monocrystalline substrates there is a temperature at which the epitaxial growth of the film begins (epitaxy temperature). That is why, for the production of high-quality samples of semiconductor films, a proportional-integral-differential (*PID*) controller, in our case an "OVEN TRM10", for the control unit of the TRIACs and thyristors (*CUTT*) is a necessary technological element for obtaining good-quality samples of semiconductor films (Figure 2.23) [196].

2.5. Close-spaced vacuum sublimation technique (CSVS)

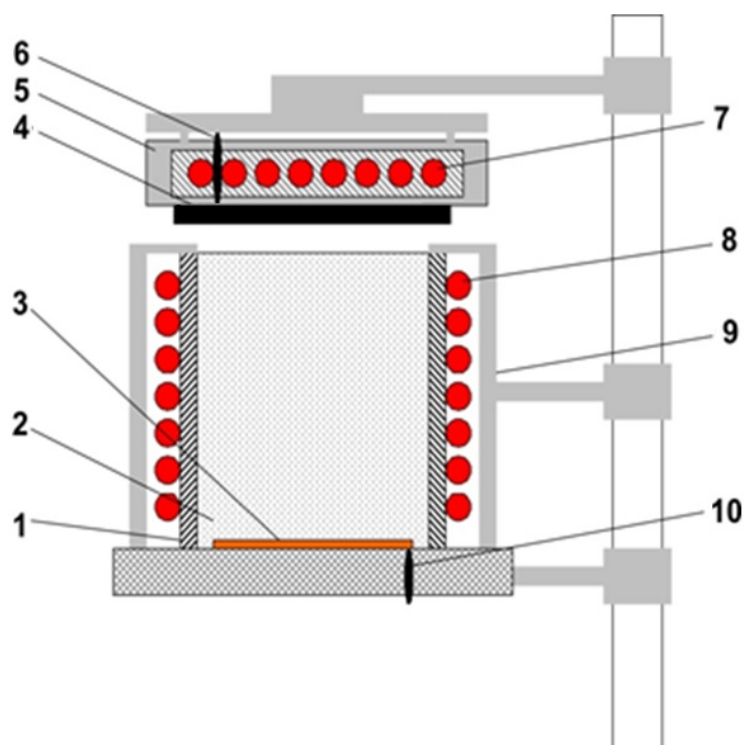


Figure 2.22: Diagram of the device for the synthesis of chalcogenides by the *CSVS* method:
1 - CSV walls; 2 - evaporation compartment; 3 - evaporator; 4 - substrate; 5 - holder of the substrate; 6, 10 - thermocouples; 7, 8 - heating elements; 9 - thermal screen [197].

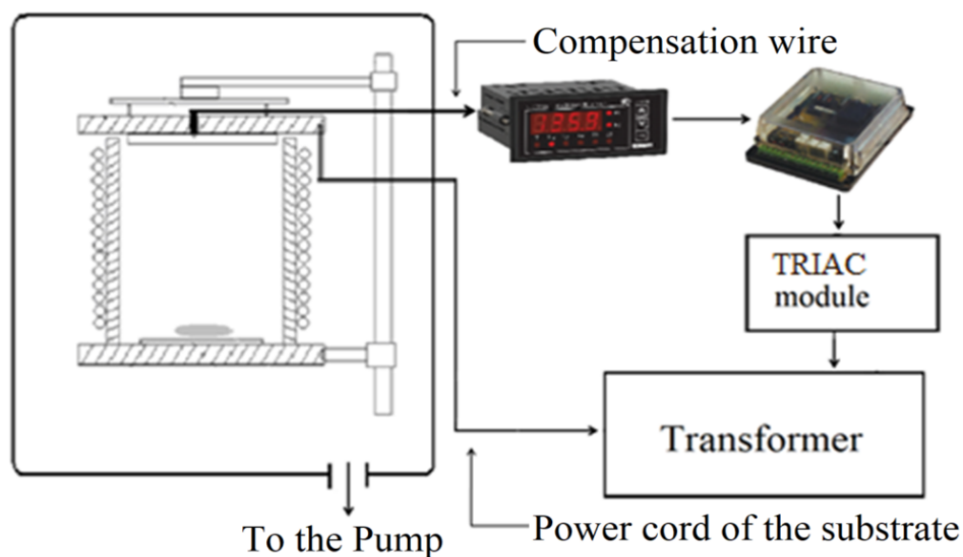


Figure 2.23: Functional scheme for obtaining $A_{II}B_{VI}$ semiconductor film compounds by condensation in a vacuum environment with temperature stabilization by using a "OVEN TRM10" PID-controller [196].

The microprocessor programmable TRM10 type regulator with an input sensor (thermal converter or unified source) is intended for control and management the technological processes, which requires increased accuracy of the value of the measured parameter [198].

The parameters of the device are set by the user and stored when the power is turned off in the non-volatile memory of the device.

2.5.3 Our working system

The growth of samples by the CSVS method was carried out at the laboratory of the "Research of nanoelectronics material" group at the Sumy State University. As charge, $ZnMnS$ (7 %) and $ZnMnTe$ (5 %) were prepared in Chernivtsi National University in laboratory of Fochuk P.M. by sublimation of elementary components of these materials. $ZnMnTe$ and $ZnMnS$ compouds were deposited in the vacuum system *VUP-5M* (OJSC Selmi, Sumy) (Figure 2.24). The residual gas pressure in the chamber was no more than $5 \cdot 10^{-3}$ Pa.

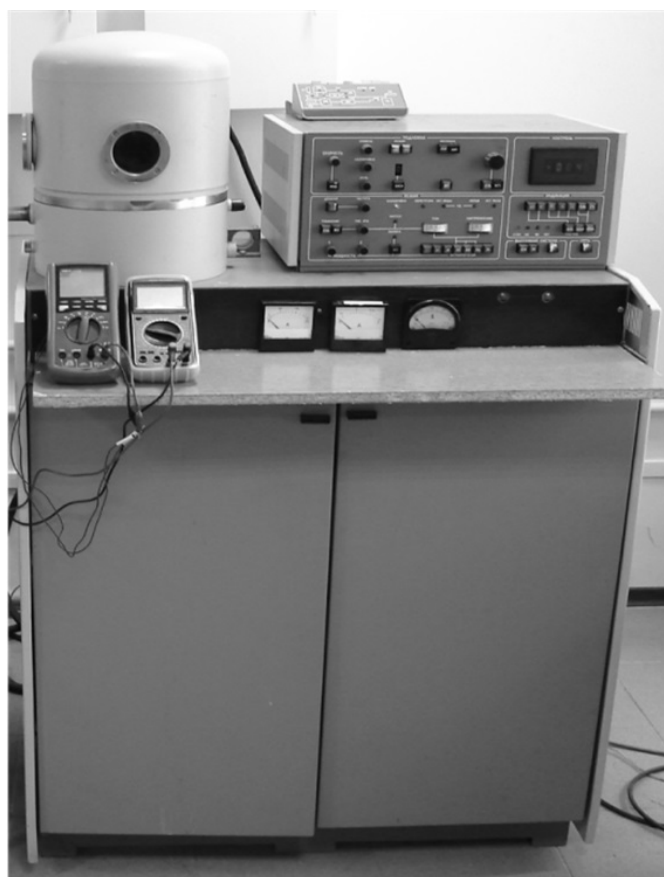


Figure 2.24: General view of equipment *VUP-5M*.

The getting of $ZnMnS$ and $ZnMnTe$ layers was carried out in the CSV in several stages, the main of which are:

2.5. Close-spaced vacuum sublimation technique (CSVs)

- 1) loading of material charge at the evaporating compartments;
- 2) closure of the ceramic cylinder by the substrate;
- 3) creation of a vacuum in the working volume;
- 4) warm up of ceramic walls and substrate;
- 5) direct evaporation of the loaded substance;
- 6) cooling the substrate with the film to room temperature.

Structural and optical studies were performed for the obtained samples, the results of which are given in Section 5.

2.5.4 Substrates

As before commented substrates play an important role in obtaining high-quality deposition, and the best substrate would be one that ideally matches the lattice of the resulting material, as in homoepitaxy. Nevertheless, the achievement of homoepitaxy is not always possible, therefore, other materials, resistant to chemical reactions and/or diffusion processes are chosen as substrates. With the development of the solar cell industry, there has been an increase in the need for low-cost transparent substrates that can grow highly textured polycrystalline thin films. Glass as such type of substrate, which is widely used for growing various materials. Some parameters of some glass substrates are presented in Table 2.9.

Glass is an amorphous material (Figure 2.25), that lacks a long range periodic crystalline structure [199]. At ordinary temperatures, glass is solid with high heat and electrical insulating properties and is very resistant to many aggressive environments. To obtain glass, the most

Property	Soda-lime Silica	Borosilicate	Phosphate
Primary compounds	SiO_2 (73 %), Na_2O (14 %), CaO (7%), MgO (4%), Al_2O_3 (2%) [200]	SiO_2 , B_2O_3	P_2O_5
Density (gcm^{-3})	2.49	2.23	2.6 [201]
Max. service temp. ($^{\circ}C$)	500	550	-
Softing point ($^{\circ}C$)	750	820	-
Termal-expansion coefficient α , $^{\circ}C^{-1}$	$85-95 \times 10^{-7}$	33×10^{-7}	15×10^{-7} [201]
Thermal shock resistance	Low	Average-High	Low
Chemical resistance	Average	High	Low, exept high resistance to hydrofluoric acid
Application	Food containers, windows, lamp envelopes	Industrial equipment, labora- -tory and kitchen glassware	Bone scaffolds, optical fibers, heat absorbers

Table 2.9: Some properties and applications of 3 most common commercial glass slider [199, 202]

common method involves heating raw materials into a molten liquid and then rapidly cooling the liquid in such a way that the atoms remain in a randomly arranged atomic state. In this case, the atoms are less densely packed than in the quartz crystal, leaving large interstitial spaces or holes between the atoms, which reduce the density [202].

In the process of glass formation by melting/cooling, mixtures of several raw material powders are often added (Figure 2.26), which consist of many different components, each of which plays a role [199]. The addition of components not only increases the density, but also affects the physical properties and characteristics of the formed glass. One of these characteristics is the expansion of the glass during heating and compression during cooling.

Although most glasses contain charged metal ions that can carry electric current, the high viscosity of the glass at room temperature prevents their movement and electrical activity. Thus, glass is an effective electrical insulator - although this property varies with viscosity, which in turn is a function of temperature [202]. The high throughput of glass is explained by the fact that electrons in glass molecules are confined to particular energy levels and they cannot absorb and reemit photons.

Unlike Soda-lime silica and Phosphate glasses, Borosilicate glasses are usually used in harsh and demanding conditions. They have good thermal shock resistance and can withstand extreme thermal cycling with minimal effect. For instance, Pyrex, a commercial borosilicate composition created by Corning, Inc., is commonly used for baking at home or performing experiments in the lab. Low coefficient of thermal expansion allows the glass to develop fewer internal stresses during the heating and cooling processes that cause cracking or breaking [199].

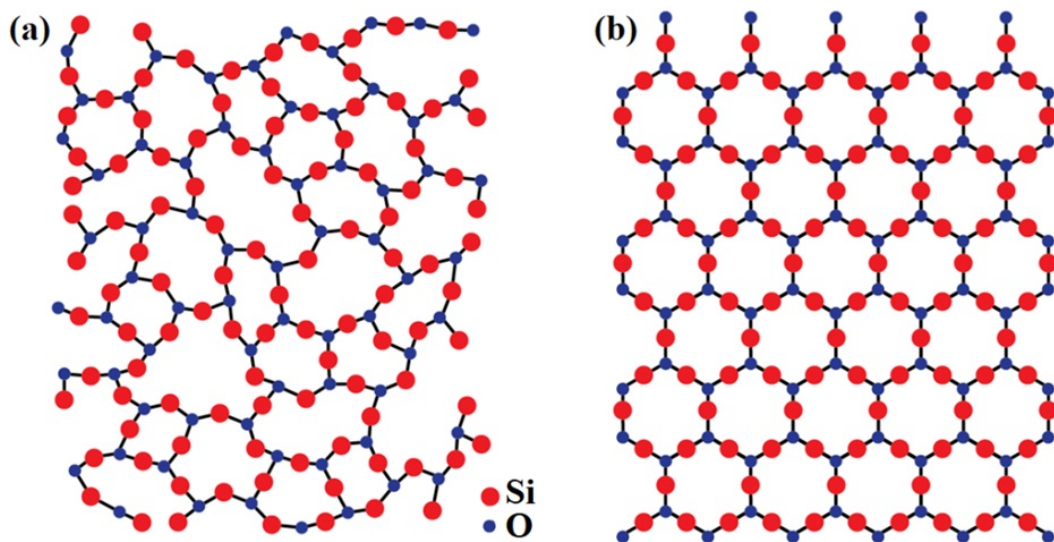


Figure 2.25: Crystal structures of (a) an amorphous SiO_2 - glass and (b) a crystalline SiO_2 -quartz [203].

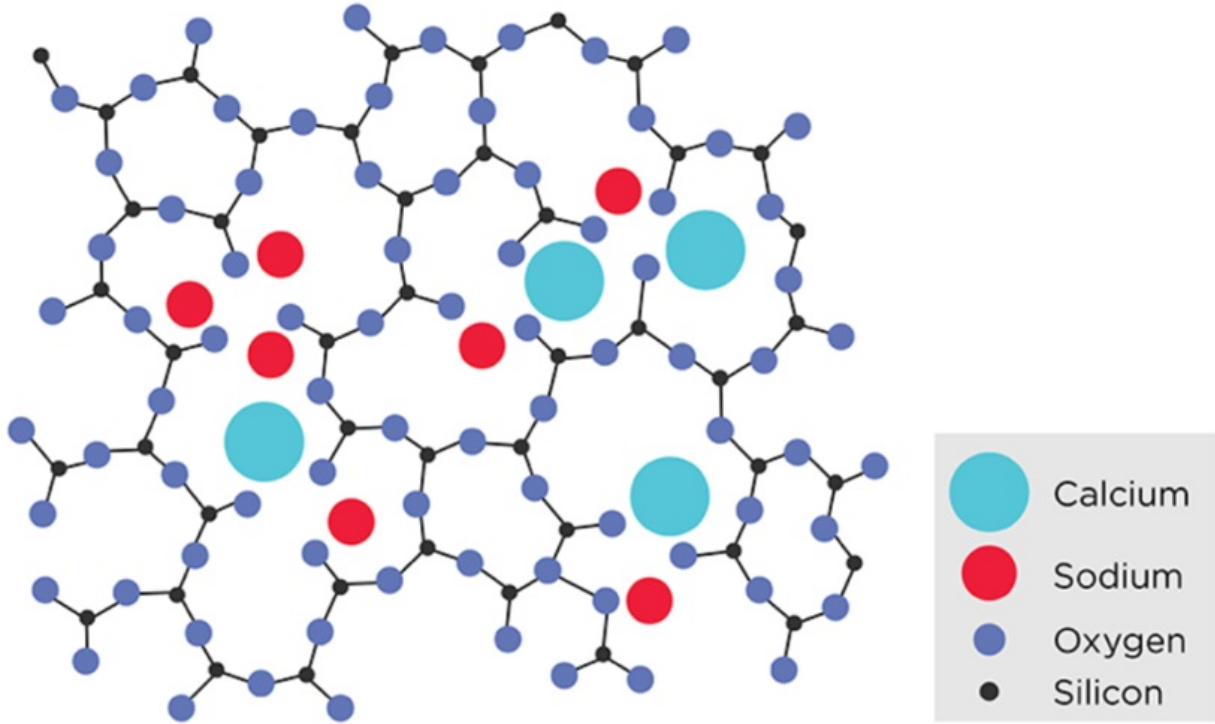


Figure 2.26: 2D representation of a soda-lime silicate glass with random atomic nature [199].

Thin films of $ZnMnTe$ and $ZnMnS$ were prepared onto borosilicate glass substrates. Before the growth of the films, the glass substrates were ultrasonically cleaned. Each glass plate had a size of $75 \times 25 \times 10$ mm and was cut to obtain smaller substrates for the growth experiments.

2.5.5 CSVS growth parameters

A suitable substrate makes easier to obtain films with the desired properties, but the selection of growth parameters also affects the formation of films. Any change in the growth parameters will influence the structural features of the obtained films, which in turn will affect the optical and electrical characteristics. The used growth conditions are shown in Tables 2.10.

Thin films of $ZnMnS$ and $ZnMnTe$ films were grown by using CSVS method by sublimation of the prepared charge in the form of powder after grinding the synthesized materials with the required Mn content. An important advantage of synthesizing films of $ZnMnS$ and $ZnMnTe$ by this method is that the vapor phase is in a small volume limited by heated walls. The high vapor pressure of chalcogenides during condensation significantly exceeds the pressure of residual gases in the external working volume of the installation by a value of about 10^3 Pa. This leads to a decrease in the contamination of the layers of the materials obtained by uncontrolled impurities from the residual gas atmosphere [197].

Parameter	ZnS:Mn	ZnTe:Mn
	Values	
Growth time (min)	15	4 and 10
Substrate temperature ($^{\circ}C$)	100-450	350-650
Evaporation temperature ($^{\circ}C$)	1000	800
Nominal Mn content at the source (%)	7	5
Chamber preassure (Pa, $\times 10^{-3}$)	5	
Substrate	Borosilicate glass	
Distance <i>evaporator-substrate</i> (mm)	~ 25	

Table 2.10: The growth parameters of $ZnMnTe$ and $ZnMnS$ thin films obtained by *CSVs* method

In the selection of the growth parameters, we applied the previous experience of our scientific group with ZnTe [197] and ZnS [204], respectively. Several series of samples were obtained over a wide range of substrate temperatures. The evaporation temperature remained constant. The condensation time was usually 10 minutes. Cooling of the resulting films to room temperature was carried out in vacuum. The results of the experiments are given in Chapter 5.

Chapter 3

Characterization techniques

For the synthesis of crystals, whose high-quality needs to be tested, it will be necessary to use adequate growth conditions. Thus characterization of the obtained material is fundamental, because allows to adjust the growth parameters in order to obtain (if possible) or to be near of the desired requirements. Therefore, by using an iterative process of synthesis and characterization of the samples, it is possible to advance in optimizing the process for the selected material.

In this chapter, we will present various methods used in this thesis to characterize the obtained layers, the results of this characterization will be presented in the following chapters.

Thus, firstly, electron microscopy methods and used equipment will be shown, later the basics of particle induced X-ray emission and X-ray diffraction, then the method of measuring the optical transmittance, and finally, the contact potential difference and surface photovoltage based on atomic force microscope instrumentation system will be presented.

3.1 Scanning Electron Microscopy (SEM)

Traditionally the optical microscope, often referred as the light microscope, is used to obtain enlarged images of objects (or details of their macroscopic structure), invisible to the naked eyes. Nevertheless, the spatial resolution is, in some cases, not sufficient, remember that unaided eye has a resolution ~ 0.1 mm, and light microscopy showing a resolution of ~ 0.2 μm . With the improvement of technical capabilities it has been possible to develop instruments with higher spatial resolution, as the electron microscopes (EM), with resolutions in the order of ~ 1.0 nm in the case of scanning electron microscopies (SEM) or ~ 0.1 nm for transmission electron microscopies (TEM). Electron microscopy is a general term to characterized by the use of an electron beam, which is impinging on the testing samples.

Chapter 3. Characterization techniques

Focusing now on scanning electron microcopies, when a beam of primary electrons impinge on the surface of a sample, the electrons penetrate and propagate through the material. The depth of interaction or the decrease in the electron beam energy is related with the properties of the material [205]. In this process, the primary electrons can interact inelastically with atomic electrons or elastically with atomic nuclei, and generate various types of signals. Detecting and analyzing these signals [206] allow to get various types of information, as we will see in next sections.

Figure 3.1 shows the interaction of the incident beam with the surface of the material. They involve different kind of electrons and consequently generate different types of signals and information about the materials:

- *Elastic interaction*: primary electrons, which can have an energy more than 50 eV, depending on the microscope, do not lose energy when interacting with the material.
- Dispersed and retro-dispersed electrons are electrons that are deflected by the atomic nuclei of the sample. Retro-dispersed electrons show a large scattering angle.
- Transmitted electrons that cross the material without losing energy.
- *Inelastic interaction*: the primary electrons transfer energy to the electrons of the material.
- Secondary electrons (SE) are electrons from the surface of the material (less than 10 nm), which are rejected as a result of the incidence of a beam of primary electrons. SE have an energy lesser than 50 eV.
- Auger electrons (AE) are electrons emitted from the inner layers of the sample that interact with the primary beam.
- Cathodoluminescence (CL) is an electromagnetic radiation, from the ultraviolet to the infrared spectrum, which is associated with the emission of photons from relaxation of the excited of the energy levels at the material that occurs when interacting with the primary electron beam.

Light elements allow deeper penetration of the beam, while the scattering volume of heavy elements lies closer to the surface. It should be noted that in addition to the signals described, other phenomena such as continuous X-ray emission or heat generation also occur. At the same time, depending on the information collection technique and the type of secondary radiation, various types of microscopes are used. Below we describe the methods and equipment for microscopy used in this work.

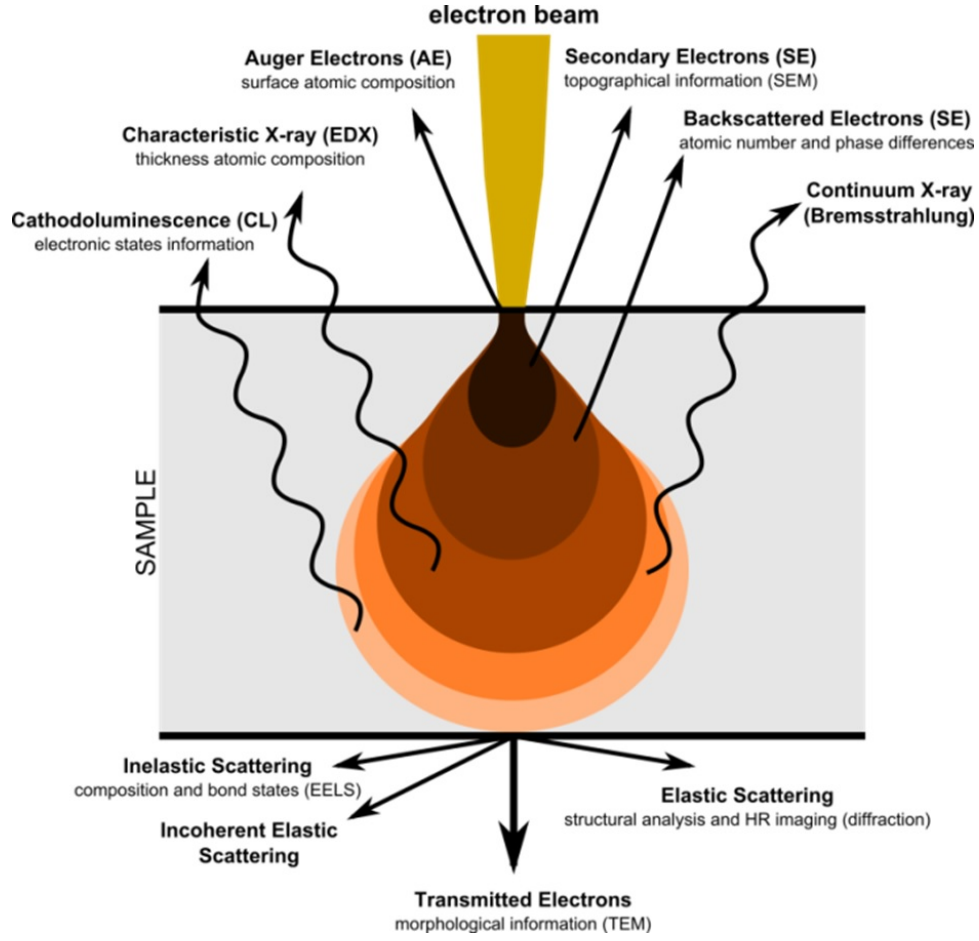


Figure 3.1: Interaction volume of electron beam showing different generated signals [207].

3.1.1 The principle of the scanning electron microscope

Using the scanning electron microscope, we can study the morphology of the samples. That is, scanning microscopes are magnification system that allows to observe the surface characteristics of the investigated materials. The combination of higher magnification, greater depth of field, greater resolution ($\sim 1 \text{ nm}$) and simplicity of observation of the sample makes SEM a very useful tool with which we can get a first information about the morphology of our samples.

In the scanning electron microscopy, an electron beam accelerated by a potential difference of some kV (usually $< 30 \text{ kV}$, but it could be higher) focuses on the sample using a set of electromagnetic lenses. Higher accelerating voltage implies smaller wavelength of electrons and higher possible achievable resolution.

We can imagine how the wavelength of the incident beam will depend on the applied voltage. Louis de Broglie showed that every particle or matter propagates like a wave. The wavelength of a particle or a matter can be calculated as follows [208].

$$\lambda = \frac{h}{p} \quad (3.1)$$

where λ is the wavelength of a particle, h is Planck's constant (6.626×10^{-34} J·s), and p is the momentum of the particle. Since the momentum is the product of the mass and the velocity of the particle,

$$\lambda = \frac{h}{m_0 v} \quad (3.2)$$

The velocity of the electrons is determined by the accelerating voltage (V), giving a kinetic energy eV . The potential energy must equal the kinetic energy, thus

$$eV = \frac{1}{2} m_0 v^2 \quad (3.3)$$

The velocity of electrons can be calculated by

$$v = \sqrt{\frac{2eV}{m_0}} \quad (3.4)$$

Therefore, the wavelength of propagating electrons at a given accelerating voltage can be determined by

$$\lambda = \frac{h}{\sqrt{2m_0 eV}} \quad (3.5)$$

Since the rest mass of an electron (m_0) is 9.109×10^{-31} kg and the charge of the electron is $e = 1.60 \times 10^{-19}$ C,

$$\lambda = \frac{6.62 \times 10^{-34}}{\sqrt{2 \times 9.1 \cdot 10^{-31} \times 1.6 \cdot 10^{-19} \times V}} = \frac{12.25 \times 10^{-10}}{\sqrt{V}} = \sqrt{\frac{1.5}{V}} \times 10^{-9} \quad (3.6)$$

On the other hand, equation 3.5 does not take into account relativistic effects and for transmission electron microscopes (TEM) at energies > 100 keV relativistic effects cannot be ignored because the velocity of electrons (as particles) becomes greater than half the speed of light. In this case, to be precise, equation 3.5 must be modified [209],

$$\lambda = \frac{h}{\sqrt{2m_0 eV \left(1 + \frac{eV}{2m_0 c^2}\right)}} \quad (3.7)$$

The resolution of the SEM is determined by the electron wavelength and the interaction volume. Compared with the distance between atoms, these parameters are large; therefore, SEM cannot be used to analyze information about individual atoms.

As described above, the interaction of the electron beam with the sample causes the emission of electrons and photons. A significant proportion of the emitted electrons will be detected,

3.1. Scanning Electron Microscopy (SEM)

which will provide us information about the sample. Using a number of magnetic coils, the primary beam is scan the sample in the x and y directions. Thus, information is obtained about its radiation, with the help of which the obtained images are created after processing. SEM equipment, in order to eliminate electron beam scattering in collisions with air particles, operates in high vacuum ($\sim 10^{-6}$ Torr). Figure 3.2 shows a schematic representation of the scanning electron microscope.

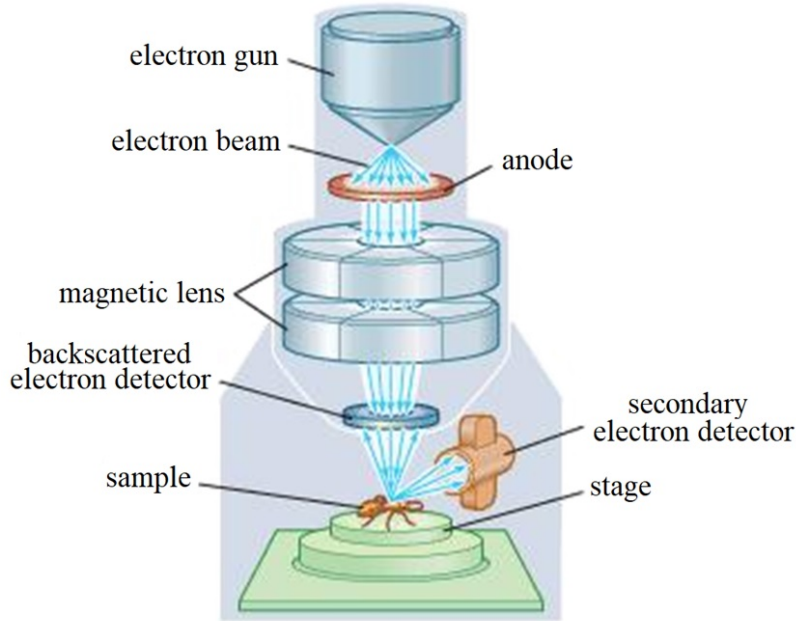


Figure 3.2: Schematic representation of the design of the scanning electron microscope [210].

A microscope of this type is used to form an image of the signal corresponding to the secondary electrons and retro-dispersed electrons. They come from the area closest to the surface of the sample, since the secondary electrons generated in the inner part lose energy on the way to outside, being absorbed and interacting with the atoms of the material itself. The number of secondary electrons depends on the angle of collision of the electron beam with the sample surface, that is, on the topography. Therefore, the signal of secondary electrons is applied to reproduce the morphology of the sample [211].

3.1.2 Sample's preparations

In order to prepare the samples for SEM measurements, the samples are placed in a conductive aluminium holder specially designed for the simultaneous placement of various samples both horizontally and vertically. The used microscope allows us to automate movements, such as displacement along three axes, in addition to rotating or tilting the sample holder.

In our case, the samples were glued to the holder using a carbon tape and small silver contacts were placed between the sample holder and the surface of the sample in order to avoid the accumulation of electron charge on the layer, that makes easy to obtain optimal and sharp images. For the same reason, the samples with low electrical conductivity were subjected to an electroconductive coating of conductive material, a metal such as an alloy of Gold and Palladium (Au-Pd) in composition 4/1 of the order of 2 nm. This coating is also very useful for increasing the signal-to-noise ratio [212].

3.1.3 Used equipment - Experimental set-up

Hitachi S-4800 scanning electron microscope

To measure the surface morphology of the oxides and heterostructures studied in this thesis we used a Hitachi S-4800 electronic microscopic scanning device belonging to the *Servei Central de Suport a la Investigació Experimental(SCSIE)* of the University of Valence (Figure 3.3). This equipment has a prechamber access for the introduction of samples in order to avoid rupture of vacuum in the microscope column and, thus, ensures optimal working conditions. The voltage in the microscope column was ~ 20 kV and an approximate working distance of 8 mm for obtaining images with good resolution. The degree of image magnification was in the range of 250 to 800,000. In addition, the microscope has a retro-dispersed electron detector, a Bruker X-ray detector, and a Quantax 400 software, which can be used to perform microanalysis of samples. The ability to move along three axes, rotating or tilting (-5 to $+60^\circ$) the sample holders together with automatic control of the system makes a very versatile and useful.

REMMA-103-1 scanning electron microscope

To measure the surface morphology of ZnMnTe and ZnMnS, as well as the cross section of these samples, a REMMA-103-1 scanning electron microscope of the “Nanoelectronics materials research” group of the Sumy State University was used (Figure 3.4). The accelerating voltage was 30 kV with a secondary electron imaging (SEI) mode resolution of 5 nm. The pressure in the column of the microscope was not more than 1.33×10^{-3} Pa. The microscope has a console, which allows X-ray electron probe microanalysis from beryllium (4) to uranium (92) using a wave dispersion spectrometer with a sensitivity of 10-100 ppm for both bulk and thin-film samples. The microscope chamber allows the installation of a sample with a maximum diameter of at least 100 mm. The sample is moved along the x and y coordinates by ± 50 mm with steps no more than $0.5 \mu\text{m}$. The tilt of the platform gives access to a range from -20° to 48° .

3.1. Scanning Electron Microscopy (SEM)



Figure 3.3: Scanning electron microscopy Hitachi S-4800.



Figure 3.4: Scanning electron microscope REMMA-103-1.

3.2 Transmission Electron Microscopy (TEM)

Unlike SEM, the information in TEM is obtained from the primary beam of electrons incident on the sample. Due to the high voltage, reaching up to 1 MeV, research with atomic-scale resolution of tenths of nm can be carried out. Since these microscopes use very high accelerating voltages, TEM equipment must operate under ultrahigh vacuum conditions (10^{-7} – 10^{-9} Pa) to prevent damage of the filament.

3.2.1 Measurement technique

Transmission microscopes mainly operate in two modes: in the parallel beam mode and in the convergent beam mode. The first mode is the most used and it is applied to form an image from the signal of electrons transmitted through the sample. On the other hand, the convergent beam regime is usually used to analyze the chemical composition of a sample using X-ray dispersive energy spectroscopy. In this thesis, the first mode of operation was used.

For the formation of an imaging of the samples, the TEM detects and processes the electrons of the beam that has passed through it. Currently, many microscopes make possible to obtain high-resolution images (HR-TEM) using structural interference of signals from the sample in the so-called face-contrast imaging [209]. Image of the crystal structure of the sample obtained by this method allows determining the crystal defects of the material, such as dislocations or stacking fault. The atomic resolution of these microscopes also makes possible to obtain images on which atomic lines are observed and values of interatomic distances can be obtained. To do this, the software applies *Fast Fourier Transform* (FFT) methodology for processing digital signals with Fourier transform used in processing analogue signals.

In crystalline samples, part of the primary electron beam is diffracted forming diffraction patterns (Figure 3.5). These diffraction patterns consist of a series of points formed by different diffractions of the crystal, around a central point (000), corresponding to a beam that passes through the sample without any deviation. When studying a polycrystalline sample, these figures will concentrated circles due to the multi-directional orientation of the single-crystals of the sample [213]. By analyzing the diffraction patterns, one can determine the structural characteristics of the samples, since the radius of the r_{hkl} rings and the corresponding interplanar distance d_{hkl} are related by the expression:

$$r_{hkl} \cdot d_{hkl} = L_s \cdot \lambda \quad (3.8)$$

where, L_s is the distance to the sample and $L_s \cdot \lambda = 1$ is the camera constant of the used transmission electron microscope. By calculating the radius of the diffraction rings (r_{hkl}) and using the transformed equation 3.9 we can determine the interplanar distance of the material.

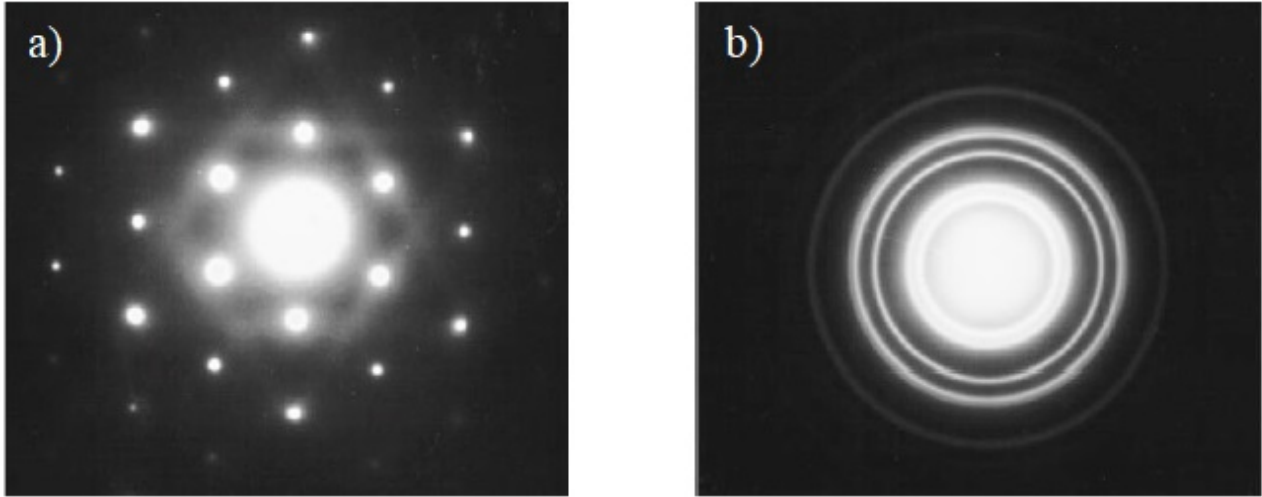


Figure 3.5: a) Diffraction patterns obtained in a conventional 100-kV TEM: a) an Al single crystal, b) polycrystalline Au [209].

$$d_{hkl} = \frac{1}{r_{hkl}} \quad (3.9)$$

In equation 3.9 it can be seen that the interplanar distances are obtained from the reciprocal of the measured radius between the point under consideration and the central point.

3.2.2 Sample's preparations

The HRTEM method is very sensitive to the sample thickness. In order to be able to carry out measurements, it is necessary that the thickness of the material studied be < 100 nm, so that the electron beam can pass through them. There are several ways to achieve this condition. One of them is the process of cutting and polishing samples, which is very useful for a detailed observation of the interfacial characteristics between the substrate and the sample. But this method is slow, time-consuming and costly, and can also lead to a partial loss of information about the material studied. If we are only interested in the properties of the material and not in the interface with the substrate, an easier way to prepare the sample is to scratch the material from the substrate.

The sample is usually placed in standard grating adapted for the microscope (Figure 3.6). The TEM grid is an ultra-thin disk whose surface consists of a pattern of nanometric windows that are transparent to electron radiation. The grid is made of conductive material to avoid charge accumulation in the sample. Silicone or copper are the usual materials for the manufacture of these nets. Usually these nets have a standard diameter of 3.05 mm and a thickness lesser than a tenth of a millimeter [214].

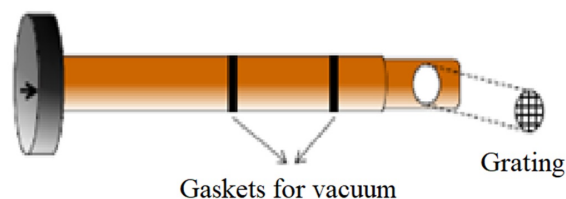


Figure 3.6: Schematic image of the sample holder and grating for TEM [214].

3.2.3 Used equipment - Experimental set-up

Analysis of samples were performed by high resolution transmission electron microscopy (*HRTEM*) with a field emission gun TECNAI G2 F20 S-Twin microscope (Figure 3.7) operated at 200 kV , having the capabilities of selected area electron diffraction (*SAED*) and energy dispersive X-ray spectroscopy (*EDX*) in the facilities of the *SCSIE* at the University of Valencia. Vacuum level was 1×10^{-5} Pa for the specimen chamber, and 1×10^{-7} for the electron gun zone, respectively. Digital Micrograph software was used to collect and post-process data, making Fast Fourier transforms (*FFT*). TEM measurements were conducted by Dr. Said Agouram, who is a member of our research team and the person in charge of the TEM at SCSIE.



Figure 3.7: Microscope FEI Tecnai G2F20 S-Twin.

3.2.4 Energy Dispersive X-Ray Spectroscopy

Although Energy dispersive X-ray spectroscopy (EDX or EDS) is not an electron microscope method, it was included in this section, since most electron microscopes provide the ability to perform such measurements, including both X-ray detectors and relevant informative tools for the quantitative determination of the composition of the material. Thus, in this thesis, EDX measurements were carried out in the SEM S4800 Hitachi and TEM FEI Tecnai G2F20 S-Twin.

As shown in the introduction of this section, the interaction of the primary electron beam of an electron microscope with the atoms of the material under study gives different types of secondary signals. Among these signals, we can find the emission of X-ray characteristics of each element caused by the release of electrons or the inner layers of an atom (Figure 3.8). That is, the energy of this radiation is characteristic of each chemical element and therefore gives us information about the composition of the sample under study.

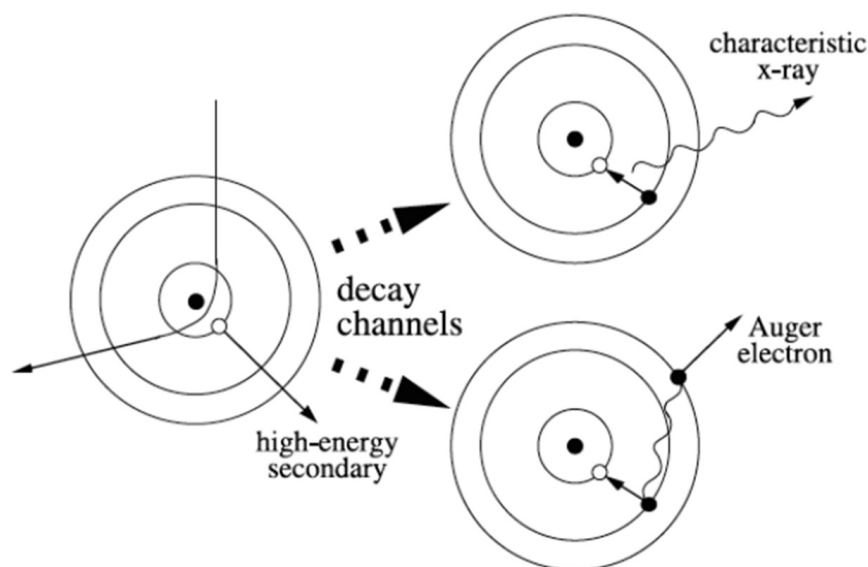


Figure 3.8: Scheme of electron scattering mechanisms [213].

Qualitative analysis in the EDX system is used to identify the elements present in the sample and quantitative analysis is used to determine the composition. In principle, all chemical elements with an atomic number greater than 4 (Be) can be detected using this characterization technique [215, 216].

Finally, in addition to quantifying the chemical elements, compositions can be performed at a specific point in the sample. That is, SEM-based EDX allows comparing the morphology with the composition of the sample. Another very useful tool, for determining the characteristics of heterostructures, is the possibility of carrying out quantitative analysis along the sample cross section [217].

As was shown above, the accelerating voltage of electrons determines the depth of the interaction volume. In SEM microscopes, when thin layers are analyzed in order to avoid masking information about a material layer with information from a substrate, a compromise must be reached between the electron energy and the depth of interaction. That is, the more energy in the electron beam, the deeper the interaction volume and, therefore, there is a fraction of the detected signal that comes from the substrate. On the other hand, if the accelerating voltage is low, the detected information will come from a superficial layer, but it may not be enough energy to detect the heavier atoms.

Taking this into account, an accelerating voltage of 10 kV was used for the EDX analysis in this thesis, to detect the cadmium and zinc content on unmetallized samples.

3.3 Particle Induced X-ray Emission (PIXE)

Modern scientific achievements in the field of microanalysis and a high level of technology in this field of activity have made possible to find a solution to many macro tasks by studying the laws of the microworld. The elemental composition of the substance and the location of elements in it determine its physicochemical properties. Among the wide variety of methods that allow determining the distribution of elements in the samples under study, methods using focused beams of charged particles have several advantages. And, first of all, this is due to the possibility of non-destructive quantitative microanalysis with a high spatial resolution. In the past few decades, microanalysis methods using nuclear scanning microprobe (NSMP) have been developed. The main principle of the microprobe operation is that an accelerated beam of light ions up to energies of several megaelectron-volts (using electrostatic accelerators, as a rule) is focused on the surface of the test sample into a spot with dimensions of about one micrometer. As a result, scanning with the beam and recording the interaction of the particles of the beam with the atoms of the sample, it becomes possible to determine both the elemental composition of the tested substance and the map of the arrangement of elements. In contrast to a scanning electron microscope, there are no fundamental physical restrictions on the spatial resolution in the NSMP, which is associated with the size of the beam spot due to its small expansion during passage through the substance.

3.3.1 Principle of PIXE (Particle Induced X-ray Emission)

When a charged particle with sufficient energy (of the order of several MeV), passes through a material, it loses energy due to ionization of the inner shell of the atoms through which it passes. This creates X-rays with wavelengths characteristic of a particular element. This phenomenon is called Particle Induced X-ray Emission (PIXE) [218].

When the ion interacts with the electrons in the inner shells of the atoms (mainly the shells K and L), the electrons can get enough energy to throw them out (see Figure 3.9). Quantum theory states that the electrons of an atom should occupy discrete energy levels in order to be stable. X-rays are emitted due to the filling of free vacancies with the electron of the outer shell, but only certain transitions are allowed. The energies of these X-rays are characteristic of the element, and therefore, if an appropriate energy-dispersive detector is used, spectra can be recorded and measured to identify the elemental composition of the sample exposed to the beam.

PIXE is relatively simple and multielemental analytical technique that can be used to identify and quantify elements ranging from Na to U . Due to the high signal to background ratio, PIXE is also a nondestructive technique and very sensitive for a wide range of measured elements with detection limits close to 1 ppm (part-per-million) [219]. Typically, analysis takes

place in a vacuum chamber using protons and/or α -particles. Due to the large mass of protons with respect to electrons, the deflection of the beam in the transverse direction is smaller, which is an advantage and important for proton recording. The lower detection limit for a PIXE beam is given by the ability of the X-rays to pass through the window between the chamber and the X-ray detector. The upper limit is given by the ionization cross section, the probability of the K electron shell ionization, this is maximal when the velocity of the proton matches the velocity of the electron (10 % of the speed of light), therefore 3 MeV proton beams can be optimal [220]. Due to its longer probe depth (tens of μm) scanning ion beams can be used not only to obtain the surface maps measuring, but also the spatial distribution of elements in the sample.

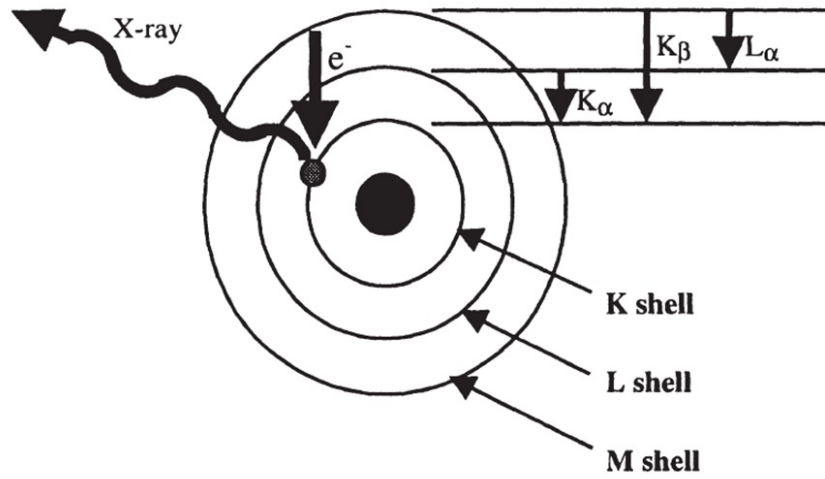


Figure 3.9: X-ray nomenclature based the shell of the hole and the number shell above it from which an electron comes to fill the vacancy [221]

Usually 2 detectors are installed in the working chamber. Silicon drift detector (*SDD*) is used for the analysis of light elements (*Na* and above). On the other hand, a *Si(Li)* detector having large solid angle and a Mylar filter is optimized for the heavy elements (*K*, *Ca* and above) as shown in Figure 3.10. Since protons can interact with atomic nuclei in a sample through elastic collisions, Rutherford backscattering (*RBS*) can occur when a proton is repelled at angles close to 180 °. Backscatter provides information on the thickness and composition of the sample. This technique is powerful for studding the depth profiling of heavy elements in light substrates. When RBS is done in combination with PIXE, it can be used to determine light element concentrations, which is not possible by PIXE. Combination of two methods allows a better analysis. RBS spectra quantification can be done by the SIMNRA software [219].

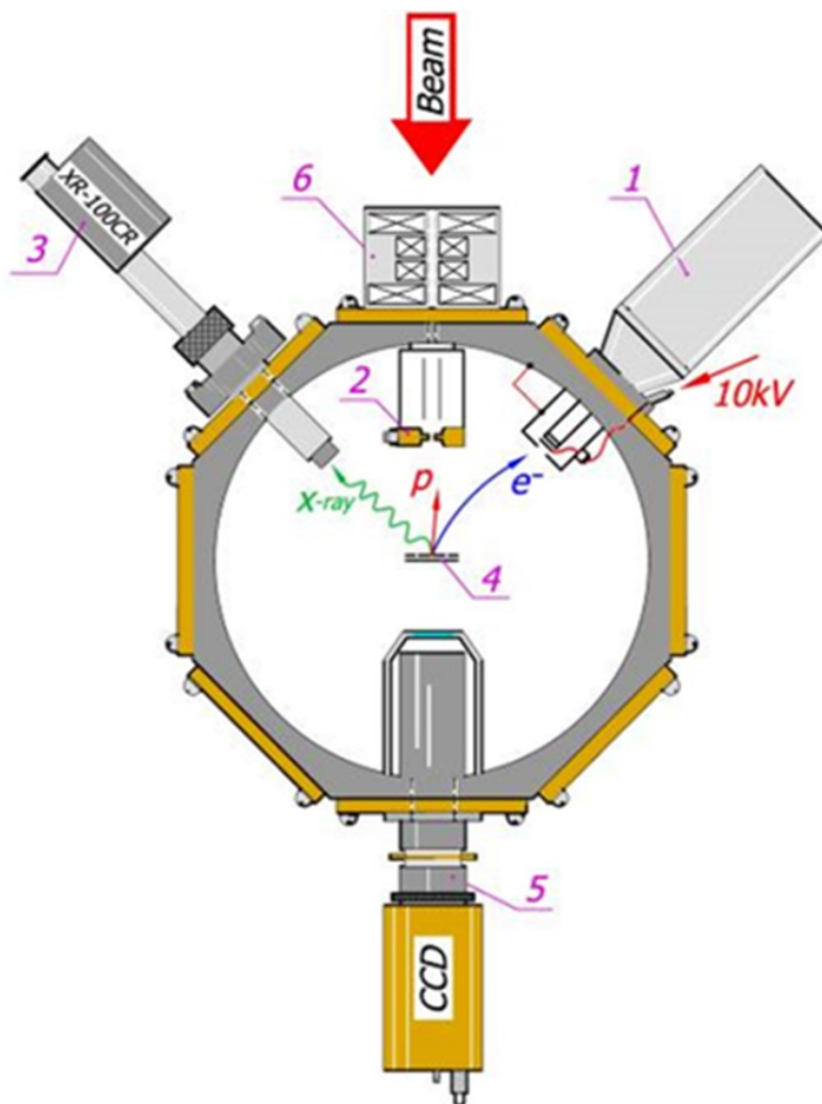


Figure 3.10: Schematic representation of the working camera:

1) secondary electron detector; 2) annular surface-barrier detector for RBS; 3) semiconductor detector for PIXE; 4) target; 5) optical microscope with CCD (x100); 6) scanner.

Since the PIXE analysis method is simple and can be used to analyze almost all elements at the same time with high sensitivity, it is currently used in a wide range of applications including medicine, materials science, pollution monitoring, mineral exploration, metallurgy, a criminal investigation, food, and more. In particular, in archeology, geology and art, the method helps to answer questions about origin, dating and authenticity.

3.3.2 Used equipment - Experimental set-up

The analysis of the films was carried out, in ZnMnTe and ZnMnS samples, by using characteristic X-ray radiation induced by the proton beam [222]. The investigations were made by means of the electrostatic accelerator "Sokil" with a proton beam energy up to 3 MeV (Institute of Applied Physics, NAS of Ukraine, Sumy) as present in Figure 3.11 [223]. Summary spectra from several areas of the sample surfaces (PIXE) were scanned and point-by point studied using the micro-beam (μ -PIXE). The typical region size was about $200 \times 200 \mu\text{m}$. The cross-section of the probe was $4 \times 4 \mu\text{m}^2$, the charge $Q = 4 \times 10^{-10} \text{ C/pixel}$, the scan region was about $50 \times 50 \text{ pixel}$, the scanning step was $4 \mu\text{m}$, the proton energy was $E_p = 1.5 \text{ MeV}$. Under «pixel» one means a stationary position of the probe at discrete scanning. These studies resulted in a map of the distribution of the alloyed element (*Mn*) on the surface area and the element composition in some regions of the films. The working-out of the PIXE spectra was carried out by using the program GUPIX 3.

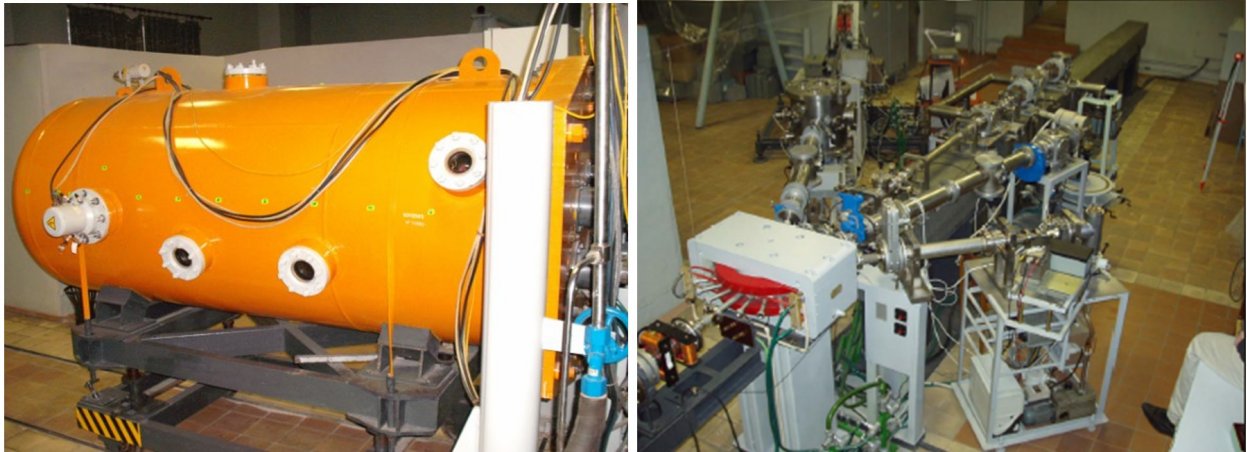


Figure 3.11: Electrostatic accelerator (a) and microanalytical accelerator complex “Sokil” of the IAP NAS of Ukraine (Sumy) (b)

3.4 X-Ray Diffraction (XRD)

In 1895, Wilhelm Conrad Röntgen discovered a phenomenon that was later called X-ray radiation. It soon becomes known that X-rays have wavelengths in the range of $10^{-2} - 10^2$ Å, are energetic enough to penetrate into solid materials, and are well prepared to study their internal structure. Based on these results, many useful tools and techniques for the analysis and evaluation of materials were developed and tested. This section discusses some of the basic principles of XRD and the hardware that was used to study the samples described in this thesis.

3.4.1 X-ray diffraction

To perform X-ray diffraction measurements, in addition to an emitter and a detector of this type of radiation, it is also necessary to have a positioning system of the samples. In this sense, commercial diffractometers have more or less complex systems that allow the angular movement in different axes to perform different types of measurements.

In the geometry of Bragg-Brentano, with which we have worked to identify the structural phases of the materials considered in this thesis, the incident beam and the diffractometer form an angle 2θ , being θ the Bragg angle, the angle between the incident beam and the surface of the sample. Thus, scans 2θ - θ are those in which the intensity of the diffracted beam is measured as a function of the diffraction angle, keeping constant this relationship between the angles. We can find instruments in which the X-ray source is already fixed while the sample rotates on angle θ and the detector an angle 2θ in the same direction. In this case, we talk about the configuration 2θ - θ . On the other hand, other diffractometers have the configuration θ - θ in which they fix the sample and rotate the X-ray tube and detector at an angle θ , but in opposite directions.

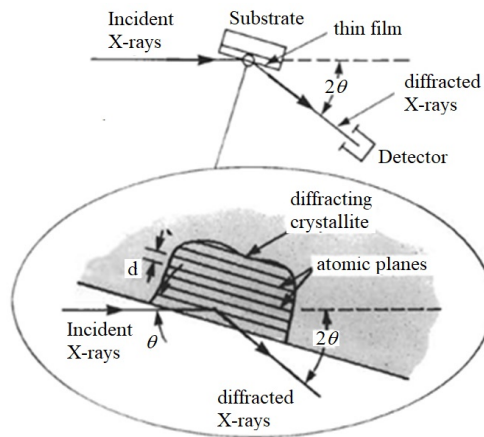


Figure 3.12: Basic features of a typical XRD experiment [215].

Figure 3.12 shows the diffractometer geometry, where the beam from the X-ray tube interacts at some angle with the sample surface. This angle can vary depending on the position of the sample and its rotation. The detector measures the intensity of the diffracted beam and can also be rotated to position it in the desired angular position. The intensity of diffraction as a function of 2θ and the orientation of the sample gives diffraction patterns that allow the identification of the crystalline phases and crystallite size/microstrain analysis.

3.4.2 Basic principles

Using Miller indices, the distances between the plans of a certain family (hkl) can be related to the lattice parameters of the crystal structure. This ratio depends on the type of the structure and can be a complex expression in structures with low symmetry, such as Rhombohedral or Triclinic. To work with hexagonal lattices, it is convenient to use four Miller - Bravais indices ($hkil$), in which the third element i denotes a convenient but degenerate (carrying no additional information) component equal to $-h -k$. The angle between the h , i and k components of the index is 120° , so they are not orthogonal. The l component is perpendicular to all three directions h , i , and k [224]. For hexagonal crystals, as for instance ZnO, the interplanar distance is given by

$$d_{hkl} = \left(\frac{h^2 + k^2 + l^2}{3a^2/4} + \frac{l^2}{c^2} \right)^{-\frac{1}{2}} \quad (3.10)$$

In the case of a cubic structure, such as the structure of CdO, CdTe, ZnMnTe or ZnMnS, the relationship between the interplanar distance d_{hkl} of the (hkl) plan family and the lattice parameter of the structure is determined by

$$d_{hkl} = \left(\frac{h^2 + k^2 + l^2}{a^2} \right)^{-\frac{1}{2}} \quad (3.11)$$

Figure 3.13 shows the Miller indices of lattice planes and indices of directions depending on the intersection of the line with the face of the unit cell.

On the other hand, for the analysis of diffraction phenomena we have another very useful tool, such as the Bragg's law. This law relates the angle of diffraction, with the interplanary distances d and the wavelength of the incident radiation. Thus, in Figure 3.14 we have a flat wave that affects a lattice of atoms that spread it in all directions. Due to the difference in paths of the waves diffracted by the different atoms, depending on the angle of observation we can find constructive or destructive interferences. The condition for which a constructive interference is produced is known as the Bragg's law:

$$n \cdot \lambda = 2 \cdot d \cdot \sin \theta \quad (3.12)$$

where $n=1,2,3,\dots$ is an integer representing the order of diffraction, λ it is the wavelength of the radiation, d is the distance between planes and θ is the Bragg angle, that is, the diffraction angle for which the constructive interference occurs. Finally, if we introduce in the Bragg's law the first order diffraction, the indexation of the interplanar distances d_{hkl} we can express as [225]:

$$\lambda = 2 \cdot d_{hkl} \cdot \sin(\theta_{hkl}) \quad (3.13)$$

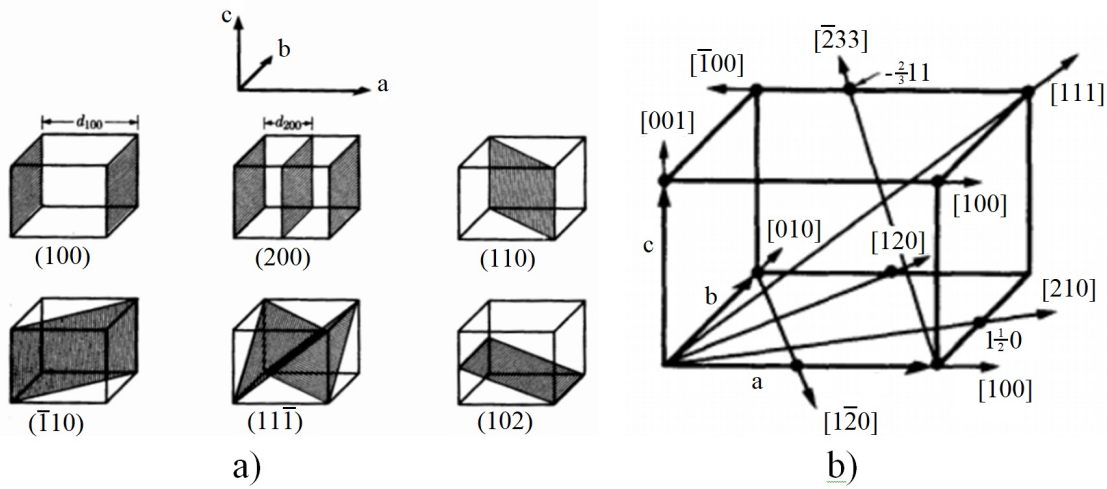


Figure 3.13: (a) Miller indices of some lattice planes; (b) Indices of directions. The distance d_{hkl} is the (hkl) plane spacing [226].

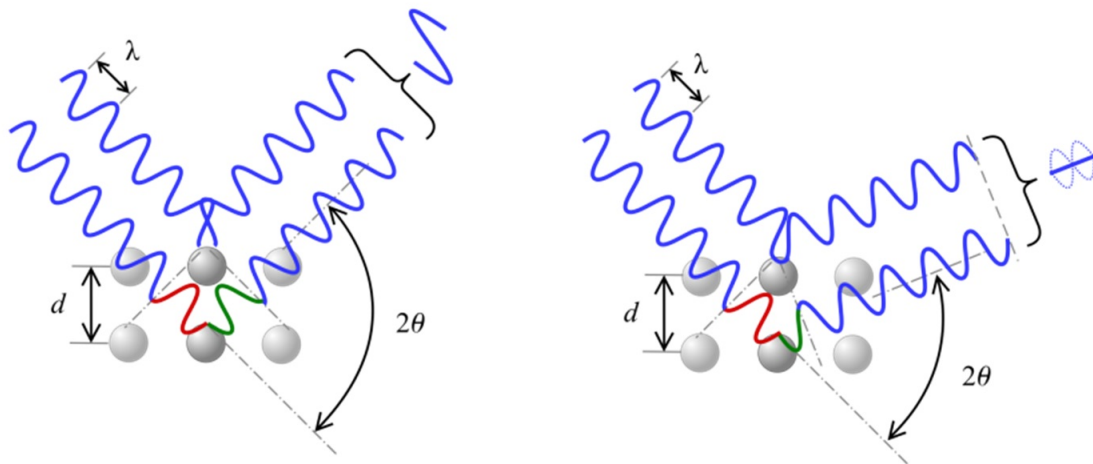


Figure 3.14: The geometry of constructive and destructive interference arising in the crystal lattice, which generates the Bragg law. Image retrieved from [227].

3.4.3 Coherent scattering size and microdeformation

During the growth on the surface of a substrate, a kind of crystalline layer forms. The mosaic model is one of the most commonly used models for describing the crystal layer, which consists of a set of coherent scattering domains (CSD), also called crystallites (Figure 3.15). These single crystal domains do not have a perfect orientation, so they can be tilted or rotated relative to each other. Thus, the length of these domains in the direction perpendicular to the surface, is called length of vertical coherence L_{\perp} , whereas in the direction parallel to the surface we call it the length of the horizontal coherence L_{\parallel} .

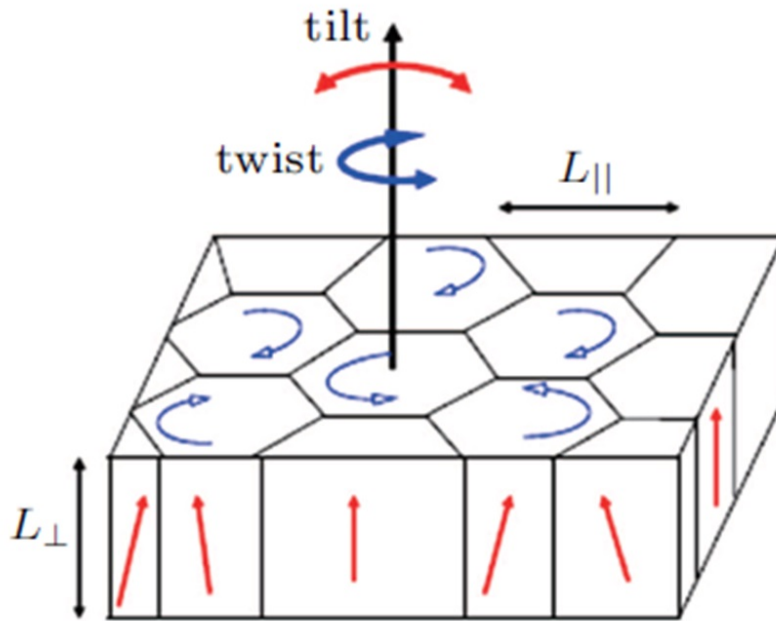


Figure 3.15: Illustration of a mosaic structure with characteristic parameters [228].

Since each crystal can grow with its own unique orientation, this leads to a relative misorientation between crystalline domains. When there is an *out-plane* misorientation of the single-crystal domains (that is, relative to the axis perpendicular to the sample), we call it as *tilt*. On the other hand, we call *twist* the rotation of domains about the same axis, or, in other words, *in-plane* misorientation. These characteristics of crystallites (limited size and misorientation) are produced by defects, as dislocations which are a linear or one-dimensional distortion of the structure. In the layer, each type of dislocation is associated with a local distortion of the lattice. There are 2 types of dislocations (Figure 5.10). First type is represented by an additional part of the plane of atoms or a half-plane, the edge of which ends inside the crystal. They are called edge dislocations and are represented by the symbol \perp , which also indicates the position of the dislocation line. Another type of dislocations, called screw dislocations, can

be considered as formed by shear stress, where the upper front region of the crystal is shifted one atomic distance to the right (or left) relative to the bottom. Most dislocations found in crystalline materials are probably neither a clean edge nor a clean screw, but have components of both types, then they are called mixed dislocations. The magnitude and direction of the lattice distortion associated with the dislocations in a crystal lattice are expressed in terms of the Burgers vector, denoted by b . In addition, even if the dislocations change their direction and nature inside the crystal (for example, from the edge to the mixed screw), the Burgers vector is the same at all points along the dislocations line [229].

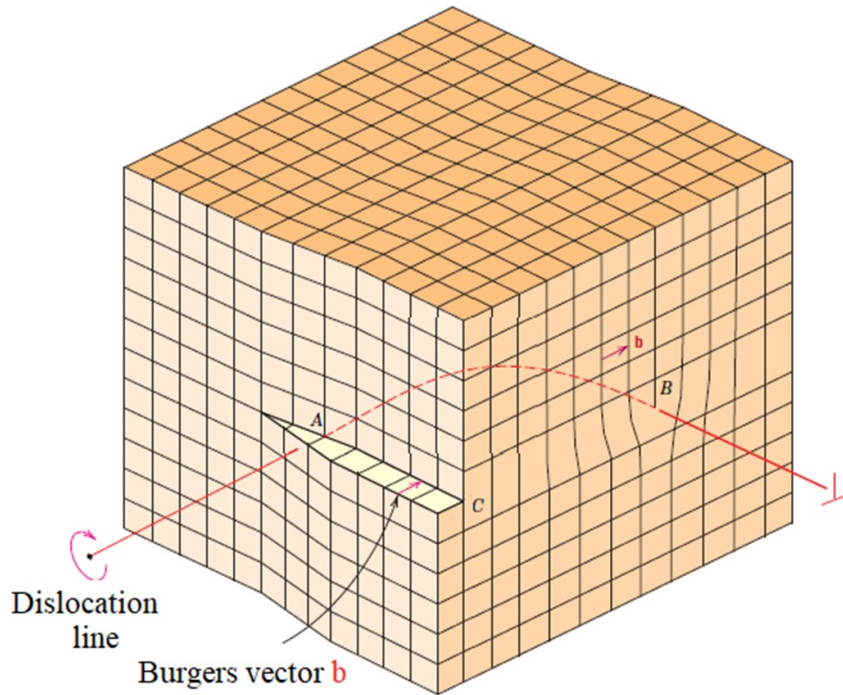


Figure 3.16: Schematic representation of a dislocation having an edge, a screw and a mixed one. At point A, the dislocation is a clean screw, and at point B is a clean edge. For regions in between where there is the curvature in the dislocation line, the character C is mixed edge and screw [229].

In addition, single crystals may have a deviation in the interplanar space, whose statistical value is called microstrain of the lattice and can be expressed as:

$$\varepsilon = \frac{\Delta d}{d} \quad (3.14)$$

where d is the interplanar distance and Δd is its statistical variation.

All these factors, in addition to the instrumental ones, contribute to the broadening of diffraction peaks (ideally Dirac's deltas) and therefore can be detected.

3.4.4 Williamson-Hall plot

The kinematic theory of X-ray scattering shows that crystallite size and lattice distortion are diffraction order independent or dependent, respectively, enabling the separation of the two effects. Williamson and Hall suggested [230] that the broadening ΔK of peak profiles in the reciprocal space due to these two broadening effects can be written as

$$\Delta K = \frac{0.9}{D} + 2\mu K \quad (3.15)$$

where 0.9 is dimensionless shape factor used for domains approximated to be roughly spherical, $K = 2 \sin \theta / \lambda$ is the module of the scattering vector, $\Delta K = \Delta(2\theta) \cos \theta / \lambda$ is the broadening in the reciprocal space $\Delta(2\theta)$ is the full width at half maximum (FWHM) of the diffraction peaks in the 2θ - θ scans, θ the Bragg angle, λ the wavelength of radiation, D the average crystallite size and $\mu = \langle \epsilon^2 \rangle^{1/2}$ the square root of the quadratic lattice microstrain (or microdeformation). The classical Williamson-Hall plot (WH) follow this equation and is a linear function of K .

When there is no microstrain, equation 3.15 can be rewritten as the known Debye-Sherrer's formula [231] :

$$D = \frac{0.9\lambda}{\Delta(2\theta) \cos \theta} \quad (3.16)$$

where the shape factor of 0.9 can vary with the actual shape of the crystallite, λ is the wavelength of the X-ray and $\Delta(2\theta)$ is the line broadening at half the maximum intensity in radians.

This approach is useful in isotropic cases which can be interpreted with simple spherical crystallite shapes and isotropic microstrains. However anisotropic situations require further efforts. When strain broadening is caused by dislocations, line broadening is generally anisotropic [232] and it depends on the hkl reflection, that is, it depends on the orientation and the length of the diffraction vector. In this case, line broadening can be described in terms of a logarithmic series expansion of the Fourier coefficients of a peak profile and the average contrast factor of dislocations \overline{C}_{hkl} [233]. As a consequence, the proper scaling factor of breadths of peak profile is $K\overline{C}_{hkl}^{1/2}$, instead of merely K . This is known as the modified Williamson-Hall plot (MWH) [234–236].

If crystallites are non-spherical, then an additional anisotropy has to be considered [237]. In such a case, the crystallite size must be described by multi-dimensional lengths, with their lengths dependent on the order of diffraction. With these considerations, the modified Williamson-Hall method can be adapted and the line broadening can be written as:

$$\Delta K = \frac{0.9}{\overline{D}_{hkl}} + \alpha K^2 \overline{C}_{hkl} \quad (3.17)$$

where \overline{C}_{hkl} is the average contrast factor of dislocations for the Bragg reflection (hkl) , \overline{D}_{hkl} the average crystallite size for the Bragg reflection (hkl) and α is a constant that depends on the Burgers vector and the density of dislocations.

The mean contrast factor for a cubic crystal is related to the mean contrast factor of the Bragg reflection $(h00)$ as given by the equation

$$\overline{C}_{hkl} = \overline{C}_{h00}(1 - qH^2) \quad (3.18)$$

where $H^2 = (h^2k^2 + h^2l^2 + k^2l^2)/(h^2 + k^2 + l^2)^2$ and q is a parameter which depends on the elastic constants and type of dislocations.

The value of q can be obtained by inserting eq. 3.18 into eq. 3.17

$$\frac{\Delta K - 0.9/\overline{D}_{hkl}}{K^2} = \alpha \overline{C}_{h00}(1 - qH^2) \quad (3.19)$$

and by solving this equation in H^2 by the least-squares method.

3.4.5 Density of dislocations

As said, the CSD size boundaries are formed by dislocations located at their boards, but at the same time, dislocations in the subgrain are responsible of microdeformations in the material. To determine the CSD size and microdeformation in chalcogenide films, the used method of approximation consists in the representation of the X-ray line by triple convolution [238]. The relationship between the parameters of the film substructure can be found from the equations:

$$L = \frac{\lambda}{\cos \theta_1} \cdot \frac{tB_1 - cB_2}{t\beta_{f1}^2 - \beta_{f2}^2} \quad (3.20)$$

$$\varepsilon^2 = \frac{c\beta_{f1}^2 B_2 - \beta_{f2}^2 B_1}{16tg\theta_1(cB_2 - tB_1)} \quad (3.21)$$

where,

$$t = \frac{\tan^2 \theta_1}{\tan^2 \theta_2}, c = \frac{\cos \theta_1}{\cos \theta_2}, \beta_{fi} = \sqrt{(B_i)^2 - (b_i)^2}$$

θ_1 and θ_2 are the diffraction angles of the pair of analyzed X-ray lines (for example, [111] and [222])

B_i, b_i, β_{fi} are the measured, instrumental and physical broadening of the respective X-ray lines.

The CSD size L in the films and the microdeformation value ε allow to determine the averaged density of the dislocations ($lines \cdot m^{-2}$) formed at the subgrain boundaries. This density of dislocations assuming a cubic-shaped CSD with size L is [239, 240]:

$$\rho_L = \frac{3n}{L^2} \quad (3.22)$$

where n is the mean number of dislocations at each face of the six planes of the block.

If the dislocations are mostly located in the middle of the subgrains and creates microdeformation, the dislocation density ($lines \cdot m^{-2}$) is obtained from the expression:

$$\rho_\varepsilon = \frac{Y}{F} \left(\frac{2\varepsilon}{b} \right)^2 \quad (3.23)$$

where 2ε is the width of the microdeformation distribution; b is the modulus of the Burgers vector; F is a constant taking into account the increase of the dislocation energy under interaction with other dislocations; Y is a constant depending on the dislocation distribution function. Y and F are dimensionless constants. In this approach, $Y=25$ for the Cauchy function and $Y=4$ for the Gauss one.

Accepting $n=F=1$, equations 3.20 and 3.21 give an estimation the lower limit of ρ_L and the upper limit of ρ_ε . Somewhat other equation for estimation the total dislocation concentration ($lines \cdot m^{-2}$) in the material is given in [241] as:

$$\rho = \frac{15\varepsilon}{d_0 L} \quad (3.24)$$

Thus, equations 3.22-3.24 make possible to estimate the concentration of dislocations in the CSD bulk, at their boundaries, and the total concentration.

Supposing that the CSD's are of equal axes and the additional broadening of (111) and (222) X-ray lines compared with (200) and (400) lines is due to the stacking fault (SF) presence, one can calculate the total concentration of the deformation and growth defects (in %) in the films [239, 240]:

$$\alpha' = 1.5\alpha + \beta = 3.04 \left(\frac{1}{L_{(h00)}} + \frac{1}{L_{(hhh)}} \right) d_{111} \quad (3.25)$$

where α' is the deformation defects concentration, β stands for the growth defects concentration, and $d_{(111)}$ is an interplanar distance.

3.4.6 Pole figures

Pole figures are $2D$ stereographic projection of distribution of the orientation of crystal presents in the sample. For a single crystal, these projections will be points that indicate the symmetry of the considered plane. In the case of polycrystalline samples, each grain has or may have a different crystallographic orientation, thus exhibiting a randomly distribution of points. For crystals with a preferred orientation, points tend to be grouped with respect to

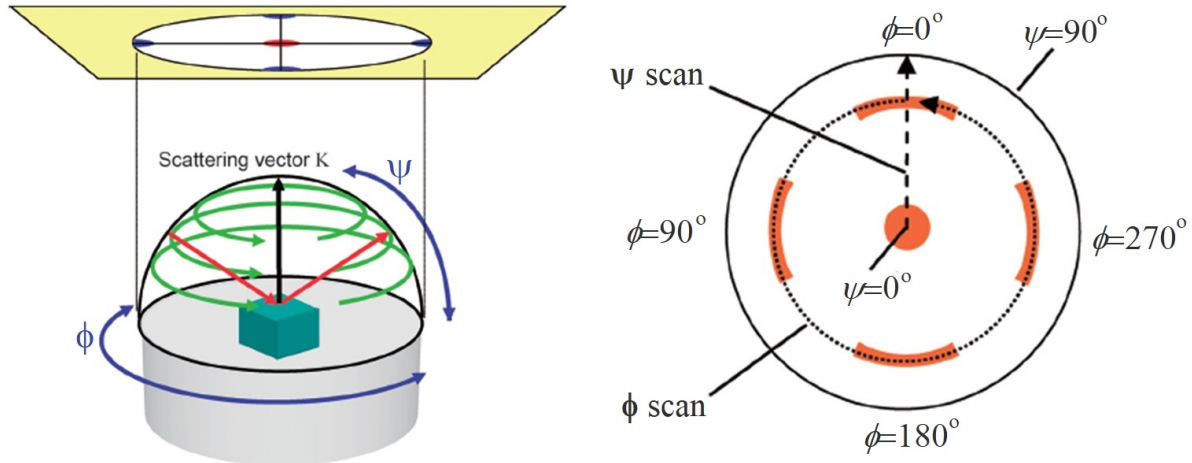


Figure 3.17: Schematic representation of scan patterns and some pole figure with the definition of angles [242].

some particular orientation. Since pole figures give the mean orientation of grains relative to a given reference system, the orientation of both substrate and film can be determined relative to the same reference system and, therefore, it will be possible to establish epitaxial relations between them.

For obtaining pole figures, the rotation angle (ϕ) of the diffractometer (see Figure 3.17) was changed from 0 to 360 ° and the inclination angle (ψ) was changed from 0 to 90 °, while the diffraction angle 2θ was held fixed for the reflection of interest. The stereographic projection of the three-dimensional intensity distribution is constructed as a function of two types of quantities, one of which is represented by the distance from the center of the projection, and the second of which is represented by the distance measured along a circle of constant radius from a given radial axis.

3.4.7 Vegard's law for ternary compounds

Sometimes, to change the properties of binary material it is alloyed making a ternary compound from the host material but with some changes in the lattice parameters and properties. It could be supposed that the lattice parameters of the ternary compound can be found by a linear interpolation. This empirical rule is known as Vegard's law [243, 244]. Structural, optical and electrical properties, however, can deviate from this linear approach. For a compound of the type ABC , where AC and BC are the initial binary compounds, the expression for the lattice parameter would be:

$$a^{A_xB_{1-x}C} = x \cdot a^{AC} + (1 - x) \cdot a^{BC} \quad (3.26)$$

This law is partially fulfilled in some binary compounds having a crystalline structure of the same type. In the case of materials such as CdO and ZnO, a change in the structure of the material from rock salt to wurtzite does not allow the direct application of this interpolation.

Similarly to the lattice parameter of a semiconductor we can also write a linear dependence of the band gap energy E_g in respect to the band gap of its binary constituents. Sometimes linear interpolation between the band gap energy is not accurate enough, and therefore an additional term is added to take into account the curvature of the band gap energy as a function of the composition. Empirically, the band gap of the composite semiconductor alloy $A_xB_{1-x}C$ could be fitted [245] as:

$$E_g^{A_xB_{1-x}C} = x \cdot E_g^{(AC)} + (1 - x) \cdot E_g^{(BC)} + bx \cdot (1 - x) \quad (3.27)$$

where b is the deflection (nonlinearity) or bowing parameter.

Vegard's law is rarely fully observed, and more often, deviations from linear behavior occur. However, it can be used in practice to obtain approximated values when experimental data are not available for the system of interest.

3.4.8 Used equipment - Experimental set-up

Bruker D8 Advance A25

Bruker D8 Advance A25 diffractometer (figure 3.18) was used to measure the diffraction peaks of ZnO, CdO and CdTe films obtained using the MOCVD method. Configurations of Bragg-Brentano geometry was used. The configuration of the 2θ - θ angles was obtained using an X-ray tube with a *Cu* anode ($K_{\alpha 1} = 1.54056 \text{ \AA}$) and a fast *Lynx-eye* detector, which allows us to simultaneously measure an interval of 3° from the angle of 2θ . In addition, diffractometer has an automatic sample changer where 45 samples can be loaded.

The diffractometer (Figure 3.18 b) consist of a goniometer (1), the tube, tube stand (2), the slit system (3 and 5), the sample holder (4) and the detector (6).

The unit is installed horizontally or vertically in a radiation protected housing. A lead glass window at the front of the radiation protection housing enables the samples to be changed or the diffractometer mounts to be modified. The window shutter of the tube stand closes automatically when this window is opened. The equipment available allows the characterization of a wide range of materials of diverse nature such as minerals, plastics, semiconductors, ceramics, pigments and in general powdery products obtained from chemical synthesis.

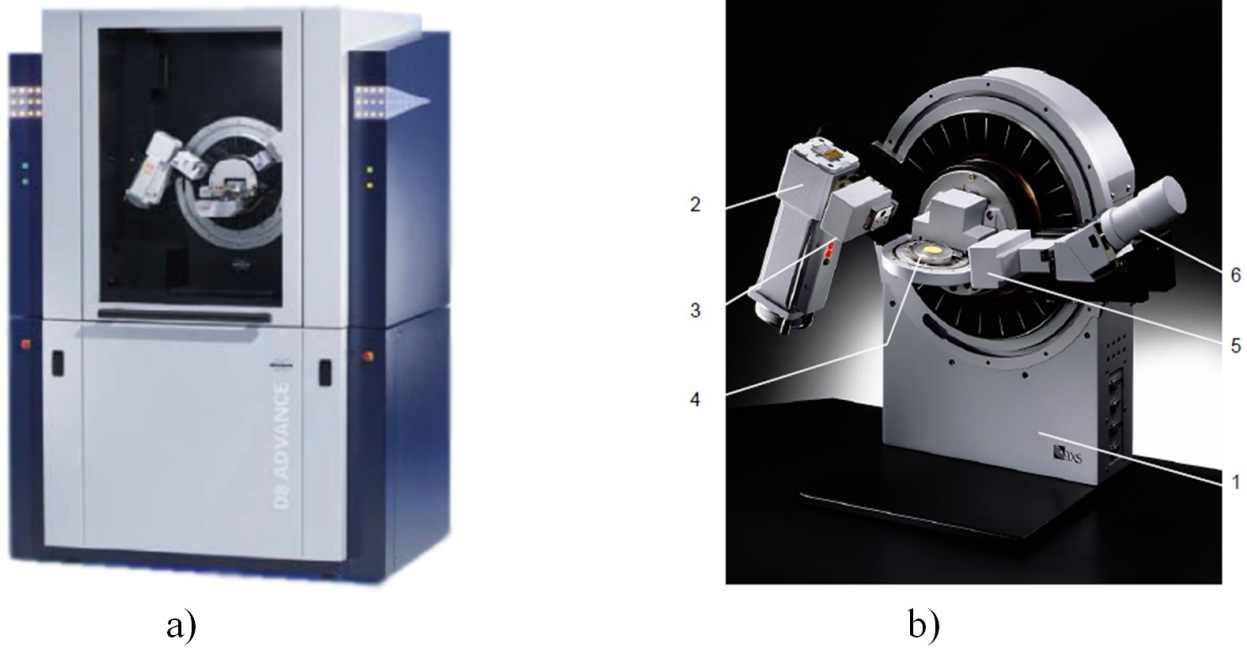


Figure 3.18: Diffractometers of laboratories SCSIE of the University of Valencia:
a) Bruker D8 Advance A25 diffractometer; b) D8 diffractometer, vertical installation [246].

Diffractometer DRON-4-07

The structural investigations of the ZnMnTe and ZnMnS films were performed by using the diffractometer DRON 4-07 (Figure 3.19) with Ni-filtered $K\alpha$ radiation of the copper anode in the range of angles of movement of the Bragg's angles 2θ from 5° to 90° . This unit is designed for X-ray diffraction studies of polycrystalline materials. The Bragg-Bretano configuration is used. The step of the angular movement of the detection unit in automatic mode is from 0.02° . The signal accumulation time for each angle of movement of the detection unit is 2 sec. Qualitative and quantitative phase analysis can be carried out using open structural databases and packages (GSAS, PSW, XPOWDER et al.). The appearance of the laboratory setup is shown in the figure.

XRD patterns were used for determining the coherent scattering domain (CSD) size and the microdeformation grade ε in thin films by the broadening of the XRD lines. To resolve the diffraction broadening caused by physical (β_i) and instrumental (b_i) effects Cauchy and Gauss approximations were used [247]. Besides that, the above mentioned parameters were found by the threefold convolution method [248]. All procedures of the working-out the X-ray line profiling (background removing, smoothing, $K\alpha$ doublet resolution) were performed using the software DIFWIN.



Figure 3.19: X-ray Diffractometer DRON-4-07 [249].

PANalytical X'Pert MRD

For a more detailed study of the layers of ZnMnTe films, we used the High resolution diffractometer PANalytical X'Pert Pro (Figure 3.20 a). Williamson-Hall plots and pole figures were obtained. This diffractometer has a parabolic mirror, which converts a divergent beam from the X-ray source into an almost parallel beam. The diffractometer has a high resolution goniometer with four rotation axes and a sample holder, which allows to program movements along different axes and angles of the system with a resolution of 0.01° for ψ and ω , and 0.0001° for 2θ and ω , respectively (Figure 3.20 b). Unlike a conventional diffractometer, $K_{\alpha 1}$ is the only radiation source in this line, thanks to a monochromator of four Ge (220) crystals.

The ability to move along the x , y , and z axes allows to make measurements of samples at different points. For obtaining pole figures, the rotation angle (ϕ) of the diffractometer was changed from 0 to 360° and the inclination angle (ψ) was changed from 0 to 90° , while the diffraction angle 2θ was held fixed for the reflection of interest.

Thus, this device allows to get measurements with a high level accuracy, but a longer measurement time. The instrumental contribution to the broadening of diffraction peaks in this diffractometer is considered not significant.

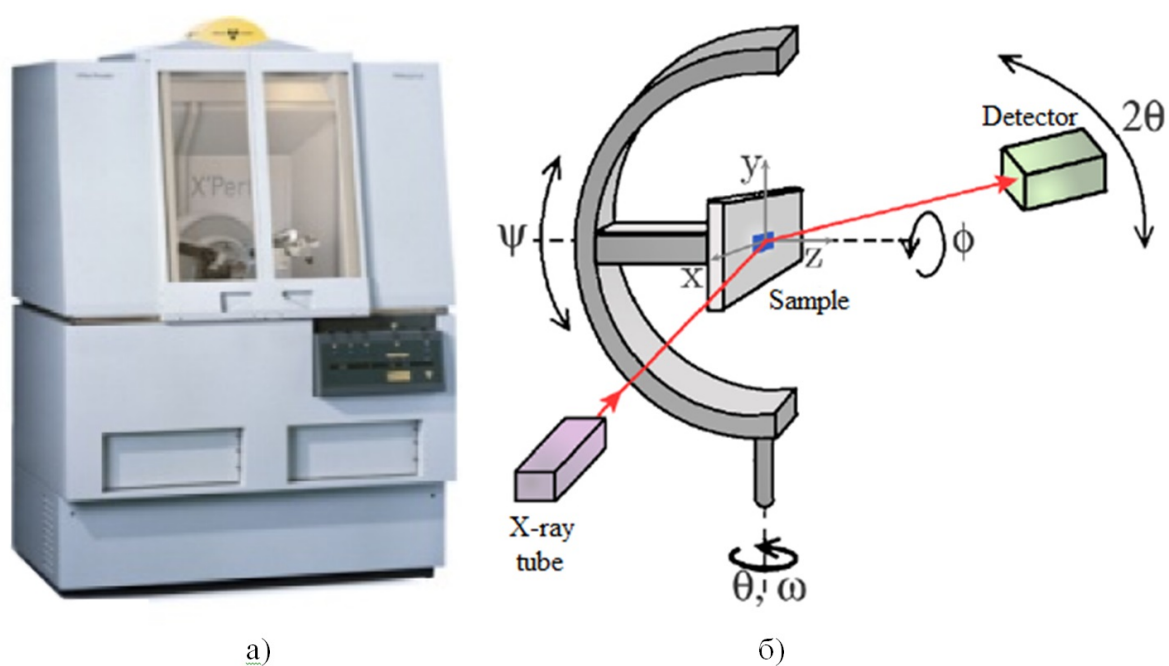


Figure 3.20: High resolution diffractometer PANalytical X'Pert Pro (a), goniometer with rotation axes (b)

3.5 Optical transmission measurement

The response of semiconductors to electromagnetic radiation is the basis for the implementation of optoelectronic devices. The search for optimal compounds for their use as optical sensors, photodiodes, optical coatings, or active layers of solar cells is a priority task, so long as productivity increases, so do energy costs. The synthesis of new materials with a high interaction of light with the surface should help to obtain compounds for optoelectronic devices that can operate in the range from infrared to ultraviolet radiation.

The optical characteristics of the studied films were determined using transmittance and absorbance spectra by optical spectrophotometry. This characterization method determines which part of the monochromatic light beam is absorbed and which part is transmitted through the sample, depending on the energy of the incident light beam. The results makes possible to obtain absorption curves depending on the beam energy with the help of which we determined the optical band gap of the compounds.

3.5.1 Basic principles

When a beam with a certain energy $h\nu$ incide on the surface of semiconductor material with band gap energy E_g , the beam can be transmitted, reflected, absorbed, or scattered. There are 2 situations:

- When $h\nu > E_g$, that is, when the energy of the light ray is greater than the energy of the band gap, photons can excite electrons from the valence band to the conducting band.
- When $h\nu < E_g$, photons do not have enough energy to excite electrons and pass through a semiconductor, which will behave as if it were transparent to these electrons.

To determine how much light passes through the investigated material, the transmittance is used. This parameter shows the ratio of the intensity of the light beam that crossed the sample, and is calculated as:

$$T = \frac{I(d)}{I_0} \quad (3.28)$$

where, $I(d)$ is the intensity of light that passes through the sample of thickness d , I_0 is the intensity of light without the sample.

On another hand, the amount of absorbed light will depend on the probability of the transition of the electrons of the valence band to the conducting band. The absorption coefficient (α) that characterizes the amount of absorbed light depends on the band gap of the material and the energy of the incident light, as shown in equations 3.29 and 3.30 for direct and indirect transitions, respectively:

$$\alpha \propto \frac{(h\nu - E_g)^{\frac{1}{2}}}{h\nu} \quad (3.29)$$

$$\alpha \propto \frac{(h\nu - E_g)^2}{h\nu} \quad (3.30)$$

It is known that the absorbance coefficient of one layer of a certain material can be found using the relations:

$$A = \int_0^d \alpha(x) dx \quad (3.31)$$

where A and d are the absorbance and layer thickness, respectively, and $\alpha(x)$ is the absorption coefficient at x . It should be noted that the units of the absorption coefficient are cm^{-1} and, therefore, the absorbance has no units. If the absorption coefficient is uniform along the path x , then we get the absorbance [250]:

$$A = \alpha \times d \quad (3.32)$$

On the other hand, using the absorption coefficient, it is possible to calculate the depth of the material, since the light intensity of which will decrease with a depth of $1/e$ (and $1/10$). This dependence is expressed by the Lambert-Beer law:

$$I(x) = I_0 \times e^{-\alpha'x} \quad (3.33)$$

$$I(x) = I_0 \times 10^{-\alpha x} \quad (3.34)$$

where $I(x)$ is the beam intensity at point x , and I_0 is the incident beam intensity.

Comparing equations 3.28, 3.32 and 3.34, we derive the dependence of the transmission and absorption coefficients using the expression:

$$T = 10^{-A} = e^{-A'} \quad (3.35)$$

The logarithm of all parts of the equation gives the expression Beer's law:

$$A = \log_{10}\left(\frac{1}{T}\right) = \log_{10}\left(\frac{100}{\%T}\right) = 2 - \log_{10} \%T \quad (3.36)$$

where $\%T$ is the transmittance expressed in percent by doing $\%T = 100 \times T$.

Equation 3.36 shows that from measuring the transmittance as a function of the wavelength of the incident light beam, we can determine the absorbance and, therefore, the optical band gap. That is, from the transmission spectrum we can determine for what energy the layer of a certain material absorb radiation, and for what other energies this layer is transparent. The boundary between transparency and absorption marks the energy of the band gap.

Chapter 3. Characterization techniques

To obtain the absorption coefficient of a semiconductor, we will measure the transmittance of the sample with plane-parallel faces and thickness d . The transmittance of the specified sample will be determined by the equation:

$$T = \frac{I(d)}{I_0} = \frac{(1 - R)^2 e^{-\alpha d}}{1 - R^2 \cdot e^{-2\alpha d} - 2R \cdot e^{-\alpha d} \cdot \cos \frac{4\pi n d}{\lambda_0}} \quad (3.37)$$

where the R is reflectance of material than can be find from the Fresnel equations for waves with normal incidence as:

$$R \approx \frac{(n - 1)^2}{(n + 1)^2} \quad (3.38)$$

where n is reflective index of material.

The cosine term that appears in equation 3.37 in the denominator reflects the interference between waves successively reflected from both sides of the film and leads to the appearance of maxima and minima in the transmittance spectra for low absorption coefficients. Obviously, this term tends to zero at high absorption coefficients. Usually, this term is removed by averaging over the oscillation period, getting:

$$T = \frac{I(d)}{I_0} = \frac{(1 - R)^2 \cdot e^{-\alpha d}}{(1 - R^2 \cdot e^{-2\alpha d})} \quad (3.39)$$

When the absorption coefficient is zero, the transmittance of the sample is reduced to the equation:

$$T_0 = \frac{(1 - R)^2}{1 - R^2} \quad (3.40)$$

In this case, equation 3.39 gives the absorption coefficient as a function of transmittance:

$$\alpha = \frac{1}{d} \cdot \ln \left[\frac{(1 - R)^2}{2T} + \sqrt{\left(\frac{(1 - R)^2}{2T} \right)^2 + R^2} \right] \quad (3.41)$$

One of the most commonly used methods for quantifying the energy of the optical gap band of samples is the linearization of absorption curves representing $(\alpha h\nu)^{1/x}$ as a function of the energy of the photon beam, where depending on the type of transition, takes the value 1/2 (for direct transitions) or 2 (for indirect) [251]. This curve linearly depends on photon energy $h\nu$ and, therefore, the extension of the straight line to the energy axis makes possible to determine the band gap of the material [252]. Another option for calculation optical band gap is based on determining the point of maximum slope of the absorbance curve, since it will be more accurate and eliminates the human factor when converting the tangent to the slope of the absorption curve.

When calculating the transmittance spectra of the material, the transmittance curves of the samples were normalized to the value of the transmittance spectra of the substrate on

which they were grown. After that, all spectra were normalized in such a way that their maximum curve value corresponded to 100 % of the possible transmission. This was done so that, when calculating the absorption spectra from the transmittance spectra, the curves had a minimum value at low energies. If the transmittance curves have an oscillating character at high transmittance, then the average value between the maximum and minimum of the transmittance curve was taken and this value was used to normalize the spectra. This method can be used only for materials with a direct band gap because, for materials with indirect transitions, normalization can affect the slope of the transmittance spectra and distort the correctness of the calculated results. For direct transitions, similar to those studied in this thesis, according to equation 3.29 we find that the point of maximum slope is exactly at $h\nu = E_g$. For this, after calculating the numerical derivation of the absorbance curves, the maximum of their derivatives was determined and, thus, we obtained an estimate of the energy of the band gap. Only for a series of CdZnO samples that have indirect transitions the extension of the straight line of the tangent to the maximum slope of the absorption curve to the energy axis to determine the band gap of the material will be applied.

3.5.2 Used equipment- Experimental set-up

Jasco V-650 spectrophotometer

Spectral studies of the transmittance were obtained using a Jasco V-650 spectrophotometer in the ISOM laboratories of the Polytechnic University of Madrid. This equipment has two radiation sources: a Deuterium lamp, which covers a range of 190-350 nm, and a Halogen lamp in a range from 330 to 900 nm. By changing lamps during the study, any wavelength between 330 and 350 nm can be selected. Wavelength repeatability is ± 0.05 nm.

The monochromator generates monochromatic light rays for measurements. Before making a study of the material of interest to us, a check is carried out without a sample to determine the reference value $I_0(\lambda)$ in the selected wavelength range. Then, placing the samples in the system, the transmitted radiation intensity $I(d; \lambda)$ is determined. The detector of the photomultiplier detects the emitted radiation and, using computer software, calculates the transmittance of the material depending on the wavelength of the incident radiation $T(\lambda) = I(d; \lambda)/I_0(\lambda)$. These values are substituted into equation 3.38 and absorption curves are constructed, the derivatives of which allow calculating the optical band gap of the material. A picture of the spectrophotometer is shown in the Figure 3.21.



Figure 3.21: Spectrophotometer Jasco V-650

Spectrophotometer SF-2000

Investigation of the spectral transmittance coefficient of ZnMnS and ZnMnTe was carried out at room temperature by using the spectrophotometer SF-2000 at the National Technical University “Kharkiv Polytechnic Institute” (Figure 3.22). This device allows to measure the spectrum from 190 to 1100 nm in just a few seconds with a speed of ~ 9100 nm/min. Spectrophotometer has a single-beam optical scheme with an aberration-corrected concave rifled grating as a monochromator. As sources of UV radiation, high-quality Hamamatsu deuterium lamps were used, and Philips halogen lamps were used in the visible light channel. The accuracy of the reproduction of the wavelength is 0.004 nm. The hole for optical measurement of the samples of the spectrophotometer has a diameter of 1 cm, the size of the light slit for ultraviolet light is 0.5 nm and the smallest spectral slit width for visible light is 1.0 nm.



Figure 3.22: Spectrophotometer SF-2000

To expand the functionality of the spectrophotometer, a SFO-2000 console for specular and diffuse reflection was developed and used, which allows recording spectra of specular and (or) diffuse reflection of various objects. The size of the light spot on the sample can be in the range of 2-5 mm. The spectrophotometer allows the analysis of the spectra of both liquid and solid samples. The measurement of the reference sample and several (up to 9) samples can be carried out automatically by one command from the operator of the device. It supports to use of several reference samples with respect to the measurement of two or more studied samples in a single measurement session. This spectrophotometer allows not only to automate measurements but also to plot measurement curves for a series of samples.

3.6 Kelvin probe force microscopy (KPFM)

In this section we have turned to an electrical technique, which uses a modification of the conventional atomic force microscope based on the observations that the Scottish scientist William Thomson (later Lord Kelvin) performed in 1861 while studying metals. He constructed a capacitor using two plates made of different metals. By using an electrometer, he observed that there was an exchange of charge between the two metals when they were approached. This exchange of charge leads to an electrical force between the plates of the capacitor.

We know that the interaction between the capacitor plates is due to the different values of the work function of the metals. Lord Kelvin described, as well, a technique for measuring this work function difference by applying an adequate external bias voltage to the metals which cancels the force. In this way, he measured the contact potential difference between the two metals.

Kelvin probe force microscopy (KPFM) was introduced as a tool to measure the local contact potential difference between a conducting atomic force microscopy (AFM) tip and the sample, thereby mapping the work function or surface potential of the sample with a high spatial resolution [253].

Figure 3.23 gives a rough idea of an atomic force microscope set up.

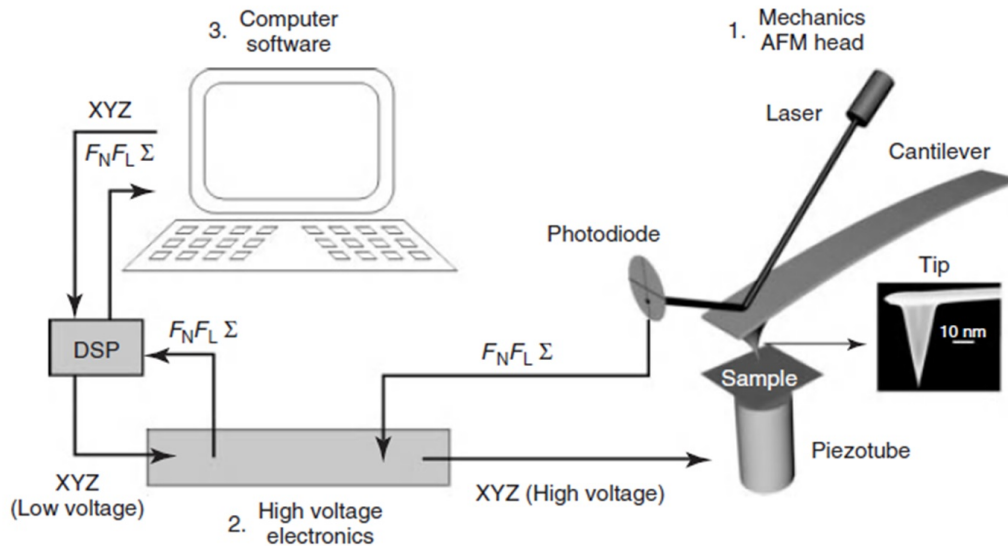


Figure 3.23: Components of a standard atomic force microscope. (F_N) and (F_L) vertical and lateral deflections of the laser beam and (Σ) its total intensity [254].

The principle of operation consists of scanning the sample surface using a tip with a nanometer radius and determining the force resulting from tip-sample interaction [255]. The main elements of the microscope are:

3.6. Kelvin probe force microscopy (KPFM)

- *Cantilever-tip system*: This is a probe, which consists of a tip with a 20-30 nm radius attached to the end of the cantilever beam of micrometric size. When an image of a surface is obtained, the distance between the tip and the sample is kept constant by means of a feedback loop. The signal obtained by the interaction of the tip with the sample is used as a source of feedback.
- *Laser beam detection system*: As a result of the interaction of the tip with the sample, the cantilever beam deflects, which, in accordance with Hooke's law and taking into account the cantilever spring constant (c_{lever}), creates a normal force (F_z) that can be measured as [256]:

$$F_z = c_{lever} \cdot \Delta Z \quad (3.42)$$

The laser beam is focused at the end of the cantilever, and the reflected beam is detected in a split photodiode, which has 4 segments (see Figure 3.23). When the position of the cantilever changes, the angle of the beam reflection changes, which leads to a change in the position of the spot on the photodiode. By changing the photocurrent on the photodiode segments, you can accurately measure the deflection of the beam.

- *Piezoelectric Ceramics*: This is a high-resolution position element that is used to adjust the tip-sample distance, as well as to change the relative position between them. The sample is fixed and mounted in the piezoelectric tube, so when scanning, it is not the sample that moves.
- AFM control and adjustment system, which consists of a computer, software and digital signal processor (DSP)

KPFM is mainly based on the AFM instrumentation system. The AFM operates either in contact (static) or intermediate (tapping) or contactless modes [253].

In the static mode, the AFM tip has direct physical contact with the sample surface, and the repulsion force of the tip-sample deflects the cantilever tip, allowing to make the surface topography map with atomic resolution. The deviation of the cantilever proportional to the load force is monitored and used as a feedback signal.

As the tip moves along the surface of the sample, it may cause damage to soft or brittle samples. Damage to the surface will be suppressed in the tapping mode. In the dynamic (intermediate and non-contact) mode of operation, the cantilever oscillates at or near its resonant frequency. The interaction between the tip and the sample varies depending on the distance between them, which affects the vibration amplitudes (intermediate mode) and the resonant frequency (non-contact mode). The deviation of the amplitude and frequency of measurement,

with respect to the reference values is used as feedback signal to obtain the surface topography of the sample. Therefore, these modes are also called amplitude modulation (AM) and frequency modulation (FM), respectively [253].

Image processing is performed using the software designed for the microscope. Most often, polynomial fitting is used to correct the tilt of the substrate, since AFM images usually measure the absolute height of the sample. Each line in the image is fitted to a polynomial equation. Then the polynomial shape is subtracted from each scan line, leading to their flatness. Having processed data and obtained surface topography function $h(i, j)$, it is possible to calculate the most commonly used parameter for assessing surface quality, that is the Root Mean Square average (RMS) roughness [257]:

$$RMS_{roughness} = \sqrt{\sum_{i=1}^I \sum_{j=1}^J [h(i, j) - \bar{h}]^2} \quad (3.43)$$

where the summations are performed over all the image pixels (i, j) of the scanned area, maximum value for the length (I) and width (J) of this area and \bar{h} is the mean height.

3.6.1 KPFM operation mode: FM mode

As shown in Figure 3.24, the amplitude of oscillations (Figure 3.24 (a)) increases when increasing the tip-sample distance due to a decrease in the interaction. The feedback system controls the amplitude change in order to keep a constant value, providing the topography of the sample surface. The change in amplitude depends on the force between the tip and the sample.

In this work, we used the FM mode AFM, in which the oscillation frequency of the cantilever changes as the distance between the tip and the sample changes (3.24 (b)). A feedback system regulates the frequency change to keep the frequency constant value, allowing the topography of the sample surface to be acquired. The changes in oscillation frequency are dependent on the force gradient between the tip and sample. Since the FM mode detects a gradient of force, rather than the force itself, compared to the AM mode, this mode has a higher spatial resolution [253].

Figure 3.25 (a) shows the experimental setup for FM-AFM. The detected cantilever deflection signal is sent back to the piezoelement through a phase shifter and an automatic gain control (AGC) circuit to form a self-oscillation circuit, where the cantilever works as a mechanical resonator and determines the oscillation frequency [255].

3.6. Kelvin probe force microscopy (KPFM)

Figure 3.25 (b) shows the curves of amplitude and φ as a function of the resonant frequency f_0 . The total phase delay in a self-oscillating circuit must be a multiple of -360° for continuous sinusoidal output. Under these conditions, φ is always maintained at -90° and the oscillation frequency f_i is always maintained at the cantilever resonance.

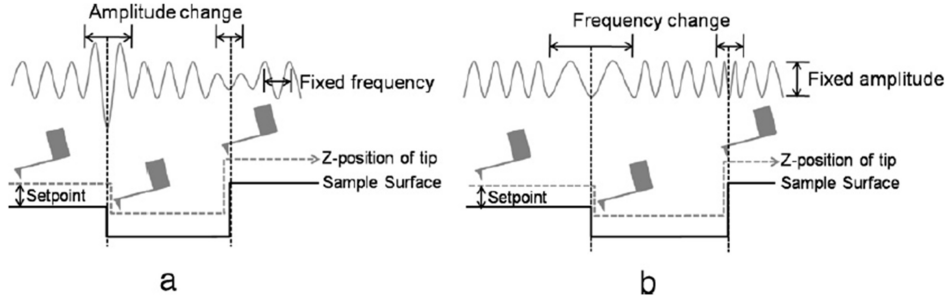


Figure 3.24: Schematic image of non-contact AFM operation mode [253]:
(a) Amplitude modulation mode and (b) Frequency modulation mode.

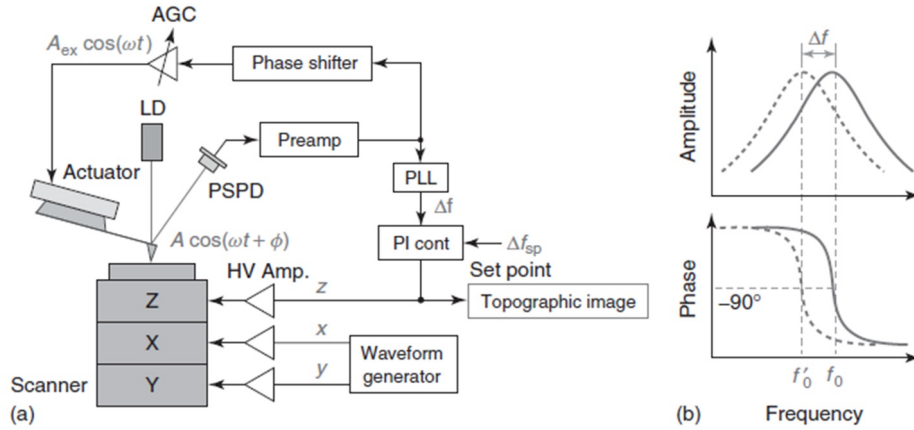


Figure 3.25: (a) Experimental setup for FM-AFM. (b) Amplitude and phase versus frequency curves with (dotted lines) and without (solid lines) a tip-sample interaction [255].

As the tip approaches to the surface of the sample, it causes a phase shift Δf . Using the self-oscillation scheme, f_i is also shifted by a similar value. The deviation signal is fed to a frequency detector, which generates a voltage signal proportional to Δf . A phase-locked loop (PLL) circuit is typically used as a frequency detector. The signal Δf is fed to the phase-intensity (PI) controller, which outputs a z -signal to control the distance between the probe and the sample [3.58].

3.6.2 Contact potential difference (CPD)

The main feature of KPFM is to measure the contact potential difference (CPD) between the conductive AFM tip and the sample surface. The expression for calculating CPD can be represented as [258]:

$$V_{CPD} = \frac{\Phi_1 - \Phi_2}{-e} \quad (3.44)$$

where e is the elemental charge of the electron with sign, and Φ_1 and Φ_2 are the work functions of the AFM tip and the sample surface, respectively.

Upon electrical contact between the AFM tip and the surface, due to differences in the vacuum energy levels, an electrostatic force is generated. Figure 3.26 is a schematic of the energy levels depending on the work function of the sample surface (Φ_1) and the AFM tip (Φ_2).

In the first situation (Figure 3.26 (a)), the tip and the sample are at a considerable distance from each other. Two materials have different Fermi levels (E_F) and, if there is no electrical contact, the vacuum level is aligned. When electrical contact occurs (Figure 3.26 (b)), there is an alignment of the Fermi levels of the AFM tip and the sample. The electron moves to the material with a larger work function. In this case, due to the change in the vacuum level, a potential difference is formed, which is called a contact potential difference (V_{CPD}). If we apply an external bias voltage (V_S), with the same value as V_{CPD} , but in the opposite direction, then the potential difference between the vacuum level of the AFM tip and the sample surface can be eliminated (Figure 3.26 (c)).

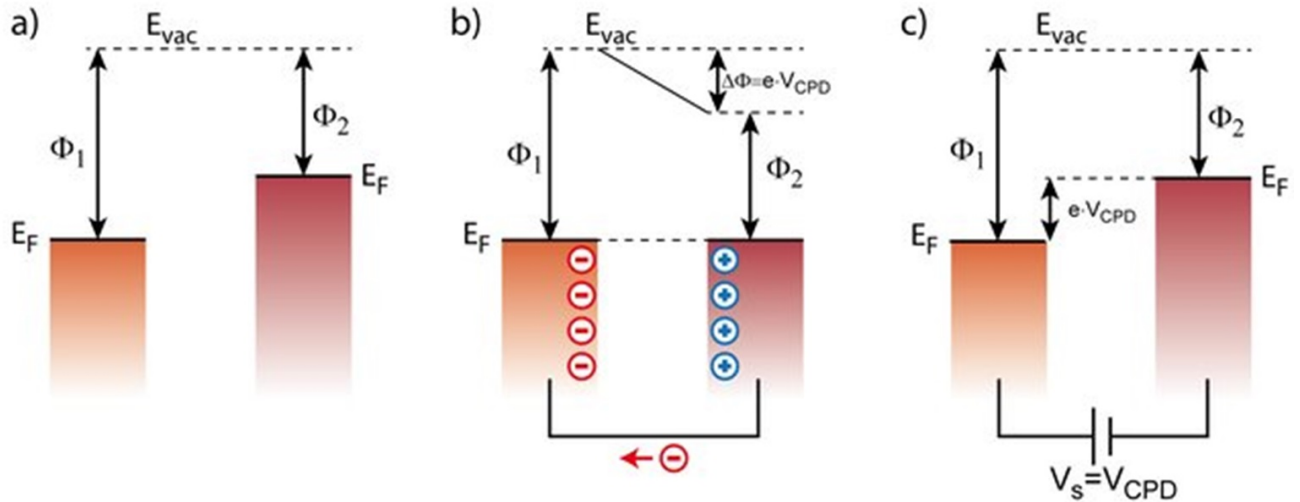


Figure 3.26: Three cases of energy levels between different materials. a) The two materials are separated. b) Two materials are energetically connected, which leads to the occurrence of a Contact potential difference. c) Contact potential difference minimized by applied external bias voltage V_s [259].

By applying an AC voltage (V_{AC}) plus a DC voltage (V_{DC}) to the AFM tip, KPFM measures the work function of the sample. (V_{AC} generates oscillating electrical forces between the AFM tip and sample surface, and (V_{DC} cancels the electrical forces that are originated from CPD between tip and sample surface [260].

3.6.3 Surface photovoltage (SPV)

Surface Photovoltage (SPV) is a well-known non-contact method based on the analysis of changes caused by the illumination of surface voltage. The pioneers in this area were Brattain and Bardeen in the early 1950's [261] that studied the effect of surface radiation on surface stress. SPV has been used in the past decades to study semiconductors and semiconductor interfaces. Using this method, one can investigate the surface and subsurface of a material, defects, leakage currents on the side of the conductor surface, the optical band gap, and electron-hole recombination.

The periodic structure of an ideal crystalline semiconductor results in the appearance of allowed energy bands separated by band gaps. The ending of the periodic structure of a semiconductor at its free surface may form surface-localized electronic states within the semiconductor band gap and/or a double layer of charge (surface dipole). The formation of surface- and interface localized states typically involves additional, more complex phenomena than the symmetry-breaking lattice ending, such as: “dangling bonds”, i.e. the formation of surface atoms with no upper atom to bind to; surface reconstruction or relaxation, i.e. a change in the position and/or chemical bonding configuration of surface atoms that minimizes the surface energy; steps and kinks at the surface; impurity atoms adsorbed on the surface, etc [262].

The appearance of surface-localized states induces charge transfer between the bulk and the surface in order to establish thermal equilibrium between the two.

The effect of SPV is the change of the surface potential caused by the illumination of the surface of the material and the subsequent absorption of photons. These photons induce the formation of free carriers by creating electron-hole pairs via band-to-band transitions (typically dominant for super-bandgap photons) and/or release captured carriers via trap-to-band transitions (typically dominant for sub-bandgap photons) [263]. The equation for the SPV is [264]:

$$SPV = V_{S(illumination)} - V_{S(dark)} \quad (3.45)$$

If the energy of the incident radiation is greater than or equal to the energy of the band gap of the material, then a band-to-band transition occurs between the valence band and the conduction band. In materials of good quality, the probability of interband absorption is, as a rule, several orders of magnitude greater than the probability of absorption in a trap

Chapter 3. Characterization techniques

[263]. Incident photons generate electron-hole pairs, which are collected by the surface barrier, which leads to a decrease in the surface potential. Such transitions reduce the bending of the surface band for a p-type semiconductor (shown in Figure 3.27). When the photon energy is equal to the width of the band gap, the resulting SPV (negative in p-type, since the bending of the descending strip is positive by definition) increases significantly [264]. For an n-type semiconductor, the situation is the opposite. This change allows obtaining the optical width of the band gap of the material.

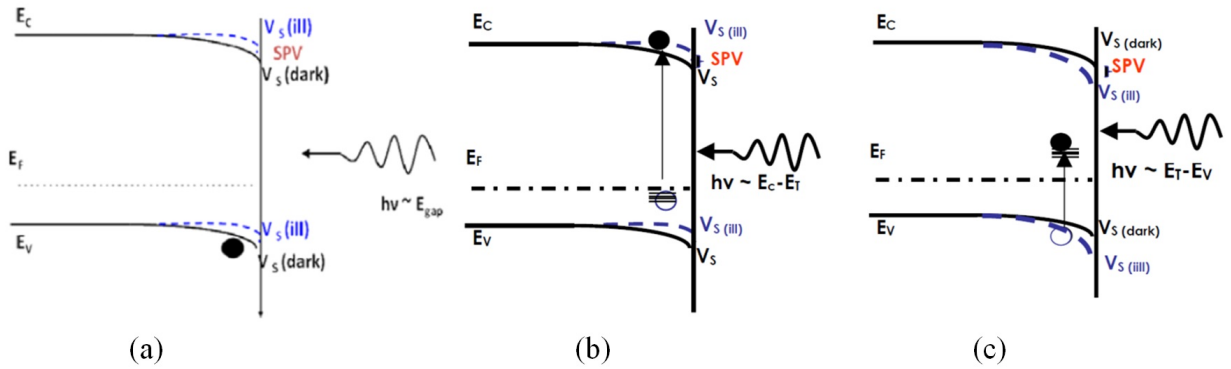


Figure 3.27: (a) Schematic band diagram of p-type semiconductor : (a) Band-to-band transition with illumination energy more o close to band gap energy; (b) Trap to band transition from defect level to conduction band; (c) Trap to band transition from valence band to defect level [264].

When a photon has energy $h\nu$, which is below the band gap, the probability of absorption between the bands is practically zero, since the photons do not have sufficient energy to induce such transitions [263]. In this case, two different situations are considered. If photons with energy $h\nu$ are able to stimulate the optical transition from a defect level E_T to the conduction band (Figure 3.27(b)), then the surface of the band bending increases, that is, the SPV increases. In another case, if photons with energy $h\nu$ are able to stimulate an optical transition from the valence band to the defect level E_T (Figure 3.27 (c)), the surface band bending reduces, i.e. SPV decreases [263]. With the foregoing, it turns out that the spectroscopy of the defective state can be performed on a semiconductor in a contactless and non-destructive way.

3.6.4 Used equipment- Experimental set-up

Images of the surface topography and KPFM (Kelvin probe or surface potential scans) were obtained by means of a NanoTec S.L. atomic force microscope (Figure 3.28) of *POE-MAS* (*Processos optoelectrònics en materials avançats i superfícies*) group. The system is equipped with a phase-locked loopboard (bandwidth ~ 2 kHz) which maintains the cantilever at resonance. *Pt* coated cantilevers (HQ:NSC14/*Pt* from μ -Masch, 4.5 N m^{-1} force constant, resonance frequency ~ 140 kHz) were used for the experiment. Topography and surface potential were acquired using the oscillation amplitude as feedback parameter in a single-pass mode. Measurement of the contact potential difference (CPD) between tip and sample proceeded by applying a fixed AC voltage (1-1.5 V) at 7 kHz to the AFM tip while the sample was held at ground potential following the so-called frequency modulation procedure. A second feedback adjusts the DC bias between tip and sample in order to minimize this interaction and determine the CPD. The tip-sample distance was maintained around 5-10 nm, resulting in surface potential imaging with high spatial (~ 20 nm) and potential (~ 20 mV) resolution [265].



Figure 3.28: KPFM of the POEMAS group of the University of Valencia

For making SPV measurements as a source of radiation we used a red laser (633 nm). The laser beam was focused to hit the point of contact of the microscope needle tip with the sample surface. The study of CdTe top layer for a series of CdTe/CdO samples was carried out both with and without laser illumination. Power of laser was changed in the range from 100 to 5 mW.

The measurement results were processed using the software package WSxM5.0 Develop 8.3.

Chapter 4

Growth and characterization of ZnO, CdO, CdZnO, CdTe and their heterostructures

In the previous chapter, we examined the techniques for performing the characterization of the samples. This chapter will show the results of the growth analysis and characterization of each of the studied materials of the II-VI group.

Regarding the oxides of cadmium and zinc, the structural features of the films obtained under different growth conditions will be studied. Later, the results of structural and optical characterization of CdO-based ternary compounds with different concentrations of alloyed Zn will be shown. Finally, structural characteristics of the CdTe/CdO heterostructure, electrical properties of films upon laser irradiation, and the surface potential distribution depending on the surface morphology of the upper layer of the structure will be presented.

4.1 Zinc oxide: morphological and structural study

4.1.1 SEM and XRD measurements

In order to build electronic devices, the material quality of their constituent components is of main significance. Control of the growth parameters and selection of the optimal conditions for obtaining the desired properties has always been a main task in device making. On the other hand, every year the size of electrical equipment is decreasing to increase ease of use. The rise in compactness not only reduces weight, cost price and power consumption, but also increases the velocity, and also simplifies the design of both individual electronic devices and devices based on them.

Chapter 4. Growth and characterization of ZnO, CdO, CdZnO, CdTe and their heterostructures

In respect to ZnO, our task has been to find the growth conditions for obtaining ZnO layers with the smallest thickness and smoothest surface. To do that, samples were grown using the MOCVD system (see section 2.4), since this method is suitable for film growth and allows obtaining samples with good reproducibility [69]. Sapphire substrates with R -, A - and M -planes, which corresponds to the $(1\bar{1}02)$, $(11\bar{2}0)$ and $(10\bar{1}0)$ planes, respectively, were chosen to find the parameters for the growth of films with good crystalline quality [266]. The relatively low cost and availability of different orientations of sapphire, their high optical transparency, and other characteristics make them a good choice among other substrate options (such as glass, GaAs, Si, GaN, etc.) for the growth of ZnO films. All samples were placed in 2 rows of 3 samples. The closer row to the precursor inlet to the reactor will be labeled Front (F), and the more distant Rear row (R). The first position of the substrate holder is at a distance of 6.4 cm from the entrance to the reactor, and the second is 5.3 cm further. In turn, the samples are indexed as L , C and R , which meant Left, Center and Right, respectively (as shown in Figure 4.1). Due to the features of the reactor which was designed for using H_2 as carrier gas and the location of the samples on the substrate holder, the intake of the N_2 carrier gas, charged with the precursors is not completely uniform at the overall of the reactor and the amount of material for each sample was slightly different. Following the literature, in which R -sapphire has shown that is able to introduce a little distortion on ZnO grown on it, first samples were obtained onto R -plane one side polished epiready sapphire without any chemical or thermal treatment. Film growth conditions are shown in section 2.4.6.

As said before, Nitrogen (N_2) was used as carrier gas for the precursors. The reactor pressure was the atmospheric one. At first, a long growth time (90 min) was chosen to see the effect of the temperature on the formation of the material layer. In a set of samples, the temperature was changed in the range of 300-400 °C with a step of 25 °C. Some representative results of the experiments are shown in Figure 4.2.

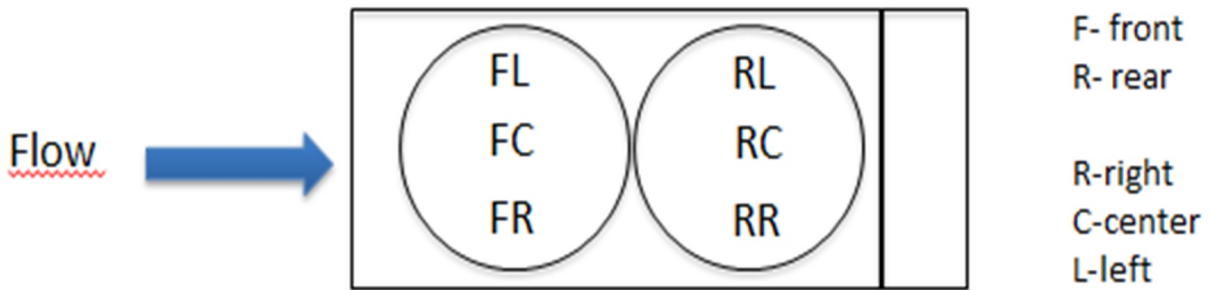


Figure 4.1: Arrangement of the samples.

4.1. Zinc oxide: morphological and structural study

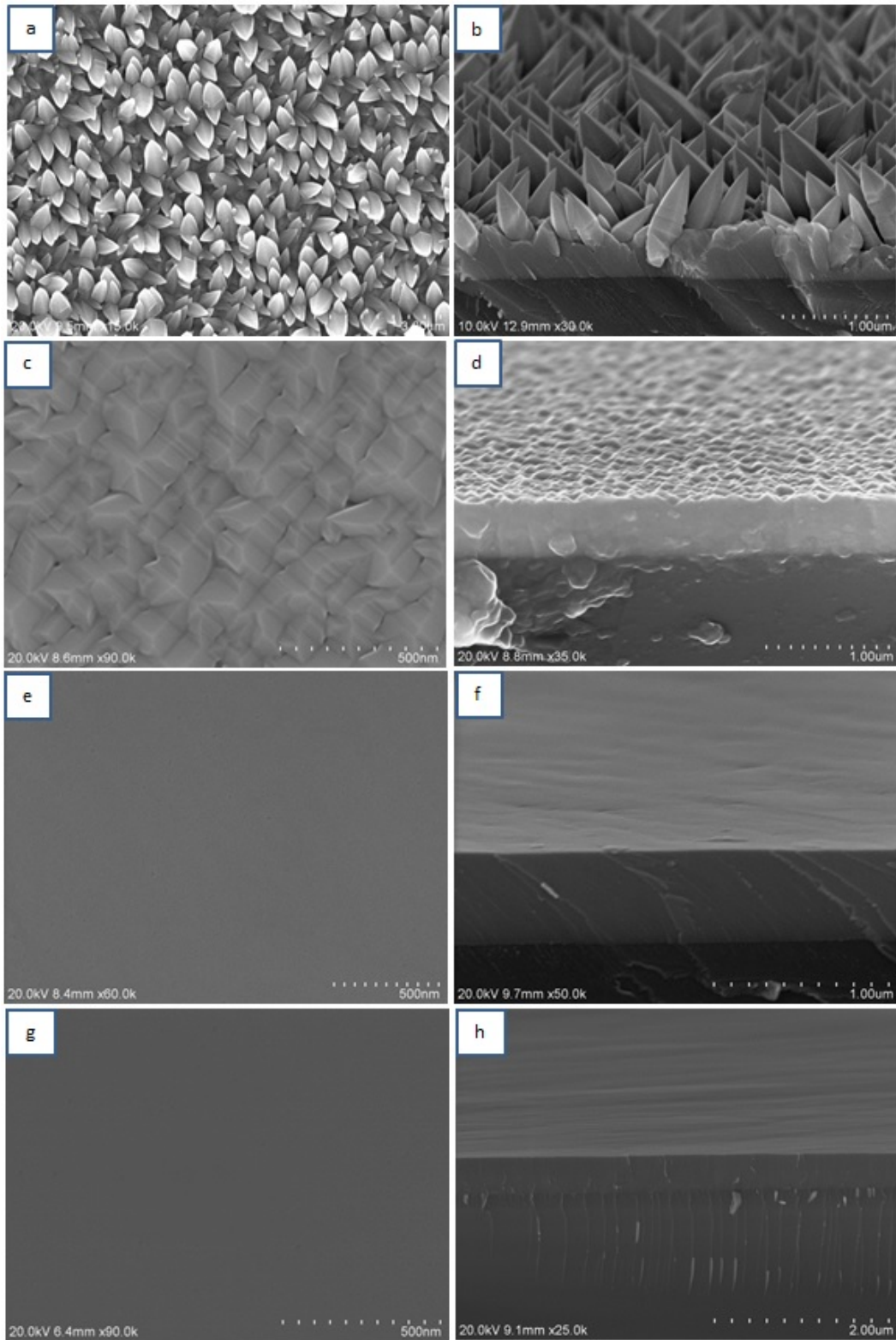


Figure 4.2: Morphology of surface (a,c,e,g) and cross-section (b,d,f,h) of ZnO grown samples at different temperatures. The surface temperature was: 300 °C (a, b), 325 °C (c,d), 375 °C (e,f) and 400 °C (g, h).

Chapter 4. Growth and characterization of ZnO, CdO, CdZnO, CdTe and their heterostructures

The Figure shows that, depending on the growth temperature, the surface morphology of the films is very different. It was found that at low temperatures ($\sim 300\text{ }^{\circ}\text{C}$), a thin layer of the material ($\sim 220\text{ nm}$) forms on the surface of the substrate, after crystals of the order of $1\text{ }\mu\text{m}$ are grown. This indicates a columnar growth of the films after a relatively thick and compact transition layer has been formed. At medium temperatures, these columnar ZnO structures become less noticeable, and the upper morphology is flatter. The transition from three-dimension growth to two-dimensional with an increase in temperature was reported by Ogata et al. [267] in the growth of ZnO structures on R-sapphire, similarly as the results here obtained. The better temperature conditions in respect the flatness for our samples were in the range of $350\text{--}400\text{ }^{\circ}\text{C}$. At the same time, the film thickness of almost all samples was about 540 nm and did not depend too much on the temperature in this range except for the higher temperature ($400\text{ }^{\circ}\text{C}$) where film thickness decreases to 420 nm , which can be due to re-evaporation of material from the sample substrate as well as reduction of the grain size in the thermodynamic regime at the higher temperature.

The temperature $375\text{ }^{\circ}\text{C}$ was chosen for further studies, since at this temperature the samples in all the 6 positions showed smooth surface morphology as determined by SEM measurements. In order to built ZnO-based devices composed of multi-layer structures, e.g., lasers, sensors, or transistors, flat epilayers are essential. Samples obtained at a relatively higher temperature ($400\text{ }^{\circ}\text{C}$) had a smooth surface only in the group of samples, which were closer to the entrance of the precursor to the reactor (Front group). It was experimentally found that in the second group of samples, the heating temperature was slightly higher. Similarly to the thickness decrease, the degradation of the surface due to the presence of holes can be associated with a high-temperature regime of growth (Section 2.4.1) in which the growth rate decreases due to thermodynamic factors and homogeneous reactions [171] or even due to depletion of reagents or re-evaporation of precursors caused by high temperature.

For obtaining ZnO samples that should help in reducing the size of potential devices, we decided to concentrate on reducing the thickness of the films while maintaining the crystalline quality of the samples, by acting on other growth parameters as the growth time and the precursor fluxes that enters into the reactor during the experiment. Therefore, first of all we reduced the time of deposition of the material to find the limit at which the films still have a flat surface morphology.

Thus, our attention was focused in obtaining films both morphologically and structurally of high-quality by optimizing the experimental parameters. It was determined that with a deposition time < 10 minutes and precursors flows 71.77 (for O precursor) and $14.22\text{ }\mu\text{mol}/\text{min}$

(for Zn precursor), surface morphology changes and becomes rougher as shown in Figure 4.3. The film thickness was approximately 65 and 42 nm for 10 min and 5 min of growth at 375 °C, respectively. The sample obtained at 3 min of growth had thickness ~ 40 nm and a more complex non-planar surface structure. At the same time, the samples that were closer to the inlet of the carrier gas with the precursor (Front group) were smoother and had more thickness than those that were further (Rear group). Since usually the thickness of the samples in the *R*-group was lesser than in the near group and given the complex surface morphology even at relatively high temperatures, we could infer that this could be due to the fact that in the rear part a higher temperature is present leading to less favorable growth conditions as described above. Moreover, in addition to morphological analysis, a structural analysis was also performed using XRD studies, that showed that all films had (102) and (110) preferred growth orientation (Figure 4.4). Peaks at 2θ angles of 25.58° , 52.55° and 83.22° correspond to peaks (01 $\bar{1}$ 2), (02 $\bar{2}$ 4) and (30 $\bar{3}$ 6) of *R*-sapphire.

Without changing the ratio $R_{VI/II}=5$ between the precursors, we reduced the material flow in order to achieve a slower speed of film formation, which should allow to obtain smooth ZnO films with lower thicknesses. For this, we changed the amount of material entering the reactor during the growth of the film. Thus, the incoming gas flow with precursors was reduced 5 times from 71.77 and 14.22 $\mu\text{mol}/\text{min}$ to 14.35 and 2.85 $\mu\text{mol}/\text{min}$ for oxygen and zinc precursors, respectively. Starting from 5 minutes, we gradually increased the time from 5 to 45 min. As a result, it was found that with a deposition time of 45 minutes, the surface morphology and thickness of the samples were very similar to the values obtained earlier with 10 minutes of growth at higher precursor fluxes (Figure 4.5). It can be seen that although the precursors flow was reduced, the growth time increased equally, and the total amount of introduced substance did not change very much. This fact shows that we are working in a regime of growth in which the growth is driven by the total amount of material and not by the rate in which it is injected. The numerical values of the total amount of precursor used during growth will be presented later in page 107 (section 4.1.1). At the same time, among the 6 samples of the film, *FC* and *FR* had the best quality. Due to the design features of the reactor, the precursors flow more to the right side and mix before deposition on the substrate, which can lead to non homogeneous distribution of the material to all samples or a change in the flow rate depending on the distance to the reactor inlet. At the same time, samples that are further from the inlet (*R*-group) have a higher heating temperature which could cause re-evaporation of the material and the formation of holes on the surface. The XRD measurements made for samples with growth times of 30 and 45 min showed similar results to those shown in Figure 4.4.

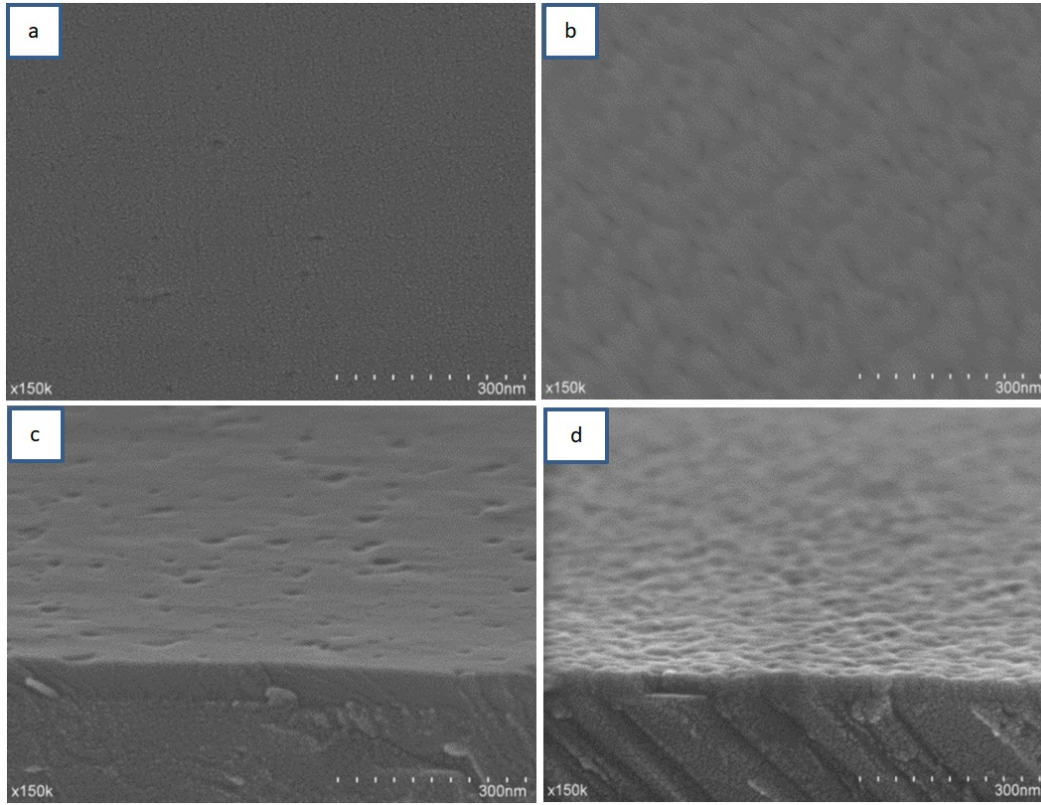


Figure 4.3: Morphology of surface (a,b) and cross-section (c, d) of ZnO samples deposited during 10 min (a, c) and 5 min (b, d). Samples were in position Front Center (*FC*).

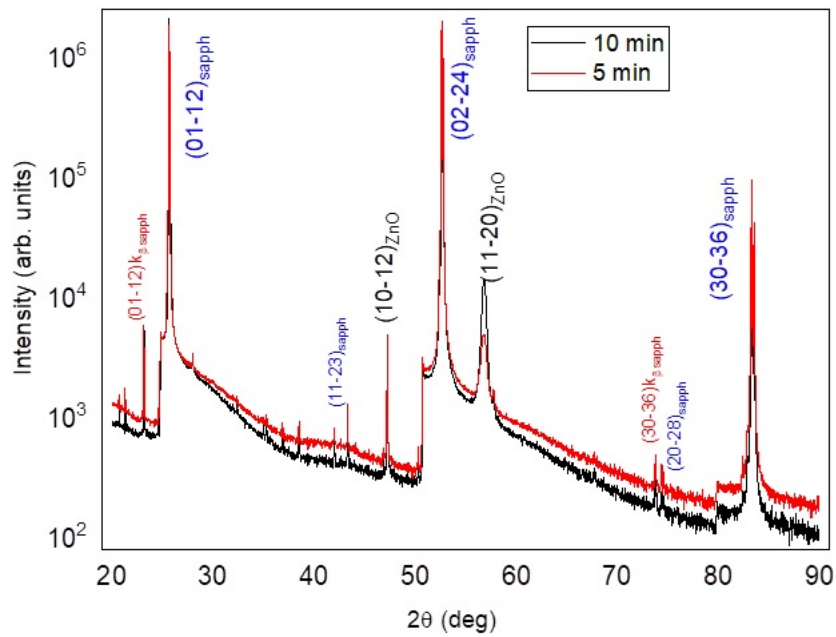


Figure 4.4: X-ray diffraction of ZnO samples grown over $(1\bar{1}02)$ sapphire during 5 and 10 min

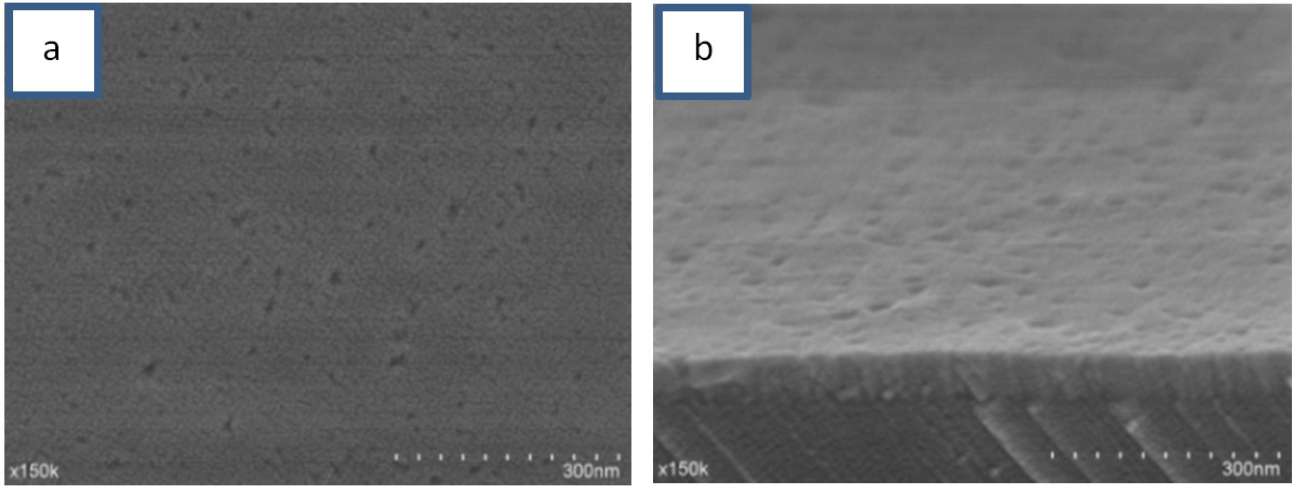


Figure 4.5: Morphology of surface (a) and cross-section (b) of ZnO samples deposited during 45 min (14.35 and 2.85 $\mu\text{mol}/\text{min}$ for oxygen and zinc precursor, respectively). Thickness was $d \approx 68$ nm

Previous results show that using the same quantity of material with different precursor's flow smooth films can be obtained. In the last series of experiments with low flow, this took a long time. In order to reduce the growth time, we took an intermediate value of the precursor flow between the previous series of experiments and increased its value in 3 times up to 43.06/8.54 $\mu\text{mol}/\text{min}$ for O/Zn precursors. Gradually lowering the growth time from 45 min, it was found that at time of < 15 min, the films lose their smoothness. Since we previously found that smoother films are obtained in the temperature range of 350-400 $^{\circ}\text{C}$, these temperatures were also used for this precursor flow to obtaining homogeneous films with shorter growth time. Unfortunately, slight variations in temperature (375 ± 25 $^{\circ}\text{C}$) at 10 min of growth did not improve the quality of the final films (Figure 4.6). At these conditions and higher temperature (400 $^{\circ}\text{C}$), the surface morphology worsens with the appearance of holes that may be associated with high-temperature conditions [268]. As before, the samples located closer to the reactor inlets shown better results, in particular, *FC* and *FR* films. Samples with growth times of 10 and 15 min have XRD patterns similar to those previously measured (Figure 4.4). Neither temperature change nor precursor flow affects the structure phase condition of the resulting films as expected. It was found that an increase in the precursor flux led to an increase in the thickness of the resulting films from 32 nm (for 14.35/2.85 $\mu\text{mol}/\text{min}$), 66 nm (for 43.06/8.54 $\mu\text{mol}/\text{min}$) to 100 nm (for 71.77/14.22 $\mu\text{mol}/\text{min}$ of O/Zn precursors, respectively) for 15 min of growth.

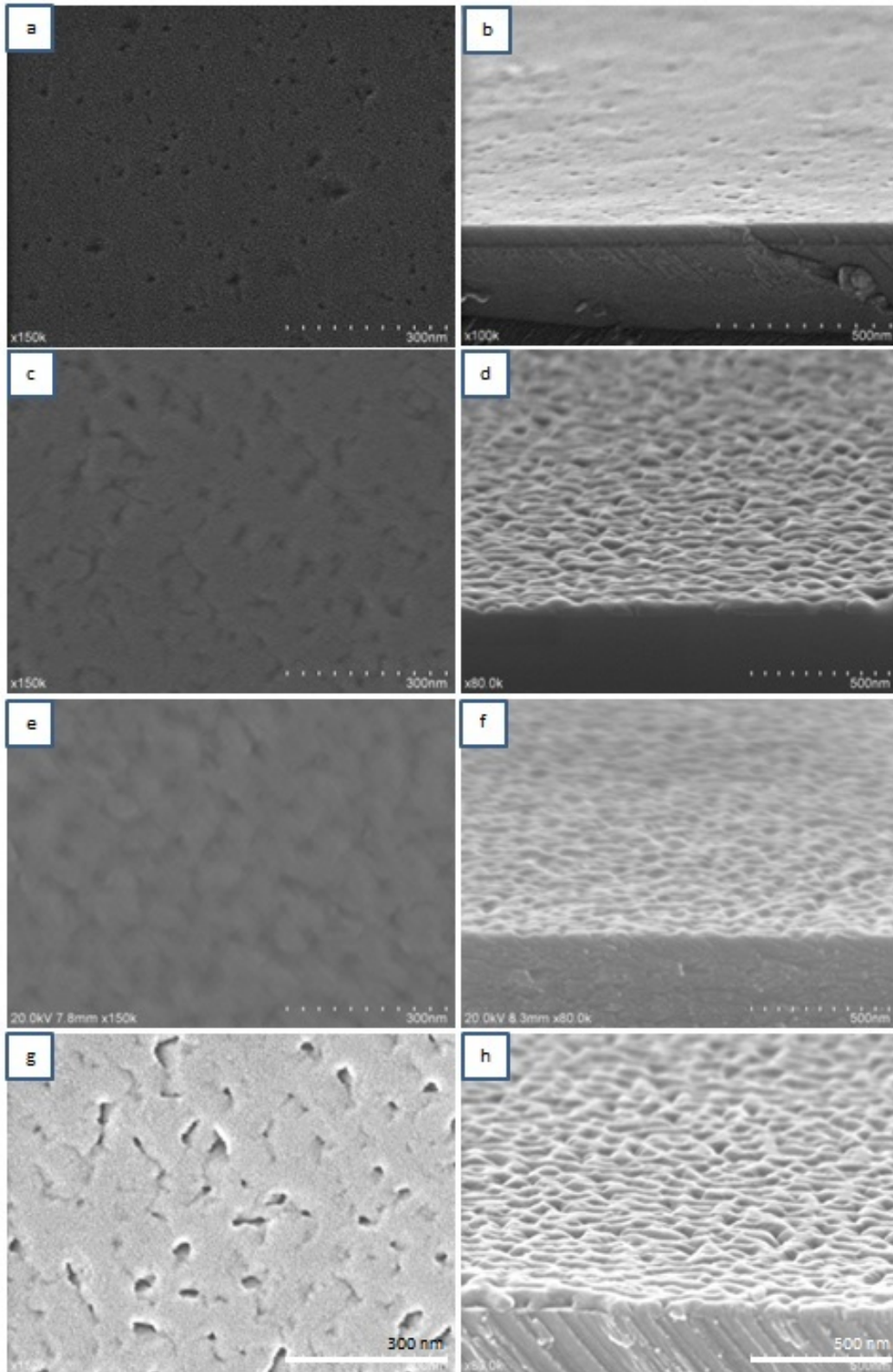


Figure 4.6: Morphology of surface (a,c,e,g) and cross-section (b,d,f,h) of ZnO samples deposited during 15 min [375 °C] (a, b) and 10 min [(375 °C, c, d), (350 °C, e, f), (400 °C, g, h)]

4.1. Zinc oxide: morphological and structural study

When comparing the results, it was found that the thickness and morphology of the film surface at 15 minutes for 43.06 and 8.54 $\mu\text{mol}/\text{min}$ (or 774 μmol in total) are comparable with those obtained for a film with large flow and 10 minutes of growth of 71.77 and 14.22 $\mu\text{mol}/\text{min}$ (or 859.9 μmol in total) and a smaller flow and 45 minutes of growth for 14.35 and 2.85 $\mu\text{mol}/\text{min}$ (or 774 μmol in total). It seems that at a given temperature (375 °C) at 3 different growth parameters, samples presented similar results and the films are ordered in a similar way respect to the morphology.

Knowing the approximate amount of material to obtain thin films with a smooth surface, the next step was trying to find the growth parameters at which smooth films could be obtained, while the material flow was increased to reduce the growth time less than 5 min. Incoming flow of oxygen and zinc precursors was increased up to 100.48 $\mu\text{mol}/\text{min}$ and 19.91 $\mu\text{mol}/\text{min}$ for O and Zn precursors, respectively. Several samples were obtained at temperatures below 375 °C to avoid possible re-evaporation of the material during film growth. As it turned out, neither a decrease in growth time of fewer than 5 minutes, nor a decrease in growth temperature (340, 350 °C) made possible to obtain a thin film with a smooth surface (Figure 4.7).

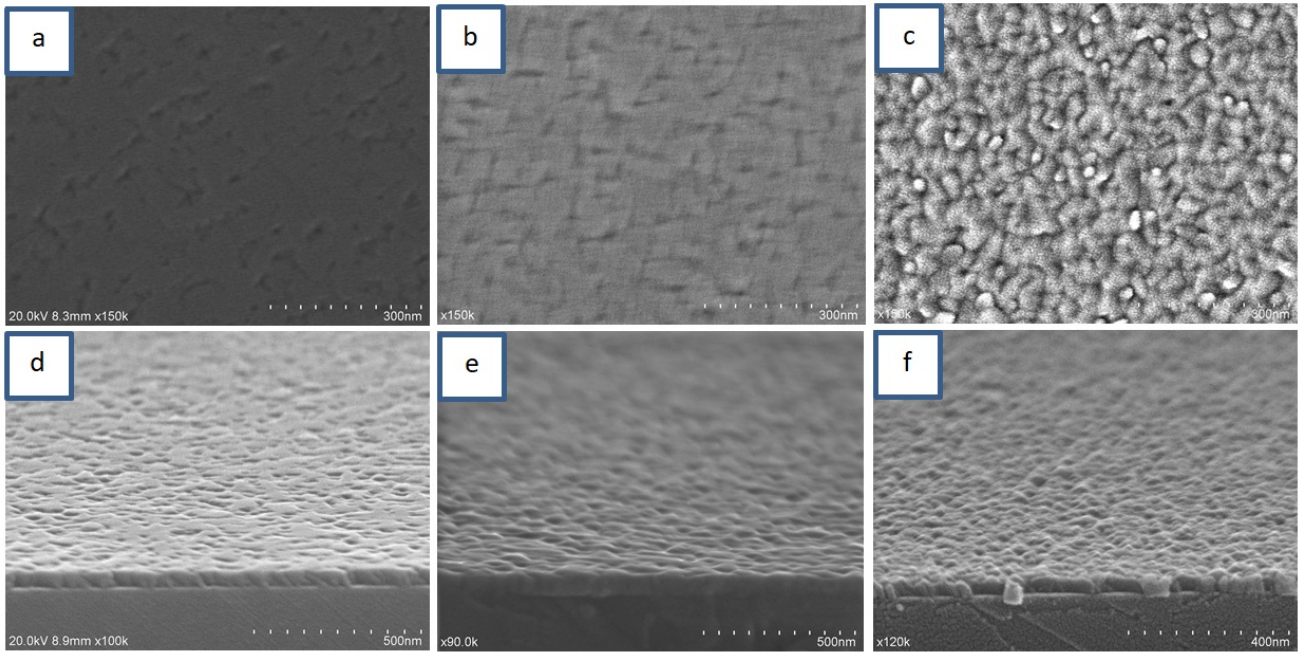


Figure 4.7: Typical morphology of surface (a-c) and cross-section (d-f) of ZnO samples deposited during 5 min [375 °C] (a, c); and 3 min at [375 °C] (b, e) and [340 °C] (c, f)

Chapter 4. Growth and characterization of ZnO, CdO, CdZnO, CdTe and their heterostructures

After analyzing the results, we decided to etch the substrate before the growth of the material, in order to promote more initial nucleation points as it was presented in paper [269]. Thus chemical etching of the substrate surface was carried out with a solution $H_3PO_4 : H_2SO_4$ in a volume ratio of 1:3 during 3 hours at 120 °C. The etched substrate was washed with plenty of distilled water and purged with pure Nitrogen. For the growth of the films, conditions (growth temperature 375 °C, time 5 min, flows 71.77 and 14.22 $\mu\text{mol}/\text{min}$ for oxygen and zinc precursors, respectively) were selected under which the morphology of the film visually becomes less smooth. Unfortunately, as the results showed, chemical treatment did not improve a lot the surface flatness of the sample. The sample thickness decreased from 42 to 34 nm, but the surface was not uniformly smooth and has a small dimples on it. (Figure 4.8).

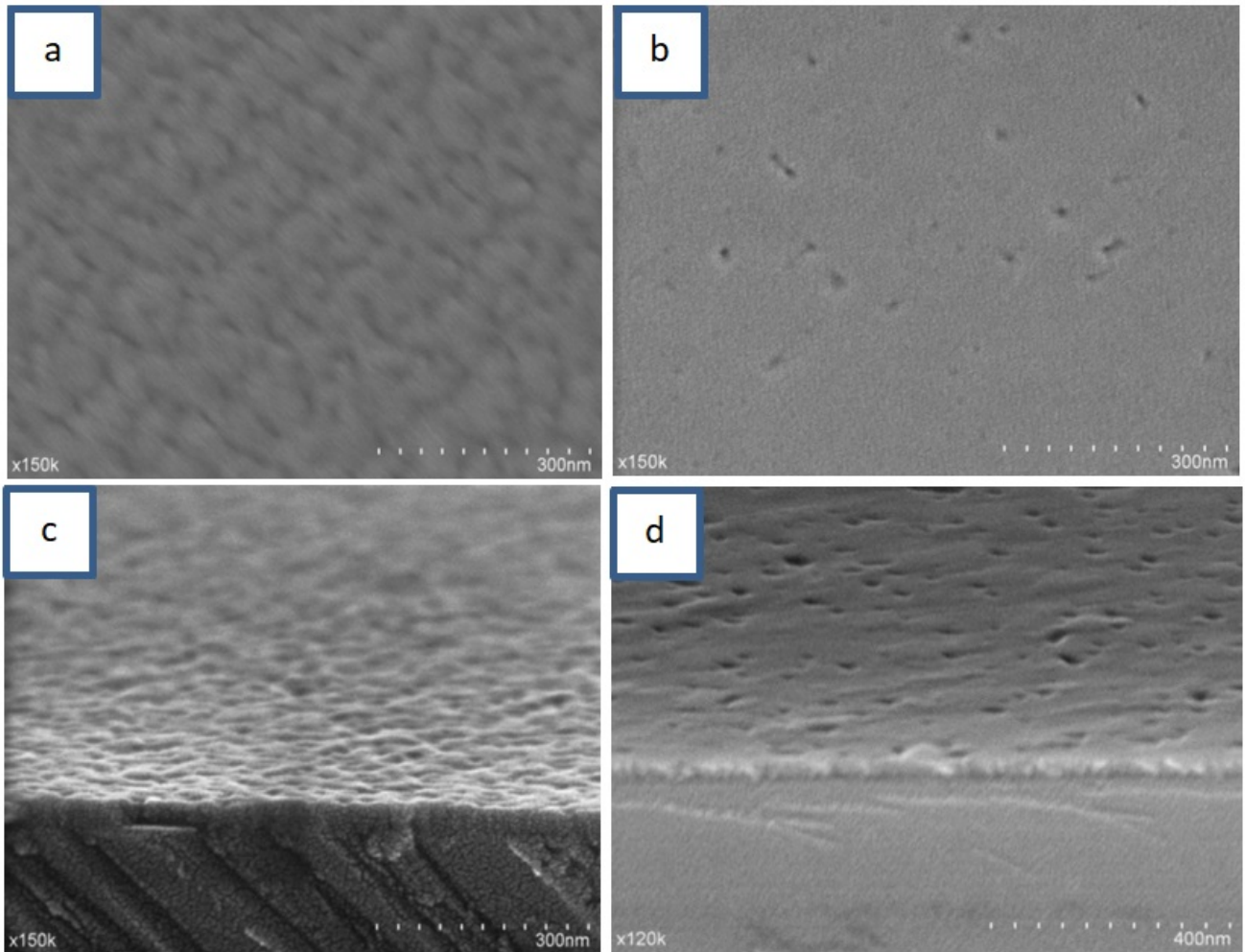


Figure 4.8: Morphology of surface (a, b) and cross-section (c, d) of ZnO samples deposited during 5 min: (a, c) without chemical treated substrate and (b, d) with chemical treated substrate.

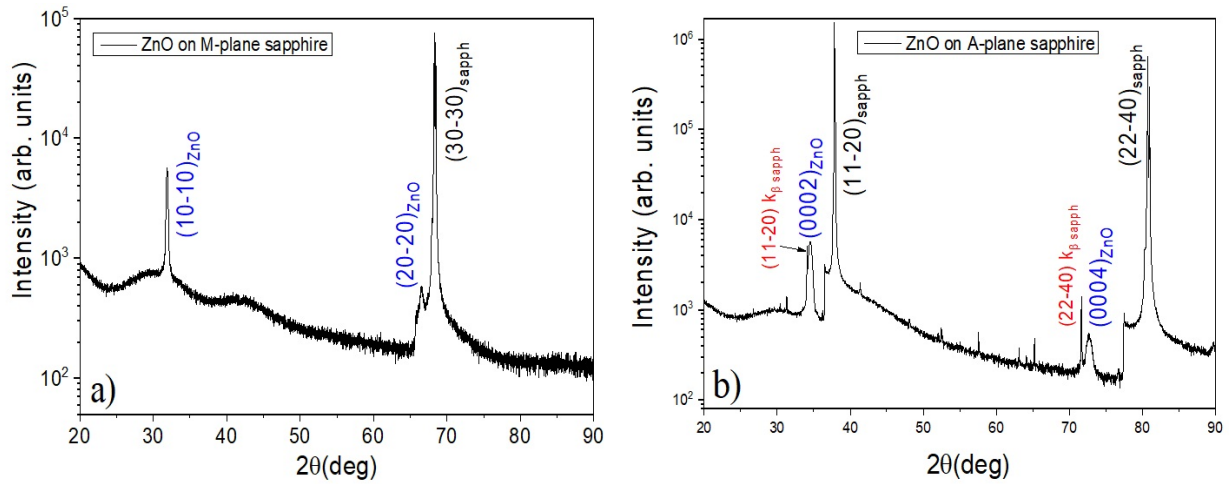


Figure 4.9: XRD patterns of the ZnO samples with 5 min of growth time deposited onto the substrate without chemical treatment: a) *M*-plane; b) *A*-plane sapphire

Besides *R*-plane, *M*-plane and *A*-plane sapphires were used as substrate. In the paper [266] Wang et al. founded that different oriented sapphire substrates can obviously affect types and content of intrinsic defects, which regulates the structural, optical and Raman properties of ZnO films. For this reason, using different types of substrate could help in solving the problem of obtaining more smooth uniform films with low deposition times. As before, these substrates were also chemically treated to see changes in the resulting films and to compare the results. The XRD results for the *M*-plane and *A*-plane are shown in Figure 4.9, where can be seen that both of the obtained Zinc Oxide films have a hexagonal structure, which is reflected by the presence of a family of peaks $(10\bar{1}0) - (20\bar{2}0)_{hex}$ and $(0002) - (0004)_{hex}$, respectively. Figure 4.10 and Figure 4.11 represents morphology measurements results for *M*- and *A*-planes sapphire, respectively what are similar between themselves.

As can be seen from figures 4.10 and 4.11 after chemical etching of the substrate surface before the film growth, the quality of the films has not been improved to much. In both cases, the samples grown on untreated substrates had smoother surfaces with a number of holes. Zinc oxide films obtained on substrates after chemical treatment most likely changed the growth mechanism from planar to columnar. As can be seen from the figures below, the films were not homogeneous and consisted of large crystalline grains closely spaced to each other. The thickness of the samples obtained on the *M*-plane $(10\bar{1}0)$ sapphire before and after the chemical treatment of the substrate remained practically unchanged and amounted to about 80 nm. For a sample on *A*-plane $(11\bar{2}0)$ sapphire film thickness of the film thickness of the films decreased slightly from 60 to 50 nm, as a result of chemical treatment. In contrast to the ZnO growth on *R*-sapphire, the samples obtained on the *A*-sapphire surface after chemical treatment do not have a homogeneous layer, and, like the film obtained on the *M*-plane, there were polycrystal-

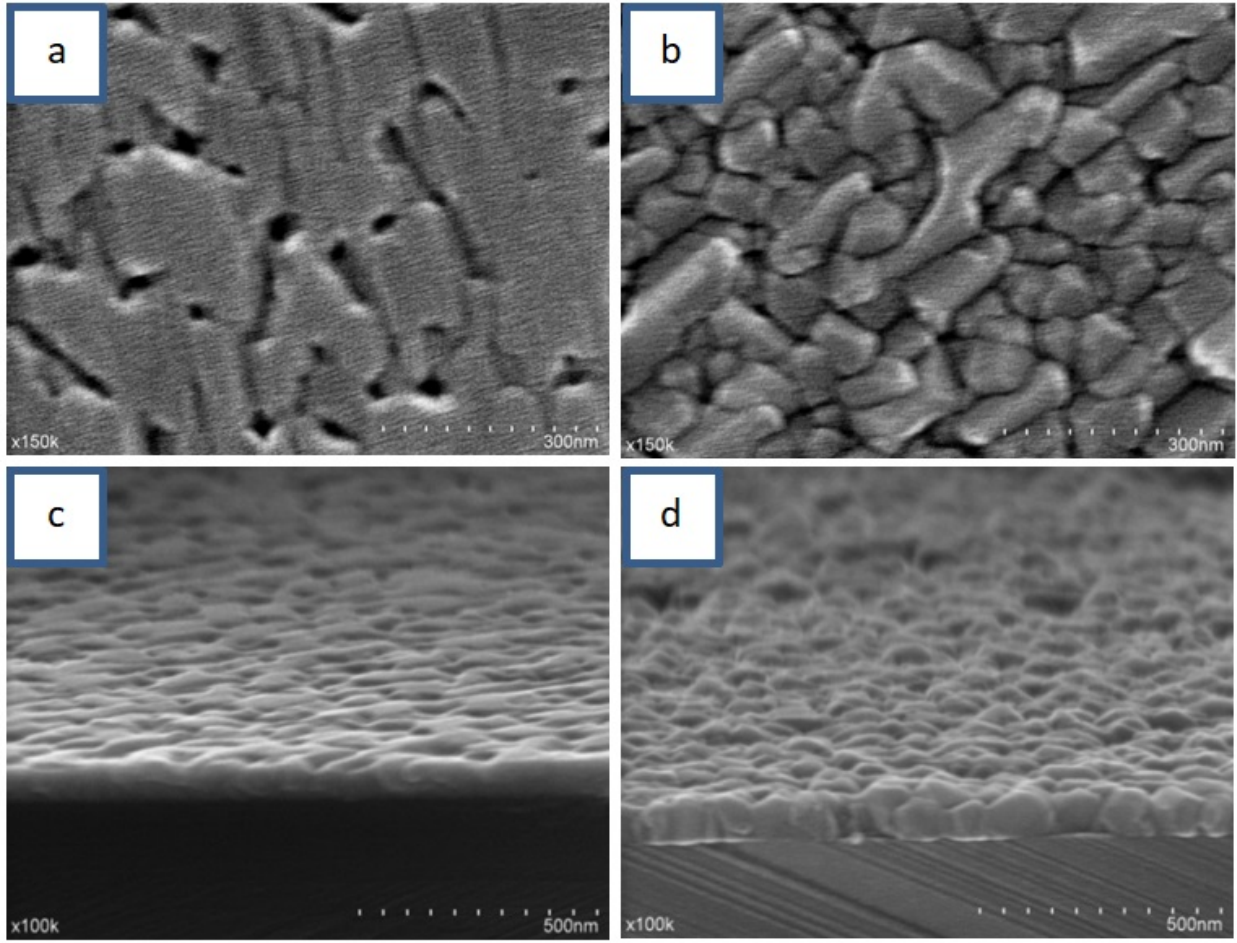


Figure 4.10: Morphology of surface (a, b) and cross-section (c, d) of ZnO samples deposited onto *M*-plane sapphire during 10 min [71.77 and 14.22 $\mu\text{mol}/\text{min}$ for O/Zn]: (a, c) without chemical treated substrate and (c, d) with chemical treated substrate.

line. Reducing thicknesses with growth and crystallite formation corresponds to increasing the number of nucleation points, which reduces the *1D* growth and increases the *2D* growth of the material.

Among the 3 types of substrates used for film growth, the R-plane ($1\bar{1}02$) sapphire showed the best surface morphology with lower film thickness with the same growth conditions. Therefore, further research will be carried out for films grown on ($1\bar{1}02$) sapphire without preliminary chemical processing of the substrate.

Zuñiga-Perez in his work [180] conducted a study of pure sapphire of different orientations. It was found that the surfaces of the *A*-plane and *R*-plane sapphires consist of clearly delineated terraces, separated by steps with a height of the order of (0.2-0.4) nm. These steps may have formed when cutting and polishing sapphire plates (miscut substrates is less than 0.1°). A series

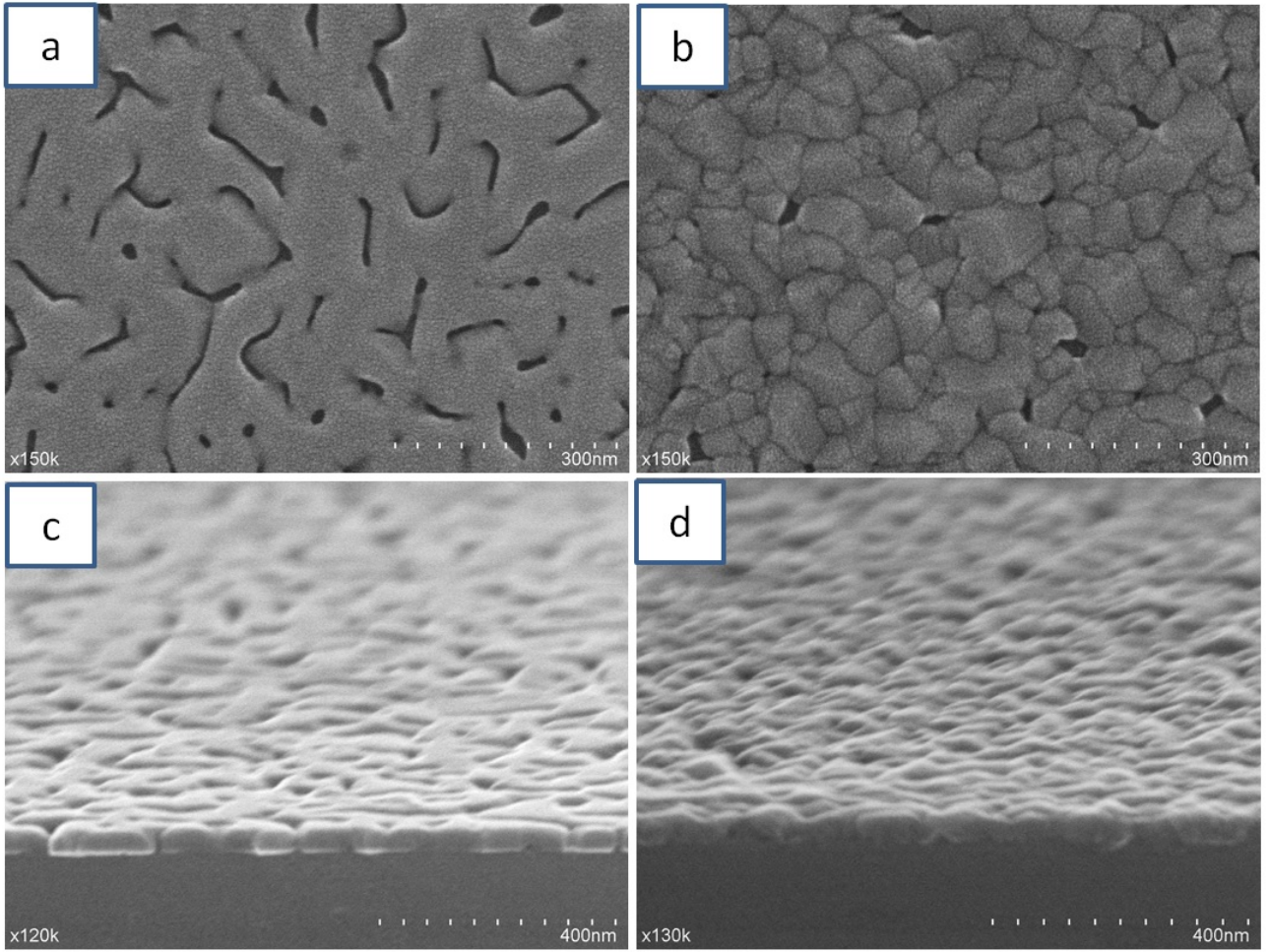


Figure 4.11: Morphology of surface (a, b) and cross-section (c, d) of ZnO samples deposited onto *A*-plane sapphire during 10 min [71.77 and $14.22 \mu\text{mol}/\text{min}$ for O/Zn]: (a, c) without chemical treated substrate and (c, d) with chemical treated substrate.

of stripes appear, parallel to the stepped lines, which act as preferred nucleation sites where ZnO grains begin to grow. Step – terrace morphology creates a diffusion barrier between step and terrace, which leads to a distribution of the material on the facets of the steps as islands, which develop along stepped lines to form ordered rows and reproduce the underlying pattern. With a long deposition time, the periodic order begins to be violated, since the grains nucleated on adjacent stepped lines cover the substrate and completely mask the underlying periodicity. In this case, grain nucleation will occur randomly over the surface. Meanwhile, *M*-plane sapphire substrates have atomically flat surfaces. ZnO grains dispersed on the surface of the *M*-plane ($10\bar{1}0$) begin to form a continuous film, which grows in the transverse direction due to the grains appearing on it. A continuous and flat film is gradually formed. At higher deposition times, the flatness of the ZnO film (Figure 4.10 a, c) is only perturbed by grain boundary grooves [180].

Chapter 4. Growth and characterization of ZnO, CdO, CdZnO, CdTe and their heterostructures

An increase in the nucleation points using a chemical treatment will accelerate the initial self-organizing growth of material adatoms on the ridges of the substrate terrace, followed by the growth of adatoms on the initial deposited one, which will eventually lead to a gradual film growth [269]. In this case, ZnO nanoparticles will be randomly placed on the surface of the substrate. The growth of nucleation points allows the material to be deposited more compactly, which will lead to a decrease in the thickness of the grown structures during 3-D film growth. Since the *M*-plane sapphire substrate did not have a step-terrace morphology from the very beginning, the thickness of the films obtained on *M*-plane substrates with and without chemical treatment practically did not change. For *R*-plane and *A*-plane sapphire, the treatment resulted in a decrease in the thickness of the deposited ZnO layers as shown above.

4.1.2 AFM studies

For a more complete study of the sample's surface, AFM quantitative roughness analysis was made. Samples grown with different precursor's flow, temperature and deposition time were measured. First of all, we tested a series of samples with a long time of growth (90 min) and deposition temperatures in the range of 325-400 °C (Figure 4.12). The figure shows a clear change in surface morphology that was not so obvious in the SEM. With the rise of the growth temperature, the morphology becomes more uniform and should affect the surface roughness of the films. It was found that the roughness decreased from 11 nm to 3 nm, when the growth temperature increased from 325 °C to 375 °C, and then again increased up to 11 nm at a temperature of 400 °C. The repeated growth of roughness may be associated with the transition to a high-temperature regime in which the growth rate decreases and a re-evaporation of material from the sample surface caused by high temperature is possible, as was mentioned above (Section 4.1). Both AFM and SEM studies showed that ZnO films grown up by 375 °C have a smoother surface, under our experimental conditions.

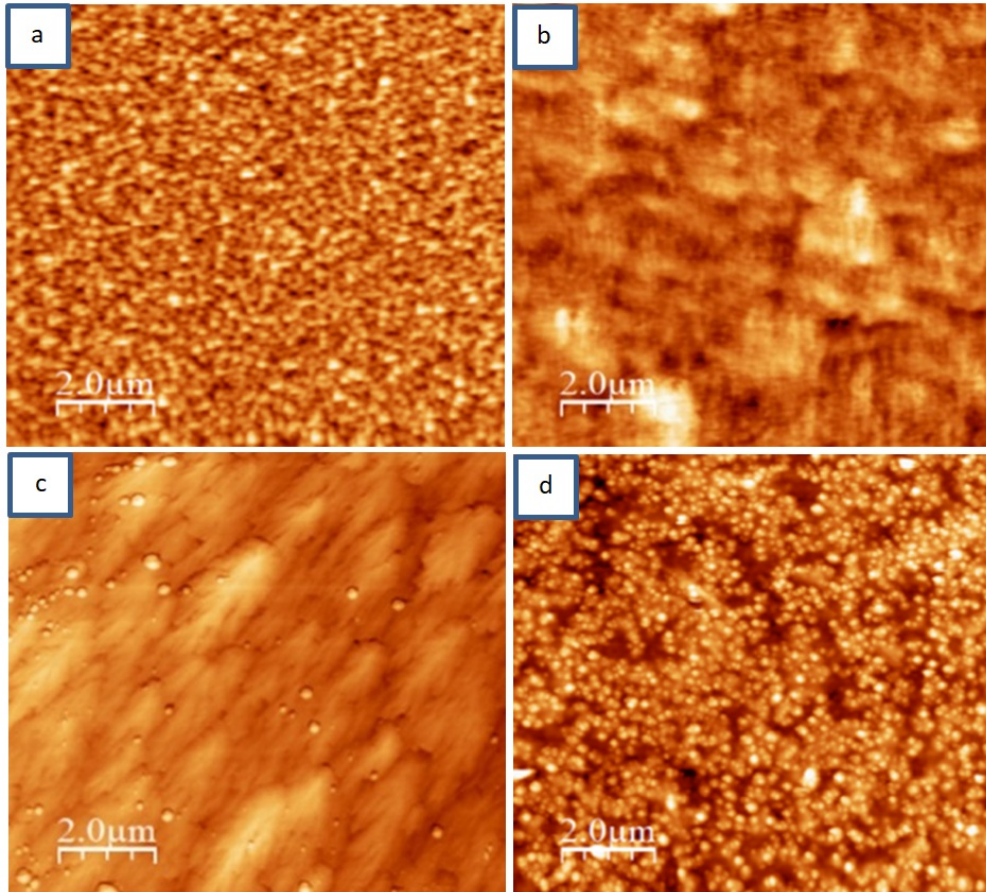


Figure 4.12: AFM patterns of ZnO samples deposited on *R*-plane sapphire with different temperature: 325 °C (a), 350 °C (b), 375 °C (c) and 400 °C(d).

Chapter 4. Growth and characterization of ZnO, CdO, CdZnO, CdTe and their heterostructures

Measuring a series of samples at 375 °C and 71.77/14.22 $\mu\text{mol}/\text{min}$ flow of O/Zn precursors, with a gradual decrease in the time of growth, we noticed that the surface rms roughness of the films remained almost constant and was in the range of 1.5-2 nm. Although the SEM measurement showed that a film with a smooth surface was formed after 10 minutes of growth, AFM shown that the sample with 5 minutes of growth had a similar rms roughness. With 3 minutes of growth the material is distributed along the edges of the substrate steps, and we can see them organized into linear and parallel arrays with an rms roughness of ~ 3 nm (Figure 4.13).

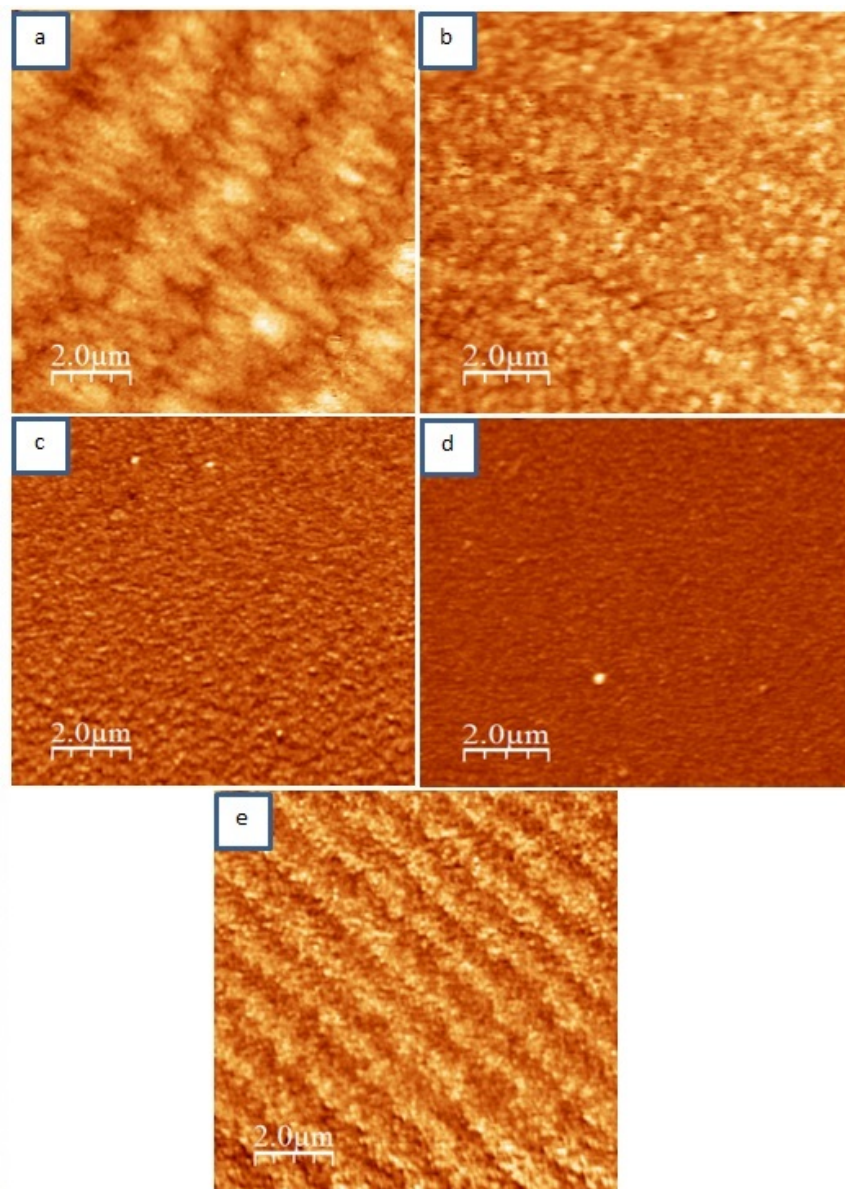


Figure 4.13: AFM of ZnO samples deposited on *R*-plane sapphire with different deposition time: 30 min (a), 15 min (b), 10 min (c), 5 min (d) and 3 min (e)

Zúñiga-Pérez [180] studied the rms roughness of ZnO films as a function of the deposition time on an *R*-plane ($1\bar{1}02$) sapphire at 420 °C with VI/II molar ratio equal 5 and a similar flow of precursors. The growth temperature was higher than the optimum to enhance surface diffusion, which is one of the dominant processes during the initial growth stages. The author showed that initially the rms roughness increased, which was caused by the appearance of the first islands on the surface of the substrates. It was found that, with a deposition time of 50 seconds to 100 seconds, despite the fact that the films became thicker, the rms roughness decreases and the minimum *rms* roughness remains almost constant at about 17 nm, regardless of the film thickness and suggesting growth in the *2D* type.

In our case, a series of samples on *R*-plane sapphire with a small amount of oxygen and zinc precursors (14.35 and 2.85 $\mu\text{mol}/\text{min}$, respectively) showed that the roughness of the films decreases with a decrease in the growth time of the material to 10 minutes (Figure 4.14). When the deposition time to ≤ 5 minutes the deposited film does not have a uniform surface. As mentioned above, *R*-sapphire substrates present steps and parallel terraces morphology that provides nucleation sites at the facet edge of the step, in addition to the free surface bonds, which act as nucleation points. A number of bands appear, with the average step distance between the lines, in this case, being about 0.9 μm . The roughness value is stabilized and does not change much regardless of the growth time. With a small amount of time, deposition material does not have time to fill the gaps between the steps, which leads to an increase in the roughness of the films.

With flows of 43.06 and 8.54 $\mu\text{mol}/\text{min}$, AFM measurements confirm the results obtained by SEM and show that the smoothness and thickness of the sample are identical to those of the conditions: $t=10$ min (71.77/14.22 $\mu\text{mol}/\text{min}$) and $t=45$ min (14.35/2.85 $\mu\text{mol}/\text{min}$) as can be seen in Figure 4.15. Measurements showed that at these growth conditions, with a decrease in the growth time, the surface roughness of the samples gradually increased from 2 to 6 nm, while this value was slightly larger for the sample, which was grown at 15 min than for the sample with a growth time of 10 min. For greater accuracy of the results, the studies were carried out at several points of the sample.

It was found, that with an increase in the oxygen and zinc flow of precursors into the chamber of the reactor up to 100.48/19.91 $\mu\text{mol}/\text{min}$, the roughness decreased with a decrease of deposition time of the material. (Figure 4.16). At the same time, comparison of the samples grown during the same time but having different precursors flow showed that, an increase in the flow of precursors leads to a sharp decrease in the surface rms roughness of the film with deposition time from 5 min to 15 min with a further gradual decrease at 25 min. The material is evenly distributed over the surface (Figure 4.17).

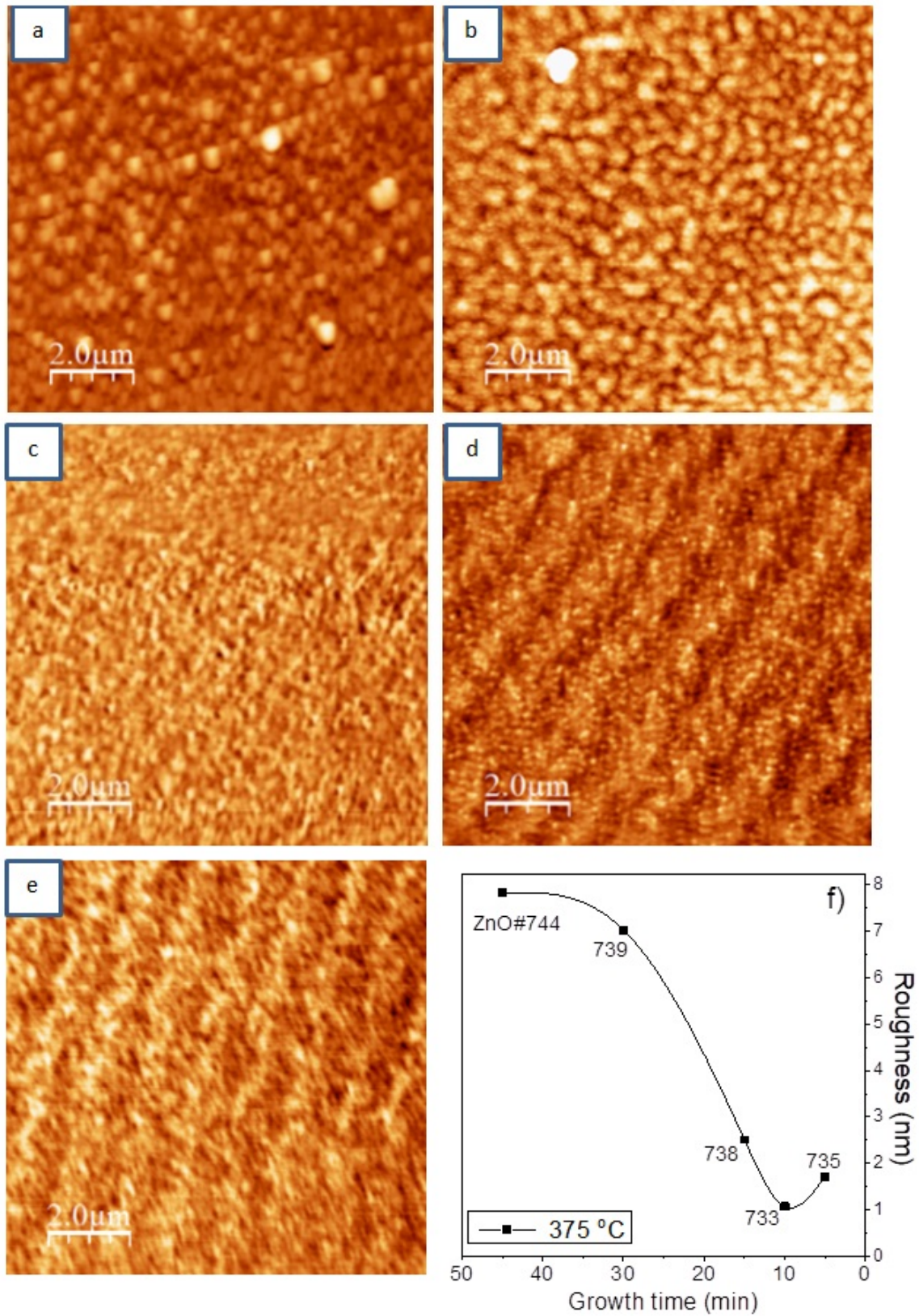


Figure 4.14: AFM patterns of ZnO samples deposited with 14.35 and 2.85 $\mu\text{mol}/\text{min}$ of O and Zn precursors) and different deposition times: 45 min (a), 30 min (b), 15 min (c), 10 min (d) and 5 min (e). Graph of the surface rms roughness change calculated using the WSxM 5.0 Develop 8.3 software (f)

4.1. Zinc oxide: morphological and structural study

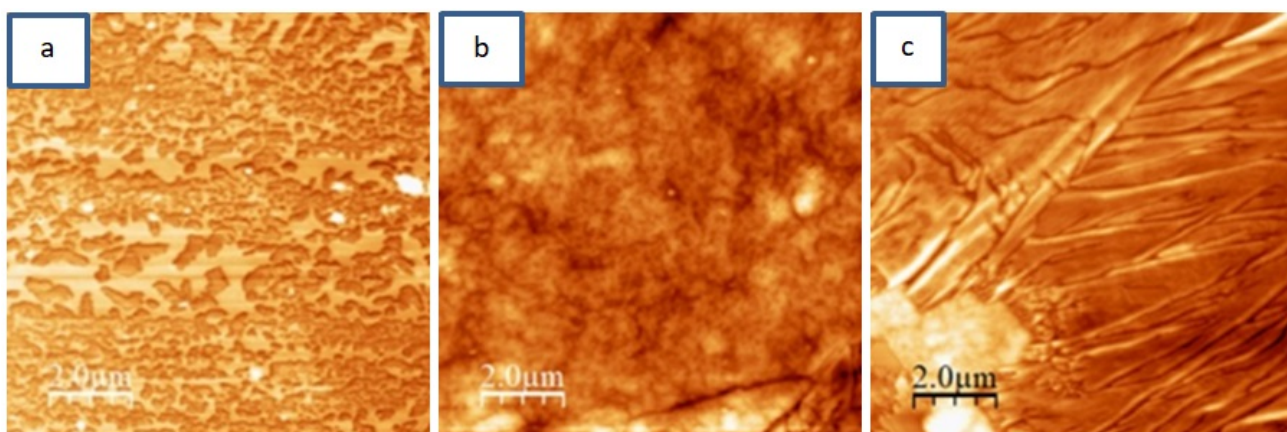


Figure 4.15: AFM patterns of ZnO samples deposited with 15 PSP (43.06 and 8.54 $\mu\text{mol}/\text{min}$) of flow and different deposition time: 30 min (a), 15 min (b), 10 min (c).

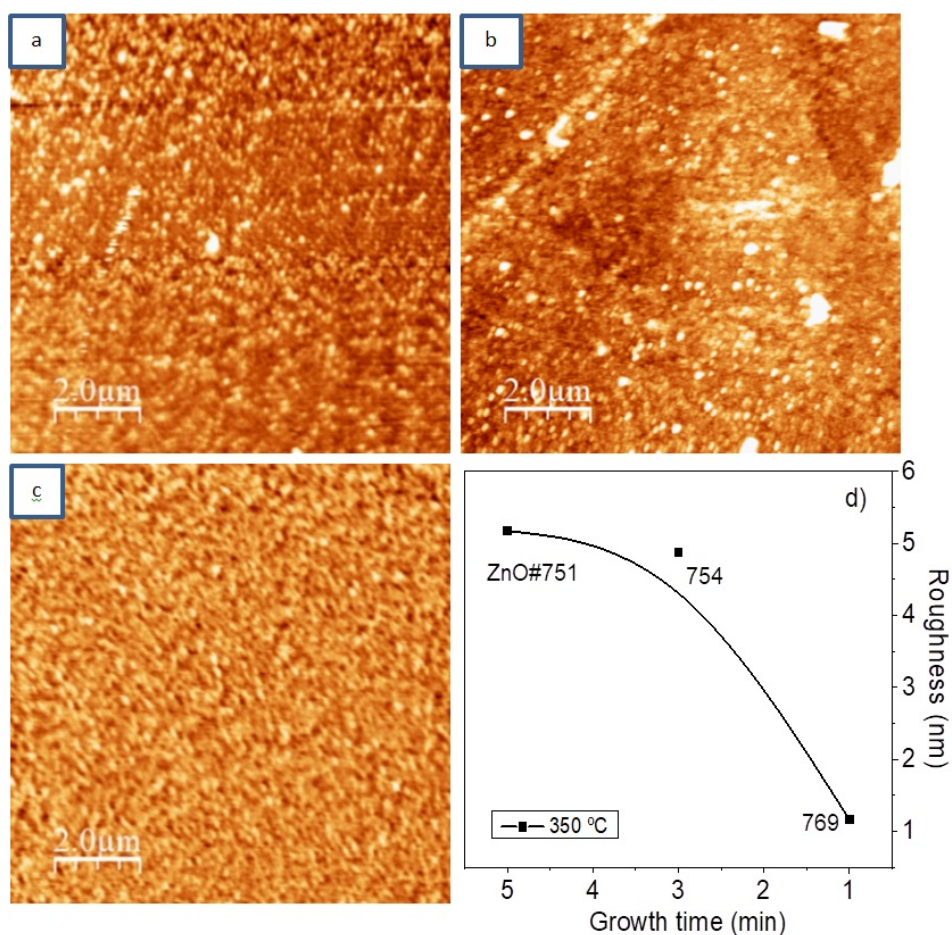


Figure 4.16: AFM patterns of ZnO samples deposited with 35 PSP (100.48/19.91 $\mu\text{mol}/\text{min}$) of flow and different deposition time: 30 min (a), 15 min (b), 10 min (c). Graph of the surface roughness change calculated using WSxM 5.0 Develop 8.3 software (d)

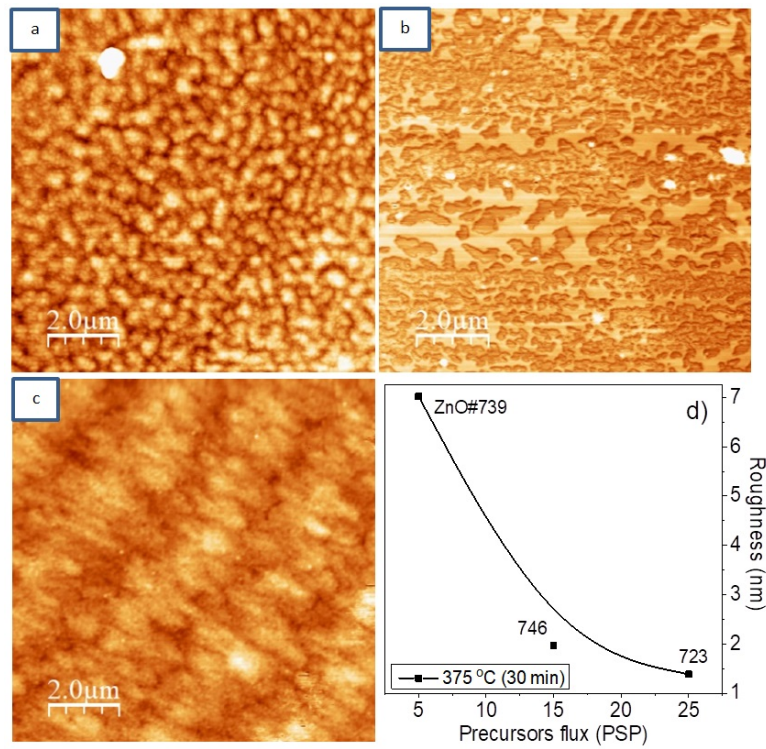


Figure 4.17: AFM of ZnO samples deposited during 30 minutes and different flow of O and Zn precursors: $14.35/2.85 \mu\text{mol}/\text{min}$] (a), $[71.77/14.22 \mu\text{mol}/\text{min}]$ (b), $[100.48/19.91 \mu\text{mol}/\text{min}]$ (c). Graph of the surface roughness change calculated using WSxM 5.0 Develop 8.3 software (d)

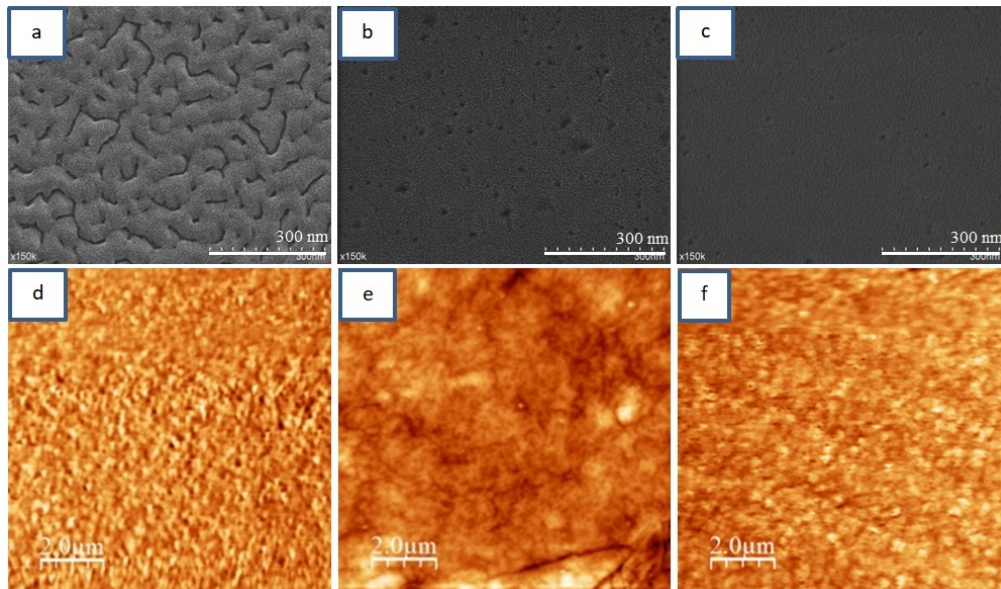


Figure 4.18: SEM (a-b) and AFM (d-f) patterns of ZnO samples deposited during 15 minutes and different quantity of precursors: $[14.35/2.85 \mu\text{mol}/\text{min}]$ (a, d), $[43.06/8.54 \mu\text{mol}/\text{min}]$ (b, e) and $[71.77/14.22 \mu\text{mol}/\text{min}]$ (c, f)).

4.1. Zinc oxide: morphological and structural study

Analysis of samples with the same deposition time (15 min), but a different amount of precursors flow showed that the sample with values in the middle of the studies range of oxygen and Zinc precursor's flow had a higher rms roughness (~ 11 nm) compared to samples obtained with a larger and smaller flow of precursors during growth (~ 2 nm). Since this sample was measured at different points and re-measured on different days, it can be concluded that the results are likely to be reliable. All samples were in the *FC* position. Comparison of surface morphology using SEM with a more detailed AFM study is shown in the Figure 4.18.

Low deposition time (5 min) does not allow obtaining homogeneous thin films and deposited ZnO NPs created step-terrace morphology on the sapphire surface. An increase in the flow leads to an increase in the surface roughness of the sample as can be seen in Figure 4.19.

Earlier it was shown that a series of samples located closer to the entrance of precursors into the reactor (*F*-group) had a simpler surface morphology and a slightly greater thickness of the films, while the surface of the second group (*R*-group) was more rough. For this reason, a sample in the FC position was selected for comparison of chemical treatment effect on the surface roughness.

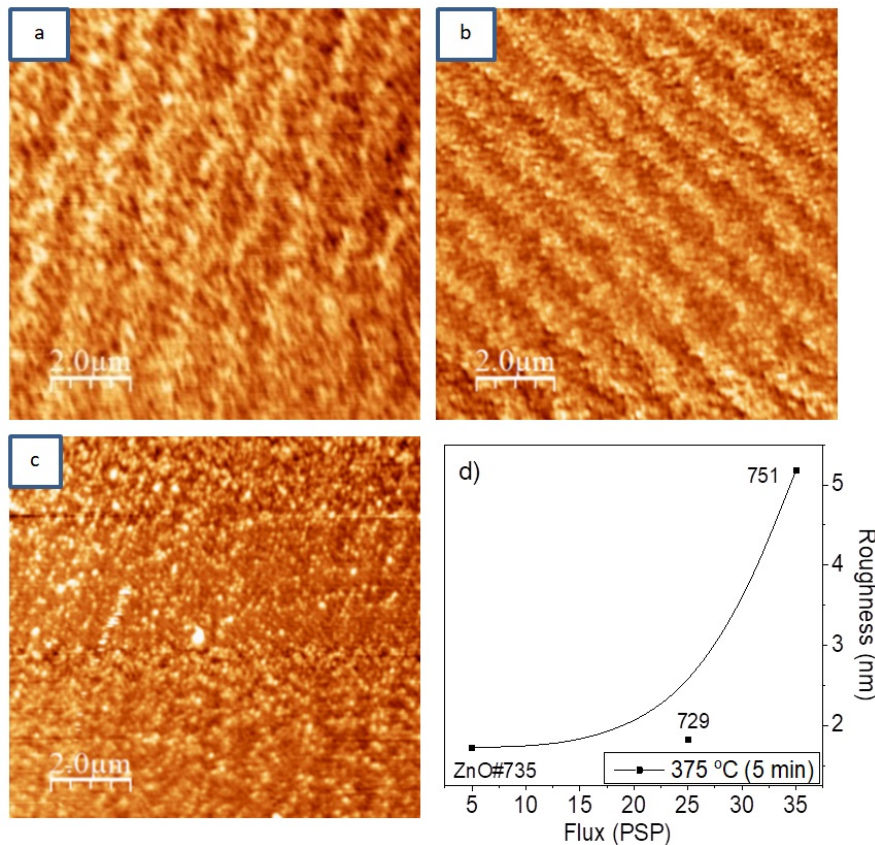


Figure 4.19: AFM patterns of ZnO samples deposited during 5 minutes and different flow of precursors: [14.35/2.85 $\mu\text{mol}/\text{min}$] (a), [71.77/14.22 $\mu\text{mol}/\text{min}$] (b), [100.48/19.91 $\mu\text{mol}/\text{min}$] (c). Graph of the surface roughness change calculated using WSxM 5.0 Develop 8.3 software (d)

Chapter 4. Growth and characterization of ZnO, CdO, CdZnO, CdTe and their heterostructures

AFM studies have shown that, the sample grown on a substrate chemical treating, slightly increased its surface rms roughness from 2 to 2.8 nm (Figure 4.20). A slight increase in surface roughness should be due to an increase in nucleation points.

ZnO films obtained in this work using the MOCVD method showed good crystalline quality at the nanoscale. Films of this quality are promising for use in both scientific and industrial fields.

In conclusion to the section, the temperature at which the largest number of smooth films of the series are obtained is 375 °C. Samples closer to the inlet the reactor are smoother and thicker than the ones at the rear positions. A decrease in the thickness while maintaining the smoothness of the films is possible up to ~ 65 nm, after which holes begin to form on the surface of the samples. Variation of the precursor flow only contributes to a change in the growth time at which the films remain smooth, while the final thickness and the total amount of the precursors used (~ 800 μmol) remain constant. Chemical treatment of the substrate by $\text{H}_3\text{PO}_4 : \text{H}_2\text{SO}_2$ solution in a (1:3) ratio at 120 °C during 3 hours at similar growth parameters, slightly reduces the film thickness and makes the sample surface smoother. Among 3 different types of substrate, used at the same growth condition, the best result of smoothness and thickness was shown by ZnO films grown onto *R*-plane sapphire.

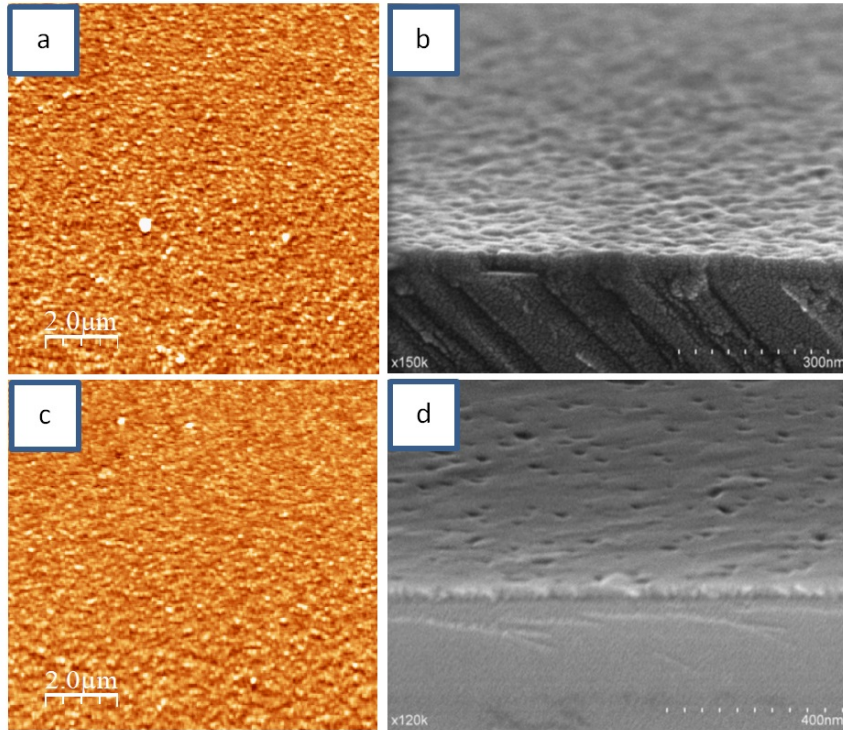


Figure 4.20: AFM images (a, c) and cross-section (b, d) of ZnO samples on ($1\bar{1}02$) sapphire without chemical treatment (a, b) and on ($1\bar{1}02$) sapphire with chemical treatment (c, d).

The AFM study confirmed the previous results and extended them. It was found that the samples grown on *R*-sapphire have the lowest surface rms roughness in the temperature range of 300-400 °C. The *rms* roughness value remains stable at 2 nm, but with a short growth time (< 5 min), the amount of precursors is not enough to uniformly fill the substrate surface and the material is distributed along the edges of the sapphire morphology steps forming linear and parallel arrays. A higher precursor flow at the same growth time makes possible to obtain films with less rms roughness. With a short growth time, an increase in the precursor flow contributes to an increase the rms roughness. The average value of the rms roughness of ZnO films obtained on substrates after a chemical treatment slightly increases, which may be a consequence of an increase in the presence of nucleation points.

4.2 CdZnO: morphological and structural study

4.2.1 SEM and XRD measurements

In some cases, the use of binary compounds, such as ZnO or CdO, does not always provide the properties we could need. For this case, alloying could be an option. In the previous section, we analyzed the growth of ZnO films, and taking into account the data that we previously obtained for a CdO film [99], we have made a study to obtain ternary compounds based on them. The growth of CdO-ZnO ternary oxides highlights the difficulty of combining materials with different crystalline structures, that is, hexagonal for ZnO and cubic the case of CdO. Films of the CdZnO compound enriched with Zn retain a cubic structure if the zinc concentration does not exceed 20 % [28–31]. Fan et al. [270] carried out a first principles analysis of the phase stabilities, chemical bonds and band gaps. Authors calculated regions of phase stability of $A_xZn_{1-x}O$ alloys ($A = \text{Ca, Cd, Mg}$), where for $Cd_xZn_{1-x}O$ cubic structure this region was located at $0.75 < x < 0.875$, which matched the with experimental data performed by Ishihara et al. [271] on *A*-plane sapphire substrates. On the other hand Yu et al. [272] grew layers via a radio-frequency magnetron cosputtering system. They observed, through using X-ray conventional diffraction measurements, that polycrystalline films had a single-phase cubic structure at $x \leq 0.21$ and mixed phases at $x = 0.29$. As can be concluded from the literature, the incorporation of Cd or Zn into the parent binary compound affects the structure of the solvent compound differently (hexagonal ZnO or cubic CdO, respectively) depending on the growth conditions.

In this section, the compound of CdZnO with different zinc contents will be considered. For the growth of CdZnO ternary compounds, a temperature of 304 °C was chosen, a relatively low growth temperature to maintain a low dislocation density, but high enough to promote the incorporation of Zn into the stable CdO cubic lattice [101]. A series of samples $Cd_{1-x}Zn_xO$ with a zinc nominal content in the range of 0-20 % was investigated. At the same time, during the growth of samples with a high Zinc content (20%), both Nitrogen, as more typical, and Helium, as an alternative gas for comparison, were used as carrier gases. Growth conditions are shown in the Table 2.7. Micrographs of the cross-section and surface morphology are shown in Figure 4.21 and thickness in respect Zinc content are collected in Table 4.1.

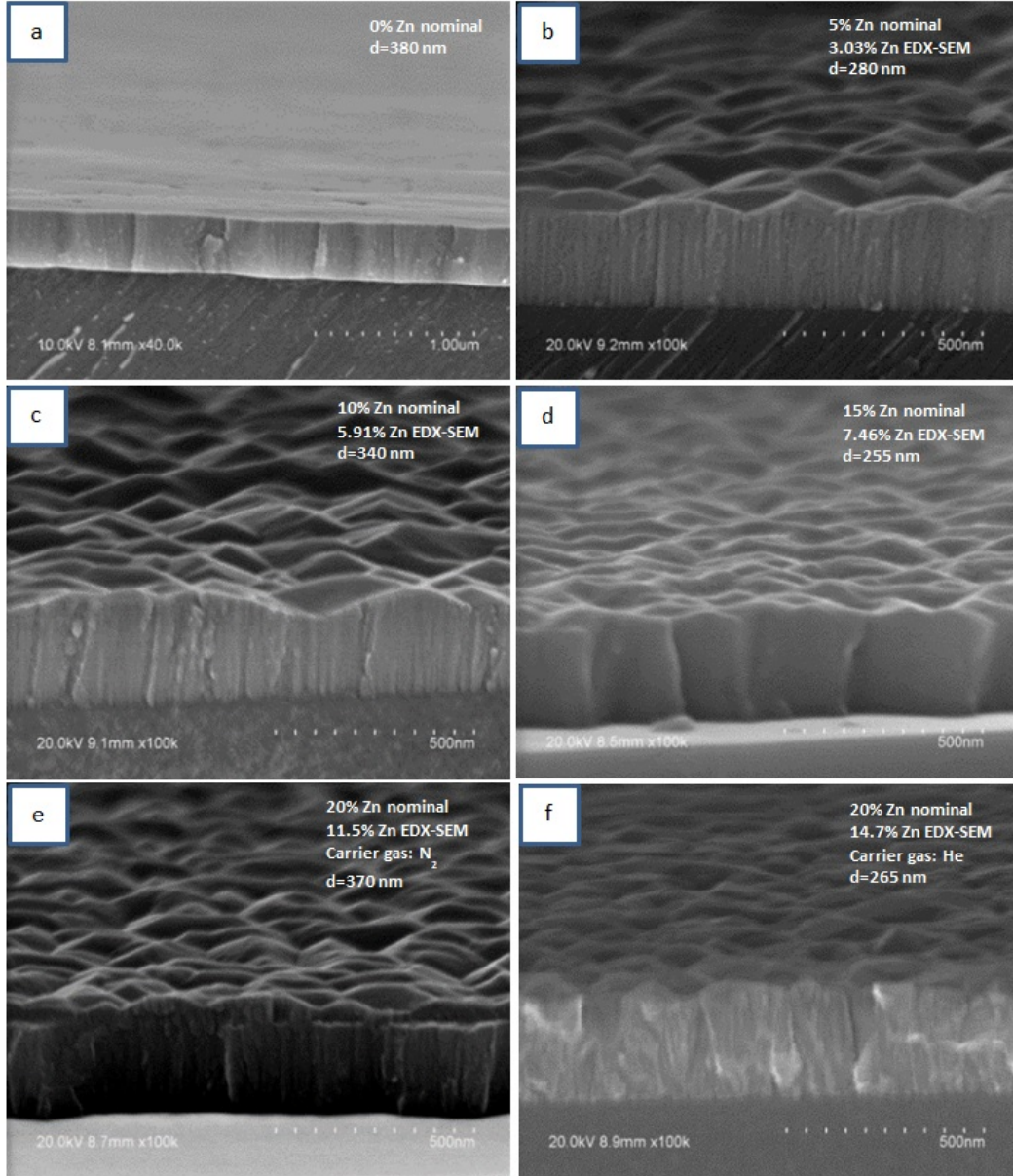


Figure 4.21: SEM micrographs of $Cd_{1-x}Zn_xO$ thin films with different Zn content: 0% (a), 5% (b), 10% (c), 15% (d), 20%- N_2 (e) and 20%-He (f). Label d mean the film thickness.

As can be seen from Figure 4.21, the incorporation of Zn atoms into the crystal lattice of the binary CdO compound leads to a change of surface morphology. The flat surface of CdO becomes rougher. The Zn atoms introduce a distortion in the host matrix, when it was included in the CdO crystal lattice during the diffusion regime of film growth (growth step 4, Section 2.4.1). Figure 4.22 shows a schematic diagram of the atomic arrangement of the R -sapphire plane and (001) $Cd_{1-x}Zn_xO$ plane at the interface, deduced from the observed epitaxial relationships. Using the axis definition given in Figure 4.22 (a), we can have the following epitaxial relationships for the out-of-plane $Cd_{1-x}Zn_xO$ (001) oriented films [273]:

Chapter 4. Growth and characterization of ZnO, CdO, CdZnO, CdTe and their heterostructures

Name of sample	Thickness, nm	Nominal Zn content, %
CO850	380	0
ZCO870	280	5
ZCO852	340	10
ZCO871	255	15
ZCO854	370	20 (N_2)
ZCO877	265	20 (He)

Table 4.1: Thickness and nominal content data of $Cd_{1-x}Zn_xO$ samples

$$Cd_{1-x}Zn_xO(001)||Al_2O_3(01\bar{1}2)$$

$$Cd_{1-x}Zn_xO[100]||Al_2O_3[\bar{2}110]$$

$$Cd_{1-x}Zn_xO[010]||Al_2O_3[0\bar{1}11])$$

These epitaxial relationships are coherent with those previously obtained for CdO films grown on R -plane ($1\bar{1}02$) sapphire substrates [83, 99] as evidence that the epitaxial coupling with the substrate is not altered as a result of zinc incorporation during the growth.

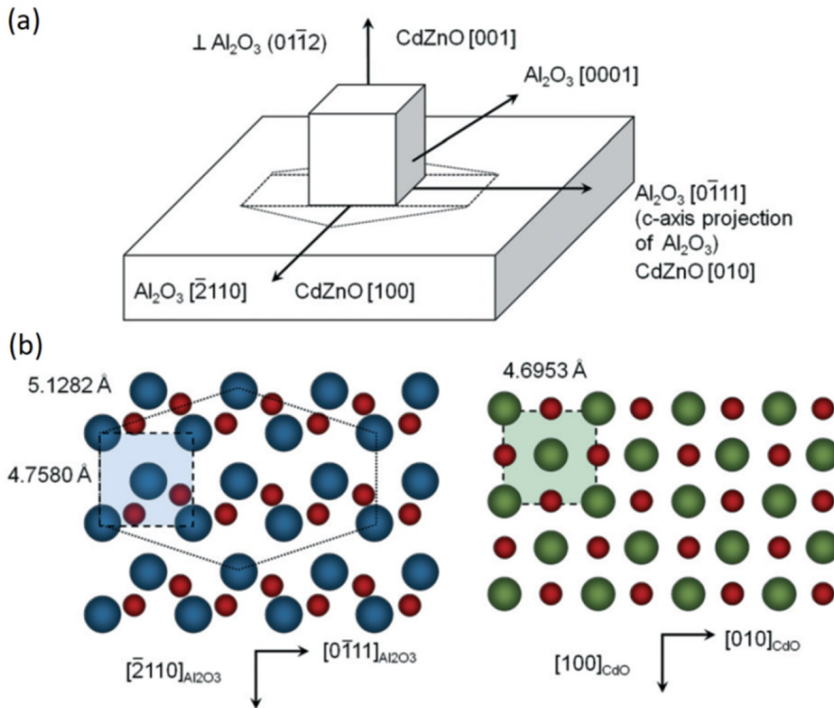


Figure 4.22: Schematic diagrams showing the crystals of $Cd_{1-x}Zn_xO$ with (001) orientation grown on R -plane sapphire; (b) schematic diagrams of r-sapphire (left) and CdZnO (right) surfaces in the case of low Zn content. The squares represent the coincident lattice points, and the indicated distances correspond to the case of $x = 0$ (pure CdO). [273].

4.2. CdZnO: morphological and structural study

For a more detailed analysis of CdO films property changes depending of Zn value be incorporated into the crystal lattice, in addition to morphological analysis of the sample, the structural analysis was also carried out using X-ray diffraction and EDX methods. The first step in the structural characterization of any material is to determine whether it is textured or not, that is, whether it shows a preferred orientation or not. For CdO films grown on R -plane ($1\bar{1}02$) sapphire substrates the typical structure is the single-phase structure of the stable cubic(ZB) with (200) plane of cubic phase [100]. The X-ray diffraction patterns from the series of $Cd_{1-x}Zn_xO$ thin films with Nitrogen as a carrier gas, are plotted in Figure 4.23. The 3 peaks of the XRD patterns corresponds to the $(01\bar{1}2)$, $(02\bar{2}4)$, and $(03\bar{3}6)$ peaks of R -sapphire substrate. As can be seen from the figure, the dominant peaks are shifted in respect to the peaks of $CdO_{(200)}$ and $CdO_{(400)}$, which corresponds to 38.31° and 82.09° for pure CdO, respectively. This fact points out the existence of a growth texture with an axis normal to the plane [100]. An increase in the Zn content leads to a shift of the peaks of the material toward large angles (Figure 4.24). For a sample with 20 % of nominal Zn content obtained with Helium, the shift of peak position has the highest value. Starting from the sample with 15 % of Zn nominal content other orientations begin to appear, which are associated with other planes of the cubic structure, making the polycrystalline character evident in the sample. As the Zn concentration increases up to 15 %, peaks, that belong to the $CdO_{(111)}$ and $CdO_{(222)}$ peaks families, appear. A hexagonal phase in the resulting series of samples was not found. Only the sample with 20 % of Zn nominal content grown with Nitrogen, presents a small peak which may correspond to CdZnO with hkl indexes $(102)_{hex}$, and indicate phase mixing at higher Zn nominal content.

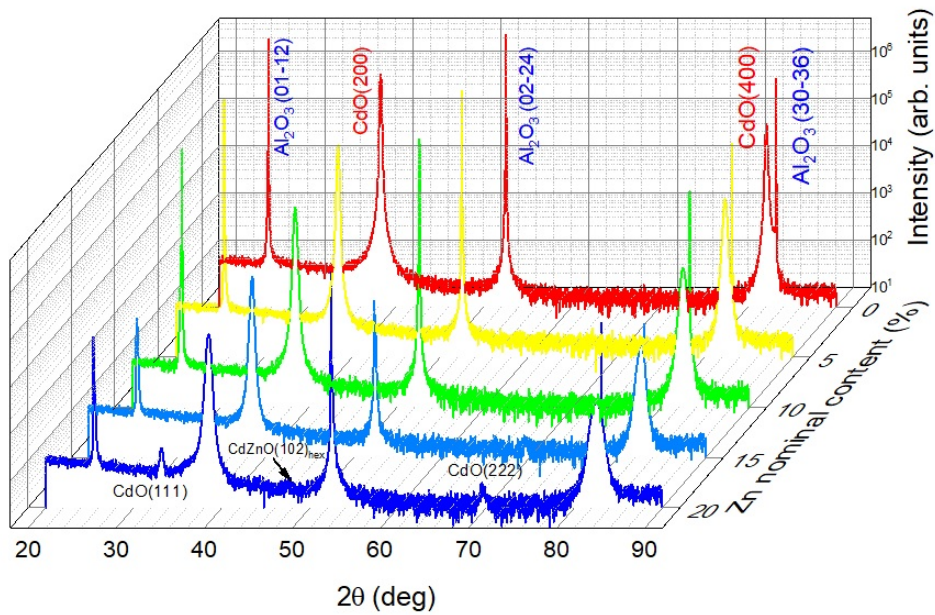


Figure 4.23: XRD patterns of $Cd_{1-x}Zn_xO$ samples with different Zn content.

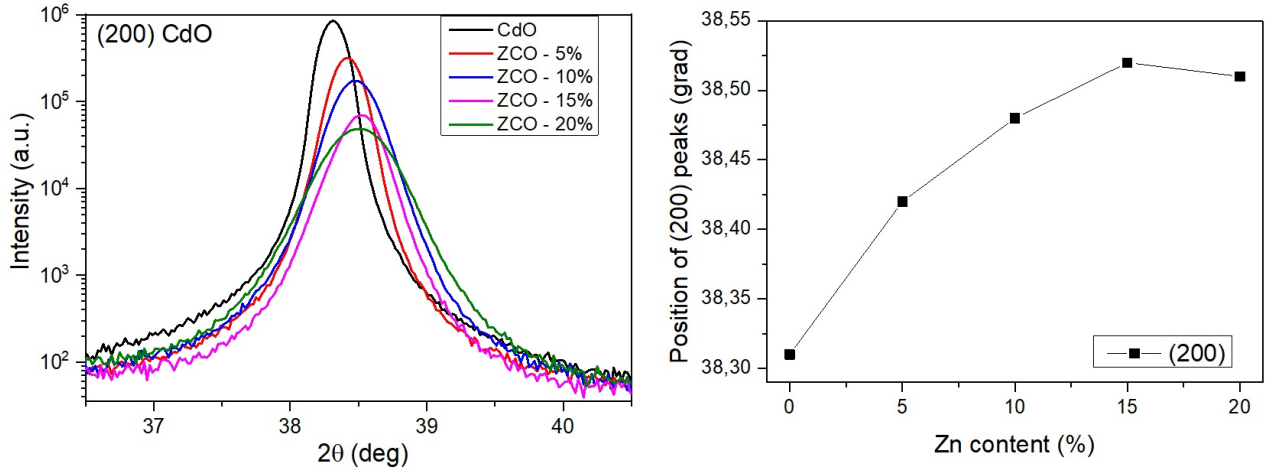


Figure 4.24: Plotting of dominant (200) peak of CdZnO films with different nominal Zn content.

Differences in the ionic radii of Zn and Cd and in the different stable crystal structures of the binary compounds limit the growth of single-phase films of ternary $Cd_{1-x}Zn_xO$ alloys over a broad compositional range. To explain the change in behaviour of the properties of samples after an increase in the Zn nominal value $x > 15\%$, consider the work of Martínez-Tomás et al. [273] who carried out investigation of crystallographic changes in $Cd_{1-x}Zn_xO$ films grown on r-plane sapphire by AP-MOCVD with Zn content $x \leq 0.5$. In the case of low Zn content ($x = 0-0.2$) the results were divided into 3 stages. In the first stage ($x \leq 10\%$), $Cd_{1-x}Zn_xO$ films have been found to preserve a single-phase cubic structure. Lattice parameter calculations using Vegard's law and average rock-salt lattice constants for ZnO and CdO were in good agreement with EDX measurements. With the rise in the Zn content in the range $10\% \leq x \leq 15\%$, the competition began to arise between the misfit stress and the shrinking of the lattice, which caused an inversion of the deformation of the lattice cell, which becomes enlarged in-plane and shortened out-of-plane. At the third stage of the transition of the samples from rock salt to wurtzite at $x \geq 15\%$, the inclination of rotated domains of two differently oriented crystals increased to 30° from each other and tends to 15° at each side of the projection of the c-axis of sapphire on the substrate surface. The authors showed the proposed scheme to explain the symmetric inclination of the array cells by $\pm 15^\circ$ and different types of orthorhombic distortions for each inclined cell in the form of a transition from the rock salt phase to the wurtzite phase, as shown in Figure 4.25. It has been hypothesized that if these crystallographic structures would be rich in Zn, this could explain both the high Zn content measured by EDX and the low Zn content determined from the application Vegard's law to the $Cd_{1-x}Zn_xO$ layers.

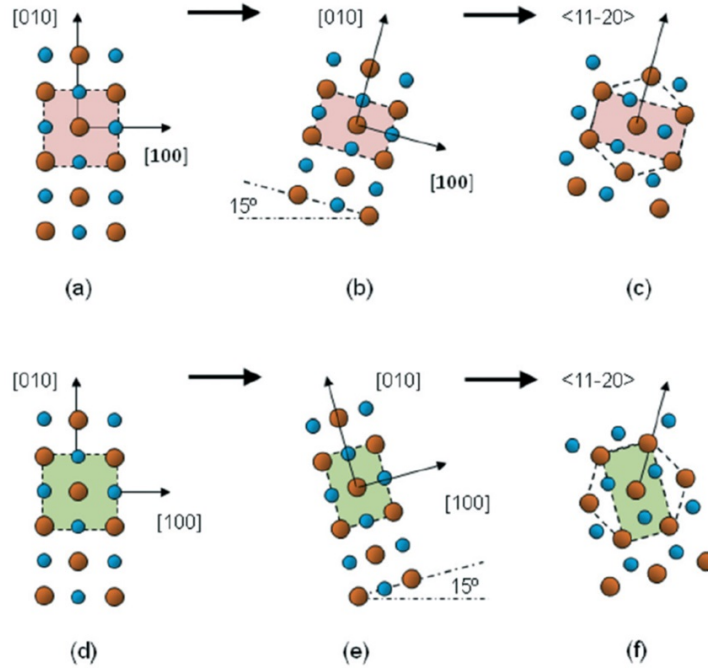


Figure 4.25: Schematic diagrams of the basal planes of the $Cd_{1-x}Zn_xO$ structure during the rock-salt-to-wurtzite transition: (a) in the early stages; (b) when tilt and orthorhombic distortion have taken place; (c) after transformation to a hexagonal structure; and (d)–(f) the same process but with tilt in the opposite direction. Small spheres: O; large spheres: Cd or Zn. [273].

Determination of Zn content in the obtained films was carried out using the EDX method and Vegard's law for peak position of cubic $CdO_{(200)}$ and $ZnO_{(200)}$. At the same time, the XRD pattern for the sample with 20% of nominal Zn content showed that the concentration of Zn slightly decreases when compared with the sample from 15% of Zn. Calculations by Vegard's law presented that Zn contents in the samples are 3.66, 5.24, 6.44, 5.93 (N_2) and 9.31 at % (He) for 5, 10, 15, 20 (N_2) and 20% (He) of nominal Zn content, respectively. Unlike the Vegard law, EDX analysis depicted the Zn content to be 3.03, 5.91, 7.86, 11.5 (N_2) and 14.7 at % (He), respectively, which indicates the incorporation of zinc into the crystal lattice of CdO. Figure 4.26 shows a graph of the content of Zn calculated using 2 different methods.

Literature review shows that the crystal structure of $Cd_{1-x}Zn_xO$ films changes with increase of the content x from rocksalt structure to wurtzite structure around $x \approx 0.30$ [271, 274]. In our work we investigate films with Zn nominal content $x \leq 20$ % and found signs of phase mixing with the appearance of a weak hexagonal $CdZnO_{(102)}$ phase at a high Zn nominal content. Substitution of Cd atoms with Zn atoms will decrease the lattice parameter of CdO, due to difference in the atomic radii of the material, which is 0.97 Å and 0.74 Å for Cd and Zn, respectively [275]. To find lattice parameter we use equation for peak position of (200) cubic phase of CdO:

$$a = \lambda \frac{(h^2 + k^2 + l^2)^{\frac{1}{2}}}{2 \sin \theta} \quad (4.1)$$

where, λ is x-ray wavelength (1.5406 Å), (h, k, l) are Miller indexes and θ is Bragg's diffraction angle for the maximum intensity. For comparison, we also use the expression for Vegard's law:

$$a(x) = (1 - x)a(\text{CdO}) + xa(\text{ZnO}) \quad (4.2)$$

where $a(\text{CdO})=4.6953$ Å and $a(\text{ZnO})=4.211$ Å [270] are the rock-salt lattice constants of the binary compounds and $a(x)$ is the undistorted lattice parameter of the ternary alloy. Results of calculations are depicted in Figure 4.27.

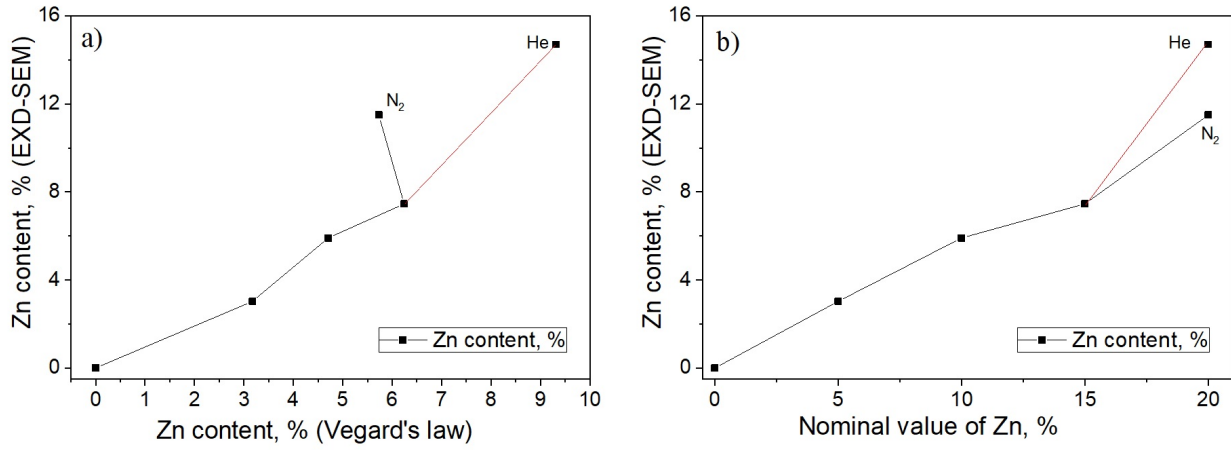


Figure 4.26: Zn content determined by EDX as a function of Zn content calculated by Vegard's law (a) and as a function of Zn nominal value (b).

As we can see, from Figure 4.27, the lattice parameter calculated by 2 different methods differs. Computation behind the (200) peak position shown that increasing Zn content in the samples leads to decreasing of lattice parameter value of the ternary structure from 4.6955 to 4.6511, due to incorporation of Zn atoms into CdO crystalline lattice. In this case, the value of the lattice parameter for a sample with 20 % of the nominal Zn corresponds to the 10 % of Zn concentration calculated using Vegard's law. This result approximately coincides with the values that we obtained above by EDX study. The smaller value of the lattice parameter with the presence of zinc suggests that the Cd^{2+} ions are partially substituted by the smaller Zn^{2+} ones. It is worth to note that a new hexagonal phase starts to appear.

Using XRD pattern and diffraction profile processing program DifWin, we found FWHM for the most intense(200) peaks of CdO of the samples. The crystallite size of the as-grown films has been calculated using Debye-Scherrer's equation(eq. 3.16) from HRXRD data, taking dimensionless shape factor $k=0.94$ and common X-ray wavelength $\lambda = 1.5406$ Å.

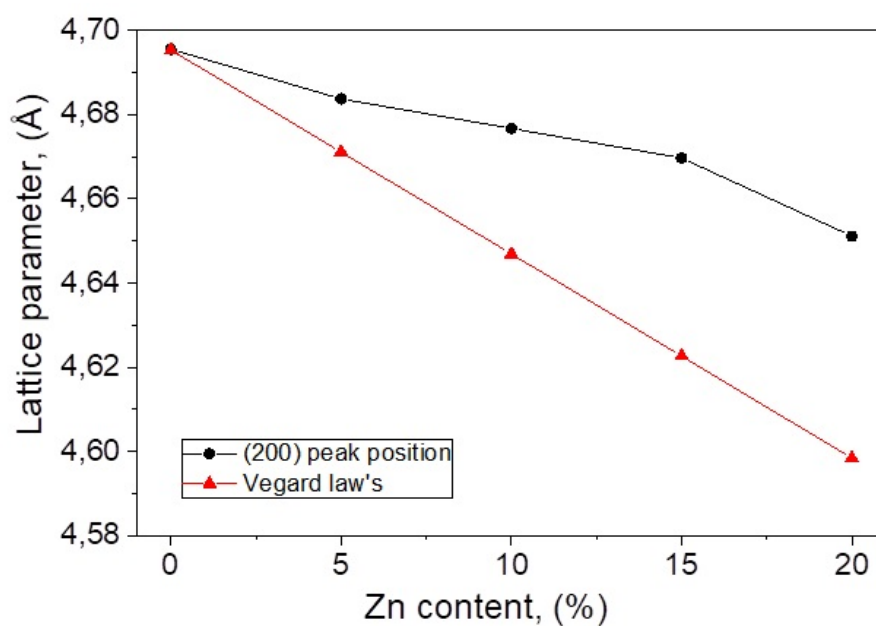


Figure 4.27: The calculated lattice constant for $Cd_{1-x}Zn_xO$ films with various Zn nominal content calculated by 2 different methods.

Figure 4.28 presents FWHM of XRD patterns and crystallite size depending on the Zn content in the samples.

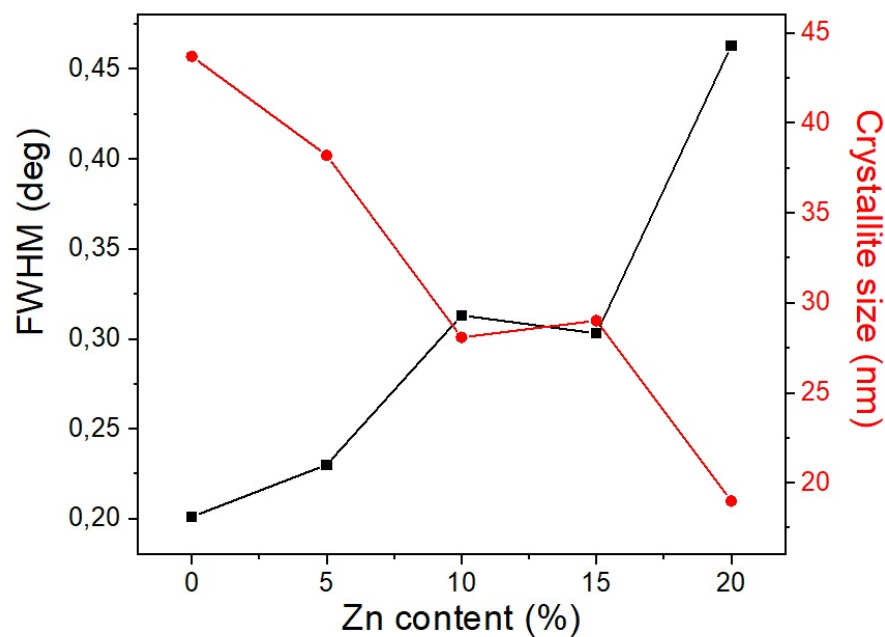


Figure 4.28: FWHM of XRD patterns and crystallite size as a function of Zn content.

Chapter 4. Growth and characterization of ZnO, CdO, CdZnO, CdTe and their heterostructures

From figure above, we can see that with increasing Zinc nominal content value of FWHM for the (200) peaks of CdO also increases in the range 0.20-0.46° (respectively, crystallite size decreases from 0.76 to 0.33 nm). A small exception to the rule is the sample with content x=15 % of zinc. This may be due to the fact that at this concentration other orientations begin to appear and are associated with other crystallographic planes of the cubic structure, which indicates the polycrystalline nature of the sample.

4.2.2 Transmittance and absorption spectra

Spectral studies of a series of samples of CdZnO with different Zn contents showed that all samples presented transmittance in the range 70-90 % that increased with the rise of Zn content in the wavelength range 300-900 nm. As mentioned before in Chapter 2, the introduction of more zinc in the CdO structures will increase the transmittance and the width of the band gap due to the blue shift of the edge of the bandwidth [18]. Above was found, that the thickness of the samples was different and did not depend on the increase in zinc concentration. Light absorbance is dependent on the transmittance of the material, which can be affected by surface roughness. Higher surface roughness can increase diffused light, which in turn will lead to reduced transparency. Light will be scattered at different angles at each interface and lead to an increase in the average optical path length. With the non-perpendicular incidence of light at the interface, the reflection coefficient will rise, and the increase in reflection at the inner interfaces leads to more efficient light trapping, which further increases the absorption of light [276]. Due to its high transparency [185], sapphire will have no effect on the results of CdZnO measurements and the spectra of pure sapphire has high transmission over the entire measurement range with a wavelength of 300-900 nm. (see Figure 4.29). The alternation of maxima and minima on the transmittance curves is associated with interference due to the small thickness of the samples. It is known that the film thickness and refractive index are important parameters for the interference of thin films. In this case, the minimum optimal film thickness will be of the order of *QWOT* (quarter wave optical thickness) and it is determined by the equation:

$$d_{min} = \frac{\lambda}{4n} \quad (4.3)$$

where, λ is wavelength, and n is the refractive index.

We can see gradually displacement of slope toward to higher wavelength in the transmittance spectrum of the samples. To find absorbance spectra of the samples we converted transmittance data using Beer's law described in equation 3.36.

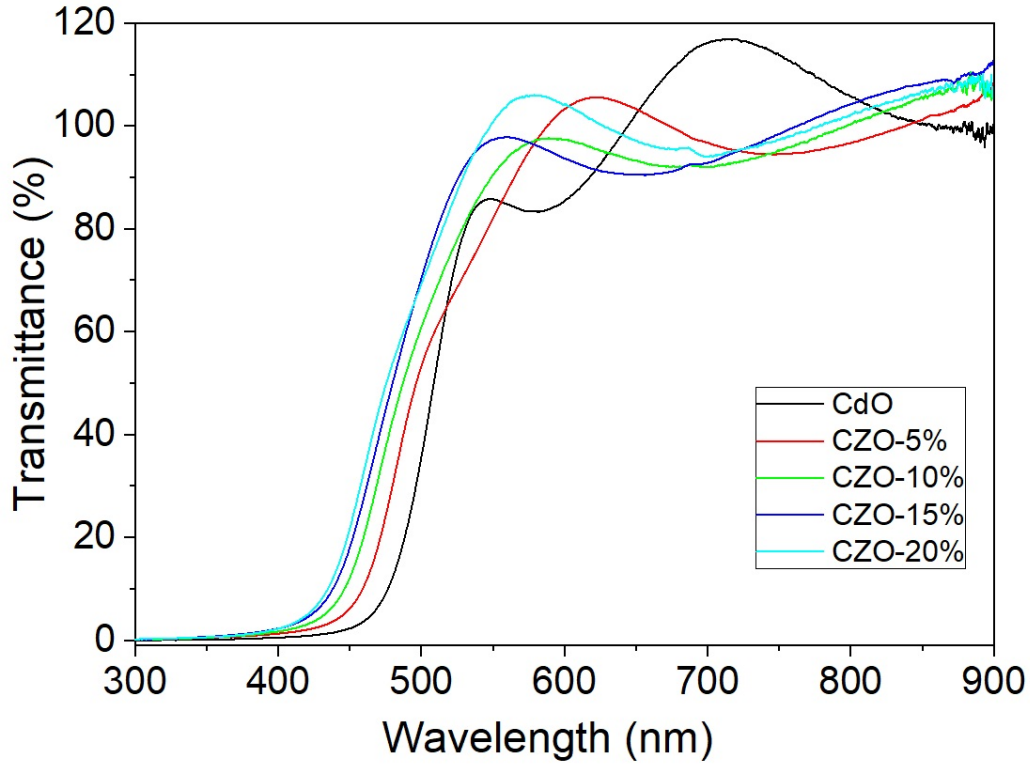


Figure 4.29: Room temperature normalized transmittance spectra of the CdZnO samples with a different nominal Zn content.

Typical absorption coefficient for $Cd_{1-x}Zn_xO$ series with the rising Zn content are shown in Figure 4.30 (a, b). The slope of the absorption coefficient of $Cd_{1-x}Zn_xO$ thin films with increasing Zn tends to blue shift, similar to those observed in the works of other authors [29,277]. To determine the optical band gap ($E_{g_{opt}}$) of compounds we used the 2 methods described in Section 3.5.1. We have applied the common expression valid for direct-gap and indirect-gap semiconductors (in case of CdZnO equation 3.29 for direct electron transition was used). Extrapolation of the linear part $(\alpha h\nu)^2 - h\nu$ dependence down to interception with the energy axis enables us to determine the band gap of the compounds as shown in Figure 4.30 (c, d). As can be seen from Figure 4.30 the introduction of Zn leads to an increase in the width of the optical band gap. The position of the energy axis intersection is clearly shifted toward higher energies with an increase in the Zn concentration from 2.53 to 2.76 eV, which means an increase in the incorporation of Zn atoms in the CdO lattice. At the same time, the sample, where Helium was used as a carrier gas, has a wider band gap. The ternary compound of CdZnO at low Zn concentrations can have an indirect band gap, due to properties of binary CdO. As already mentioned in Section 3.5.1, the normalization of the transmission spectra affects their slope and will distort the results of the determination when calculating using the method of constructing the tangent to the absorption spectra.

Chapter 4. Growth and characterization of ZnO, CdO, CdZnO, CdTe and their heterostructures

In the second method, in Figure 4.31 (a, b), it can be seen the influence of increasing of the Zn content in the CdZnO ternary compound leads on the absorbance. To estimate the approximate $E_{g_{opt}}$ value, the determination using the derivative of the absorbance spectrum was made. As can be seen from Figure 4.31 (c, d), the introduction of Zn leads to an increase in the $E_{g_{opt}}$ width. The position of the derivative peaks is clearly shifted toward higher energies from 2.60 to 2.81 eV, and, as in the calculations by the first method, similar as before the sample with He as carrier gas has higher value of band gap.

Comparing the results obtained by the two methods, it can be noticed that $E_{g_{opt}}$ calculated by the second method is wider by ~ 0.05 eV. This difference can be caused by the indirect band gap of CdO, which distorts the calculated data. Using different carrier gases should affect the thickness of the resulting films of the material due to the difference between Helium and Nitrogen in the coefficient of thermal diffusion and the probability of collisions. The thermal diffusion coefficient of Nitrogen is lower; also this gas has a higher collision probability than Helium in the gas phase. Based on these mechanisms, the average of deposition rate with Nitrogen were higher than with Helium, and therefore the material film should be thicker and favour the incorporation of Zinc, which corresponds to the results presented in the Table 4.1.

Figure 4.32 shows the value of the optical band gap as a function of the Zn content in the films calculated using EDX method. As seen from the curve of the figure the sample obtained with Helium contains more Zinc and therefore its band gap is wider since cubic ZnO has a higher energy of band gap than CdO.

Yu et al. [272] presented that the curves of transmittance spectra of $Cd_{1-x}Zn_xO$ layers showed over 80 % transmittance in the visible region, which corresponds to the range 70-90 % obtained by us. However, $x = 0$ and $x = 0.29$ had an absorption tail and a gentle curvature slope, respectively, indicating a deterioration of optical properties. Thus, the band gap energies according to the x composition ratio were distributed from 2.574 ($x=0$, CdO) to 2.892 eV ($x = 0.21$). However, the band gap energy of $x= 0.29$ was observed at a slightly smaller value of 2.834 eV due to the polycrystalline character of the sample. In our case, after an increase in the nominal value of Zinc by more than 15 %, the value of the band gap increases not so rapidly for both the sample obtained with Nitrogen as carrier gas, and for the sample obtained with Helium. The value of the band gap in the latter case will be 2.82 eV for the method of the tangent to the slope of the absorption spectra (or 2.87 eV for derivatives of absorbance spectra), which is comparable to the results described above.

4.2. CdZnO: morphological and structural study

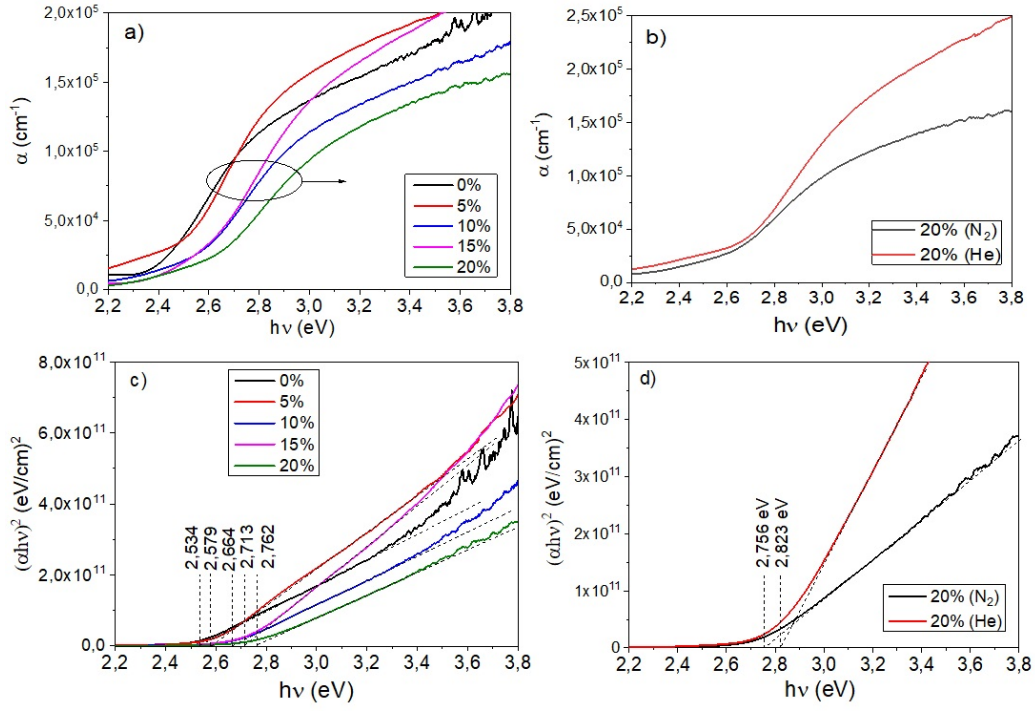


Figure 4.30: Absorption spectra (a, b) and $(\alpha h\nu)^2 - h\nu$ dependence (c, d) for series of $Cd_{1-x}Zn_xO$ samples that were used to determine the optical band gap.

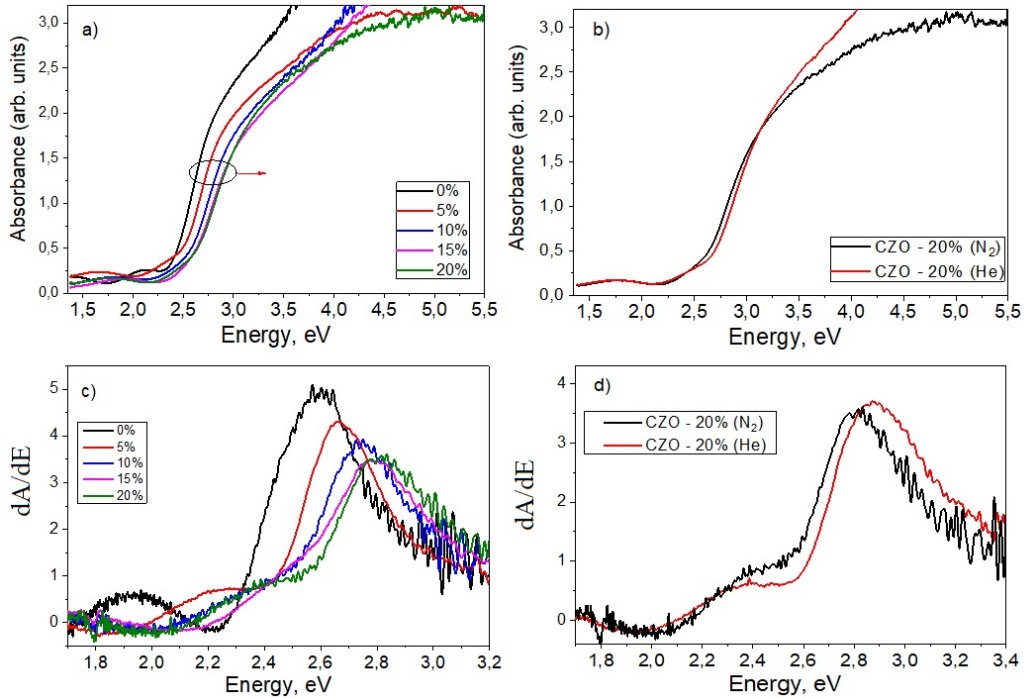


Figure 4.31: Absorbance spectra (a, b) and its derivative (c, d) that were used to determine the optical band gap of a series $Cd_{1-x}Zn_xO$ of samples.

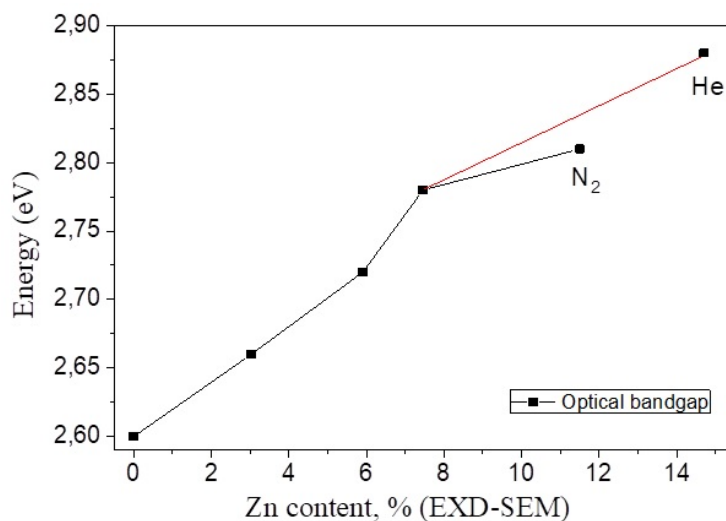


Figure 4.32: Optical band gap as a function of the *Zn* content in the films calculated using EDX method.

As can be seen, the ternary compound helps to solve the problem of obtaining high transmittance in the visible region for materials with insufficiently wide band gap. The limited transparency of CdO at shorter wavelengths is improved by alloying of films with Zn. In this case, the complexity of the problem of obtaining CdZnO will consist of competition between the symmetries of rock-salt (RS) and wurtzite (W). The study of the structure confirms the presence of both phases. (100) orientation dominates below the critical Zn content of less than 15 %; otherwise, phase mixing occurs, at the tops of the (100) planes observed the development of grains with the (111) orientation with rising the Zn content, the lattice parameter decreases and the band gap increases. At 20 % of the nominal Zn concentration, the final films have only about 10 % of real Zn content.

4.3 CdTe/CdO heterostructures

Often, to improve functional characteristics, heterostructures are used, which consist of layered structures of various semiconductors, differing in the band gap. Such a structure so-called heterojunction makes possible to efficiently control the mobility of charge carriers, their recombination, and also the light fluxes inside the heterojunction. In addition, each component plays an additional role in creating multifunctionality. Heterostructures represent an opportunity to manufacture efficient solar cells from highly absorbing thin-film materials without substantial losses through electron-hole recombination at the front surface. This is illustrated by the structures of the CdS/CdTe and CdS/CIGS solar cells where a wide-band-gap semiconductor (like CdS) serves as a “window” partner to a lower-band-gap “absorber” where most of the power is generated [278]. On the other hand, the CdTe/CdO system may be of interest due to its potential applications in short-wavelength optoelectronic devices [279]. However, the growth of high-quality CdTe/CdO heterostructures is very difficult because of the large lattice mismatch (38.4%) between both materials; therefore, the determination of the growth parameters at which the desired material properties can be obtained is an important task.

Despite the fact that there are many different methods for producing heterojunctions, MOCVD is one of the main ones. In this section, we present some of our structural and electrical results of obtained CdTe/CdO heterostructures with a smoother surface and preferred orientation [100]. Structural and morphological characterizations were carried out using SEM, AFM, and XRD research, and for electrical characterization KPFM was used.

4.3.1 Structural characterization

We have previously proved that R-plane (1 $\bar{1}$ 02) sapphire is well suited for the growing of $CdO_{(100)}$ and GaAs with orientation [100] is good to use for $CdTe_{(100)}$. In Figure 4.33, we see a diffraction pattern of CdO. The spectrum has 2 series of peaks, which correspond to sapphire (blue) and cubic CdO (red), respectively.

Before starting the study of the formation of heterostructures, we studied each of the layers separately using previous results of our scientific group [59, 180]. Following these studies the starting point for the CdTe growth was the temperature of 284 °C for the growth of CdTe on $GaAs_{(100)}$. Having a constant growth temperature value and changing the ratio of precursors from 0,12 to 1, we noticed that at a value of $R_{VI/II}=0.5$ the surface of the samples was flatter, and the CdTe films had (111) orientation, as shown in Figure 4.34.

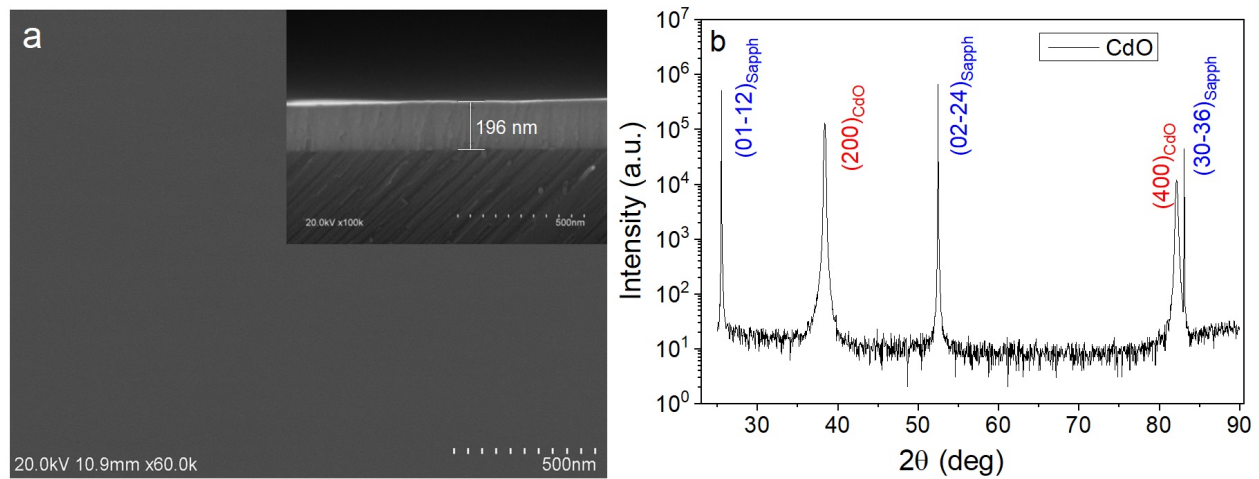


Figure 4.33: Cross-section of CdO film (a) and typical XRD patterns on CdO grown onto R-sapphire.

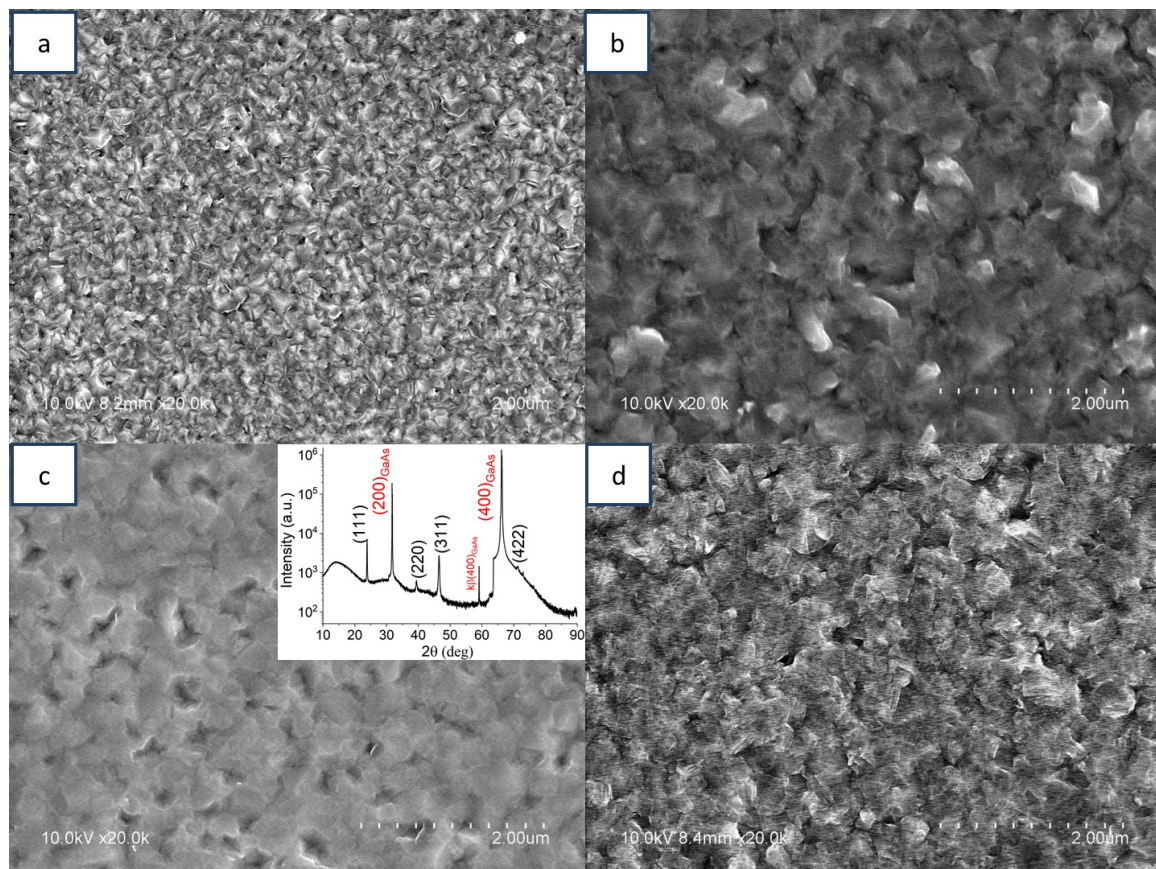


Figure 4.34: Surface morphology of CdTe grown on GaAs at 284 °C with different VI/II molar ratio: 0.12 (a); 0.28 (b); 0.5 (c); 1 (d). Thickness of the samples were 190 nm, 400 nm, 650 nm and 1 μm , respectively. The insert is the XRD pattern of typical CdTe obtained in position *FC* with VI/II molar ratio ~ 0.5 .

4.3. CdTe/CdO heterostructures

Leaving the value of $R_{VI/II}$ unchanged at 0.5, the growth temperature was varied in the range of 284-380 °C with increment of 10 °C. As can be seen from Figure 4.35, with an increase in temperature, the surface morphology becomes more uniform, but at 340 °C, pyramidal structures begin to appear, which disappear at temperatures above 360 °C. At the same time, in the temperature range of 340-360 °C, the thickness of the films slightly decreases in comparison with other temperatures. XRD studies show that the peaks (111), (311), and (511)/(333) correspond to $CdTe_{(cub)}$, as well as peaks (200) and (400), which belong to GaAs are seen at all range of growth temperature. Since the XRD pattern at 350 °C exhibits only peaks of the (100) family, this temperature was chosen for the growth. The pyramidal structure of the surface morphology observed at this growth temperature is typically related to the (100) orientation. The chosen temperature is in the middle of the growth temperature range at which we obtain a similar surface morphology. Micrographs of surface morphology and X-ray diffraction patterns are shown in Figure 4.36.

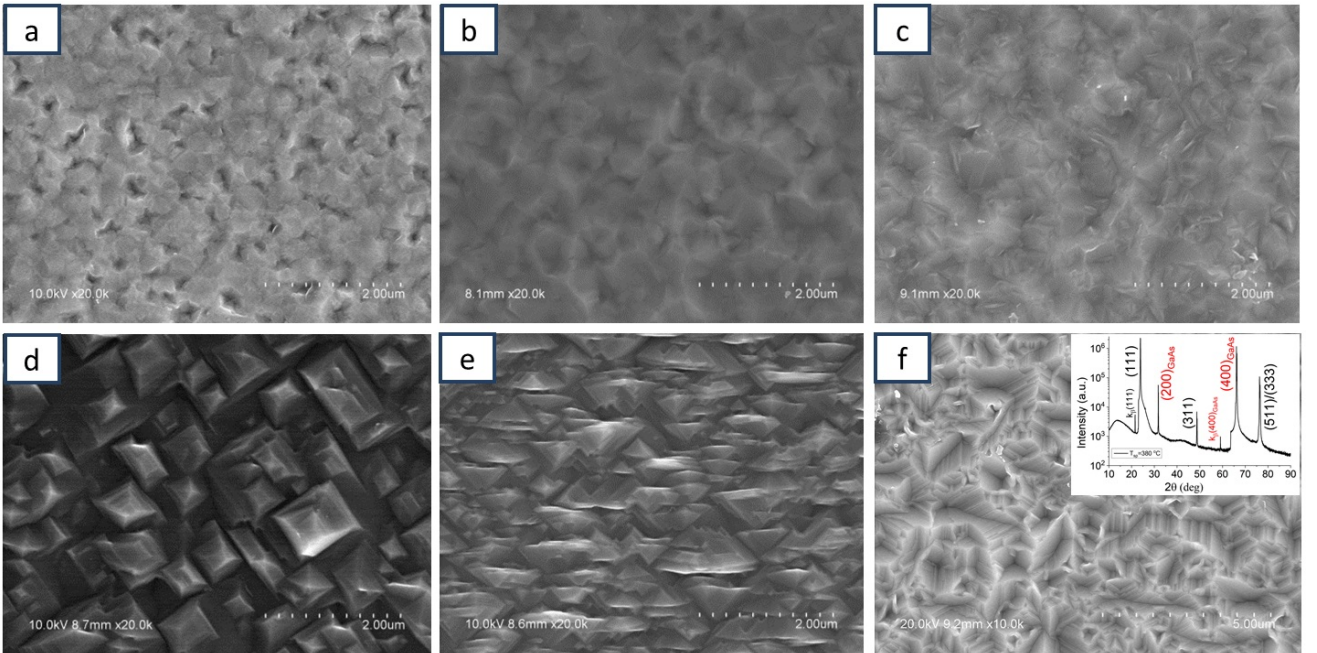


Figure 4.35: Surface morphology of CdTe grown on GaAs with VI/II molar ratio equal to 0.5 at different temperatures, °C: 284 (a); 304 (b); 320 (c); 340 (d); 360 (e) and 380 (f) Thickness of the samples 720 nm, 1 μ m, 1 μ m, 800 nm, 700 nm and 900 nm, respectively.

Using the Te/Cd precursors ratio at which the surface of the samples was flatter and more uniform ($R_{VI/II}=0.5$) and varying the value of time and temperature of growth, we conducted the growth of CdTe/CdO/R-sapphire (with VI/II molar ratio 0.5 and 2 for CdTe) and CdO/CdTe/GaAs heterostructures (with VI/II molar ratio 0.5 for CdTe). Growth time for CdO was 30 min and for CdTe - 60 min (Figure 4.37). In this case, if the CdO layer was

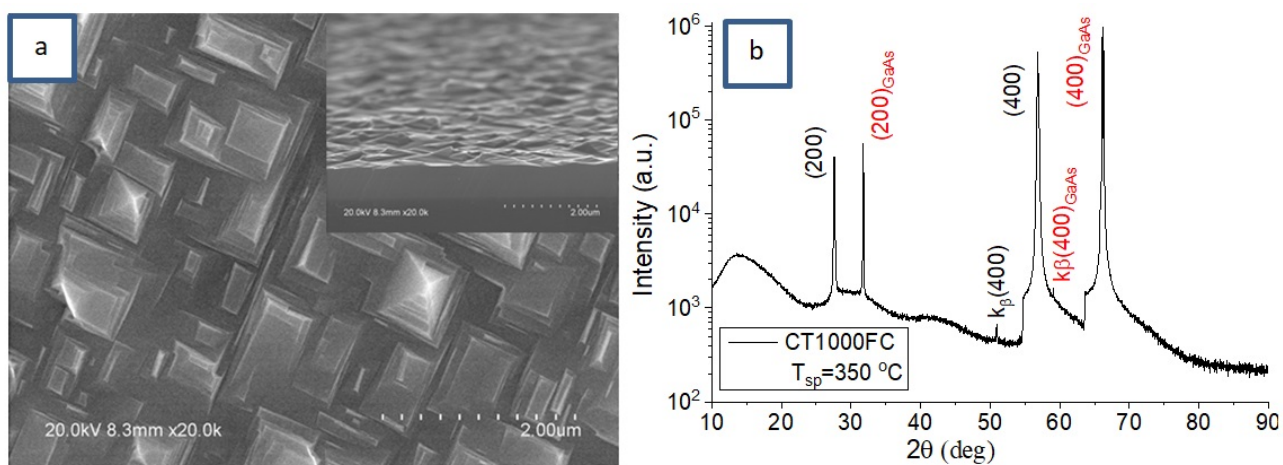


Figure 4.36: Surface morphology with cross section (a) and XRD patterns (b) of CdTe film deposited at 350 °C growth temperature on GaAs (100) substrate. Thickness of film was 750 nm.

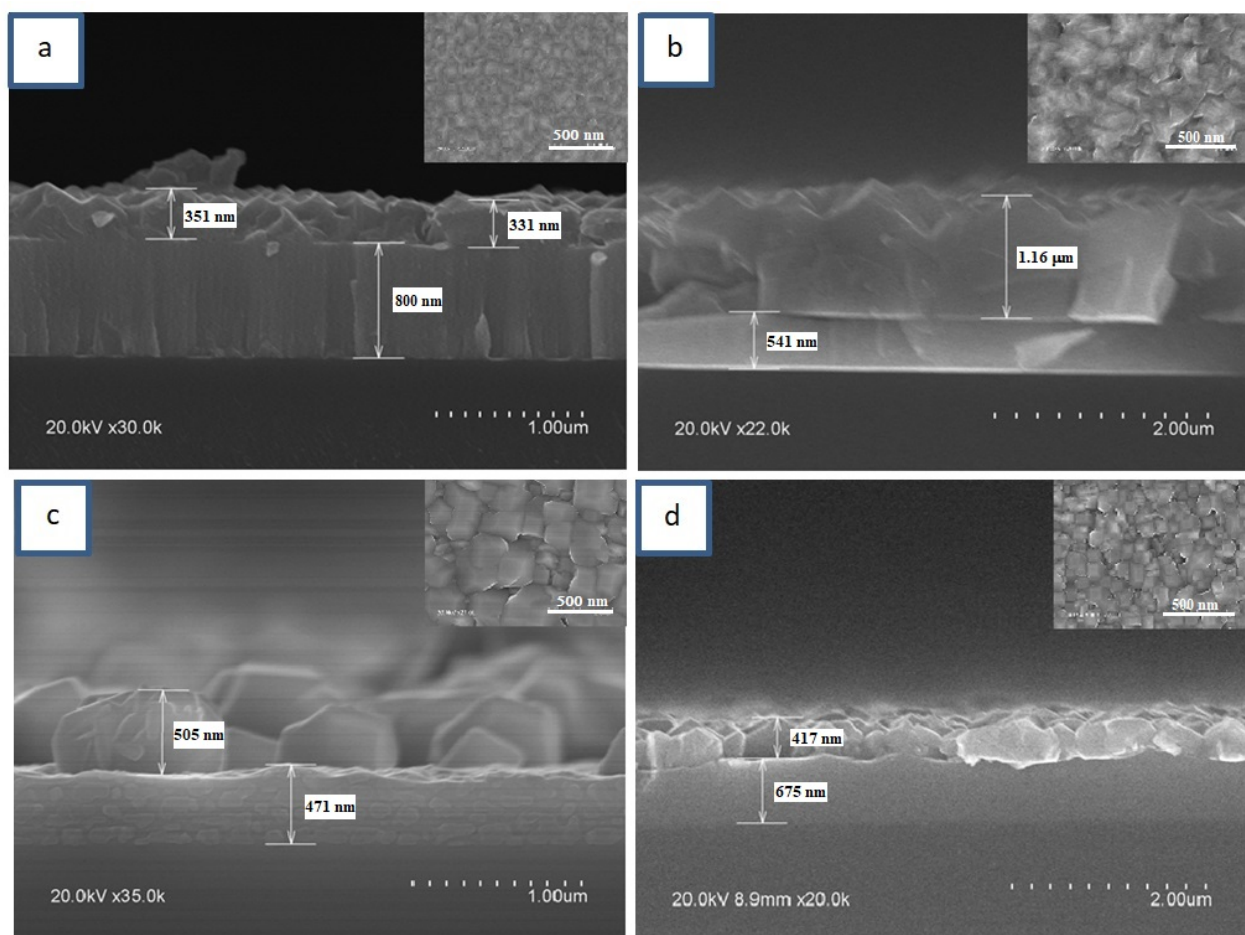


Figure 4.37: Surface morphology with cross section of CdTe/CdO (a, b) and CdO/CdTe (c, d) heterostructures grown into R-plane sapphire (a, b) and GaAs (c,d). VI/II molar ratio was: 0.5/5 (a); 2/5 (b); 5/0.5 (c and d)

deposited on the R -plane sapphire, then N_2 was used as the carrier gas, and H_2 was used for the CdTe layer grown onto GaAs substrate. This was done because it was previously found that this choice is better for CdTe films' growth. It was found that an increase in the Te ratio leads to an increase in the thickness and roughness of the film. It is worth to note that, we could not get flat heterostructures with orientation $[100]$. If the bottom CdO layer had orientation $[100]$, top layer was no flat and had orientation $[111]$ or both.

Thus, we carried out the growth of heterostructures in 2 steps, where the layer of CdTe was deposited onto the surface of CdO film previously grown on sapphire substrate. The first step consisted of the growth for a short time at a lower temperature to increase the density of nucleation points, while the second step we maintained a higher temperature, which should provide us obtain layers that meet our structural requirements.

A series of CdTe/CdO heterostructures were grown, where the CdTe layer was deposited during 60 min on a smooth $CdO_{(200)}$ layer preliminarily grown on R-sapphire. Firstly, layers were grown with reduced temperature during 2,5 min at 295 °C and later deposition temperature was increased in the range of 330-370 °C with an interval of 10 °C. Other experimental parameters for obtaining the samples are shown in Table 2.7. All samples had rough surface morphology with thickness in order 220 nm for 330 °C and 300-330 nm for the rest temperatures (340-370 °C). At lower temperature, the surface processes take place slower due to the velocity of the surface reaction, which is sensitive to temperature; therefore, the growth process is kinetically limited by the surface reaction (see Section 2.4.1). XRD studies have shown that in the obtained heterostructures, the CdTe layer had both (200) and (111) orientations. The reason for this behavior is related with the mismatch between the lattice parameter of CdO (4,69 Å) and CdTe (6,49 Å). Typical surface morphology and XRD pattern of CdTe/CdO heterostructure are presented in Figure 4.38 and growth results are shown in Table 4.2

As in previous experiments, although the lower layer had the orientation $[100]$, we could not obtain the upper layer with the same orientation. A comparison of the XRD intensities of the $CdTe_{(400)}$ and $CdTe_{(111)}$ peaks showed that the highest ratio R of 0.637 was obtained at 350 °C and decreased with increasing or decreasing temperature (Table 4.3).

The AFM characterization was used to study the surface morphology in more detail. Samples were measured at several points. The average rms roughness value for each sample was taken. Some measurements were duplicated one day after for comparison of results. All samples showed values in the range 45 ± 10 nm. Typical roughness distribution presented in Table 4.3.

Figure 4.39 (a) and (b) shows the topographic image and the contact potential difference (CPD) of the site with the same surface area for the sample grown at 350 °C, which were measured simultaneously. CPD implemented between the tip of the microscope needle and the sample surface using the Kelvin probe force microscopy (KPFM) on base on the AFM described above. The main task of measuring this series of samples was to determine a difference in the

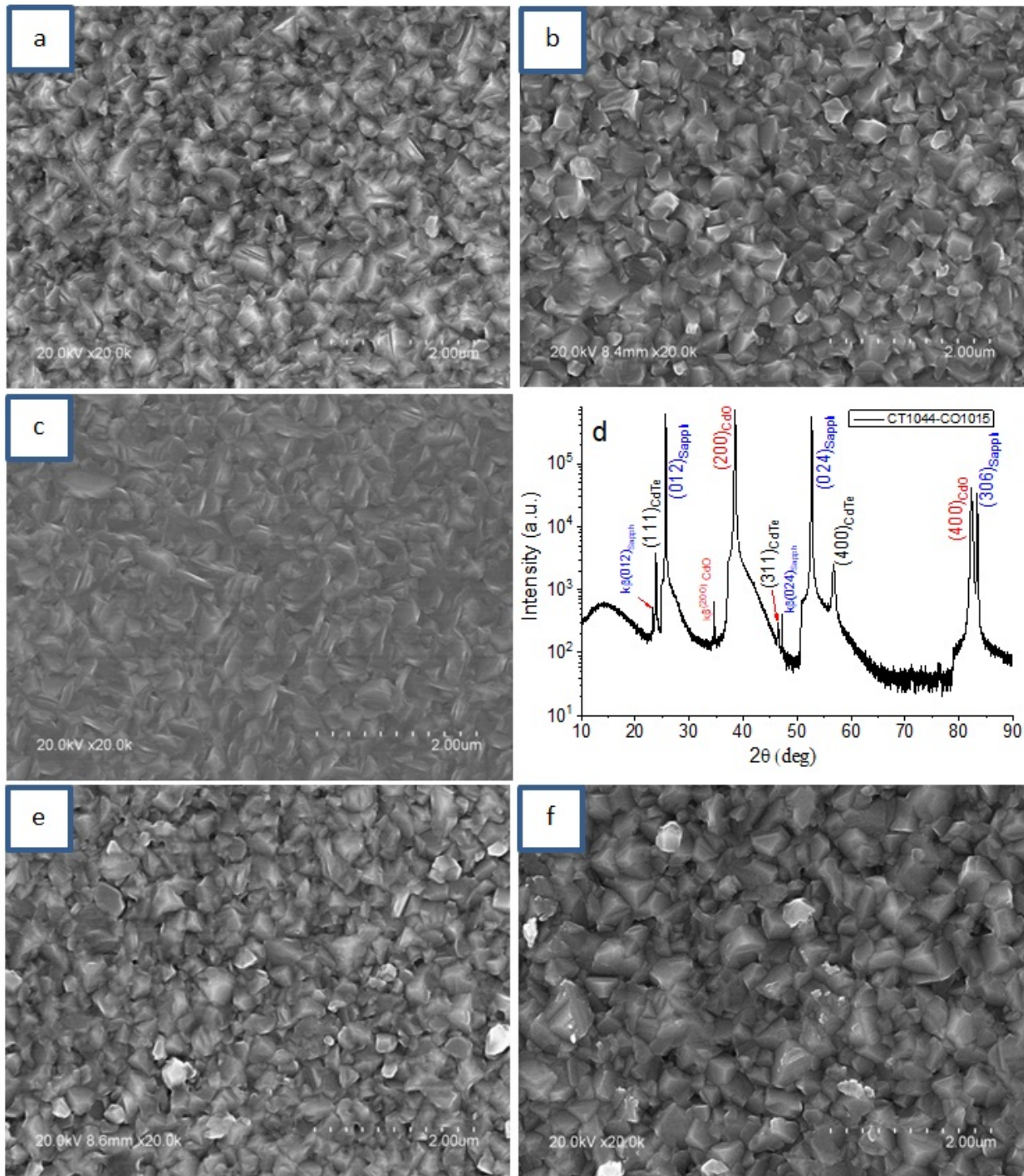


Figure 4.38: Surface morphology of CdTe/CdO heterostructures grown into GaAs substrate with different 2nd step growth temperature, °C: 330 (a); 340 (b); 350 (c); 360 (e); 370(f). In Figure (d) presented XRD pattern of the sample grown at 350 °C.

4.3. CdTe/CdO heterostructures

Sample	1 st step			2 nd step		Crystal orientation
	t_{growth} , min	T_{SP} , °C	Ratio (VI/II)	t_{growth} , min	T_{SP} , °C	
CO1012	15	304	5			(100)
CT1046					330	(111), (100)
CT1052					340	(111), (100)
CT1044	2.5	295	0.5	57.5	350	(111), (100)
CT1055					360	(111), (100)
CT1048					370	(111), (100)

Table 4.2: The main parameters of the growth of the heterostructure CdTe/CdO

Sample	Second step temperature, °C	CdTe(400)/CdTe(111)	Roughness, nm	CPD (FWHM), mV
CO1012			8	768 (63)
CT1046	330	0.065	45±5	150 (69)
CT1052	340	0.184	50±10	28 (44)
CT1044-01	350	0.637	45±5	219 (73)
CT1044-08			40±10	160 (74)
CT1055-01	360	0.316	40±5	50 (94)
CT1055-12			30±5	-72 (51)
CT1048-09	370	0.198	90±5	599 (195)
CT1048-21			60±10	321 (40)

Table 4.3: The main parameters of growth and data obtained using KFPM method.

work function of the samples in dependence of the surface morphology. This information will be important if this heterostructure will be used in the development of electronic devices and it will be necessary to form metallic electrodes for contacts. Samples were measured on the top of CdTe layer of heterostructure at several points. In Figure 4.39 (b), bright and dark areas associated with higher and lower surface CPD zones, respectively, can be distinguished.

From a comparison of both images, a clear correlation was established between the morphological faces and the surface CPD. Differences in CPD can be attributed to changes in surface charge density. Although the faces belong to the same crystallographic family, they are not electrically equivalent.

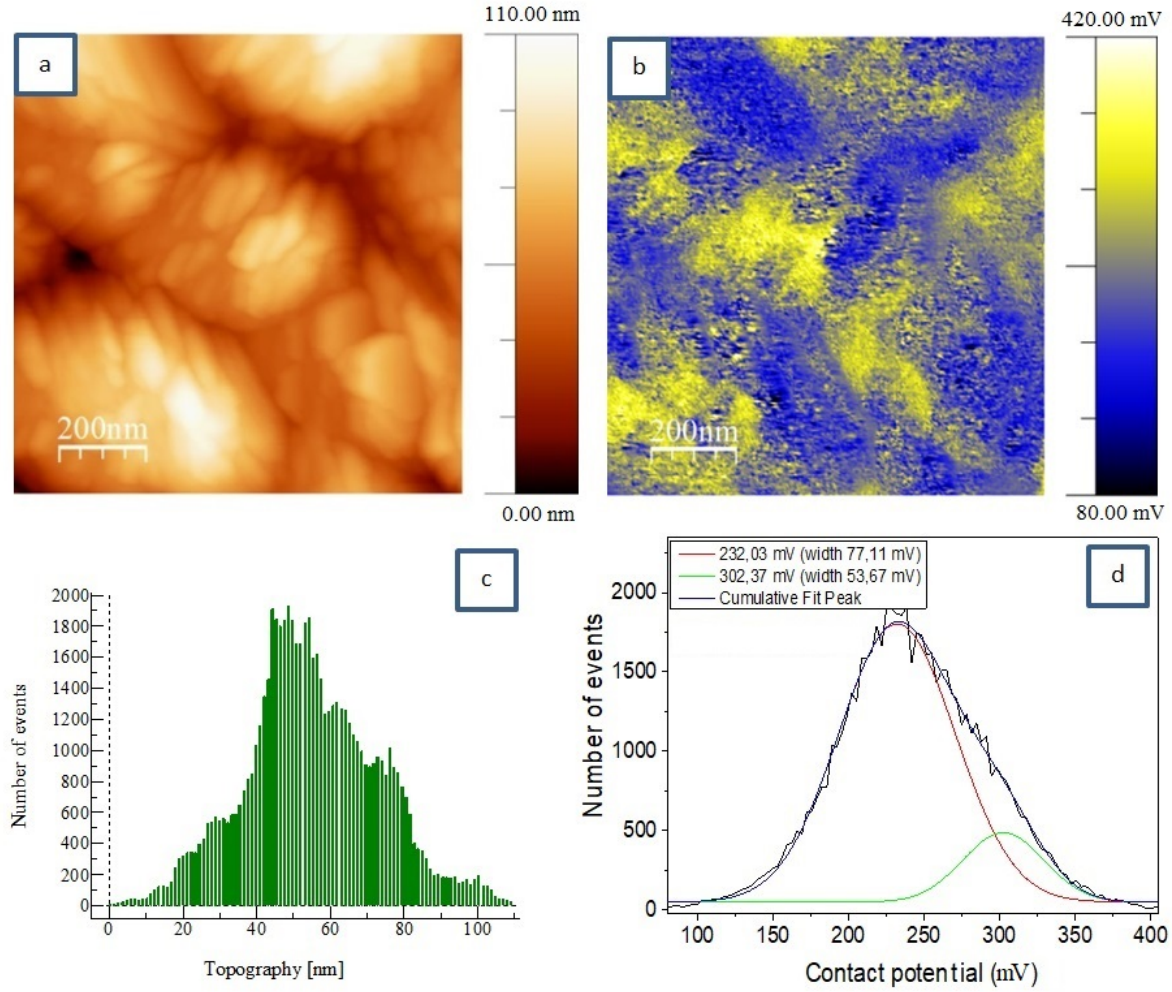


Figure 4.39: Typical AFM image (a) and Δ CPD map for CdTe surface of CdTe/CdO heterostructure (b). Distribution of roughness size (c) and distribution of potential (d) in different part of CdTe surface ($T_{growth} = 350\text{ }^{\circ}\text{C}$).

To determine the different charge regions present in the sample, the distribution of the surface contact potential within the region of Figure 4.39 (b) was measured, as shown in Figure 4.39 (d). The distribution shows only two peaks centered around +232 mV and +302 mV relative to the average surface contact potential of the entire image (Table 4.3). The width of the distribution peak is due to boundary effects and/or sample inhomogeneities. At the same time, the differences in CPD are larger than the typical noise of these measurements (20 mV) and therefore they cannot be artefacts. Therefore, only two types of “charge domains”, with an average surface contact potential difference of 70 mV, are present in the sample. Tennyson [280] claims that local variations in the open-circuit voltage (V_{OC}) are due to the fact that different grain orientations can act as distinct centers for recombination within the material. For CdTe surface different grain interfaces showed different V_{OC} .

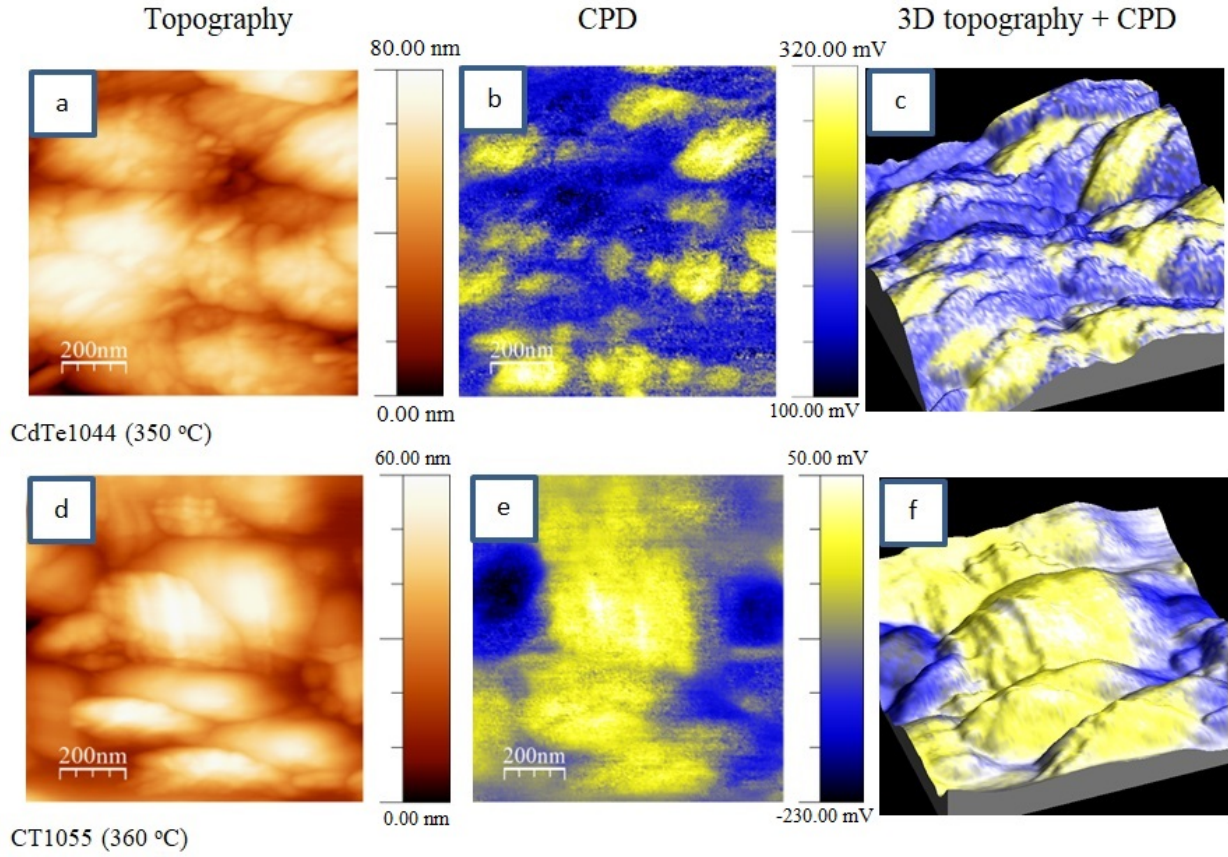


Figure 4.40: Topography of surface (a, d), CPD map (b, e) and 3D model of CPD distribution on the sample surface (c, f).

To know how the surface morphology affects CPD, we built a 3D model where the distribution of the potential over the surface was superimposed on the surface structure itself (Figure 4.40). As can be seen from the obtained image, the top of the grains has a higher value of CPD than the grain boundaries (GBs) between them. This may indicate the absence of significant recombination, which is explained by inversion in the GB core [281]. Changes in GB core currents can be attributed to changes in the GB band bending. Such changes may be due to differences in oxidation state between GB. In addition, it is likely that differences in measurement geometry due to surface roughness and physical dimensions of the AFM tip cause some variability between GB.

4.3.2 Parameters for the growth of heterostructures

Since the deposition of the material for a long time with a preliminary decrease in temperature at the first step for the formation of nucleation points did not allow to obtain CdTe/CdO/*R*-sapphire heterostructures with relatively smooth surfaces and a preferred orientation (100) of the upper CdTe layer, which would repeat the film's orientation of the CdO layer, it was decided to change the growth parameters. Therefore, the preparation of CdTe films on the CdO surface was carried out in only one step with $R_{VI/II}=0.5$, and the growth time decreased to 5 min. The final CdTe film hadn't a continuous layer, but only granules are formed, as presented in Figure 4.41 (a). Since these growth parameters of the film did not meet our expectations, the VI/II molar ratio was raised up to 4 without increasing the growth time (Figure 4.41 (b)). The deposited upper layer turned out to be very rough, and its thickness was 140 nm. Reducing the growth time to 1.5 min only reduced the layer thickness and did not allow making the surface more uniform Figure 4.41 (c).

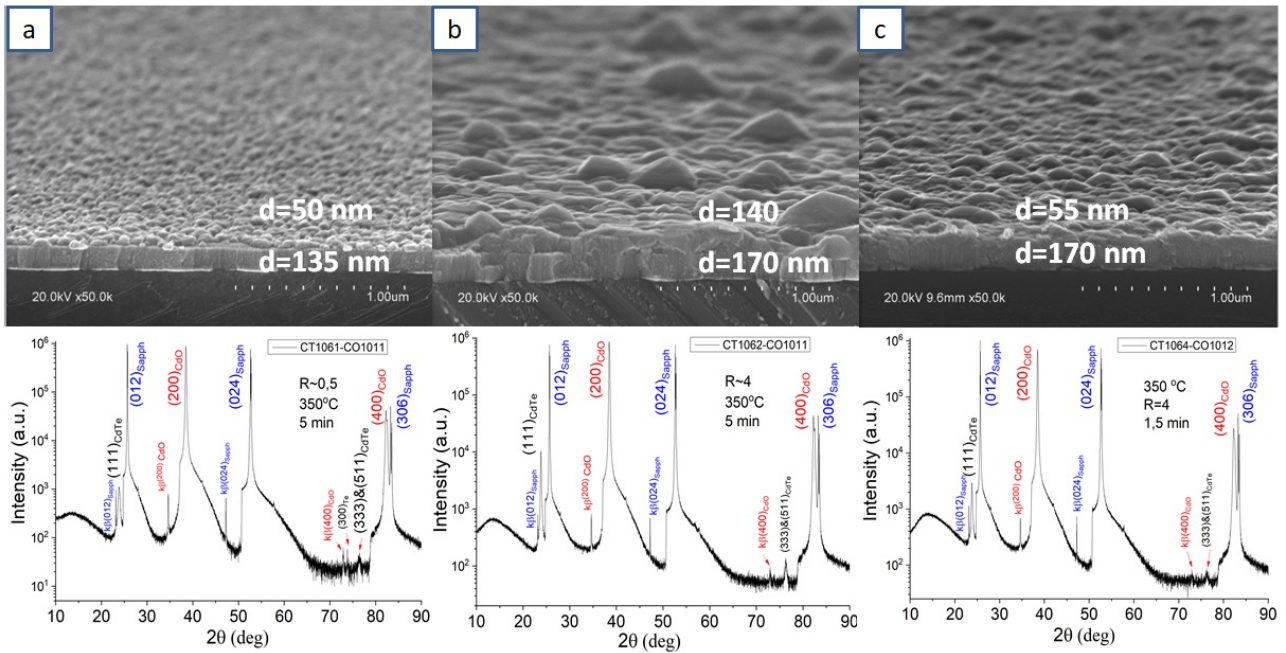


Figure 4.41: Surface morphology and X-ray patterns of CdTe/CdO/*R*-sapphire samples with shorter growth time and greater ratio: a) 5 min growth with $R_{(VI/II)}=0.5$; b) Increasing $Ratio_{(VI/II)}$ up to 4; c) Leaving the same $Ratio_{VI/II}$ but decreasing growth time to 1.5 min.

Expecting that a decrease in temperature would make possible to obtain a thinner CdTe film and a simpler surface morphology, it was decided to obtain the layer at a temperature of 295 °C with 1 min of growth time. This led to the formation of CdTe particles on the CdO surface, which did not completely cover the surface of the lower layer. An increase in the VI/II molar ratio up to 5.25 only made possible to obtain large particles. At an even lower temperature of 250 °C, no CdTe particles were formed on the surface even when the VI/II molar ratio was doubled to 10.5, as can be seen in Figure 4.42.

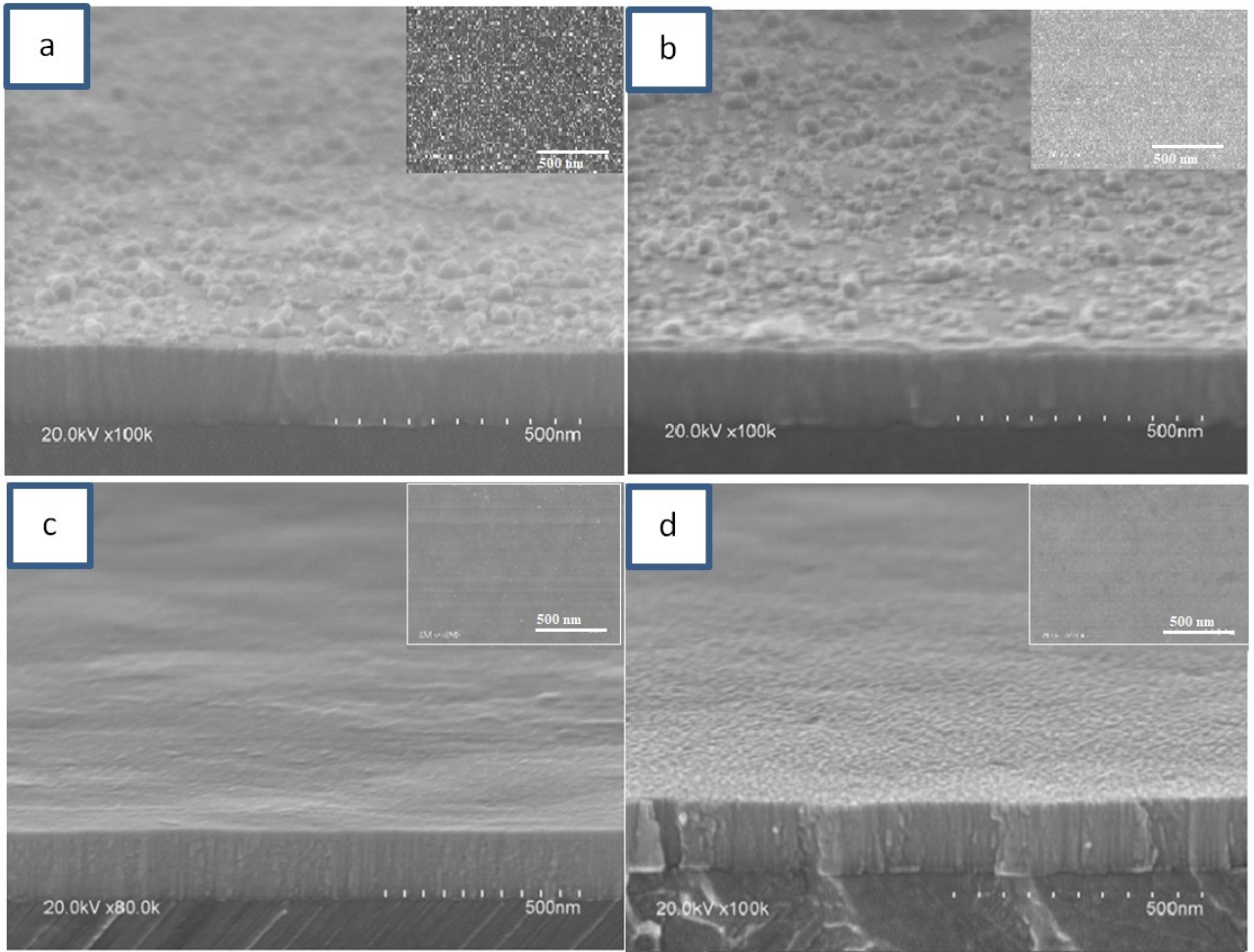


Figure 4.42: Surface morphology with top image (inlet part at the right side) of CdTe/CdO/*R*-sapphire heterostructures with 1 min of growth at 295 °C (a, b) and 250 °C (c, d) and with different VI/II molar ratio: *R*=4 (a); 5.25 (b and c); 10.5 (d).

Chapter 4. Growth and characterization of ZnO, CdO, CdZnO, CdTe and their heterostructures

Since the low growth temperature with a high VI/II molar ratio did not allow to produce of CdTe, in order to solve this problem, it was decided to return to the 2-step growth of the upper layer. First deposition step was carried out for a short time in 1 min with low temperature at 250 °C to increase the density of nucleation points and then passed evaporation of only one of element at higher temperature 295 °C during 6 min. In the case when only the DIpTe precursor was supplied in the second step, the deposited film had a no smooth surface morphology and a high thickness up to 100 nm. On the other hand, when only DM Cd was used, solitary CdTe particles formed on the surface, which did not completely cover the lower CdO layer. The results are shown in Figure 4.43.

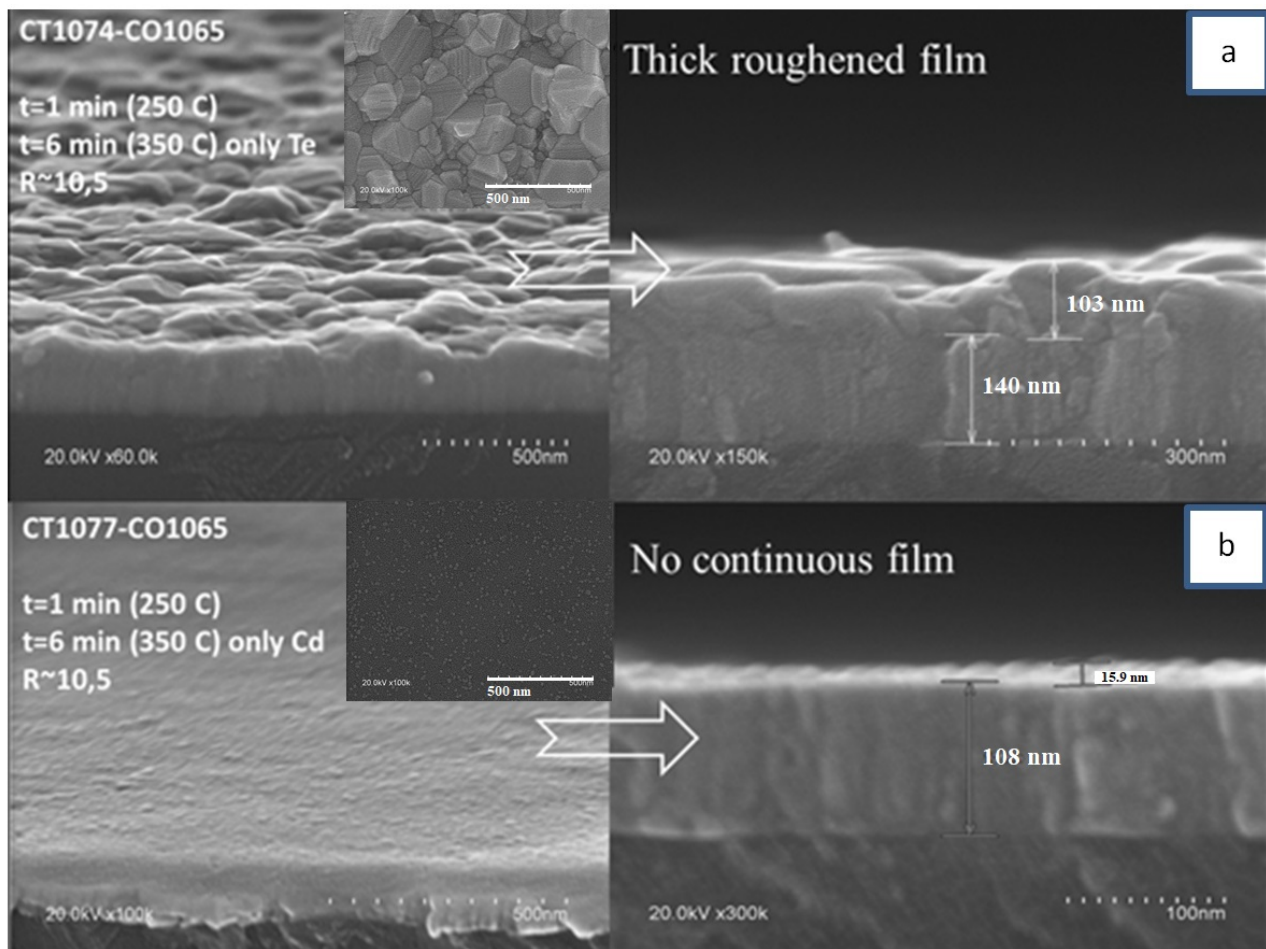


Figure 4.43: Two-step growth of CdTe layer of CdTe/CdO/R-sapphire heterostructures with a Ratio~ 10.5: a) Te precursor only; b) Cd precursor only.

None of the growth parameters considered above made possible to obtain a thin continuous CdTe layer with a relatively uniform smooth surface. Developing the idea of obtaining the top layer at a low temperature of 250 °C, single-step growth with growth time increased to 3 min was performed. Finally sample with a relatively continuous CdTe upper film about 30 nm thick was obtained. It can be seen in Figure 4.44 that the surface morphology is islands that are closely spaced.

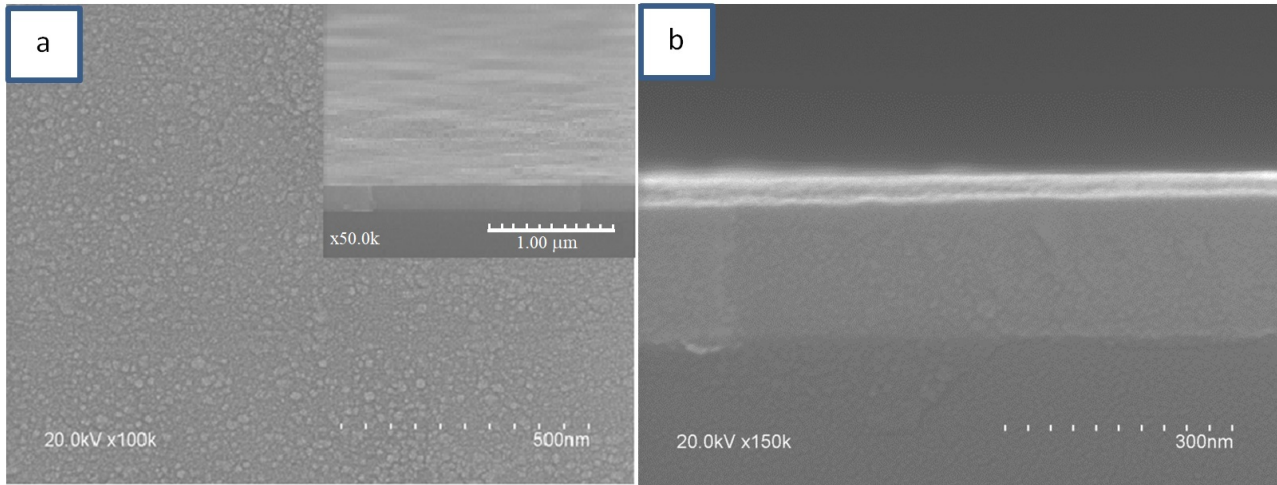


Figure 4.44: Surface morphology with tilted cross-section view (a), and films thickness determination (b) obtained for sample with a relatively continuous film.

4.3.3 Electrical characterization

The morphological and structural features of CdTe/CdO heterostructure are still largely unexplored. Methods such as atomic force microscopy (AFM) and Kelvin probe force microscopy (KPFM) allow research to be done at the nanoscopic level. Since surface defects of films can affect the surface potentials and the rate of recombination of charge carriers, the study of the magnitude of the surface potential depending on the surface morphology for different illumination power may be of scientific interest.

To conduct surface photovoltage (SPV) studies for a series of samples in the temperature range 330-370 °C we used the same AFM equipment, which system parameters for SPV measurements described in Section 3.6.4. The SPV is defined as the light-induced variation of the surface potential, in other words, the potential difference with and without irradiation [282]. Surface potential Vs what is the energy difference between the bottom of the conduction band at the surface and the bottom of the conduction band in the semiconductor bulk was measured. Due to the different signs of the equilibrium surface potential, the SPV is positive in n-type semiconductors and negative in p-type semiconductors [282]. The investigation of the local range of the samples showed that dark and light lines on the Kelvin map what corresponds to grains and hollows on the samples, respectively, are less informative. More distinct results of SPV presented plane parts of samples. SPV variety as a function of the light irradiation presented in Figure 4.45.

When the light power of the incident radiation decreased, the SPV value also decreased accordingly, as shown in the Figure 4.45. The calculated measurement values with a lamp power of 100 W for other samples are presented in Table 4.4.

Some samples were re-measured after several days to confirm the results and exclude the influence of the instrumental factor. Depending on the results obtained, the samples were divided into 3 groups:

- $SPV > 0$: 350, 370 °C;
- $SPV \approx 0$: 360 °C;
- $SPV < 0$: 330, 340 °C.

The difference in the SPV values may be due to the different surface morphology of the CdTe/CdO heterostructures, depending on the growth temperature. As mentioned in Section 4.3.1, at the temperature range 340-360 °C, the surface morphology of the samples had a pyramidal structure, which could affect the distribution of photons during irradiation of the samples.

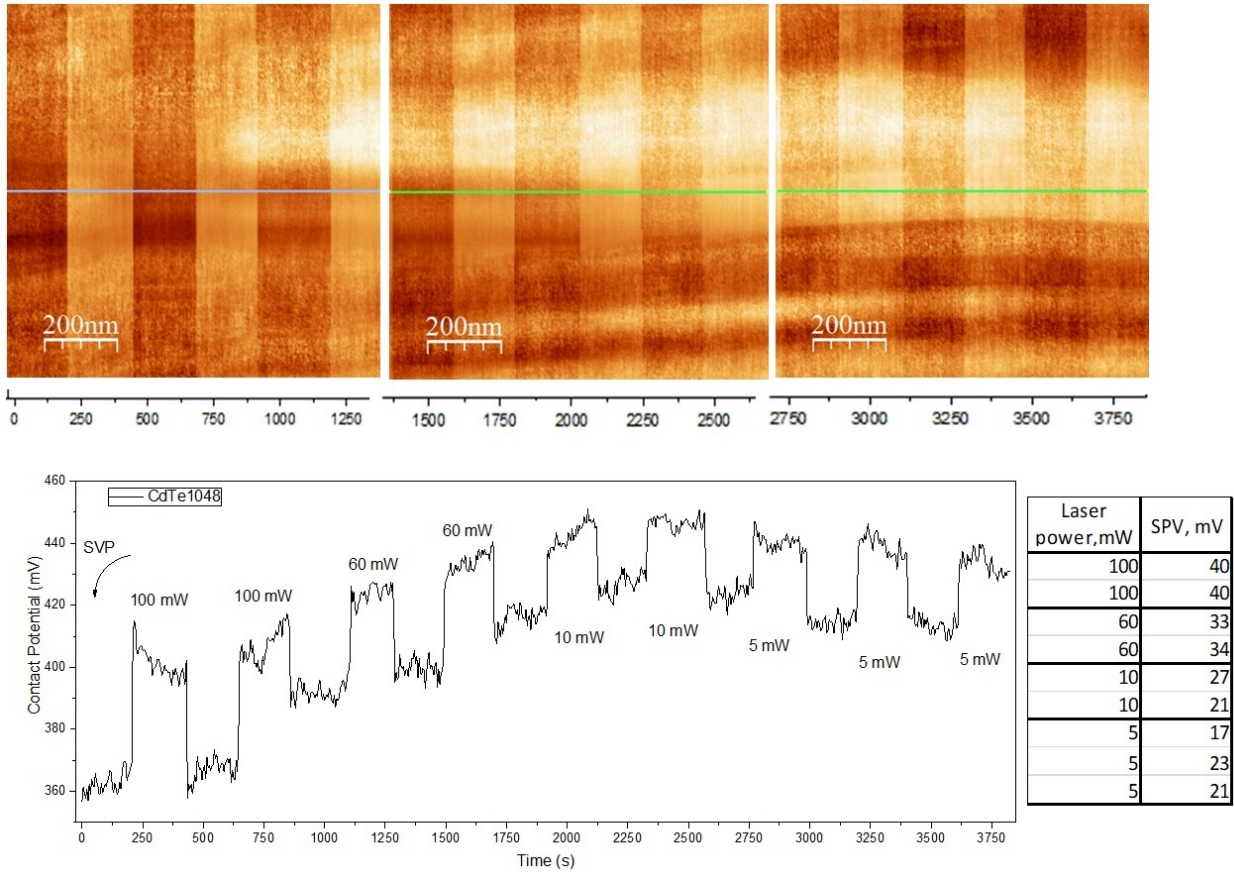


Figure 4.45: SPV distribution as a function of an applied power of laser with and without illumination obtained for sample CdTe1048 (370 °C)

Other reasons affecting the distribution of SPV are:

- At photon energies larger than the band gap a saturation value should be reached by the SPV value, but often strong electron-hole recombination at the surface significantly reduces the SPV.
- Photocarriers can also contribute to a change in tip-sample capacitance as the result of photon-generated charges in the sample or tip. A change in the capacitance gradient can lead to a potential systematic error in SPV measurements using KPFM techniques, as was shown in [283].
- Although XRD measurements showed peaks related to the composite materials of the heterostructure, in air-exposed surfaces a thin oxide layer is expected to be formed. Adsorption of oxygen may produce a TeO_2 layer. Adsorbed oxygen results in the formation of Cd and or Te oxides, which also produce surface states [284].

Chapter 4. Growth and characterization of ZnO, CdO, CdZnO, CdTe and their heterostructures

Sample	Second step temperature, °C	CdTe(400)/ CdTe(111)	CPD (FWHM), mV	SPV (100 W), mV
CO1065			768 (63)	
CT1046	330	0,065	150 (69)	-11
CT1052	340	0,184	28 (44)	-4
1044	350	0,637	219 (73) 160 (74)	10 10
1055	360	0,316	50 (94) -72 (51)	2 2
1048	370	0,198	321 (40) 440(61)/ 490(41)	40 30

Table 4.4: Data obtained using the KFPM method with a 633 nm laser and other results for films obtained with different growth temperatures.

As can be seen above, the growth conditions of CdTe/CdO compounds affect the structural state, optical and electrical properties of the material. An in-depth study of the growth, as well as the characteristics of the materials being studied, allows selecting the growth parameters for obtaining compounds with a good crystalline quality, which increases the possibility of their use in various fields of electronics. Since, over the past decades, the problem of obtaining and studying of CdTe/CdO compound was considered only in a few papers and CdTe/CdO heterostructures obtained by the MOCVD method almost were not reported, this work was supposed to show the complexities of obtaining and characterizing heterostructures. Research has shown that it is difficult to grow good compounds with a planned flat surface, not only because of the lattice mismatch, but also not easy selection of growth parameters. Because of the surface relief, the distribution of the surface potential is not uniform, which could affect the properties of the build device based on that heterostructure.

Chapter 5

Effect of Mn alloying on structural and optical properties of ZnTe and ZnS thin films

In this chapter we are going to present the influence of the alloying of Mn on the structural and optical properties of the binary compounds ZnS and ZnTe deposited by the close-spaced vacuum sublimation method onto glass at different growth conditions. The morphology of the surface, preferred orientations, grain size and density, lattice parameters, spectral dependences of the transmittance $T(\lambda)$, reflectance $R(\lambda)$ and the absorption $A(\lambda)$, as well as the optical band gap (E_g) for each material were measured and the corresponding parameters calculated.

5.1 Structural and morphological studies of $Zn_{1-x}Mn_xTe$ thin films

5.1.1 Morphological study

Magnetic and optoelectronic properties of materials depend strongly on structural and substructural characteristics. Lattice deformations and extended defects such as grain boundaries and dislocations affect the crystalline quality and can dramatically change material's properties. The knowledge of the structural and substructural characteristics can allow not only the work to the optimization of growth parameters, but also the selection of specific samples having the desired characteristics (crystallite size, dislocation content) for high quality technological devices.

Morphology of the samples was studied through scanning electron micrographs by using a Hitachi S-4800 microscope, described in Section 3.1.3. Figure 5.1 depicts the SEM micrograph

Chapter 5. Effect of Mn alloying on structural and optical properties of ZnTe and ZnS thin films

of $Zn_{1-x}Mn_xTe$ alloyed films with nominal 5 % of Mn grown over glass at different substrate temperatures during 10 min. It is worth to note that growth temperature will also act on the Mn content as we will see later. Grains in the range from 600 to 800 nm with a density $2 \times 10^{12} - 1 \times 10^{12} \text{ NPs/m}^2$, respectively, can be observed at the selected substrate temperature. The grains seem to be randomly distributed, without any organization over the substrate.

Studies have shown that a thin-crystalline transition layer was formed, followed by the growth of crystallites oriented in the plane (111) parallel to the substrate. It should be noted that the stage of nucleation is forced because it is associated with an unfavorable process of formation of a new interface - the interface between the new phase and the medium in which this phase arises. To do this, it is necessary to perform a certain work, that is, to overcome some energy barrier, after which the system already spontaneously passes into a thermodynamically equilibrium state with the formation of macroscopic components. The cross sectional study of samples shows that at high substrate temperatures there is a transit from the growth of long to small columns. This fact is due to the very rapid growth of crystallites oriented by (111) plane parallel to the film surface. As a result, an axial texture [111] of film growth was formed, perpendicular to their surface.

The thickness of the samples at lower temperatures 623-723 K (350-450 °C) was $2.5 \mu\text{m}$, and with increasing temperature, this value first decreased to $2.15 \mu\text{m}$ at 773 K (500 °C), then to $1.9 \mu\text{m}$ at 823 K (550 °C). At higher temperatures, the film thickness increased to $2.8 \mu\text{m}$, which could indicated rapid columnar growth of crystallites.

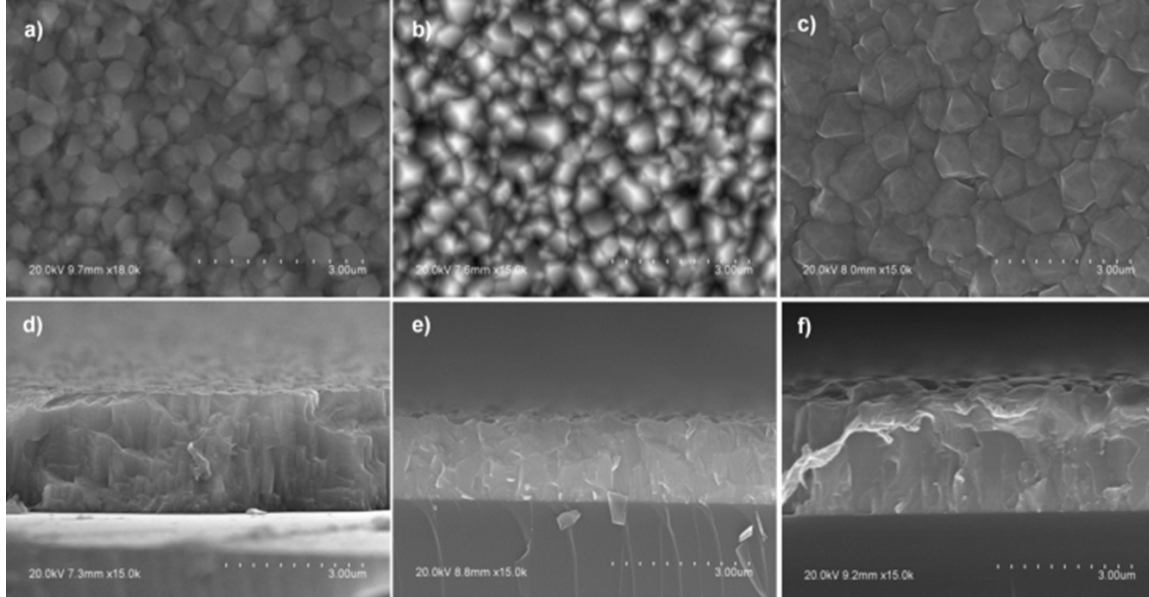


Figure 5.1: Top (upper) and cross-sectional (lower) SEM images obtained from the $Zn_{1-x}Mn_xTe$ films with 5% of nominal values of Mn deposited over glass at various substrate temperatures: (a, d) $T_s = 623 \text{ K}$ (350 °C); (b, e) $T_s = 773 \text{ K}$ (500 °C); (c, f), $T_s = 923 \text{ K}$ (650 °C).

Crystalline grains in the nano and submicron range are constituted by several crystallites, defined also as single regions separated by grain boundaries [285]. Consequently the obtained values from SEM images can only be considered as values related to the overall size of the particle, the homogeneity of films, the absence of cracks, holes, etc. If they have a single or polycrystalline structure can be only assessed by XRD and/or HRTEM measurements, as we will present in Section 5.1.6

5.1.2 Lattice constant and Mn content

The crystalline quality of an alloyed material generally decreased as a consequence of the incorporation of foreign elements into the host. Therefore, we used XRD measurements (see Section 3.4.1) to assess the degree of distortion in the parent lattice which additionally affect the substructural characteristics of the material. Figure 5.2 shows conventional 2θ - θ patterns from $Zn_{1-x}Mn_xTe$ films grown at different substrate temperatures. Diffraction peaks indicate that all samples have cubic structure with an apparent (111) preferred orientation as found also by other authors [286]. No diffraction peaks of extraneous phases were found, suggesting that Mn^{2+} ions substitute into the Zn^{2+} sites. The positions of the diffraction peaks are near to the ones corresponding to the crystallographic card of ZnTe (JCPDS-ICCD No 00-015-0746).

The lattice parameter for each sample was obtained by plotting the diffraction order ($h^2 + k^2 + l^2$) versus $2 \sin \theta / \lambda$ where θ is the Bragg angle and λ the wavelength of the X-ray beam. Calculated values of the lattice parameter as a function of the substrate temperature are shown in Table 5.1 and Figure 5.3 (a). It is observed that the lattice constant at a substrate temperature of 623 K (350 °C) is larger in respect to the value indicated ZnTe in the crystallographic card, being this enlargement indicative of the Mn incorporation. However, this incorporation decreases as the substrate temperature increases and it could be due to re-evaporation of Mn at higher temperature or non incorporation, as it will be discussed later. It can be seen from the Figure 5.3 that the lattice parameter calculated for the samples at growth temperatures more than 500 °C (773 K) does not change, in fact the calculated lattice parameter coincides with the values for ZnTe, which means the absence or reduced Mn incorporation into the samples.

The effect of Mn atoms on the ZnTe lattice can be analysed from a comparison among ionic radii. The ionic radius of Zn^{2+} ions is 88 pm but the one of Mn depends on the coordination number and the spin states of the ions [287]. The crystal ionic radius of Mn^{2+} ions for the low spin state is 81 pm and for the high spin state is 97 pm. The experimental large value of the lattice constant with the presence of manganese can suggest that the Zn^{2+} ions are partially substituted by the bigger Mn^{2+} ones, that is, those with a high spin state. The increase of the lattice constant with the Mn content has been found also by other authors during the growth of $Zn_{1-x}Mn_xTe$ ingots [288]. However a shortening has been also reported from ZnMnTe films

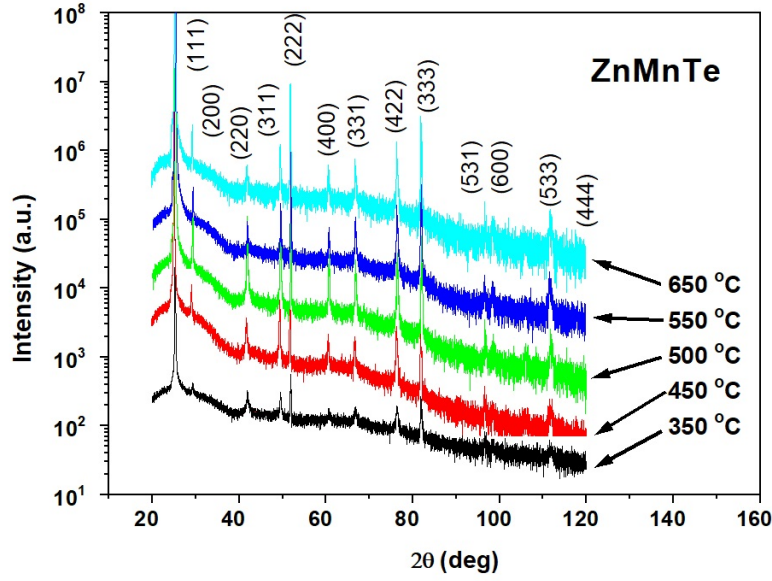


Figure 5.2: X-ray diffraction patterns from $Zn_{1-x}Mn_xTe$ films with 5% of nominal values of Mn deposited over glass at various substrate temperatures: 623 K, 723 K, 773 K, 823 K, and 923 K (350 °C, 450 °C, 500 °C, 550 °C, and 650 °C).

on MnTe buffer layers grown on sapphire [42], and it has been explained as a residual thermal strain that was not ruled out.

For determination of the content of manganese, we used the Vegard's law (section 3.4.7):

$$a(Zn_{1-x}Mn_xTe) = x \cdot a(MnTe) + (1 - x) \cdot a(ZnTe) \quad (5.1)$$

where $a(MnTe)$ and $a(ZnTe)$ are the lattice constants, that correspond to the zinc-blende phase (0.6105 and 0.6337 nm), respectively [289, 290]. The values x of the Vegard's law are reflected in Table 5.1 and Figure 5.3 (b).

The second method of Mn concentration measurement was EDX analysis coupled with HRTEM (see section 3.2.4). The partial incorporation of Mn in the ZnTe lattice can be seen in Table 5.1. Although the trend is the same, that is, the Mn content decreases as the substrate temperature increases, the interval of the EDAX values (0.7 to 2.05 at %) is lower than that from the Vegard's law expected from the XRD measurements (0 to 3.7 at %). All these quantities are considerably lower than the nominal value (5 %) thus the decrease in the concentration of manganese can be due to its re-evaporation from the substrate or not incorporation in the transport and deposition processes with increasing growth temperatures. Also as a consequence of re-evaporation or change in the growth mechanism a decrease in the thickness of the film samples with increasing growth temperature at the same deposition time can be expected, as mentioned in [291] and experimentally found by us in Section 5.1.1.

5.1. Structural and morphological studies of $Zn_{1-x}Mn_xTe$ thin films

Substrate temperature K ($^{\circ}C$)	623 K (350 $^{\circ}C$)	723 K (450 $^{\circ}C$)	773 K (500 $^{\circ}C$)	823 K (550 $^{\circ}C$)	923 K (650 $^{\circ}C$)
Lattice constant by XRD (nm) (± 0.0004 nm)	0.6111	0.6107	0.6102	0.6102	0.6102
Mn content by Vegard's law (at %) (± 0.1)	3.7	1.9	0	0	0
Mn content by EDX (at %) (± 0.1) [292]	2.1	2.0	0.6	0.6	0.7

Table 5.1: Lattice constant and Mn content determined by XRD and EDX in $Zn_{1-x}Mn_xTe$ films with 5% of nominal values of Mn deposited over glass at various substrate temperatures.

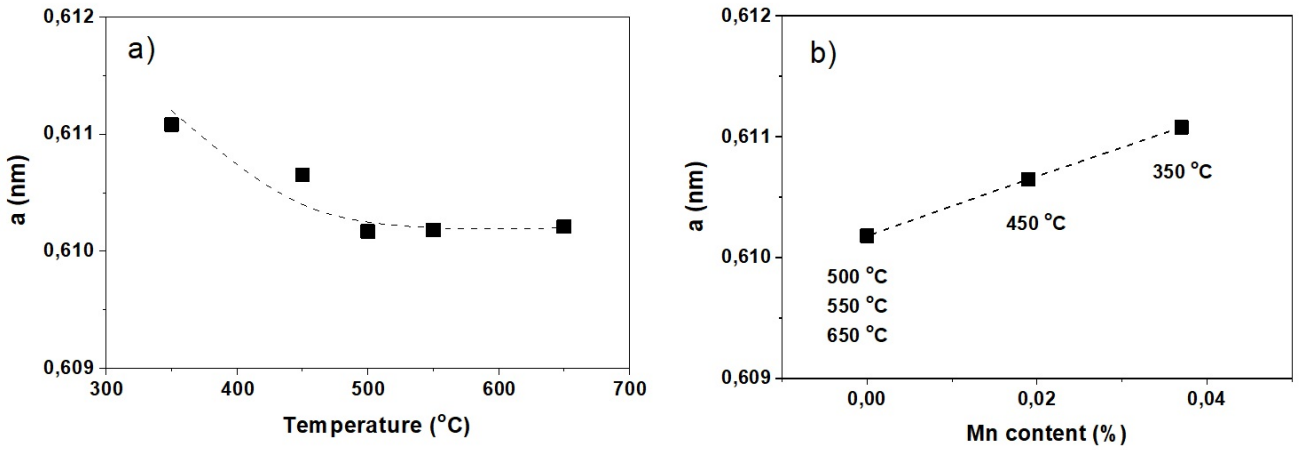


Figure 5.3: Lattice constant of $Zn_{1-x}Mn_xTe$ films deposited over glass: (a) as a function of substrate temperature [from 623 K to 923 K (350 $^{\circ}C$ to 650 $^{\circ}C$)]; (b) as a function of the Mn content, obtained from the Vegard's law.

The problem of the incorporation of Mn into $Zn_{1-x}Mn_xTe$ films was considered earlier [293] by using the PIXE method. A series of samples were used for this study, which was obtained with the same growth conditions, but with a higher content of the nominal Manganese value (10%). A typical aggregate PIXE spectrum (on the logarithmic scale) from the $Zn_{1-x}Mn_xTe$ films irradiated with a proton beam is shown in Figure 5.4. It can be seen that only the lines of the solid solution components (Zn, Mn, and Te) are present in the spectra. The results of analyzing the elemental composition of the samples are presented in the Table 5.2. The table shows that the $Zn_{1-x}Mn_xTe$ films exhibit a trend towards a decrease in the manganese concentration from 3.04 to 1.62 at % when the layer growth temperature T_s is increased from 623 to 823 K (from 350 to 550 $^{\circ}C$). The obtained films were characterized by Te predominance ($C_{Zn+Mn}/C_{Te} = 0.73-0.91$).

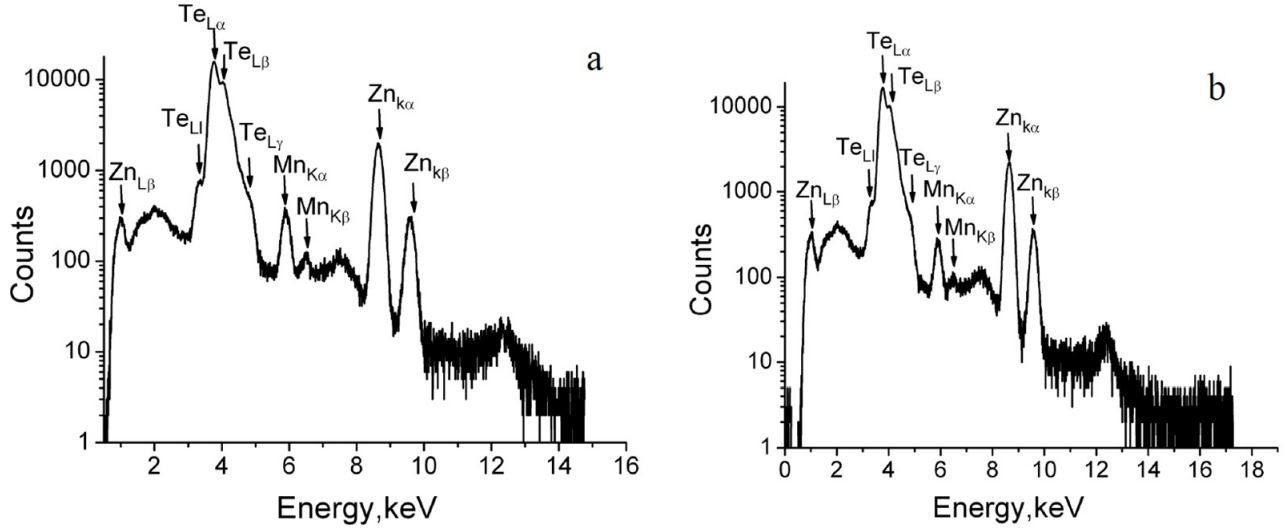


Figure 5.4: The total PIXE spectrum from the $Zn_{1-x}Mn_xTe$ ($x \simeq 10$ % nominal) films induced by the proton beam with energy 1.5 MeV (on the area $200 \times 200 \mu m$). The substrate temperature T_s : 623 K [350 °C] (a), 723 K [450 °C] (b).

Ts, K (°C)	Zn, wt %	Mn, wt %	Te, wt %	Zn, at %	Mn, at %	Te, at %	C_{Zn}/C_{Te}	C_{Zn+Mn}/C_{Te}
623 (350)	28.9	1.70	69.40	43.47	3.04	53.49	0.81	0.87
723 (450)	30.55	1.09	68.36	45.68	1.94	52.38	0.87	0.91
823 (550) (sample 1)	26.22	1.02	72.76	40.51	1.88	57.61	0.70	0.74
823 (550) (sample 2)	26.34	0.88	72.78	40.72	1.62	57.66	0.71	0.73

Table 5.2: The elemental composition of the $Zn_{1-x}Mn_xTe$ ($x \simeq 10$ % nominal) films.

The measurements were conducted at several points on the sample surface and the used method revealed no changes in the solid solution composition over the film area. The maps of manganese distribution in $Zn_{1-x}Mn_xTe$ films obtained at different deposition temperatures T_s are presented in Figure 5.5. The scales next to the maps (0–80 and 0–50) denote the number of quanta of characteristic X-ray radiation induced by the focused proton beam in the range of energies corresponding to the $MnK\alpha$ peak in the spectrum in Figure 5.4. These studies showed that the distributions of Mn denoted with different shades of green in Figures. 5.5 (a) and 5.5 (b) were somewhat different from each other, as its concentration decreases with increasing film-deposition temperature. However, the differences in the characteristic X-ray radiation yield in each pixel are at the level of statistical variability. Therefore, we may conclude that manganese is rather evenly distributed over the sample area.

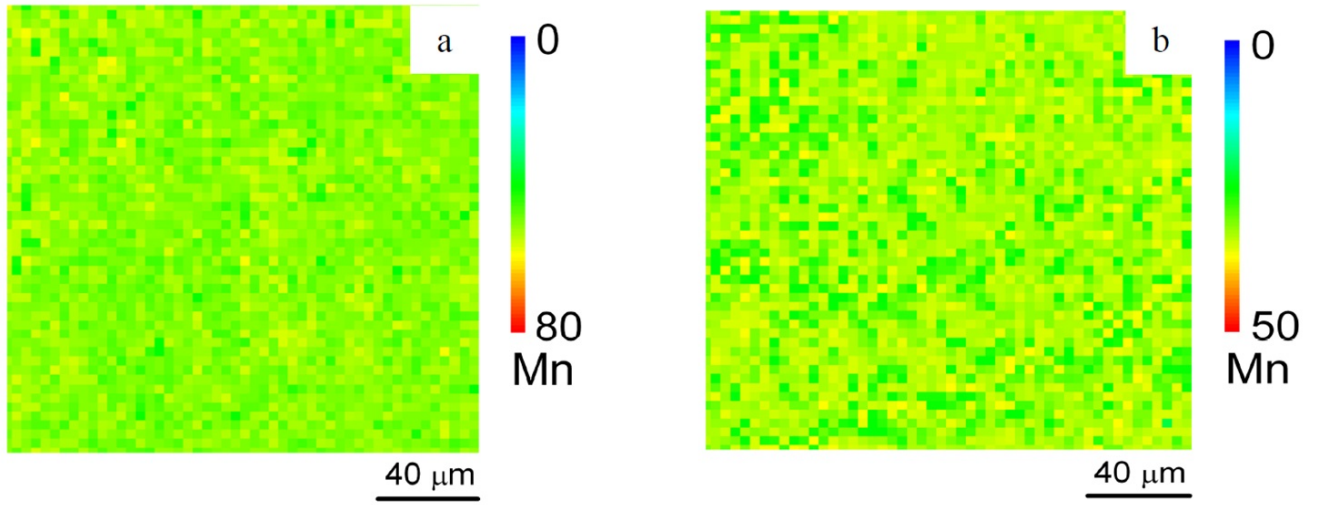


Figure 5.5: Maps of Mn distribution on the sample surface at a scanning step of $4 \mu\text{m}$ (the surface area is $200 \times 200 \mu\text{m}$). (Scan area is 50×50 pixels). The substrate temperature T_s : 623 K [350 °C] (a), 723 K [450 °C] (b).

5.1.3 Out-plane orientation of films

The high intensity of the (111) peak in XRD patterns suggests an out-plane preferred orientation. However, this can only be confirmed from texture analysis [294]. For this case, we calculated texture coefficients C_{tex} (proportional to the number of crystallites in a given orientation) and the degree of preferred orientation, f (numerical value that indicates how much a crystal is well oriented).

Both parameters depend on the number of analyzed peaks N . In present study, $N = 6$, since only 6 major directions of X-ray diffraction are involved (111, 200, 220, 311, 331 and 422). The corresponding value for a perfectly oriented sample is $f = \sqrt{N-1} = 2.236$. The values obtained from XRD patterns of films are reflected in Table 5.3. This table shows texture coefficients and preferred orientation of films, allowing an accurate comparison among samples.

It can be observed in Figure 5.6 that at lower temperature [623 K (350 °C)] the dominant crystallographic planes of crystallites are the (111) for all temperatures. This means that the film has a degree of preferred orientation f near to that of a perfectly (111) oriented sample. As the substrate temperature increases, the number of crystallites with a (200) orientation increases and f decreases. Finally at high temperatures the value of f is again almost equal to that of a perfect oriented sample. This preferred orientation (111) is typical for ZnTe films, mainly when it is alloyed with metals [295].

Chapter 5. Effect of Mn alloying on structural and optical properties of ZnTe and ZnS thin films

	(111)	(200)	(220)	(311)	(331)	(422)	f	Mn content by EDX (at %) (± 0.1)
Perfectly oriented							2.236	
623 K (350 °C)	0.567	0.119	0.020	0.048	0.042	0.104	2.087	2.1
723 K (450 °C)	0.518	0.409	0.029	0.103	0.076	0.198	1.875	2.0
773 K (500 °C)	0.520	0.379	0.045	0.123	0.088	0.165	1.881	0.6
823 K (550 °C)	0.572	0.109	0.005	0.027	0.040	0.101	2.110	0.6
923 K (650 °C)	0.568	0.149	0.005	0.027	0.039	0.104	2.092	0.7

Table 5.3: Texture coefficients and degree of preferred orientation (f) in $Zn_{1-x}Mn_xTe$ films with 5 % of nominal values of Mn deposited over glass at various substrate temperatures.

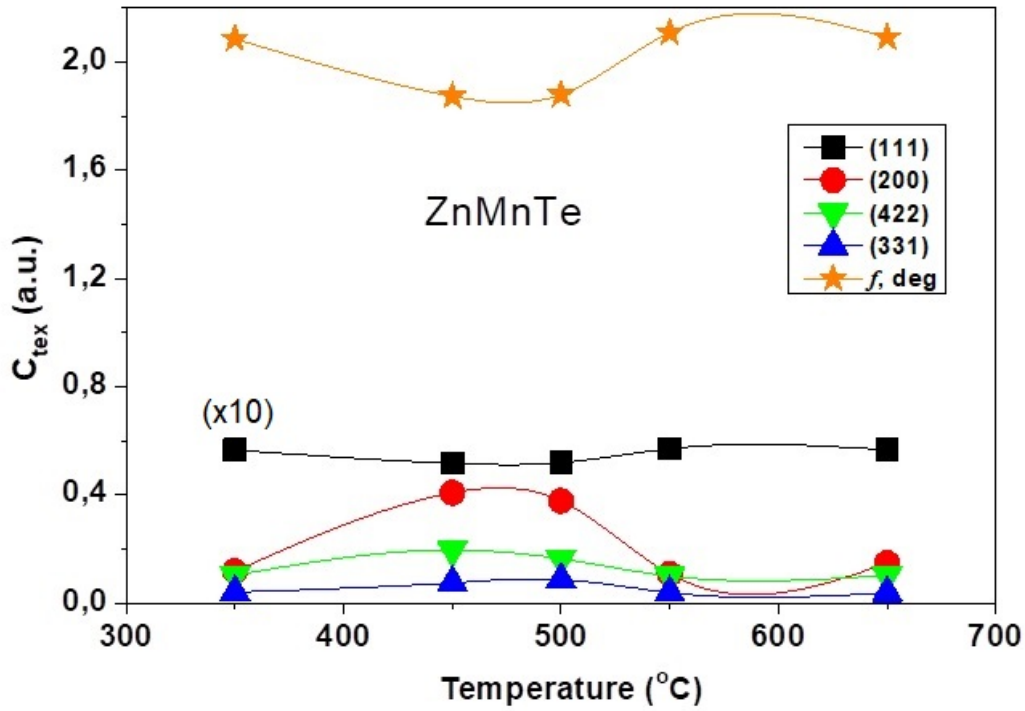


Figure 5.6: Texture coefficients for some major directions obtained from $Zn_{1-x}Mn_xTe$ films deposited over glass at various substrate temperatures [from 623 K to 923 K (350 $^{\circ}C$ to 650 $^{\circ}C$)].

5.1.4 In-Plane orientation of films

Pole figure analyses from HRXRD measurements were performed to determine both the relative quantity of (111)-oriented crystallites and the in-plane orientation of films (more details in Section 3.4.6).

The experimental pole figures of the $\{111\}$ reflection for all samples are shown in Figure 5.7. All of them exhibit a broad peak with its maximum at an inclination angle $\psi = 0^\circ$ and a broad ring at an inclination angle at $\psi \approx 70^\circ$. As a reference, the theoretical position of poles for a perfectly oriented sample is also shown, where three poles can be observed 70° apart from the central one. The measured broad ring corresponds to these lateral poles, indicating a random azimuthal orientation. This is known as uniaxial orientation or fiber texture, being in this case the $[111]$ direction the fiber axis [296]. In other words, the films possess an out-plane preferred orientation but no in-plane preferred orientations.

The area under the peak (111) is related to the amount of material that diffracts in this direction; consequently, we can use this area to evaluate the quantity of crystallites that are oriented within a certain inclination angle. Figure 5.8 supplies, for all samples, the calculated mean diffraction intensity in the azimuthal angle as a function of the inclination angle ψ from 0 to 90° . The central peak is broad, with a half-width at half maximum of about 10° . From the integration of this peak intensity, we can determine the percentage of (111)-oriented crystallites as the ratio of the area named A (reaching an inclination angle of 10°) in respect to the sum of the two areas named A and B. Results are shown in Table 5.4 for (111)-oriented crystallites within two inclination angles.

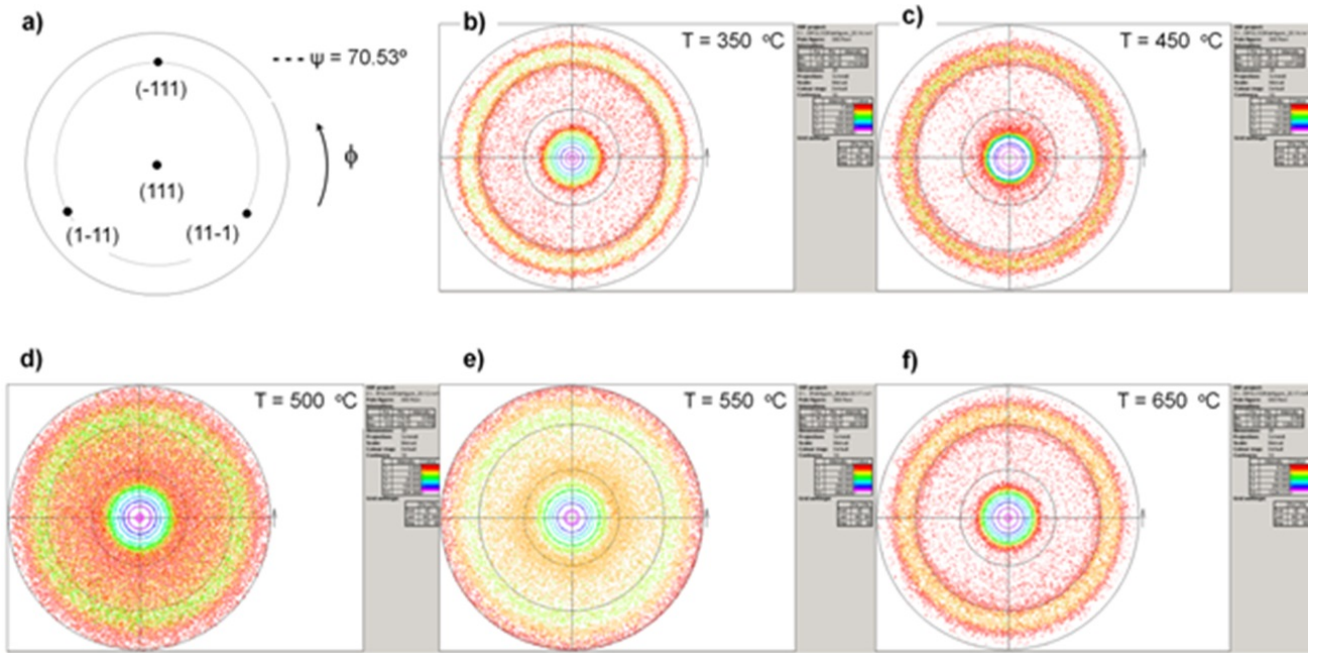


Figure 5.7: Poles for the (111) reflection: (a) theoretical position for a perfect oriented sample in the cubic system. Experimental values for $Zn_{1-x}Mn_xTe$ films deposited over glass at various substrate temperatures: (b) 623 K (350 °C), (c) 723 K (450 °C), (d) 773 K (500 °C), (e) 823 K (550 °C), (f) 923 K (650 °C).

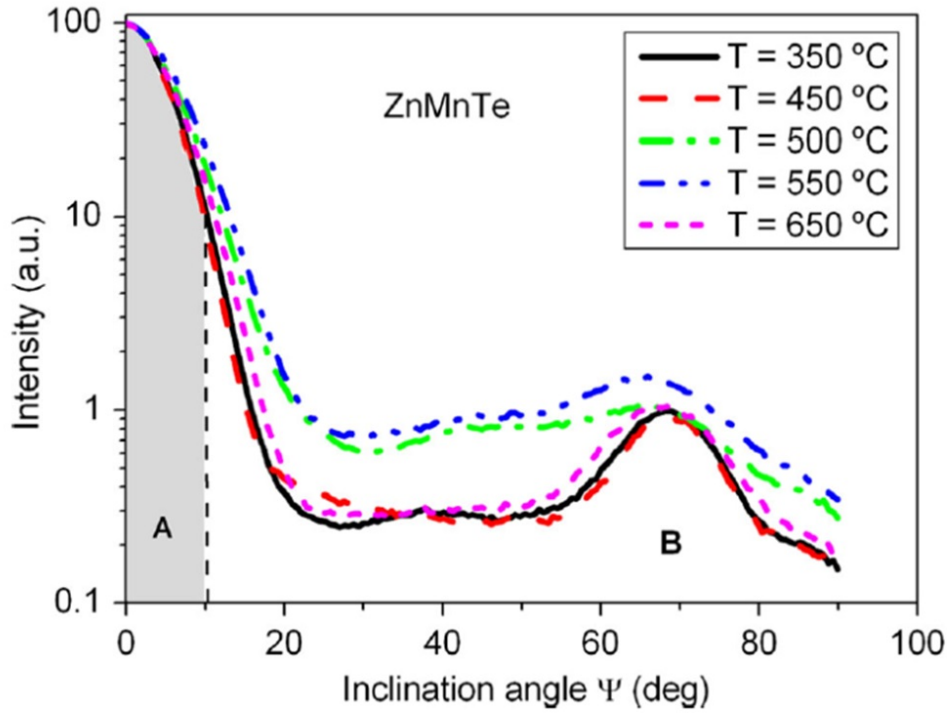


Figure 5.8: Average intensity over the rotation angle of the symmetrical (111) reflection as a function of the inclination angle ψ from $Zn_{1-x}Mn_xTe$ films deposited over the glass at different substrate temperatures: T : 623 K (350 °C), 723 K (450 °C), 773 K (500 °C), 823 K (550 °C), 923 K (650 °C). The area marked as A is proportional to the crystallites having a (111) orientation within $\pm 10^\circ$.

Mn content by EDX (at %) (± 0.1)	2.1	2.0	0.6	0.6	0.7
Substrate temperature K(°C)	623 K (350 °C)	723 K (450 °C)	773K (500 °C)	823 K (550 °C)	923 K (650 °C)
Oriented within $\pm 10^\circ$	91.7%	92.2%	85.3%	82.9%	90.0%
Oriented within $\pm 20^\circ$	95.5%	95.4%	92.8%	91.9%	95.3%

Table 5.4: Percentage of (111)-oriented crystallites within a defined inclination angle for $Zn_{1-x}Mn_xTe$ films deposited over glass at different substrate temperatures (uncertainties ~ 0.1 percent)

The calculated values indicate that the percentage of particles with a (111) orientation within $\pm 10^\circ$ is high (in the range of 83 to 92 %) for all the substrate temperatures. The variation in the percentages is small, decreasing with the substrate temperature but finally increasing at the highest temperature of 923 K (650 °C). That is, the most of the grains (~ 90 %) present a (111) preferred orientation within an inclination angle of $\pm 10^\circ$ in all the range of growth temperatures.

Once the crystal lattice, Mn content and preferred orientation have been ascertained, substructural characteristics of films will be analyzed. This will allow the determination of the mono or polycrystalline character of grains that constitute the film.

5.1.5 Coherent scattering domain and microdeformations

As it is known, the X-ray line broadening is caused not only by the instrumental effects but also by small coherent scattering domain (CSD) sizes L , microdeformations ($\varepsilon = \Delta d/d$) and distortions of the crystal lattice. The average CSD size L and the microdeformation grade ε in $Zn_{1-x}Mn_xTe$ samples was studied by the broadening of (111)-(222) and (200)-(400) X-ray diffraction peaks of the cubic phase. This procedure has allowed defining the substructural parameters of the films in directions normal to these crystallographic planes. Table 5.5 lists the results obtained by the Cauchy and Gauss approximations as well as the more precise data from the X-ray line threefold convolution method. Figure 5.9 shows results of comparison made for the CSD size and microdeformation grade in ZnTe and $Zn_{1-x}Mn_xTe$ films calculated using the three approximations.

Table 5.5 and Figure 5.9 point out the CSD sizes and microdeformation values calculated by the threefold convolution method are intermediate between the data produced by the Cauchy and Gauss approximations having a good correlation. Further we discuss the results from the threefold convolution method as the most precise one [248].

As it can be concluded from the Table 5.5 and 5.9, in samples obtained under temperatures higher than 623 K (350 °C) the CSD size decreases from $L \sim 136$ nm down to ~ 81 nm, then it increases up to ~ 131 nm for samples grown at 773 K (500 °C) in the direction normal to the (111) planes (Figure 5.9, a). The maximum size for samples obtained at $T_s = 600$ -650 K. At the same time, the microdeformation grade in this direction decreases with increasing T_s from $\varepsilon \sim 1.12 \times 10^{-3}$ to $\varepsilon \sim 0.62 \times 10^{-3}$ and increases up to 0.89×10^{-3} (Figure 5.9, b). This behavior is similar to what we obtained before in paper [297], where values of CSD size and microdeformation grade were minimum with $T_s \approx 600$ -650 K. The nature of this phenomenon can be explained by transit from the growth of long to small columns at the higher temperature, as was commented in Section 5.1.1. It should be noted that, as mentioned earlier, that the samples obtained at the growth temperature of > 773 K (500 °C) almost do not contain manganese.

These results are in a good agreement with those obtained previously by our scientific group for pure ZnTe films at similar growth conditions [298], and the functions $L - T_s$ and $\varepsilon - T_s$ are presented in Figure 5.9 (a, b) on the curve 4. Parameters L and ε take their minimum value in the temperature range 650-750 K, where a change in the thickness of the films is observed and a transit from the long to small columns appears. At the same time, $Zn_{1-x}Mn_xTe$ films

Chapter 5. Effect of Mn alloying on structural and optical properties of ZnTe and ZnS thin films

Mn content			L, nm		$\varepsilon, 10^{-3}$			α', K	
T_s	by EDX	(hkl)	Approximation by		From	Approximation by			From
K (°C)	(at %)		Gauss	Cauchy	convolution	Gauss	Cauchy		convolution
623	2.1	(111)-(222)	122.18	196.79	136.32	1.31	0.82	1.12	0.72
(350)		(200)-(400)	42.22	48.41	42.62	1.42	0.49	1.08	
723	2.0	(111)-(222)	80.44	92.00	81.16	0.84	0.19	0.62	0.31
(450)		(200)-(400)	63.77	90.95	63.98	1.76	1.05	1.38	
773	0.6	(111)-(222)	122.91	178.96	131.69	1.08	0.58	0.89	0.04
(500)		(200)-(400)	101.22	200.07	125.64	1.88	1.41	1.69	
823	0.6	(111)-(222)	132.56	210.46	146.98	1.18	0.71	1.00	0.01
(550)		(200)-(400)	109.14	243.10	146.05	2.05	1.61	1.88	
923	0.7	(111)-(222)	123.36	174.91	130.96	1.01	0.51	0.82	0.03
(650)		(200)-(400)	103.63	198.22	126.20	1.75	1.28	1.56	

Table 5.5: Substructural characteristics of $Zn_{1-x}Mn_xTe$ thin films.

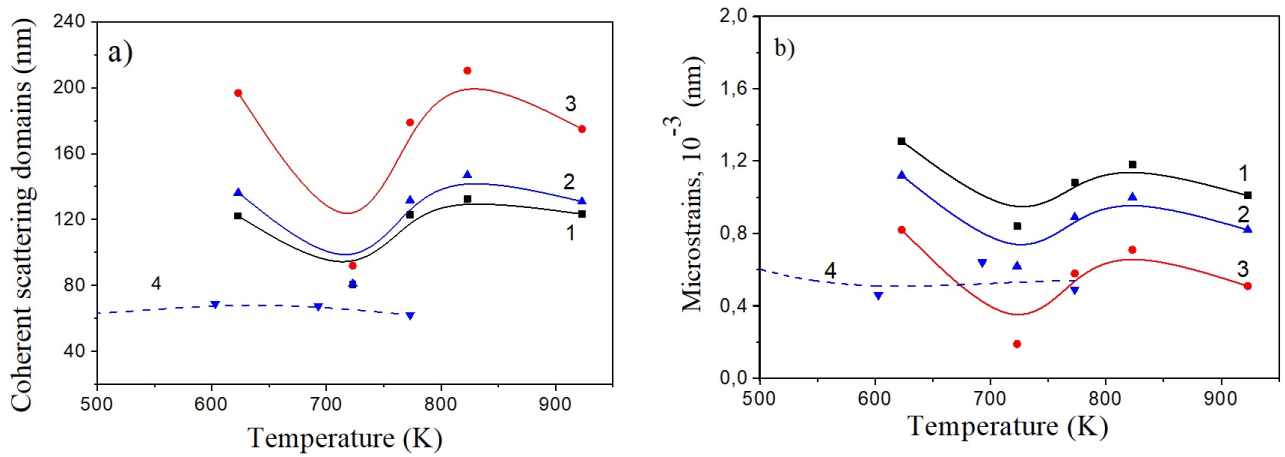


Figure 5.9: The effect of a decrease in Mn content with growth temperature T_s on the CSD size (a) and the microdeformation grade (b) of the films $Zn_{1-x}Mn_xTe$ (1-3) and ZnTe (4) films. The approximation is done according to Cauchy (1), Gauss (3), and to the method of threefold convolution (2).

had the larger CSD size and microdeformation grade compared with pure ZnTe films (Figure 5.9 a, b).

Using the known microdeformation values and well-known expression for Hooke's law $\sigma = E \varepsilon$ (where, E is the modulus of elasticity and ε is the strain) we have calculated the microstress grade in the $Zn_{1-x}Mn_xTe$ samples (Table 5.5). Microstress level in $Zn_{1-x}Mn_xTe$ was calculated according microdeformation (Table 5.5) and using the Young's value ($E = 64$ GPa) for ZnTe [298]. It is shown that the microstress grade in $Zn_{1-x}Mn_xTe$ films changes in the interval $\sigma = 39.5$ -71.7 MPa. These values are close to the values of ZnTe films ($\sigma = 20$ -83 MPa) [298]

5.1. Structural and morphological studies of $Zn_{1-x}Mn_xTe$ thin films

and lesser than $\sigma = 67.5\text{-}130.7$ MPa, that was found by us for $Zn_{1-x}Mn_xTe$ samples with 10 % Mn nominal content grown in the range $T_s = 423\text{-}823$ K (150 -550 °C) during 15 min. [297].

The three different ways of the CSD size calculation show a typical feature: the calculated values $L_{(h00)} > L_{(hhh)}$. Suppose as in [298–301] that the CSD have equal axes but the microdeformations mainly contribute to the line broadening responsible for the reflection from the (hhh) planes. Then, it is possible to determine the total concentration of deformation and growth defects α' in $Zn_{1-x}Mn_xTe$ films according to the equation 3.25. These results are listed in Table 5.5.

T_s , K (°C)	(hkl)	L, nm	ε , 10^{-3}	σ , MPa	ρ_L , 10^{14} lin/m ²	ρ_ε , 10^{14} lin/m ²	$\rho_{L\varepsilon}$, 10^{14} lin/m ²
623 (350)	(111)-(222)	136.32	1.12	71.7	1.61	1.47	3.49
723 (450)	(111)-(222)	81.16	0.62	39.5	4.55	0.45	3.23
773 (500)	(111)-(222)	131.69	0.89	57.0	1.73	0.93	2.88
823 (550)	(111)-(222)	146.98	1.00	64.0	1.39	1.17	2.90
923 (650)	(111)-(222)	130.96	0.82	52.5	1.75	0.80	2.68

Table 5.6: Microdeformations and dislocation density in $Zn_{1-x}Mn_xTe$ films.

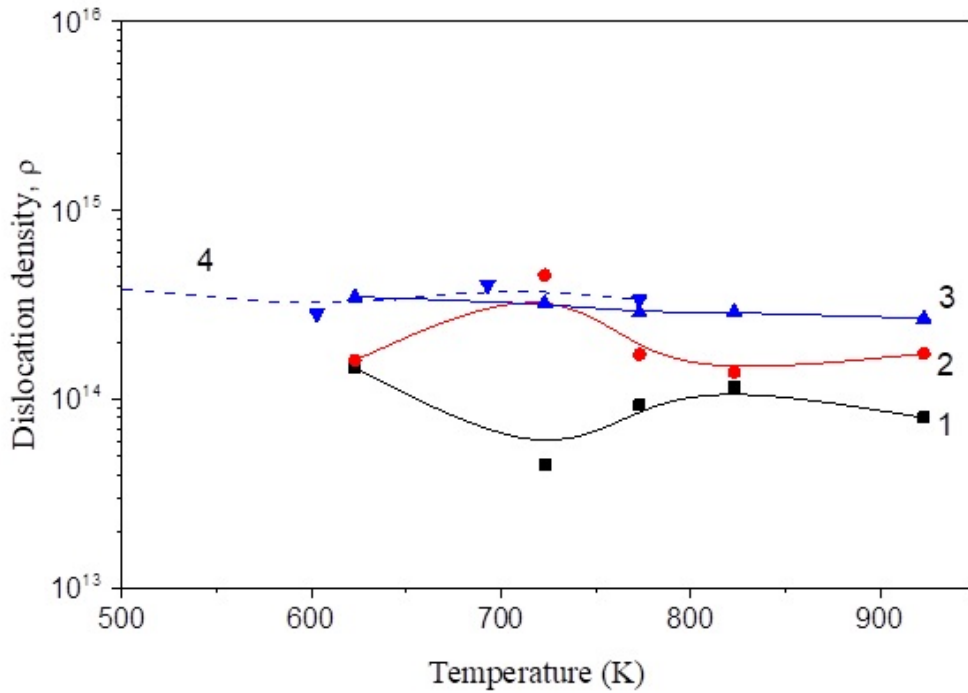


Figure 5.10: Dependence of the dislocation density with growth temperature in $Zn_{1-x}Mn_xTe$ (1-3) and ZnTe (4) films: at the subgrain boundaries (1), in their bulk (2) and the general dependence (3, 4) using the reflexion (111)-(222).

Chapter 5. Effect of Mn alloying on structural and optical properties of ZnTe and ZnS thin films

As can be seen, the average deformation's concentration in $Zn_{1-x}Mn_xTe$ films decreases with reducing Mn content from 1.73 % ($T_s = 623$ K [350 °C]) up to 0.03% ($T_s = 923$ K [650 °C]) where very small content of Manganese was found. For unalloyed ZnTe films these values decreased in the growth temperature range $T_s = 323-693$ K from 0.67 % to 0.04 % [299]. As established, the size of the CSDs is significantly smaller than the grain size. If we assume that the CSDs are equiaxed, and the additional broadening of lines (111) and (222) is associated with the presence of microdeformations, then with the rising of T_s the value of the Mn content decreases, the stability of the cubic phase of the compounds increases, the probability of disruption of the order of planes (111) alternation decreases, the concentration of microdeformations decreases accordingly.

Table 5.6 and Figure 5.10 illustrate the results of calculating density of dislocations at the CSD boundaries, in the CSD bulk and the total dislocation density in $Zn_{1-x}Mn_xTe$ films made according to the equations 3.20-3.22. As it is seen, the data have a good correlation within order of magnitude. These films are characterized by considerably low values of the dislocation density $\rho_{L\epsilon} = (2.68 - 3.49) \times 10^{14}$ (see, for example, [241], where for ZnTe films $\rho = (6.3 - 16.6) \times 10^{14}$ *lin/m*²). As the Mn content decreases with rising substrate growth temperature, the total dislocation concentration in the films defined from the (111-222) reflexions is decreasing (Figure 5.10). However, this value is larger than in pure ZnTe films $\rho_{L\epsilon} = (7.8 - 21.4) \times 10^{-13}$ *lin/m*² obtained by our scientific group at similar growth conditions [298]. Thus, the manganese alloying leads to the degradation of the substructure of ZnTe films: the microdeformations and microstresses as well as the concentration of the dislocations are increased, as could be expected due to the incorporation of the foreing element into the host ZnTe.

5.1.6 Crystallite size and density of dislocations

In polycrystalline materials, as is our case, information about the average shape, crystallite size, and lattice strain can be determined by X-ray line profile analysis [302].

The classical Williamson-Hall plot (equation 3.17) of data from $Zn_{1-x}Mn_xTe$ films grown at 350 °C is shown in Figure 5.11 (a) and reveals a strong anisotropy. To avoid misleading, in this section we will use the celsius degress (°C) for temperatura and K for the dimensionless factor (as mentioned in the section 3.4.4). When the broadening ΔK of line profiles is plotted as a function of $K^2 \overline{C}_{hkl}$ to determine the value of α (constant that depends on the Burgers vector and the density of dislocations) and \overline{D}_{hkl} (Figure 5.11, b), it can be seen that points are grouped along three straight lines with more or less the same slope, but with different intersections at $K = 0$. This is indicative of different crystallite sizes that depend on the order of diffraction. The longer crystallite size is that given by planes $[hhh]$, followed by the corresponding to the

planes ($h00$), (311) and (331), being the shorter one that defined by planes (220) and (422). Taking into account the angles between crystallographic planes, the behaviour is consistent with a prismatic crystallite having the [111] direction along the column axis; this direction defines the longitudinal size of crystallite (D_{long}) and the last set of planes, the transversal size (D_{transv}). The second set of planes is constituted by planes inclined in respect to the column axis (see Figure 5.11, c). The obtained crystallite sizes follow the relation $D_{long} > D_{inclined} > D_{transv}$. If films are formed by such a type of crystallites, the intense $\{hhh\}$ peaks in the XRD pattern would be produced by a majority of crystallites in vertical position, while the other low-intensity peaks would be produced by few inclined or lying crystallites. These elongated crystallites evidence a columnar growth and confirm the strong texture of films. Columnar growth is usually explained by a faster growth in a particular direction. On non crystalline substrates, generally nuclei grow in a random orientation, but if the growth is faster in a privileged direction, this orientation eventually outgrows the other orientations and becomes dominant.

We solved the equation 3.19 in H^2 by the least-squares method (Figure 5.11, d). The value of \overline{C}_{h00} has been determined from the elastic constants of ZnTe [303] and the data indicated in [304, 305], giving in $\overline{C}_{h00}=0.24$, value which results to be the same for the screw and edge dislocations. On the contrary, the value of q depends on the proportion between screw and edge dislocations. The best linear regression provides $q \approx 2$, which indicates a clear prevalence of screw dislocations in the ZnMnTe films [303].

The mean longitudinal and transversal crystallite sizes have been calculated from XRD patterns of $Zn_{1-x}Mn_xTe$ films grown at different temperatures and are shown in Figure 5.12 (a). The mean longitudinal size of crystallites at low temperature [623 K (350 °C)] is about 170 nm, increasing considerably with the substrate temperature, when Mn content goes down. The mean transversal size also increases, but less. The aspect ratio D_{long}/D_{transv} goes from 3.5 to 5 as the Mn content decreases. Comparing the transversal size with values obtained by SEM, we conclude that columnar grains is turn consists of crystallites, that is are polycrystalline, like the whole array of the obtained films.

If the broadening of the line profile is attributed to dislocations, according to the MWH method the slope α can be expressed [305, 306] by:

$$\alpha = \frac{\pi b^2 \rho^{1/2}}{2B} \quad (5.2)$$

where ρ is the dislocation density, b is the modulus of the Burger's vector of dislocation (for f.c.c. crystals $b = a/\sqrt{2}$, where a is the lattice constant) and B is a constant that can be taken as 10 for a wide range of dislocation distribution [307]. Calculated values as a function of the substrate temperature are shown in Figure 5.12 (b).

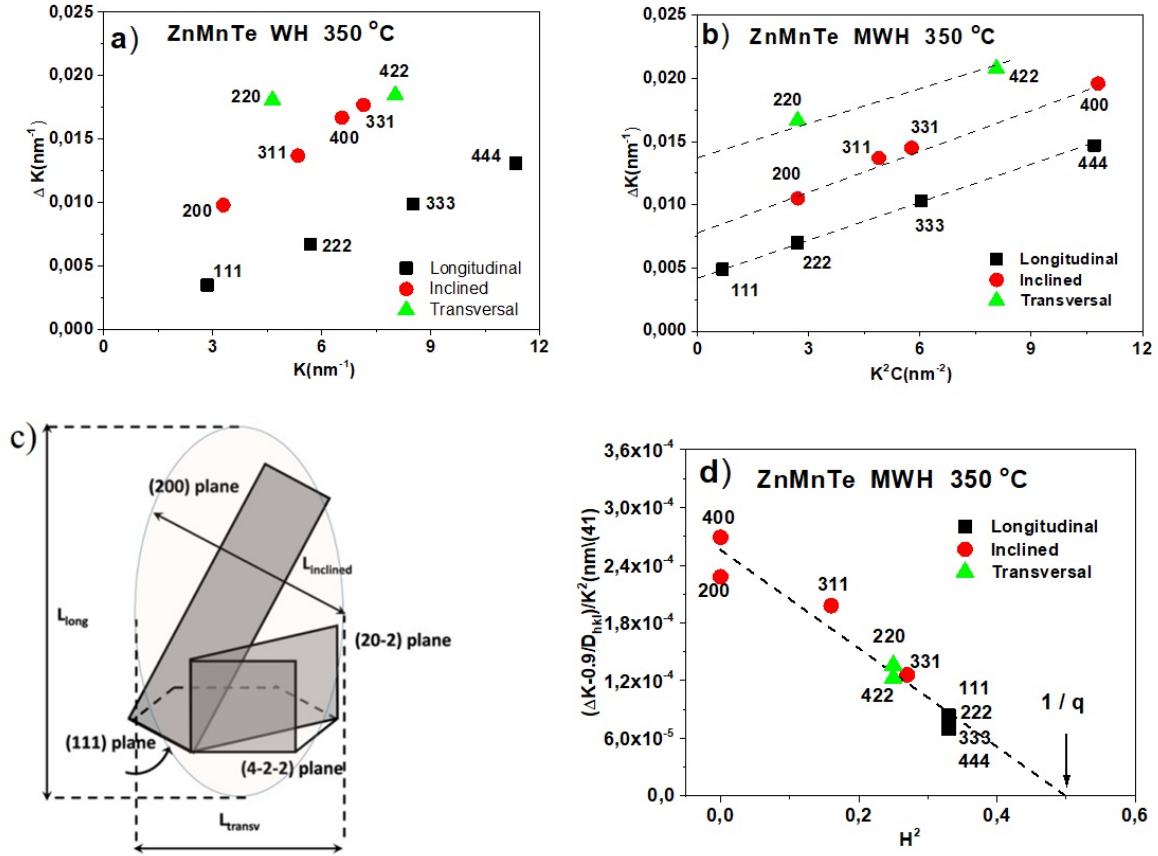


Figure 5.11: From data of $Zn_{1-x}Mn_xTe$ films grown at 623 K (350 °C): (a) Williamson-Hall plot; (b) Modified Williamson-Hall plot; (c) some crystallographic planes in a prismatic crystallite; (d) plot of eq. (3.17) as a function of H^2 .

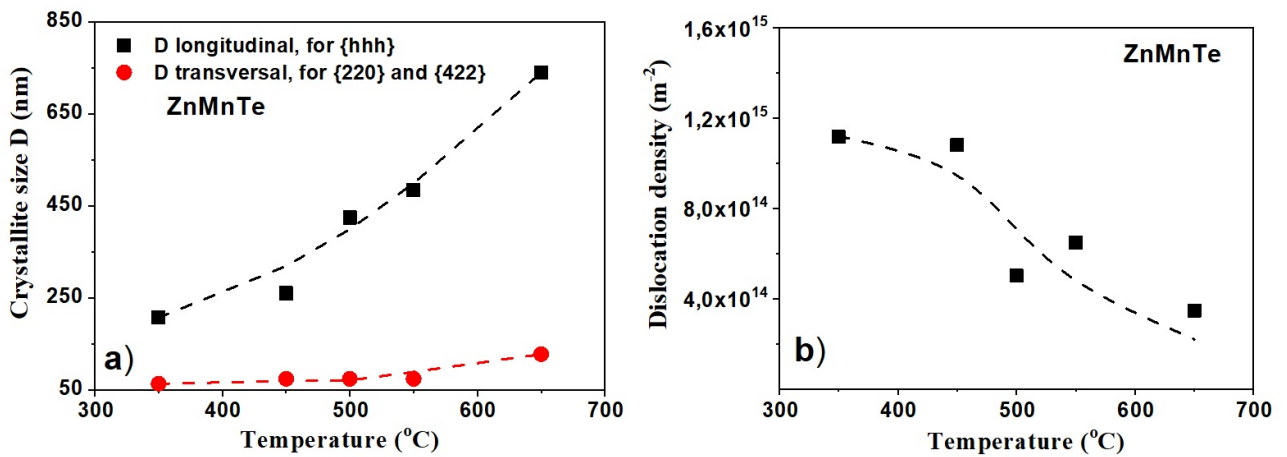


Figure 5.12: (a) Crystallite size and (b) dislocations density from $Zn_{1-x}Mn_xTe$ films deposited over glass at different substrate temperatures [from 623 K to 923 K (350 °C to 650 °C)]. Dashed lines are a guide for the eye.

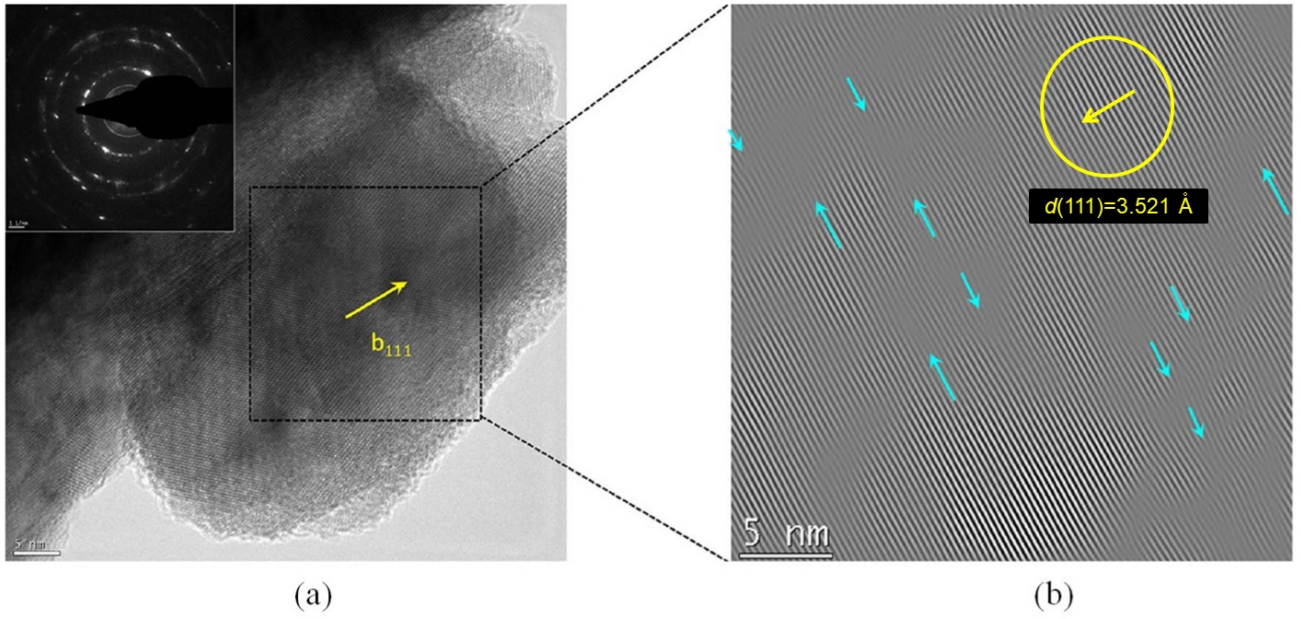


Figure 5.13: (a) HRTEM image of a $Zn_{1-x}Mn_xTe$ film grown on glass at a substrate temperature of 623 K (350 °C). The arrow indicates the direction of the Burger's vector for the screw dislocations, the same as the axis of this type of dislocation. (b) Inverse FFT (IFFT) filtered image of crystallite showing the distribution of dislocations along the [111] direction. The arrows mark some of the screw dislocations that can be observed in the squared area of the FFT image.

The average dislocation density is slightly Mn content dependent, maintaining a value of about $1 \cdot 10^{15} m^{-2}$ at low and mean temperatures and reducing its value until about $2 \cdot 10^{14} m^{-2}$ when the growth is made at the higher temperature of 923 K (650 °C) with lowest value of Mn content.

The presence of dislocations is confirmed by HRTEM. Figure 5.13 (a) shows the HRTEM image of a crystallite of a $Zn_{1-x}Mn_xTe$ film grown at 623 K (350 °C) in which the direction of the Burger's vector has been indicated. The detected interplanar distance of the $Zn_{1-x}Mn_xTe$ film is $d_{hkl}=3.521 \text{ \AA}$ and it is very close to the interplanar distance of the (111) planes of the ZnTe cubic structure (3.505 Å, JCPDS No 75-2082) [308]. The difference in the spacing may be due to the incorporation of Mn in the lattice, although the accuracy of the method does not allow to accurately guarantee the presence of Mn. For screw (111) dislocations, the Burger's vector, the dislocation line, and the axis of the screw dislocation follow the same direction. In Figure 5.13 (b), the Inverse FFT (IFFT) filtered image of this previous image is shown which reveals the distribution of dislocations along the [111] direction. The arrows in Figure 5.13 (b) mark some of the screw dislocations that can be observed in the squared area of the FFT image. Similar images for the samples, obtained at lower temperatures, exhibit a higher concentration of dislocations, thus confirming the results obtained by XRD.

5.2 Structural and morphological properties of $Zn_{1-x}Mn_xS$ thin films

5.2.1 Morphological study

The morphological studies of the obtained layers show that the $Zn_{1-x}Mn_xS$ films deposited on glass substrates at $T_s > 373$ K (100 °C) were polycrystalline, as can be seen in Figure 5.14. At growth temperatures < 373 K was not possible to obtain high-quality films of solid solutions $Zn_{1-x}Mn_xS$. In semiconductor layers, surface stress, apparently related to the thermal expansion coefficient, can lead to cracking and further destruction of the continuity of the layer. Unlike Mn-free ZnTe, Mn-free ZnS [309] has a cubic structure only at low temperatures (< 573 K [300 °C]). Therefore, it may be interesting to note how the Mn alloying will affect the structural properties of the compounds depending on the temperature. The surface morphology of the $Zn_{1-x}Mn_xS$ films deposited from semiconductor-grade blend with 7 % of nominal Mn content is depicted in Figure 5.14.

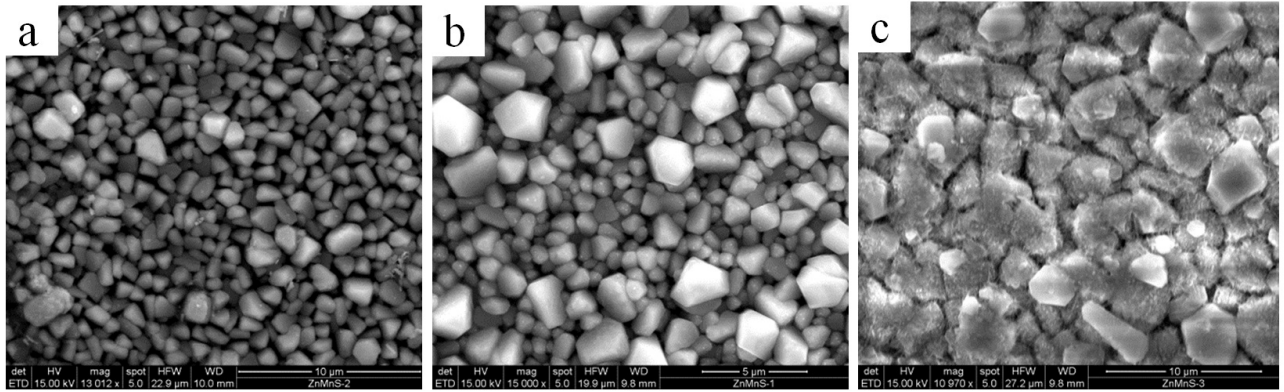


Figure 5.14: Surface morphology of $Zn_{1-x}Mn_xS$ films ($T_e = 1273$ K) obtained at different substrate temperatures T_s : 373 K [100 °C](a); 523 K [250 °C] (b); 723 K [450 °C](c).

At low substrate temperatures $T_s < 623$ K (350 °C) columnar growth of compound films was observed. This was due to secondary nucleation during the film growth, where ready-made solid particles of material become nucleation points. As a result, the shape of the grain turned to spherical and this trend disappeared at higher growth temperatures. Comparing with the results for pure ZnS [309] grown at similar conditions, it can be seen that the Mn alloying in the ZnS:Mn compound slightly changes the film morphology from uniform to granular. Further

morphology changing at higher temperatures can be explained by a change in the mode of growth of samples from planar ($T_s < 673$ K [400 °C]) to columnar ($T_s > 673$ K [400 °C]). Hwang et al. [310] grew ZnS thin films onto glass substrates using RF magnetron sputtering at various substrate temperatures ranging from 373 K to 673 K (from 100 °C to 400 °C). The XRD measurements of the films revealed that crystallinity of the films can be improved by rising temperature from 373 to 623 K (100-350 °C), where FWHM values were ranging from 0.384° to 0.141° and increased at 673 K (400 °C) to 0.154° , that indicate the deterioration of the crystallinity of the films due to defects or/and dislocations. Authors presented that crystallite size and grain size were increased from 22.3 to 60.8 nm and from 27.2 to 69.4 nm with rise in the growth temperature in the range 373-623 K (100-350 °C). For 673 K (400 °C) those values were decreased to 55.6 and 66.2 nm, respectively. Comparing with our results, it can be assumed that the deterioration of the film quality is due to a change in the growth mode.

The films had a grain size $D = 0,65-3,13 \mu\text{m}$ while it increased with increasing substrate temperature T_s from 373 to 773 K (100 to 450 °C). Thickness decreased in the range $d \sim 2.25-3.58 \mu\text{m}$ with the rise of growth temperature. As the analysis showed, the calculated values of D were similar to ZnS films deposited under similar conditions [311] and similar to those obtained in the work [157]. On another hand, authors of ref. [312] synthesized manganese-doped ZnS nanoparticles by coprecipitation of Zn^{2+} and Mn^{2+} precursors and got the size of crystallites an order of magnitude smaller than in this work. Grains density was in the range $0.18 \times 10^{12} - 1.16 \times 10^{12} \text{ NPs}/\text{m}^2$ and decreased with the rise of growth temperature, as result of reduction of Mn content, as it will be discussed later.

In [313] Mote et al. presented that the average crystallite size decreases with increasing Mn concentration in the $Zn_{1-x}Mn_xS$ samples prepared by a chemical method at room temperature. It means that the Zn^{2+} ions are replaced by Mn^{2+} ions in the ZnS matrix without changing the cubic structure. Since the ionic radius of Mn^{2+} ions can be both 0.81 Å (for the low spine state) and 0.97 Å (for the high spine state), reduction of average crystallite size may be due to small grain growth in comparison with undoped ZnS nanocrystals.

5.2.2 Lattice constant and Mn Content

It is assumed that the process of films growth of all compounds with the zinc blende structure (ZB), on glass substrates, will be basically similar. Initially, the formation of a thin-crystalline transition layer at the substrate occurred with subsequent cone-shaped expansion of crystallites oriented (111) parallel to the substrate. In the case of films with the wurtzite structure (W), the peculiarities of their structure formation were mainly determined by the rapid growth of crystallites that presented oriented plane (0002) parallel to the substrate.

Chapter 5. Effect of Mn alloying on structural and optical properties of ZnTe and ZnS thin films

Diffraction patterns of $Zn_{1-x}Mn_xS$ films obtained at different substrate temperatures are shown in Figure 5.15 (b). As can be seen from the figures on the diffractograms of the $Zn_{1-x}Mn_xS$ layers, reflections from the crystallographic planes (111), (200), (220), (311), (222), (400), (331), (420) of the cubic phase are recorded. Diffraction peaks corresponding to elemental Mn (300) observed at a lower temperature (373-623 K [100-350 °C]), disappears at higher temperatures (> 623 K [350 °C]), and this means that the Mn has been better alloyed into the crystal lattice of ZnS (or the concentration of elemental Mn has decreased greatly). At the same time, in the majority of cases the dominant intensity is the peak (111), this indicates the presence of brightly expressed texture in films.

A study using high-resolution transmission electron microscopy (HRTEM) CSS-grown polycrystalline ZB CdTe thin films [314] showed that WZ phase in A_2B_6 compounds can exist in a special form, as thin WZ layers buried in the ZB host crystals. Thus, they cannot be detected easily by x-ray diffraction. WZ phase formation occurs due to violation of the order of stacking of close-packed layers: the transition from a three-layer packaging ... $AaBbCcAaBbCc$... typical of ZB, to a two-layer ... $AaBbAaBb$..., which causes the formation of WZ, where the letters Aa , Bb , Cc indicate three possible projected positions of the atoms. The result is a cubic matrix with a large number of SF and WZ phase layers. The geometric relationship between the WZ layers and the ZB host is $[111]_{ZB} || [0001]_{WZ}$, $[1\bar{1}0]_{ZB} || [11\bar{2}0]_{WZ}$. It should be noted that the thin WZ layers are always found in high-density planar defects regions. On the other hand it is worth to note that mismatch is not found between these two structures. Dimitrova *et al.* [315] carried out the analysis of the energetic establishment of polymorphic phases in the A_2B_6 compounds, according to which the stability of the ZB structure rise in the series CdS-ZnS-CdSe-ZnSe-CdTe-ZnTe. Therefore, the existence of an unstable hexagonal phase in ZnMnS films can not be discarded.

In addition, the powder mixture (charge) that was used to obtain $Zn_{1-x}Mn_xS$ thin films was two-phase, which led to the formation of wurtzite peaks at a higher temperature (Figure 5.15 a). The reason for this lies, first of all, in the energy plan of the formation of sphalerite and wurtzite phases of compounds. Earlier it was found [309], that for zinc sulfide the difference between these energies (the formation of sphalerite and wurtzite) is equal to "0", that is, the formation of these phases has the same probability. At $T_s > 673$ K (400 °C) in the films of $Zn_{1-x}Mn_xS$, there are traces of the hexagonal phase, the amount of which somewhat increases with increasing temperature of growth. Most reflections on the diffractograms are fixed only from the plane $(100)_w$, $(002)_w$, $(100)_w$ and $(103)_w$ wurtzite, indicating the presence of a texture in this phase (Figure 5.15 b). Thus, high-temperature deposited films $Zn_{1-x}Mn_xS$ with 7 % nominal values of Mn are two-phase. Comparing with pure ZnS films [301], this compound also tends to change the cubic structure to hexagonal with increasing growth temperature

5.2. Structural and morphological properties of $Zn_{1-x}Mn_xS$ thin films

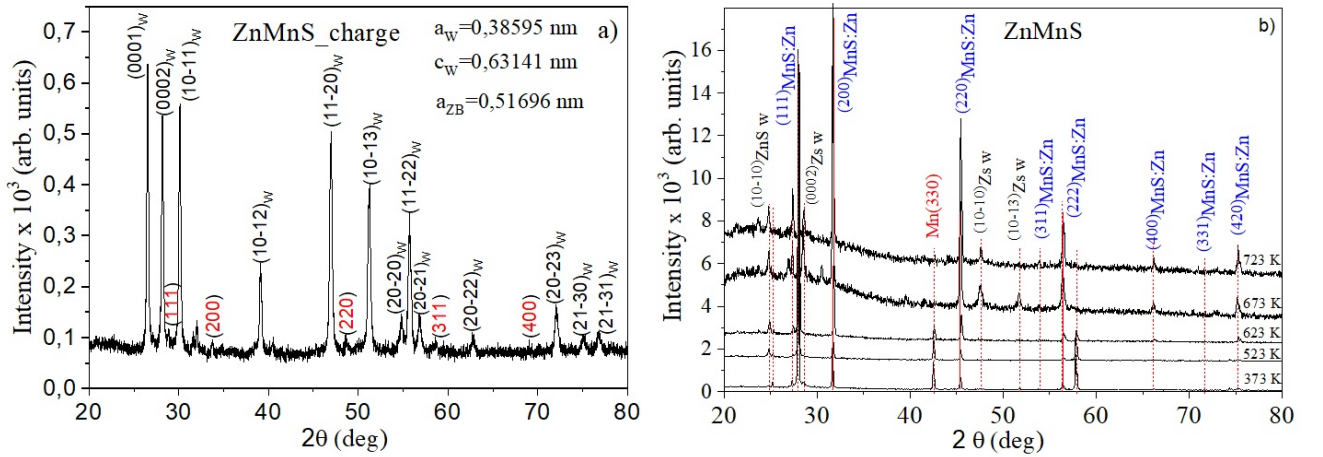


Figure 5.15: The diffractograms from the charge at RT (a) and the $Zn_{1-x}Mn_xS$ films (b) obtained under different growth temperatures.

at > 573 K (300 °C). In the works [316–319], it was shown that the main peaks for ZnMnS films are the peaks corresponding to the (111), (220) and (311) planes, of the cubic zinc blend structure.

Usually, the real concentration value of the alloyed element does not coincide with its nominal value. For this reason, it is necessary to calculate this value after the process of obtaining films. Investigation of the elemental composition of solid solutions films was carried out using a scanning electron microscope REMMA-103-01 by X-ray spectral microanalysis (EDX). For the transition from mass concentration to atomic (C_i), the standard equation is used in [320]. To estimate the deviation of films composition from stoichiometry, relations of atomic concentrations C_A/C_B , C_{A+Mn}/C_B were used. The corresponding results for a series of samples obtained under different growth substrate temperature conditions are given in the Table 5.7. Measurements were made at several points of the samples surface. It should be noted that, with the accuracy of the method, not significant changes of the solid solution composition over the area of the film was detected.

Ts, K (°C)	Zn, wt %	Mn, wt %	S, wt %	Zn, at %	Mn, at %	S, at %	C_{Zn}/C_S	C_{Zn+Mn}/C_S
Charge	72.50	6.86	20.64	59.06	6.65	34.29	1.72	1.92
373 (100)	20.94	8.55	70.51	11.97	5.82	82.21	0.15	0.22
523 (250)	73.09	3.00	23.91	58.27	2.85	38.88	1.50	1.57
623 (350)	69.70	3.17	27.14	54.11	2.48	42.96	1.26	1.33
673 (400)	69.06	2.61	28.33	53.15	2.39	44.46	1.20	1.25
723 (450)	66.69	1.96	31.35	50.16	1.75	48.08	1.04	1.08

Table 5.7: Results of the determination of the elemental composition of $Zn_{1-x}Mn_xS$ films with 7% of nominal values of Mn

Chapter 5. Effect of Mn alloying on structural and optical properties of ZnTe and ZnS thin films

The typical characteristic spectra of X-ray spectroscopic microanalysis of the blend (charge) and the $Zn_{1-x}Mn_xS$ film sample are shown in Figure 5.16. It can be seen that only the lines of major solid solution components are manifested in the spectra. Uncontrolled and residual impurities were not observable within the limits of the method accuracy. Figure 5.17 shows the dependences of the atomic concentration of C_{Mn} (a) and the ratio C_{Zn}/C_S , C_{Zn+Mn}/C_S (b) at the growth temperature of the material. The dashed lines in the figure correspond to the value of these ratios in the charge powder.

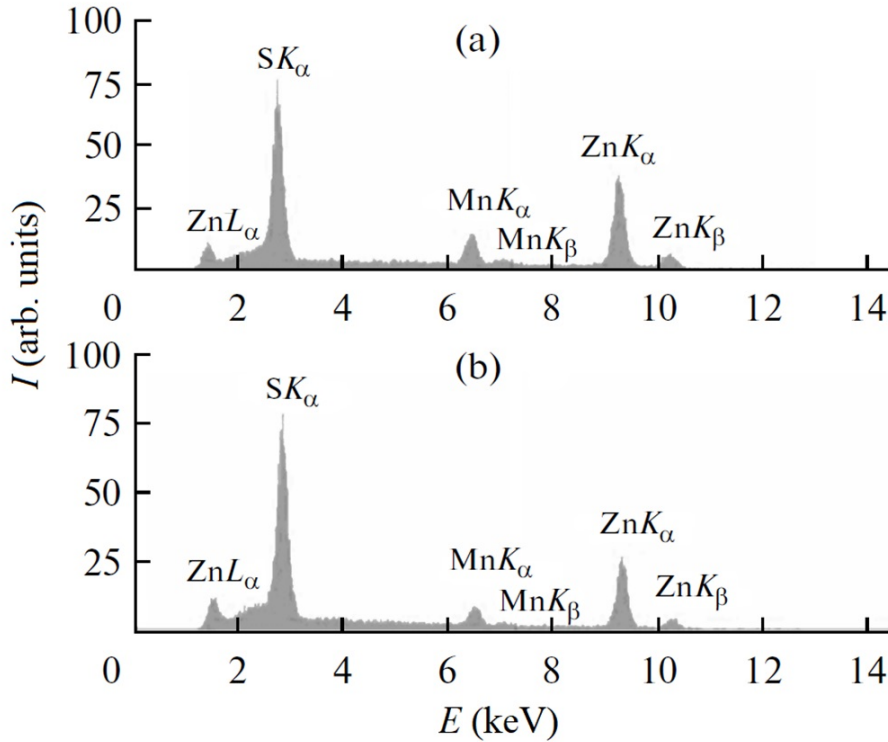


Figure 5.16: (a) Fragments of characteristic X-ray spectra (EDAX) from the charge and (b) the film of the $Zn_{1-x}Mn_xS$ solid solution obtained at $T_s = 673$ K (400 °C) and $T_e = 1273$ K (1000 °C).

Studies have shown that with increasing in the substrate's temperature from $T_s = 373$ K to 723 K (100 to 450 °C), the atomic concentration of manganese in $Zn_{1-x}Mn_xS$ films monotonically decreases from 5.82 to 1.75 at. %, while the ratio of the total atomic concentration of zinc and manganese (C_{Zn+Mn}) to the atomic sulfur concentration (C_s) initially increases from 0.22 to 1.57 ($T_s = 623$ K [350 °C]), and with further growth of the substrate temperature begins to decrease to 1.08 ($T_s = 723$ K [450 °C]) which is the more ideal stoichiometric proportion between the elements. These results correlate with EDAX analysis for ZnS films presented in paper [310] for the growth temperature 373-673 K (100 to 400 °C) where it was shown, that, the Zn/S ratio of the films decreases from 1.19 to 1.04 with rising of substrate temperature,

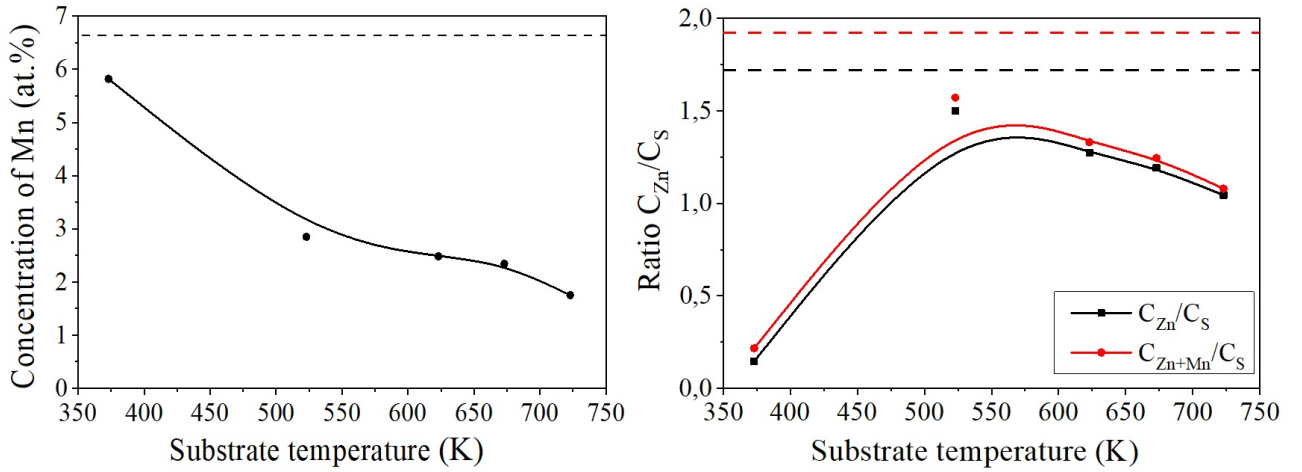


Figure 5.17: Dependence of the atomic concentration of C_{Mn} (a) and the ratio C_{Zn}/C_S (1), C_{Zn+Mn}/C_S (2) (b) at the growth temperature.

following to a more ideal value of the ratio. As can be seen from the table, the atomic Mn content in the charge did not differ much from the initial nominal values of 7 % calculated before the synthesis of the charged material that was 6.65 at. % measured using EDX.

The lattice parameter of A_2B_6 compounds is a characteristic extremely sensitive to changes in the stoichiometry of the material, the introduction of impurities, oxidation, and so on, in fact precisely the lattice parameter measurement makes possible to study these changes. The lattice constant of the material was found both at the position of the $K_{\alpha 1}$ component line (111) under the XRD definition at the large corners, and by the Bradley-Jay and Nelson-Riley extrapolation methods. It should be noted that the results obtained by both extrapolation methods are well consistent with each other, although the Nelson-Riley method is more accurate (0.001 % vs. 0.002 % for the Bradley-Jay method [321]). Therefore, we will mainly analyze the results obtained by Nelson-Riley method.

The results of determining the lattice parameter of $Zn_{1-x}Mn_xS$ films by two approximative methods are given in Table 5.8. The dependence of the stable lattice values obtained with the use of three methods from the substrate temperature is shown in Figure 5.18.

Experimental values of the lattice parameter of $Zn_{1-x}Mn_xS$ in the films are in the range of $a = 5.6406$ - 5.6424 Å. As can be seen from Figure 5.18, the dependence of the crystallographic constant of the film material on the growth temperature is complex. In the layers obtained at low temperatures ($T_s \approx 373$ K [100 °C]), the chalcogenide lattice parameter is slightly higher than in high-temperature ones. With further increasing substrate temperature up to 673 K (400 °C), an increase in the crystallographic constant to $a = 5.644$ Å was observed. Finally, in the high-temperature conditions, the lattice period again decreases to $a = 5.6406$ Å. The beha-

Chapter 5. Effect of Mn alloying on structural and optical properties of ZnTe and ZnS thin films

T_s , K ($^{\circ}\text{C}$)	Mn content by EDX (at %)	a_{ZnMnS} , Å		
		Nelson-Riley (± 0.01 %)	Bradley-Jay (± 0.02 %)	Line [111]
373 (100)	5.82	5.6423	5.6322	5.6465
523 (250)	2.85	5.6424	5.6420	5.6428
623 (350)	2.48	5.6420	5.6404	5.6430
673 (400)	2.39	5.6440	5.6353	5.6500
723 (450)	1.75	5.6406	5.6367	5.6425
$a_{\text{ZnS}} = 5.406$ Å, $a_{\text{MnS}} = 5.6147$ Å				

Table 5.8: The value of the lattice parameter of $\text{Zn}_{1-x}\text{Mn}_x\text{S}$ found by different methods.

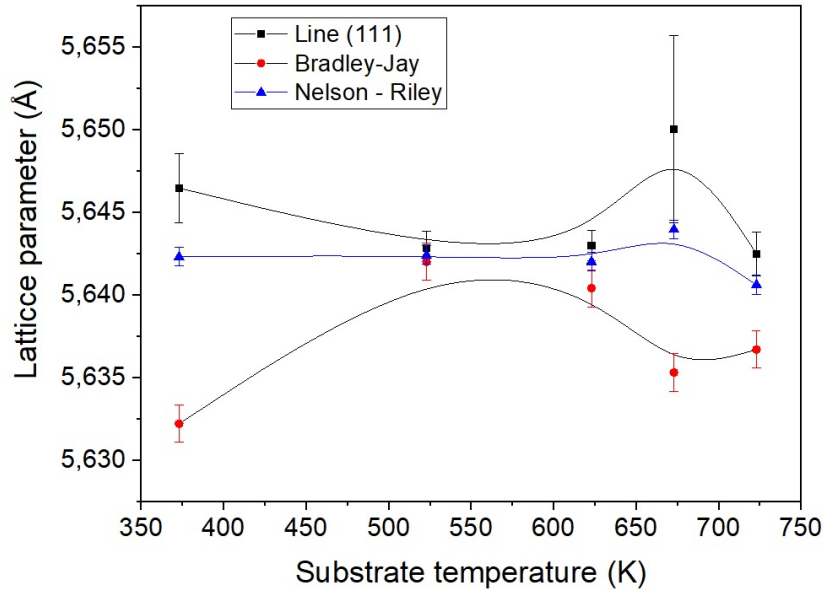


Figure 5.18: The dependence of lattice parameter of $\text{Zn}_{1-x}\text{Mn}_x\text{S}$ film as a function of the growth temperature T_s : ■ - Using position of the $K_{\alpha 1}$ component line [111]; ● - by the Bradley-Jay method; and ▲ - Nelson – Riley method. The error bar shows the deviation from the average value calculated for each point.

viour of the lattice parameter at 673 K (400 $^{\circ}\text{C}$) can be explained by the fact that this point can serve as a transition temperature when the growth mode changes from planar to columnar at $T > 623$ K (350 $^{\circ}\text{C}$). At the same time, XRD measurements showed that at this temperature the hexagonal phase begin to appear, and the number of crystallites with ones in samples obtained at the (222) orientation sharply increases in comparison with the average temperatures (523-623 K [250-350 $^{\circ}\text{C}$]). For comparison, ZnS films had smaller lattice parameter, which varied in the range $a = 5.4060$ -5.4196 Å, depending on the temperature [322]. In [323] the authors produced ZnS:Mn in nanocrystalline form by a chemical method and obtained somewhat smaller

5.2. Structural and morphological properties of $Zn_{1-x}Mn_xS$ thin films

values of the lattice period, while this parameter decreased with increasing concentration of manganese in compounds.

Earlier in Section 5.1.2 was mentioned that the crystal ionic radius of Zn^{2+} ions (88 pm) is lesser than ionic radius of Mn^{2+} ions with high spin state (97 pm). The large value of the lattice constant with the presence of manganese suggests that the Zn^{2+} ions are partially substituted by the bigger Mn^{2+} ones, which corresponds to the results obtained in this work, similarly to the case of $Zn_{1-x}Mn_xTe$.

5.2.3 Out-plane orientation of films

The high intensity of the (200) peak in the X-ray diffraction patterns indicates the preferred orientation of the films, which we will check using texture analysis (texture coefficients and the degree of preferred orientation, f). As well as $Zn_{1-x}Mn_xTe$, $Zn_{1-x}Mn_xS$ films had $N = 6$ of major directions of X-ray diffraction (111, 200, 220, 222, 400 and 420). The value for a perfectly oriented sample is $f = \sqrt{N - 1} = 2.236$. Texture coefficient values and preferred orientation of films obtained from X-ray diffraction patterns of the samples are shown in Table 5.9.

	(111)	(200)	(220)	(222)	(400)	(420)	f	Mn content by EDX (at %)
Perfectly oriented							2.236	
373 K (100 °C)	0.039	2.486	0.174	2.121	0.278	0.901	0.966	5.82
523 K (250 °C)	0.115	2.850	0.164	1.160	0.580	1.132	0.924	2.85
623 K (350 °C)	0.044	3.756	0.166	1.041	0.229	0.764	1.282	2.48
673 K (400 °C)	0.068	3.761	0.234	1.724	0.212	0.810	1.368	2.39
723 K (450 °C)	0.061	2.965	0.222	1.637	0.216	0.898	1.236	1.75

Table 5.9: Texture coefficients and degree of preferred orientation (f) in $Zn_{1-x}Mn_xS$ films with 7 % of nominal values of Mn deposited over glass at various substrate temperatures.

Figure 5.19 shows that for all temperatures the dominant crystallographic planes of crystallites are the (200). For a lower temperature [373 K (100 °C)] a large number of crystallites have an orientation (222), but this value decreases at middle temperatures (523-623 K [250-350 °C]) and again increases at high temperatures (673-723 K [400-450 °C]) when hexagonal phase appears. The degree of preferential orientation f is almost 2-2.5 times less than the corresponding to a perfectly oriented sample and increases with rising of substrate temperature. The texture coefficients of the (200) oriented samples, as well as the value of f , increase with an increase in the substrate temperature, but at 723 K (450 °C), this value decreases, which is associated with an increase in crystallites with the (222) orientation.

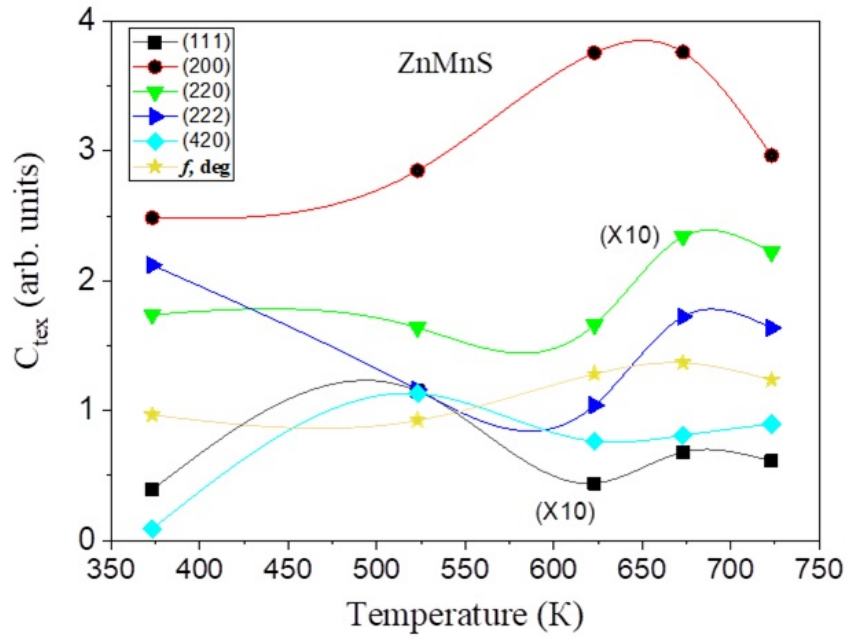


Figure 5.19: Texture coefficients for some major directions obtained from $Zn_{1-x}Mn_xS$ films deposited over glass at various substrate temperatures [from 623 K to 923 K (350 °C to 650 °C)].

5.2.4 In-plane orientation of films

Calculations using the method of reversed pole figures allowed to reveal the axial growth texture [111] in $Zn_{1-x}Mn_xS$ films with cubic structure, whose perfection improved with increasing samples thickness and depended on the growth temperature of obtained films (see Figure 5.20).

Reducing texture of layers of chalcogenides in the region of lower substrate temperatures is most likely due to the change in the mechanism of growth from planar to columnar with increasing temperature, as described above. The deterioration of the texture quality of reversed pole figures of the (111) axial cubic peak of the films with increasing growth temperature was observed. It should be noted that a similar texture in the cubic films of $A_{II}B_{VI}$ compounds is predominant, since this direction coincides with the direction of the fastest growth of crystallites. For higher temperatures, structures (220) or (420) can also be observed. These films show similar results with the ZnS compounds that was obtained by our group in another work [309].

The substructure features of $Zn_{1-x}Mn_xS$ films obtained by the CSVS method have been little studied. Nevertheless this compound has unique photoluminescence and magneto-optical properties, which can be affected by the substructural properties. Thus the study, analysis and

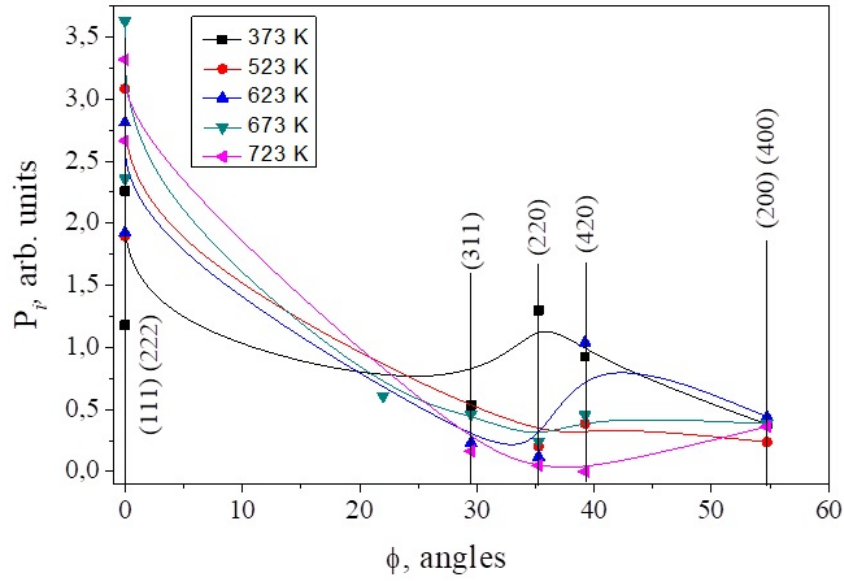


Figure 5.20: The dependence of the pole density P_i on the angle φ between the axis of the texture and the normal to the reflecting plane for the $Zn_{1-x}Mn_xS$ films: $T_s=373$ K (■), 523 K (●), 623 K (▲), 673 K (▼), 723 K (◄).

control of this properties can drive the possibility of creating a number of devices for micro- and optoelectronics, photovoltaics and spintronics. The effectivity of these devices depends on the transport properties of the free charge carriers (by the product of the mobility and the lifetime), which in turn are determined by the recombination centers concentration in the material. In this case, the surface and various types of semiconductor defects will play the role of recombination centers, which determines the carrier lifetime. At the same time, dislocations, which form small-angle edges of coherent scattering domains (CSD) and lead to microdeformation, can act as traps for charge carriers, determining the electrophysical characteristics of the material, including the lifetime of charge carriers. Similar role is played by two-dimensional defects such as dislocations. This determines the relevance of the study of ZnMnS films substructure parameters, depending on the growth parameters at which the concentration of defects is minimised.

To determine the size of the CSD, the level of microstrain and dislocations concentration in the chalcogenide films, we have chosen the X-ray method. For research of semiconductor films of chalcogenides, the newest methods of analysis of diffractograms were rarely used. It is usually assumed that the physical extension of the diffraction peaks is due only to the dispersion of the CSD, then Debye-Sherer formula can be used to determine the size of the sub-blocks $L = k\lambda/\beta \cos \theta$, where $k \sim 0,9$ – a coefficient that is weakly dependent on the grain shape.

Chapter 5. Effect of Mn alloying on structural and optical properties of ZnTe and ZnS thin films

As the study has showed, the physical broadening of reflections from planes (111) and (222) of the cubic phase was greater than (200) and (400). If we consider that the CSDs are evenly axial, and the additional extension of the lines (111) and (222) is related to the presence of the growth defects, we can calculate the concentration of the total amount of deformation and defects in films [239].

5.2.5 Coherent scattering domain and microdeformations

It is known [239, 241] that the magnitude of the microdeformations ε and the size of the CSD L can be used to estimate the average density of dislocations in films. The study of substructural characteristics of films was carried out by extension of the diffraction peaks (111) - (222) and (200) - (400).

The results of the determination of L and ε in $Zn_{1-x}Mn_xS$ films obtained using X-ray peaks of the Cauchy and Gauss functions without taking into account the anisotropy in the samples are given in Table 5.10. As can be seen from the table, the values of the substructural parameters obtained using various approaches are fairly well correlated with each other. However, these approximations allow us to determine only the largest values of the size of the CSD (L) and the smallest values of the microstrains ε in the films, because the experimental error of determination of these values can reach (30-50) %.

For films of chalcogenides with a cubic structure, the dependence of the size of the CSD in the direction [111] and the level of microdeformations in the same direction on the substrate temperature obtained using the triple convolution method are shown in Figure 5.21. As can be seen from the figure, the dependence, of L and ε the values obtained by different methods is similar.

Mn content		(hkl)	L, nm		$\varepsilon, 10^{-3}$			α', K	
$T_s,$	by EDX		Approximation by		From	Approximation by			From
K ($^{\circ}C$)	(at %)		Gauss	Cauchy	convolution	Gauss	Cauchy		convolution
373	5.82	(111)-(222)	41.7	49.1	42.3	1.73	0.71	1.32	2.12
(100)		(200)-(400)	22.8	20.0	23.0	2.08	1.47	1.35	
523	2.85	(111)-(222)	71.7	127.4	83.9	2.45	1.83	2.16	1.73
(250)		(200)-(400)	34.1	46.1	35.7	2.73	1.66	2.22	
623	2.48	(111)-(222)	41.7	47.3	42.1	1.47	0.48	1.10	1.23
(350)		(200)-(400)	70.9	121.4	81.4	2.02	1.43	1.76	
673	2.39	(111)-(222)	53.4	76.6	56.9	2.29	1.45	1.90	0.87
(400)		(200)-(400)	82.0	173.8	106.2	2.37	1.88	2.16	
723	1.75	(111)-(222)	58.0	78.0	60.6	1.82	1.02	1.47	0.02
(450)		(200)-(400)	58.7	72.1	59.9	1.22	0.50	0.94	

Table 5.10: Features of $Zn_{1-x}Mn_xS$ films obtained using various approximations.

5.2. Structural and morphological properties of $Zn_{1-x}Mn_xS$ thin films

Since the parameters of the films substructure, determined by the triple convolution method, are the most accurate and close to the real ones; further discussion of the results and additional calculations were carried out for them.

As a result of the research, it was established (Figure 5.21, a) that with increasing T_s the size of the CSD in the direction perpendicular to the planes (111) in the $Zn_{1-x}Mn_xS$ films, initially increases from $L \sim 42$ nm to $L \sim 84$ nm, and then decreases to $L \sim 61$ nm. There is an optimal temperature interval $T_s = 500$ -550 K, in which this size is maximal. The unalloyed ZnS films obtained by us [309] had a lower CSD ($L = 33.4$ -54.0 nm), which suggests that alloying with Mn increase crystalline regions of material that scatter coherently (and, in general, they show no coherence with the neighboring ones).

The level of microstrain in $Zn_{1-x}Mn_xS$ films in the direction [111] monotonically increases with growth temperature from $\varepsilon \sim 1.32 \times 10^{-3}$ to $\varepsilon \sim 2.16 \times 10^{-3}$, and then decreases to $\varepsilon \sim 1.10 \times 10^{-3}$, after that it rises again to $\varepsilon \sim 1.90 \times 10^{-3}$ (Figure 5.21, b). This generally correlates with other similar data for ZnS films [309] - the level of microstrains has changed in the range $\varepsilon = (0.83 - 2.72) \times 10^{-3}$ depending on the temperature. This change at higher temperatures can be explained by transit from the growth of long to small columns at $T_s > 623$ K ($350^\circ C$), as well as a reduction of Mn content.

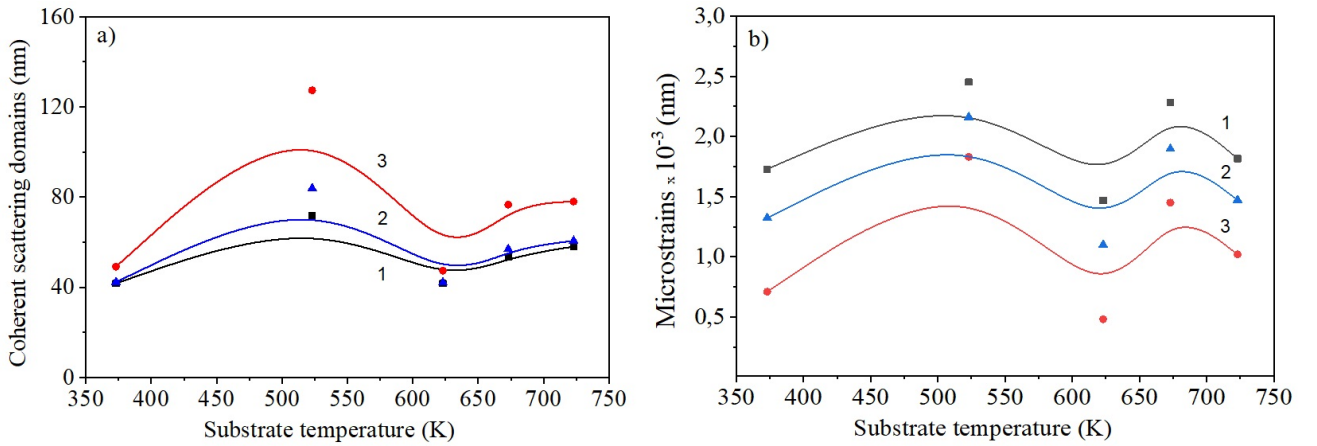


Figure 5.21: Influence of the substrate temperature T_s on the size of the CSD L (a) and the level of microstrains (b) of the $Zn_{1-x}Mn_xS$ films. Approximation was performed by the method of Cauchy (1), Gauss (2) and triple convolution (3).

5.2.6 Density of dislocations and defects

From the determined values of microdeformation, using the expression for Hooke's law $\sigma = E\varepsilon$, we have calculated the level of microstress in the investigated films (Table 5.11). In doing so, the values of Young's modulus for ZnS films $E=75$ GPa [301] and microdeformation from the table 5.10 was used. It is shown that, for example, in ZnMnS films, the level of microstress varies in the interval $\sigma = (85.5-162.0)$ MPa. The obtained values of the microstrain level in the range $T_s = 373-723$ K (100-450 °C) were commensurate with the values for pure ZnS deposited by close-spaced evaporation [301], where Kurbatov et al. showed a monotonic decrease in σ from 200 MPa to 30 MPa with an increase in substrate temperature in the range of 373-973 K (100-700 °C).

The low-angle boundaries of the CSD of different materials are formed by dislocations, while the dislocations, located in the volume of the block, lead to the appearance of microstrains. This allows us to estimate the average density of dislocations in films of chalcogenides by the magnitude of microdeformations ε and the size of CSD L .

T_s , K	(hkl)	L , nm	ε , 10^{-3}	σ , MPa	ρ_L , 10^{14} lin/m ²	ρ_ε , 10^{14} lin/m ²	$\rho_{L\varepsilon}$, 10^{14} lin/m ²
373	(111)-(222)	42.3	1.32	99.0	1.68	2.05	1.33
523	(111)-(222)	83.9	2.16	162.0	0.43	5.47	1.10
623	(111)-(222)	42.1	1.10	85.5	1.70	1.42	1.11
673	(111)-(222)	56.9	1.90	142.5	0.93	4.22	1.42
723	(111)-(222)	60.6	1.47	110.3	0.82	2.54	1.03

Table 5.11: Microdeformation and dislocation density in $Zn_{1-x}Mn_xS$ films.

We used values L and ε in direction [111]. As can be seen from Table 5.5, the obtained data, with the use of various theoretical models within the order of degree, correlate with each other. The investigated films of chalcogenides are characterized by a rather low concentration of dislocations (Figure 5.22). Calculations show that they are mainly concentrated on the boundaries of the CSD, the volume of crystallites is practically free of dislocations. Mn content of the compound films decreased with rise of growth temperature and the ρ value, determined after the (111)-(222) reflections, first decreases, and with a subsequent increase in T_s , it increases. There is an optimal Mn content ~ 2.9 at. % in the range of $T_s = 500-600$ K, at which the density of dislocations in the CSD bulk of the samples is minimal.

When determining the CSD size in chalcogenide films by triple convolution analysis, the usually calculated values of $L_{(h00)} > L_{(hhh)}$. This can be explained as follow: either the CSDs are in fact uneven, their dimensions in the direction perpendicular to the crystallographic planes

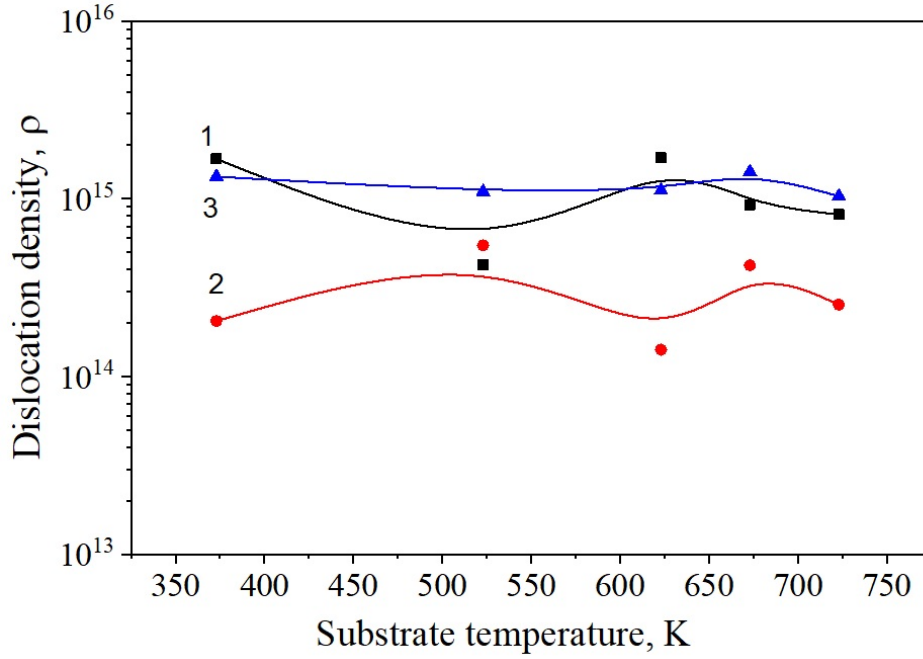


Figure 5.22: Dependence of the density of dislocations with reduction of Mn content at higher temperature in $Zn_{1-x}Mn_xS$ films: near the subgrain boundaries (1), in their bulk (2) and the general dependence (3) using reflexions (111) - (222).

(111) are smaller than in the direction perpendicular to (200), or the CSD are equal, but their contribution to the physical extension of the lines that correspond to the reflections from the planes with (hhh), gives growth defects [239, 321].

Let's consider in more detail the first assumption. As established from the research, the size of the CSD is significantly smaller than the grain size. We can assume that these sizes in the direction perpendicular to the [111] planes are confined to the twins, the deformation defects and the CSD themselves are in the form close to cylindrical. In this case, the height of the cylinder $L_{(hhh)}$, as evidenced by simple geometric constructions, is slightly smaller than its diameter.

If we assume that the CSDs are equal, and the additional extension of the peaks(111) and (222) is associated with the presence of microdeformation defects, one can calculate the concentration of the number of deformation and growth defects α' . The results of the calculation of the total concentration (in %) of the deformation and growth defects α' in the films of the compound $Zn_{1-x}Mn_xS$ are given in Table 5.10 and in Figure 5.23.

As can be seen from Figure 5.23, the total concentration of defects α' in $Zn_{1-x}Mn_xS$ films varies with the temperature of the substrate from 2.12 % ($T_s = 373$ K [100 K ($^{\circ}C$)] to 0.02 % ($T_s = 723$ K [450 K ($^{\circ}C$)]). For non-alloyed compounds, the value of ZnS was $\alpha' = 0.02$ -1.51 % and increased with increasing temperature [309].

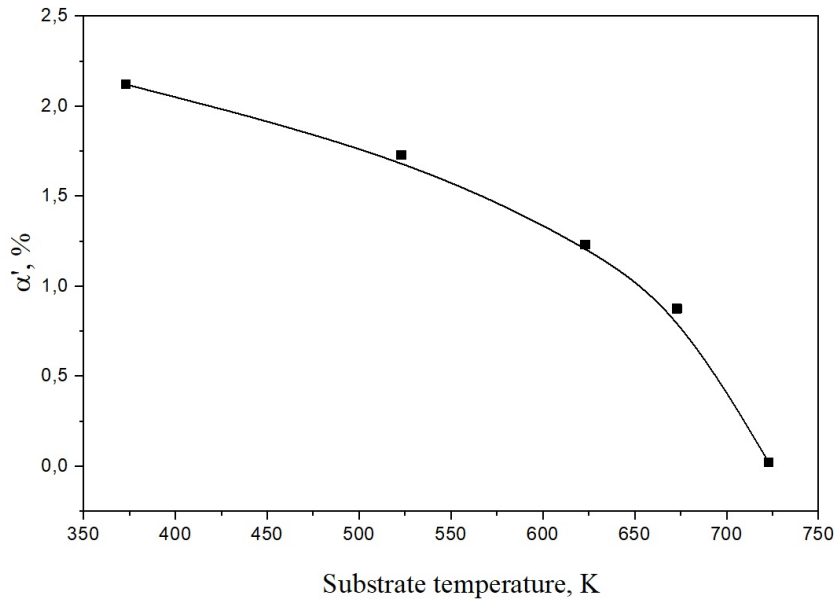


Figure 5.23: Dependence of the amount of deformation and growth defects in $Zn_{1-x}Mn_xS$ films plotted using of eq. (3.25).

With increasing T_s stability of the cubic component of the film increases, the probability of violation of the order of alternation of planes (111) decreases, respectively, decreasing the concentration of defects.

The results of the research show that the features of the substructure of the chalcogenide films are primarily due to their thermodynamic properties: small change in the energy of the crystalline lattice during the phase transition of the sphalerite - wurtzite, low interphase energy when these phases are isomorphic to the planes, and as a result of that, high probability of error in the alternation of tightly packed planes. The violation of the order of laying these planes leads to the formation of growth defects in the films, twins and layers of the hexagonal phase, specially conjugate to the cubic matrix. These defects finally determine the features of the substructure of films.

5.3 Optical (spectral) studies

5.3.1 Transmittance and Reflectance (Band gap determination)

Transmittance spectra of $Zn_{1-x}Mn_xTe$ and $Zn_{1-x}Mn_xS$ thin films was studied in the spectral range of 190-1100 nm (Figure 5.24). We studied 3 series of samples with different growth times. For the $Zn_{1-x}Mn_xS$ films the growth time was usually 15 minutes (hereinafter - series 1) and for $Zn_{1-x}Mn_xTe$ films growth time was 4 and 10 min (hereafter - series 2 and series 3), respectively. Other experimental parameters can be seen in the Table 2.10. As shown in Figure 5.24 (a), transmittance of $Zn_{1-x}Mn_xS$ films increases upon reaching the "red border" at 340-350 nm with the slight decreasing of wavelength at up growth temperature, and it was in the range of $T_1 \sim (65 - 80) \%$ at a wavelength of 1000 nm depending on the sample. This value is slightly lower for two-phase films [$T_s > 623$ K (350 °C)]. On the other hand, for $Zn_{1-x}Mn_xTe$ films a sharp fall of transmittance at wavelengths < 540 nm can be detected, which points to a good crystallinity of the deposited films. It was found that the transmittance was in the range $T_2 \sim (55 - 95) \%$ and $T_3 \sim (40 - 70) \%$ for the series 2 and series 3, respectively. The various crystallographic and phase structure and the actual composition of the samples grown under different growth conditions causes the difference in their transmittance coefficient. As shown above, the samples obtained at a growth temperature > 773 K (500 K (°C)) had a very low concentration of manganese in their composition. The analysis shows that the maximal value of the optical transmittance are for the $Zn_{1-x}Mn_xTe$ films obtained at the substrate temperature $T_s = 623$ K (350 °C), the minimal value corresponds to the $T_s = 923$ K (650 °C). In addition, for a given wavelength of the incident radiation and the thickness of the samples the transmittance curves acquire an oscillating character of interference as shown in Figure 5.24 (b) and Figure 5.24 (c). The same behavior of transmittance curves was obtained by Aqili et al. [324] for two-sourced thermal evaporated ZnTe thin films onto glass substrate.

The diffuse reflectance reached values of $R_1 \sim (1 - 9) \%$ (for $Zn_{1-x}Mn_xS$), $R_2 \sim (1 - 15) \%$ and $R_3 \sim (15 - 30) \%$ (for $Zn_{1-x}Mn_xTe$) for series 1, series 2 and series 3, respectively (Figure 5.25). A similar situation was observed when calculating the specular reflectance of light (Figure 5.26). Unlike diffuse reflection, in which light is reflected from all rough surfaces at different angles, at specular reflection, the angle of reflection of the beam coincides with the angle of the incident light. It was observed that with decreasing Mn content the coefficient R also increased, which is obviously due to the emergence of films with pronounced pyramidal relief, ie increasing the surface roughness of the samples. The distance between interference peaks, both transmission and reflection, will depend on the thickness of the films. According to the diffraction law (Fabry-Perot interference law), the distance between the maxima (minima) of the interference curves will decrease with rising material thickness.

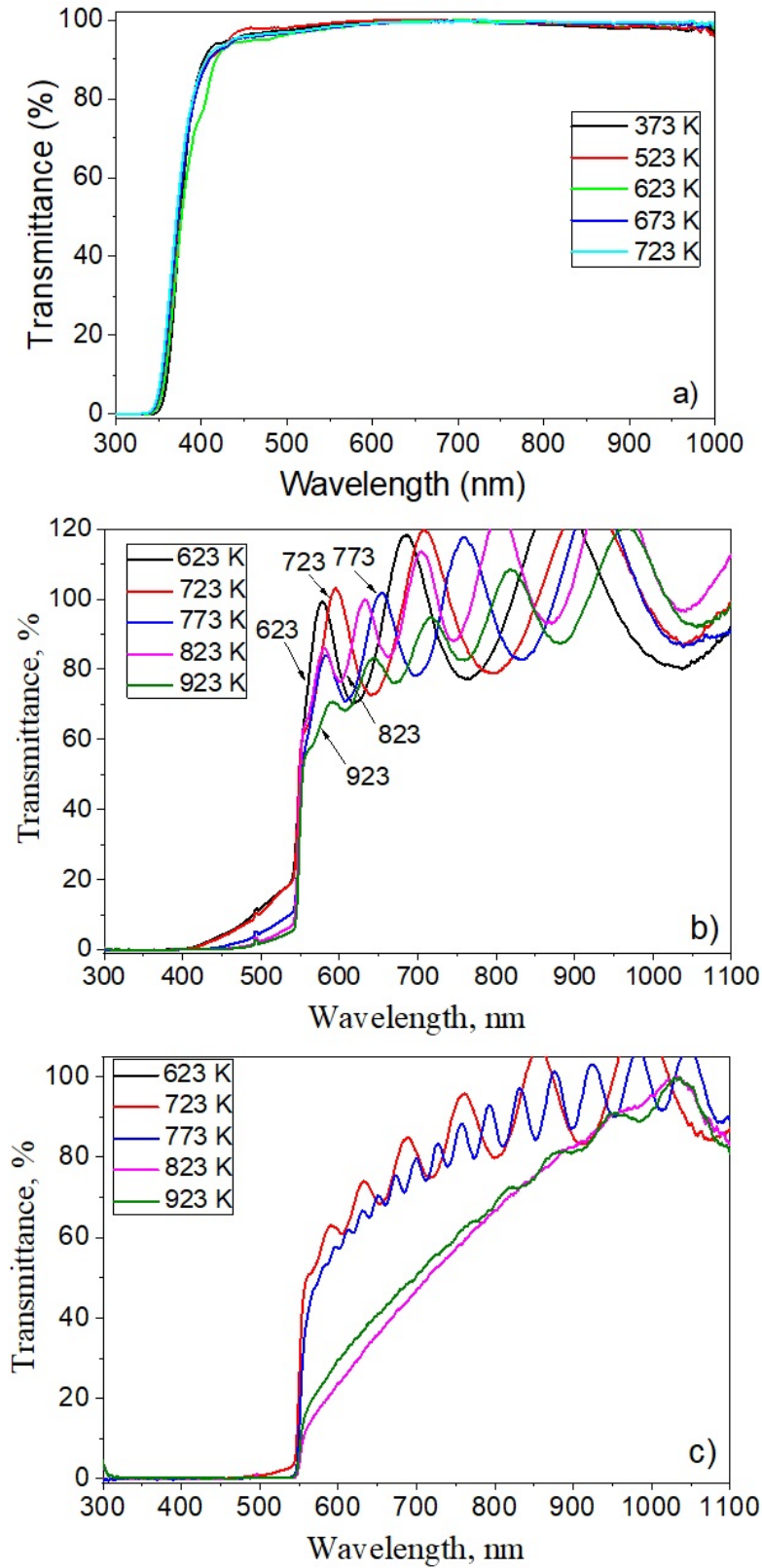


Figure 5.24: Normalized transmittance spectra of (a) $Zn_{1-x}Mn_xS$ films (series 1) and (b and c) $Zn_{1-x}Mn_xTe$ films (series 2 and series 3, respectively)

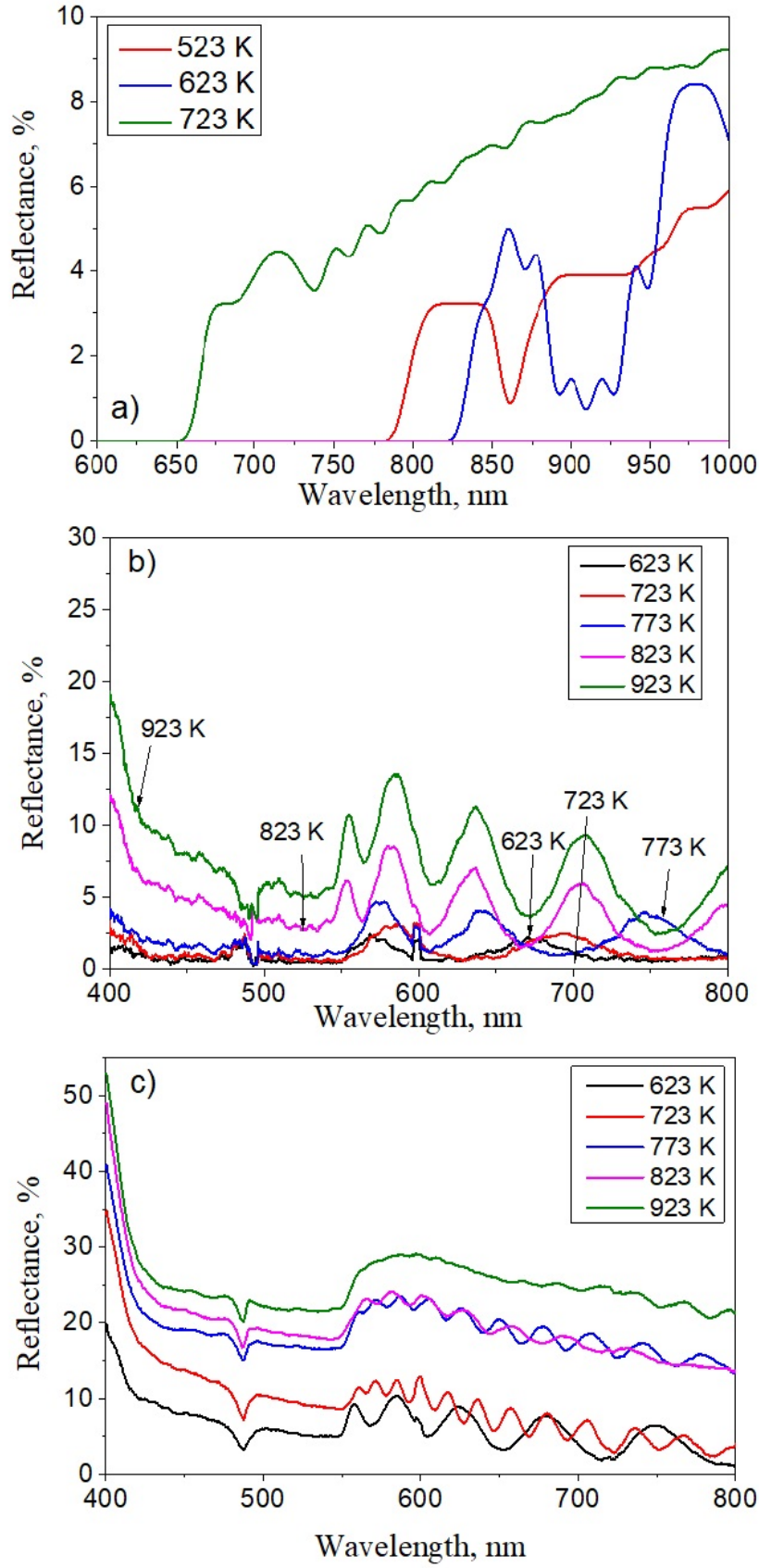


Figure 5.25: Spectra of diffuse reflectance of (a) $Zn_{1-x}Mn_xS$ films (series 1) and (b and c) $Zn_{1-x}Mn_xTe$ films (series 2 and series 3, respectively)

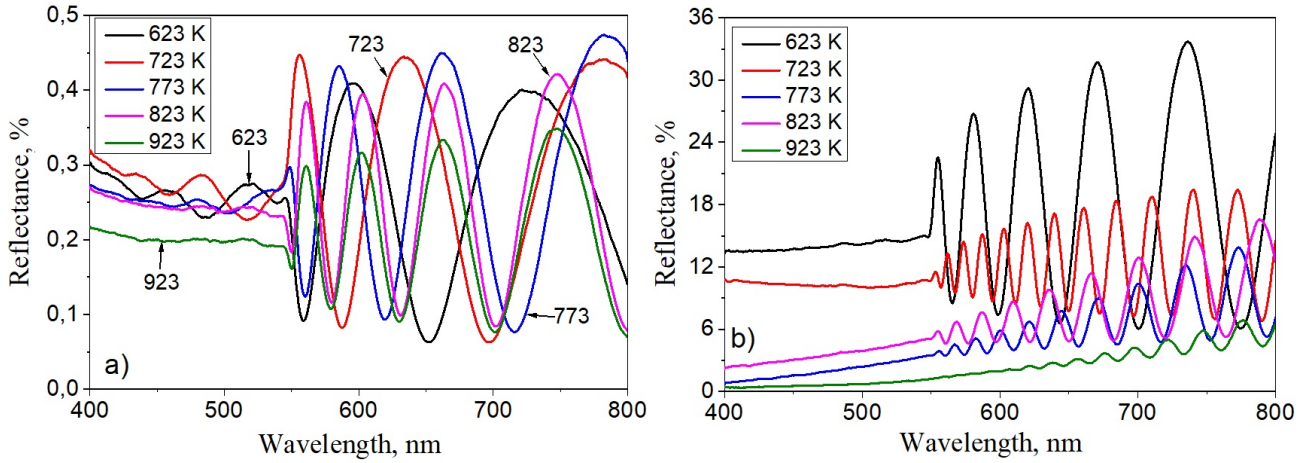


Figure 5.26: Spectra of specular reflection of (a, b) $Zn_{1-x}Mn_xTe$ films (series 2 and 3, respectively)

The difference in the transmittance and the reflectance of films obtained at different growth temperatures is due to different crystalline and phase structure of these samples, roughness, the presence of defects on their surface, and the real composition of alloyed manganese. Ozutok et al. [325] in their work showed that a decrease in the reflectivity of ZnMnS films deposited onto glass substrates by ultrasonic spray pyrolysis technique with the increase of the Mn alloying may be explained by the decrease of the film density. In our case, an increase in the deposition temperature led to a decrease in the Mn content, which corresponds to this suggestion and it is shown in the Figures 5.24 and 5.25 above.

In order to calculate the band gap of the samples, their absorbance was calculated from the transmission using Equation 3.36. Once we have the dependence of absorbance on the energy of the incident light beam, in order to determine the band gap of the layer, we look for the point of maximum slope of the function. In Figure 5.27 and Figure 5.28, we presented both the absorbance spectra for 3 series of samples, and its derivative, calculated using the ORIGIN software, in relation to the energy of the light beam. Thus, the energy of the optical band gap of the layers was determined from the maxima of the absorbance derivative. As can be seen from the Figure 5.27 with the rising of the growth temperature, the intensity of absorbance spectra increases.

In Figure 5.28 (a) can be observed that with reduction of Mn content, the position of the derivative peak shifts towards higher energies from 3.569 eV (for 373 K [100 °C]) to 3.642 eV

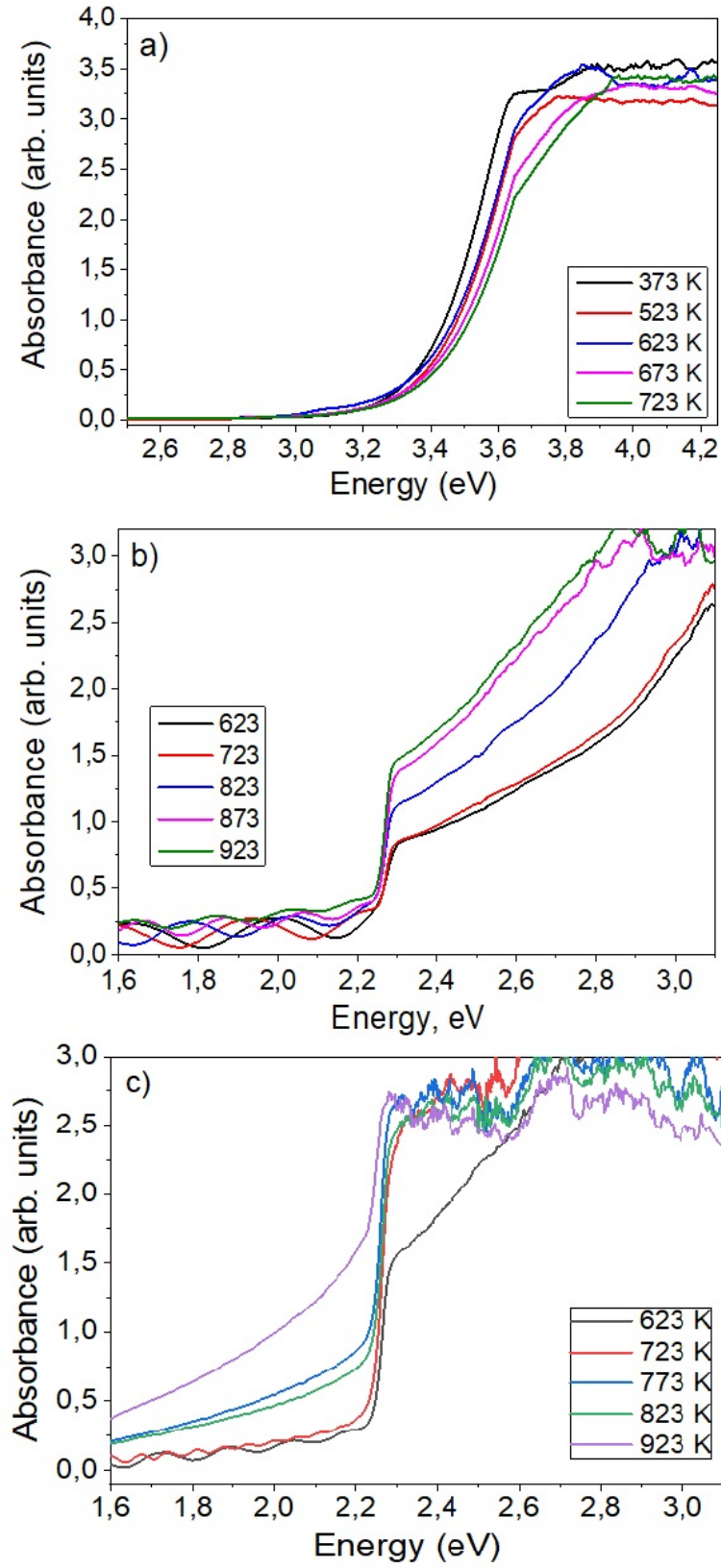


Figure 5.27: The absorbance spectra as the function of the energy of the incident radiation for (a) $Zn_{1-x}Mn_xS$ films (series 1) and (b and c) $Zn_{1-x}Mn_xTe$ films (series 2 and series 3, respectively)

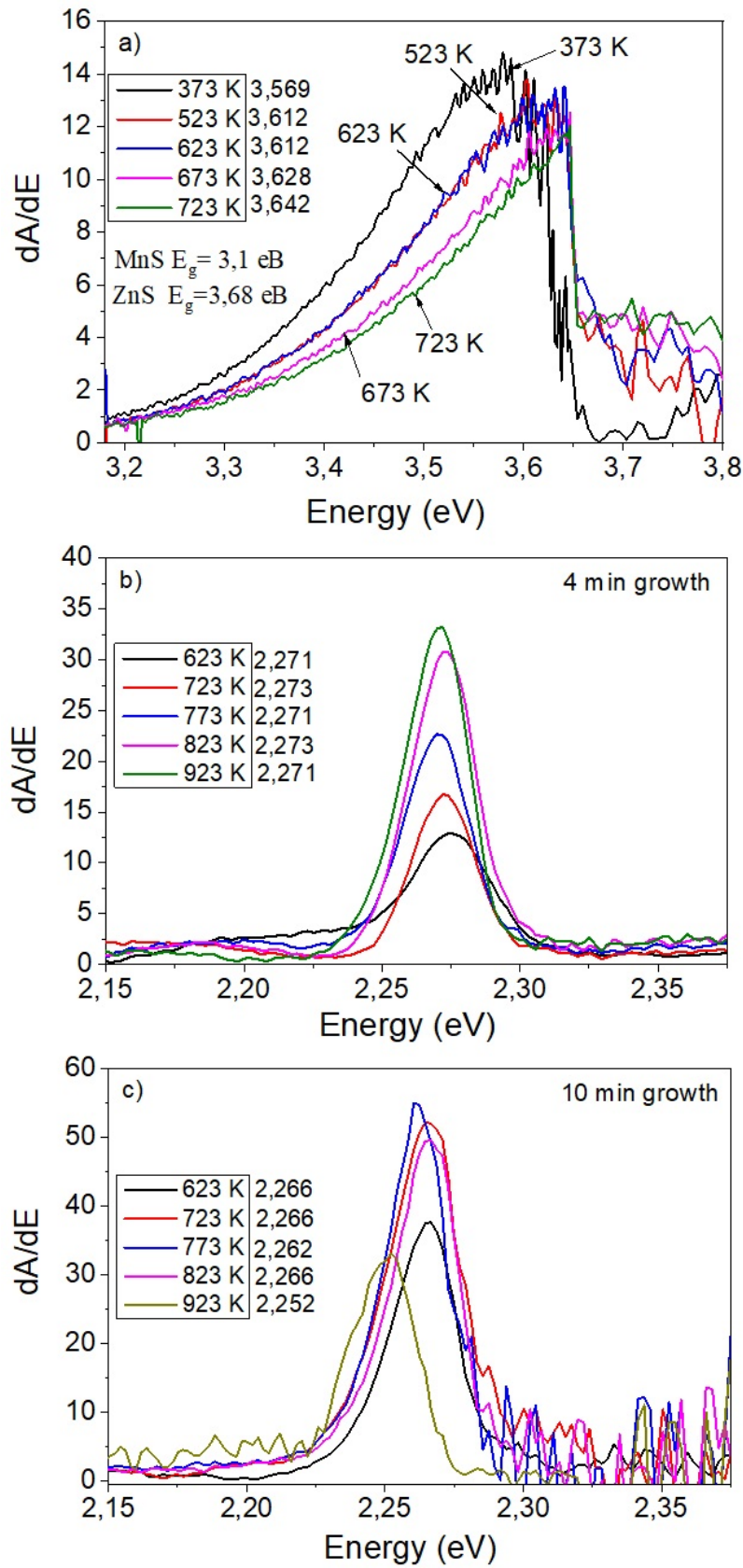


Figure 5.28: The derivative of the absorbance spectra as the function of the energy of the incident radiation for (a) $Zn_{1-x}Mn_xS$ films (series 1) and (b and c) $Zn_{1-x}Mn_xTe$ films (series 2 and series 3, respectively)

(for 723 K [450 °C]). For middle temperatures of 623-673 K (350-400 °C), the position of the peak is almost identical, which may indicate a similar manganese content in the samples. The obtained values of the band gap for $Zn_{1-x}Mn_xS$ films correspond to solid solutions based on MnS ($E_g = 3.1$ eV [326]) and ZnS ($E_g = 3.66$ eV for zinc-blende and $E_g = 3.82$ eV wurzite structure [327]) at room temperature. Hwang et al [310] indicated that in the case of ZnS films deposited by RF magnetron sputtering on glass substrate, an increase in the substrate temperature increases the band gap energy of the films. In their paper, as growth temperature changed from 373 K to 623 K (100 to 350 °C), the optical band gap was red-shifted from 3.45 to 3.79 eV, and slightly decreased to $E_g=3.76$ eV at 673 K (400 °C). In the case of our samples, the increase in the band gap with the rise of temperature is most likely associated with a decrease in the Mn content as a result of its re-evaporation or not incorporation in the transport and deposition processes at higher growth temperature.

Ghosh et al. in their paper [328] grown nanoparticles of ZnS:Mn by radio frequency magnetron sputtering technique on glass and Si substrates at a substrate temperature of 300 K. They found that with increase Mn content from 0 to 9 % the direct band gap of the films vary from 4.12 eV to 3.89 eV and indirect band gap values varied from 3.7 eV to 3.42 eV. It can be seen from previous works that a decrease in the Mn content with an increase in growth temperature as a result of re-evaporation or not incorporation of Mn in the transfer and deposition processes leads to an increase in the films band gap, which is consistent with our results. The relatively small difference in the values obtained at different temperatures is explained by the low content of Mn (or its absence).

On the other hand, in the $Zn_{1-x}Mn_xTe$ films (Figure 5.28 b and c), regardless of the temperature of deposition, the final value of the band gap is about $E_g = 2.26-2.27$ eV. This value is somewhat different from the values, which we obtained for 10 % of Mn content in paper [329] - $E_g = 2.15-2.23$ eV, which is due to changes in the concentration of manganese in films, depending on the growth conditions. The obtained values of E_g are similar with those found for ZnTe single crystals ($E_g = 2.28$ eV) [139] and they are in good agreement with the data of the study of the optical properties of ZnTe samples deposited by the evaporation method in vacuum ($E_g = (2.0-2.2)$ eV) [330] and ($E_g = (2.0-2.4)$ eV) [331].

Chapter 6

Summary and Conclusions

The world of electronics does not stand still, and gradually new interesting compounds and properties are found or already known ones are improved to satisfy all modern needs. Among the variety of II-VI materials, there are 2 sets that have aroused particular interest due to their unique properties. The first group includes the transparent conductor oxides (TCO) materials, which have a high conductivity and visible light transparency, they can be used as electrodes when the situation requires low resistance electrical contacts that do not block the light. Another group consists of Semimagnetic Semiconductors (SMSC) or Diluted Magnetic Semiconductors (DMS), which have significant magnetic and luminescent properties. Each of the materials of these groups has its own advantages and disadvantages in respect some applications, and, depending on the growth method and growth conditions, their properties can change.

In order to control the properties of the material more intentionally, heterojunctions or ternary compounds are used, which make possible to change the properties of the binary structures, thereby expanding the range of technological applications. Although it is often difficult to control the properties of materials with different lattice parameters or different crystalline phases (like wurtzite and zinc blende). Therefore, it is necessary to improve the growth process of obtaining these materials in a systematic and reproducible way, in order to solve the difficulties of put together different lattice structures, reactivity and physical properties.

In the context of the above-mentioned interest, in this thesis we have carried out an in-depth study of the growth and characterization of some functional materials, ternary compounds, and heterostructures based on them, such as ZnO, CdZnO, CdTe/CdO, ZnMnS, and ZnMnTe. In respect to the growth we have chosen two different growth methods: the relatively expensive multi-parameter control system, metalorganic chemical vapor deposition (MOCVD) with direct scale to industrial production, and the less expensive and less controlled parameters Close Sapce Vapor Sublimation (CSVS) method that in some cases and for some applications can be a good alternative.

In this chapter, we will briefly describe the main results obtained in this work and summarize the conclusions.

6.1 II-oxides, ternary compounds and heterostructures based on them.

6.1.1 ZnO studies

With the aim to study thin ZnO films, a series of samples were grown on the R-plane sapphire by the MOCVD method in the temperature range of 300-400 °C (with a step of 25 °C). Diethyl zinc (*DEZn*) and tert-butanol (*TBA*) were the precursors for Zinc and Oxygen respectively and Nitrogen was the chosen carried gas. The main conclusions about the surface morphology of the ZnO films, in correlation with the growth conditions are:

- Different surface morphology can be obtained depending on the growth temperature. Thus films obtained at 300 °C had a thin layer of ZnO material on top of which randomly oriented vertical crystals with a length of 1 μm were formed. At the range of higher temperatures of 350-400 °C, the surface of the films became flatter. A large number of samples with a smooth surface morphology were obtained at a growth temperature of 375 °C. The films that were closer to the in-let to the reactor (labelled as *Front* group) were thicker and flatter than the samples in the *Rear* group, where the heating temperature turned out to be somewhat higher. Taking in mind the growth of thin films, different experiments were performed. At growth times less than 10 min, thin films with a smooth surface were not obtained, in the range of temperatures and precursor's flow analyzed. All films had the preferred growth orientations (102) and (110).
- At growth times of 10 min, in which flat surfaces of ~ 65 nm thick were obtained at 375 °C, decreasing the input flow of precursors from 71.77 and 14.22 $\mu\text{mol}/\text{min}$ to 14.35 and 2.85 $\mu\text{mol}/\text{min}$ for Oxygen and Zinc precursors, respectively, we lost the flatness and to recover this flat surface an increase of the growth time to 45 min was necessary. The samples in the Front Center (*FC*) and Front Right (*FR*) positions turned out to be of the highest quality. Subsequent increase of precursor flow to 43.06/8.54 $\mu\text{mol}/\text{min}$ proved that an amount of 800 μmol of total precursors and 15 min of growth time, allow retaining a smooth surface with approximately the same thickness of ~ 60 nm. At higher material flow (100.48 and 19.91 $\mu\text{mol}/\text{min}$) and a growth time less than 5 min, it was not possible to obtain a smooth surface morphology.

- In order to increase the number of nucleation points, chemical treatment of the sapphire substrate with a solution of $H_3PO_4 : H_2SO_4$ in a volume ratio of 1:3 during 3 hours at $120\text{ }^\circ C$ was carried out. It was found that chemical etching did not significantly improve the morphological properties of ZnO films on *R*-plane sapphire. The sample, which lost their smoothness with growth time only 5 min at $375\text{ }^\circ C$, had reduced their thickness from 42 to 34 nm, but the surface was not uniformly smooth and had some holes. For comparison, the thickness of the ZnO film grown on the *M*-plane sapphire with and without the chemical treatment was in the range of 80 nm, while the thickness of the sample grown on the surface of the *A*-plane treated sapphire slightly decreased from 60 to 50 nm with the same treatment. After chemical treatment, the samples were grown on *M*- and *A*-sapphire were polycrystalline, due to increasing nucleation points and reducing the *1D* growth with increasing the *2D* growth of the material.
- In respect the rms surface roughness, AFM studies have shown that it decreases in ZnO films grown in *R*-plane sapphire from 11 to 3 nm with an increase in growth temperature from 325 to $375\text{ }^\circ C$. At $400\text{ }^\circ C$, the roughness returns to 11 nm, due to be working, as regards the growth process, at the high-temperature regime. With a decrease in the growth time for the samples grown at $375\text{ }^\circ C$, the rms roughness of the film surface remained practically constant and it was within the range of 1.5-2 nm. With 3 minutes of growth the ZnO is distributed along the edges of the substrate steps produced in the cutting process, and they are organized into linear and parallel arrays with an rms roughness of ~ 3 nm.
- With different precursor's flow and growth parameters at which is possible to obtain thin smooth films, the surface *rms* roughness of the samples has the a similar value, about 2 nm, and the roughness increases with decreasing the growth time, at the point in which the homogeneity of the surface starts to disappear. After chemical treatment of the substrate, the *rms* roughness of the sample's surface increased from 2 to 2.8 nm, compared to the untreated one. The increase in the surface roughness in samples of 34 nm, the thickness is related with the rise of the number of nucleation points, which will affect slightly the morphology of the sample.

6.1.2 $Cd_{1-x}Zn_xO$ studies

The introduction of Zn into the crystal lattice of the binary compound CdO, grown on *R*-plane sapphire by the MOCVD method by using *DEZn*, Dimethyl Cadmium (*DMCd*) and *TBA* as precursors, has different effects. Thus:

- In respect the surface morphology, the flat surface of CdO, obtained under optimized growth conditions, becomes rougher when Zn is added. Related to the thickness, the increase in Zn nominal content in the samples had almost no effect.
- The crystal-structure is also affected. The ternary $Cd_{1-x}Zn_xO$ compound has a stable cubic (ZB) structure with a (200) plane of cubic phase, the same as the binary CdO. XRD studies have shown the presence of predominant 200 and 400 peaks in all samples. The (200) peak position shifted towards larger angles with increasing zinc content, that is associated with the difference in atomic radii between Cd and Zn, which affects the lattice parameter of the ternary compound. No hexagonal phase was observed at low values of the Zn content, but at 20 % of nominal Zn value the $CdZnO_{(102)hex}$ peak was present, which indicates the presence of phase mixing at a higher Zn contents.
- HRXRD on CdZnO films shown that at $x < 10$ % of Zn content the compounds have a single-phase cubic structure. With the rise in the Zn content in the range $10 \% \leq x \leq 15$ %, the competition began to arise between the misfit stress and the shrinking of the lattice, which causes an inversion of the deformation of the lattice cell, which becomes enlarged in-plane and shortened out-plane. At $x > 15$ %, the slope of groups of differently oriented crystallites increases strongly, the ratio between the c/a parameters begins to increase, which will lead to the formation of a wurtzite structure.
- Related to the Zn content, from the Vegard's law the corresponding values in the samples were determined as 3.66, 5.24, 6.44, 5.93 (with N_2 as carrier gas) and 9.31 % (with He as carrier gas) for 5, 10, 15, 20 (N_2) and 20 % (He) of nominal Zn content, respectively, can be determined. Elementary EDX analysis depicted the Zn content to be 3.03, 5.91, 7.86, 11.5 (N_2) and 14.7 (He), respectively, indicating, once again, the incorporation of zinc into the crystal lattice of CdO. It is worth to note that the presence of mixing phases makes unrealistic the values that the Vergard's law could offer.
- The lattice parameter of ternary compound calculated from the position of the (200) peak decreased from 4.6955 to 4.6511 Å with rising Zn content from 0 to 20 % in the samples. For the sample with 20 % of the nominal Zn content the lattice parameter, obtained using XRD measurements is similar to the calculated one by the Vergard's law for a 10 % of the Zn concentration. This Vegard's law calculation roughly coincides with the values obtained by the EDX method Cd^{2+} substitution by smaller Zn^{2+} ions. The affects the crystallite size, which is decreased from 0.76 to 0.33 nm, while the FWHM for the (200) peak is increased in the range of 0.2-0.4 °.
- With respect to the transmittance of the $Cd_{1-x}Zn_xO$ with increasing the Zn content, a gradual shift in the maximum slope of the transmittance curves towards the shorter

wavelength of the transmitted light was observed. The position of the peaks of derivatives of the absorption spectra is clearly shifted towards higher energies from 2.60 to 2.81 eV, but after 15 % of nominal Zn content, the tendency of rising bandgap decreases due to the presence of mixed phases. The sample in which helium was used as carrier gas had a higher shift of the peak position (200) towards larger angles and showed wider value of optical bandgap ($E_g \approx 2.87$ eV).

6.1.3 CdTe/CdO heterostructures

- In order to optimize the growth conditions of the binary compounds for the heterostructure, a series of CdTe samples were grown by the MOCVD method, on GaAs (100) substrates, in the temperature range of 285-380 °C with steps of 20 °C by using Diisopropyl Telluride (DIpTe) and DMCD as precursors. XRD of these samples shown the presence of the planes (111), (311) and (511)/(333). An increase in the flow ratio by increasing the flow of the DIpTe precursor resulted in a rise in thickness and roughness of the films. At temperatures in the range of 340-360 °C, the film's surface became smoother with the formation of pyramidal structures with film orientation [100], and the thickness decreased compared with other temperatures.
- In respect to the CdTe/CdO heterostructure, where a CdO layer was deposited on the *R*-plane sapphire substrate, the CdO bottom layer had a growth orientation [100], and the upper CdTe layer was oriented in the [111] direction or both. The two materials have a big lattice mismatch of ~ 38.4 %, which makes harder to get structures with similar structures orientation. A two-step film's deposition process was carried out with the growth of a layer during 2.5 min growth at a lower temperature at 295 °C in the first step, and with subsequently growth of a layer during of 57.5 min at a given temperature in the range 330-370 °C in the second step. This two step procedure did not allow obtaining a CdTe top film with the orientation of the underlying CdO layer. The ratio of the XRD intensities for $CdTe_{(400)}$ and $CdTe_{(111)}$ peaks had the highest value $R = 0.637$ at 350 °C and decreased for increased or decreased when changing the growth temperature in the range of 330-370 °C with the growth step of 10 °C.
- At 295 °C of growth temperature and with reduction the growth time to 1 min, only individual particles were formed, the size of them varied depending on the ratio between the Cd and Te precursors. Using a two-steps growth procedure, with 1 min growth at 250 °C and utilization of only one of the precursors during 6 min at 350 °C in the second growth step, made possible to obtain either a thick layer (using *DipTe* precursor), or individual CdTe particles (using *DMCd*), which did not completely cover the lower CdO

layer. Only with one-step growth for 3 min with a growth temperature of 250 °C was it possible to obtain a sample with a relatively continuous upper CdTe film about 30 nm thick.

- The contact potential difference (CPD) studies of the sample surface showed that different grain interfaces have distinct work functions, suggesting that the grain boundaries (GBs) act as distinctive recombination centers. The top of the grains has a higher *CPD* value than the *GBs* between them. Although the faces belong to the same crystallographic family, they are not electrically equivalent. Electrical holes are expected to be accumulated in the *GBs*, and electrons removed, which reduces recombination at such *GB* defects. Due to the surface relief, the distribution of the surface potential was uneven.
- Decreasing the irradiation power of the incident red laser (633 nm) leads, as expected, to a decrease in the surface photovoltage (SPV). We have studied a series of samples growth at different temperatures in the range of 330-370 °C. The results could be divided into 3 groups in which at lower growth temperatures of 330-340 °C the SPV value was negative, at middle temperatures of 350-360 °C its value was close to zero, and at high temperatures of 370 °C the *SPV* was positive. The difference in the SPV values may be due to the appearance of morphology with the pyramidal structure in the temperature range 340-360 °C, which could affect the distribution of photons during irradiation of the samples. A negative value could be caused by a strong electron-hole recombination at the surface, which significantly reduces the *SPV*. Also, photo carriers can contribute to a change in the capacitance of the probe-sample using KPFM method, which leads to a potential systematic error in *SPV*. Finally, adsorption of oxygen with formation of oxides on the surface of the films could lead to the formation of surface states, which affect the electrical properties.

6.2 $A_{II}MnB_{VI}$ materials

6.2.1 $Zn_{1-x}Mn_xTe$ studies

$Zn_{1-x}Mn_xTe$ thin films with 5 % of nominal Mn content were grown by the CSVS method on glass substrates in the growth temperature range of 350-650 °C. The main conclusions of the subsection will be devoted to the structural and substructural properties of the compound.

- Grains in the range from 600 to 800 nm with a density of $2 \times 10^{12} - 1 \times 10^{12}$ *NPs/m*², respectively, were observed. The grain size increased with the rise of growth temperature, which leads to a decrease in the Mn content, that seems to be randomly distributed,

without any organization over the substrate. Samples had a fine-crystalline transition layer, followed by the secondary nucleation growth of crystallites oriented in the plane (111) parallel to the substrate, the presence of them decrease with increasing growth temperature. At high temperatures the growth mode changed from long to short columns, which led to a decrease in the film thickness in the range of 2.5–1.9 μm at temperatures of 623–823 K (350–550 $^{\circ}C$).

- All samples had a cubic structure with a preferred orientation (111), and their position approximately corresponds to that of pure ZnTe. At low substrate temperatures of 623 K (350 $^{\circ}C$), the lattice parameter (a) of the $Zn_{1-x}Mn_xTe$ samples was greater than that of ZnTe, which indicate the substitution of larger Mn^{2+} ions at the Zn^{2+} sites, but with rising of growth temperature over 500 $^{\circ}C$ (773 K), the lattice parameter showed the constant value close to that of pure binary ZnTe, which means the absence or reduced content of Mn in the films. The high intensity of the (111) peaks in XRD patterns suggests an *out-plane* preferred orientation and the dominant crystallographic planes of crystallites are the (111) for all temperatures. Samples have a degree of preferred orientation near to that of a perfectly (111) oriented sample and this orientation is typical for ZnTe films.
- The real value of the Mn content calculated using EDX was in the range of 0.7 to 2.05 % with rising of substrate temperature, which is significantly below the nominal value (5 %) in the charge. The reason can be the re-evaporation of Mn in the samples surface or not incorporation in the transport and deposition processes at higher temperature. The series of $Zn_{1-x}Mn_xTe$ samples with 10 % nominal Mn content, measured using the PIXE method, presented that manganese is rather evenly distributed over the sample area.
- The pole figures of the {111} reflection showed that $Zn_{1-x}Mn_xTe$ samples exhibit a broad peak with its maximum at an inclination angle at 0 $^{\circ}$ and a broad ring at an inclination angle at $\approx 70^{\circ}$, indicating a random azimuthal orientation. This uniaxial orientation shows, that the films possess an out-plane preferred orientation but no in-plane preferred orientation. The percentage of particles with a (111) orientation within an inclination angle of $\pm 10^{\circ}$ is 83-92 % and mostly ~ 90 % in all the range of growth temperatures. The variation in the percentages is small, decreasing with reducing Mn content, but finally increasing at the highest temperature of 923 K (650 $^{\circ}C$), which is associated with a change in the growth mode from long to small columns.
- $Zn_{1-x}Mn_xTe$ film has a clear prevalence of screw dislocations. The mean longitudinal size of crystallites on the samples growth at low substrate temperature 623 K (350 $^{\circ}C$) increases considerably with falling down of Mn content. The mean transversal size also increases, but less. The aspect ratio D_{long}/D_{transv} goes from 3.5 to 5 when Mn content is

reduced with increasing of the substrate temperature. Comparing the transversal size with values obtained by SEM, it can be concluded that columnar grains are polycrystalline. The average dislocation density of the samples is weakly Mn concentration dependent at low and middle growth temperatures and decreases when the growth is performed at a higher temperature of 923 K (650 °C). For screw (111) dislocations, the Burger vector, the dislocation line, and the axis of the screw dislocation follow the same direction. Samples at lower temperature show a higher concentration of dislocations, which confirms the results obtained using XRD.

- CSD value decreases with reducing of Mn content with the temperature and then increases at 773 K (500 °C) in the direction of the (111) plane. The maximum value exists in the temperature range $T_s = 600-650$ K, where values of Mn content was minimum. On the other hand, the microstrain degree in this direction decreased with reducing of Mn with slightly increasing at higher temperatures. This may be due to a change in the growth mode from long to short columns. The experimental values of the CSD size and microstrain degree were higher than for ZnTe films deposited under similar growth conditions. The average defects concentration in the $Zn_{1-x}Mn_xTe$ films decreases with reducing of Mn content, that indicate improving stability of the cubic phase. Thus, growth alloyed ZnTe films with Mn atoms leads to degradation of the substructure parameters of ZnTe films, which is shown as microstrain and CSDs increase, as well as the defects concentration.

6.2.2 $Zn_{1-x}Mn_xS$ studies

- As in the previous case, polycrystalline $Zn_{1-x}Mn_xS$ thin films with a 7 % of nominal Mn content were grown by the CSVS method on glass substrates in the growth temperature range of 100-450 °C. At substrate temperatures < 100 °C the integrity of the films is destroyed due to the appearance of surface tensions associated with the difference in the coefficient of thermal expansion between layer and substrate. The Mn alloying of ZnS changes the film morphology from a more uniform to granular. A change in the growth mode from long to short columns was observed. With the reduction of the Mn content at growth temperatures rising from 100 to 450 °C, the grain size (0.65-3.13 μm) increases with a reduction of the grain density ($0.18 \times 10^{12} - 1.16 \times 10^{12}$ NPs/m^2). The thickness of the films, on the contrary, decreased with an increase in the T_s , which can be caused by a change in the growth mode, re-evaporation and non-incorporation of the Mn atoms at higher temperatures.

- At lower growth temperatures 373-623 K (100-350 °C) the dominant peak intensity for $Zn_{1-x}Mn_xS$ samples was the peak of (200) plane, which indicates the presence of brightly texture in films with this cubic structure. Similar texture in the cubic films of $A_{II}B_{VI}$ compounds is predominant, since this direction coincides with the direction of the fastest growth of crystallites. At temperatures of 673–723 K (400-450 °C), the intensity of the (111) peak decreases strongly, and the reflection from the (200) plane becomes dominant. Diffraction peaks corresponding to elemental Mn(300) observed at a lower temperature $T_s = 373-623$ K (100-350 °C), disappears at higher temperatures [> 623 K (350 °C)], which may be due to decrease of Mn content.
- Charge of the Zinc Sulfide compound with Manganese has both, cubic and wurzite phases, which at high temperatures led to the formation of a wurtzite phase in the films. The existence of 2 phases is explained by the absence of a difference between the formation energy of both sphalerite and wurtzite phases for a pure ZnS compound and their equal probability of existence. For all growth temperatures the dominant crystallographic planes of crystallites was (200), and degree of preferred orientation was 2-2.5 times less that the value correspond to a perfectly oriented sample, increases with reducing Mn content at mean substrate temperatures of 623-673 K (350-400 °C), but decreased again at $T_s > 723$ K (450 °C).
- The real Mn content decreased with growth temperature, and the ratio between the atomic concentration of Zinc and Manganese ($C_{(Zn+Mn)}$) to the atomic Sulfur concentration (C_S) increased and at a high temperature [$T_s = 723$ K (450 °C)] being approximately 1.08 which is close to ideal stoichiometric proportion between the elements. The lattice parameter of $Zn_{1-x}Mn_xS$ films was in the range of 5.6406-5.6424 Å and decreased with increasing growth temperature, which was expected since $a_{ZnS} < a_{MnS}$ and the Mn content tended to decrease.
- The CSD size was significantly smaller than the grain size and changed, with increasing the growth temperature, in the range 42-84 nm, while in the temperature range $T_s = (500-550)$ K with a 2.9 at % of Mn the grain size was maximum. The CSD themselves are in the form close to the cylindrical, where the height of the cylinder $L_{(hhh)}$, as evidenced by simple geometric constructions, is slightly smaller than its diameter. The level of microstrain in the $Zn_{1-x}Mn_xS$ films in the [111] direction is not uniform with reducing Mn content. A monotonic increase was recorded, after which there was a decrease in the value and a second increase at high temperatures. This behavior is associated with a change in the growth mode at $T_s > 623$ K.

- The microstrain level varies in the range of $\sigma = (7.04-13.83)$ MPa and was mainly concentrated on the boundaries of the CSD, whereas the volume of crystallites is practically free of dislocations. With an increase in temperature, the value of the microstrain level, determined from the reflections of the plane (111) - (222), decreases, reaching its minimum at ~ 2.9 at % in the growth range $T_s=500-600$ K, after which the value gradually increases. With the reduction of Mn content, the stability of the cubic component of the film increases, the probability of violation of the order of alternation of the (111) planes decreases, and the defects concentration, correspondingly, decreases. Low interfacial energy during the transition from the cubic to the wurtzite phase and small energy changes in the crystal lattice at phase changes will lead to a high probability of errors in the alternation of tightly packed planes and the formation of defects, which will affect the structural and substructural features of the films.

6.2.3 Optical (spectral) studies

With the help of spectral studies, transmission and reflection of the samples were determined.

- The transmittance of $Zn_{1-x}Mn_xS$ films increases reaching the “red border” at 340-350 nm, while for a series of $Zn_{1-x}Mn_xTe$ samples rising of transmittance intensity is observed at wavelengths < 540 nm. At high values of the wavelength of the incident radiation the transmission curves acquire the oscillatory character of interference. The diffuse reflection coefficient for a series of $Zn_{1-x}Mn_xS$ films turned out to be lower than for a series of $Zn_{1-x}Mn_xTe$ samples obtained at the same growth time. As the Mn content decreases, the R coefficient increases, which is obviously associated with the appearance of films with a pronounced pyramidal relief. $Zn_{1-x}Mn_xTe$ films with a shorter growth time have a lower reflection, and this dependence is retained when calculating the specular reflectance of this material.
- The values of optical bandgap, determined by the peak maximum of the derivative of the absorption spectra of the material, shifted towards higher energies from 3.569 eV (for 373 K [100 °C]) to 3.642 eV (for 723 K [450 °C]) with increasing substrate temperature, which indicated reduction of the Mn content in the samples. For average temperatures of 623-673 K (350-400 °C), the position of the derivative maximum is almost similar, which point to a similar manganese incorporation. On the other hand, both series of $Zn_{1-x}Mn_xTe$ samples, irrespective of the growth temperature, had a bandgap of approximately $E_g = 2.26-2.27$ eV, which is associated with a very low Mn concentration in the films or its complete absence.

6.3 General conclusions

The work done under this thesis contributes to the study of the growth and characterization of the binary zinc and cadmium oxides, their associated ternary alloy and the heterostructure CdTe/CdO, as well as ZnMnTe and ZnMnS.

The effect of growth parameters at the MOCVD method on the structural properties of thin ZnO films was shown. In $Cd_{1-x}Zn_xO$ films, it was found that at a nominal Zn content of more than $x > 15\%$, phase mixing and the formation of a hexagonal phase in the cubic $Cd_{1-x}Zn_xO$ ternary compound were observed. The sample obtained by using helium (He) as a carrier gas had a higher bandgap in respect to the one obtained by using N_2 instead.

Difficulties in obtaining high-quality heterostructures based on $CdTe/CdO/R-sapphire$ are associated with a large mismatch of their lattice parameters, as a result of which the obtained upper films do not follow the preliminary orientation of the lower one. Optimized growth parameters were chosen, at which the upper CdTe layer most closely reproduces the preferred orientation of the underlying CdO layer. Due to the complex morphology, the surface contact potential is not evenly distributed over the surface of the samples.

It was found that in $Zn_{1-x}Mn_x(Te, S)$ functional materials, the Mn content decreased with the rise of growth temperature as a result of its re-evaporation or not incorporation in the transport and deposition processes at high growth temperatures. For $Zn_{1-x}Mn_xTe$ films, an out-plane preferred orientation was observed with a clear predominance of screw dislocations. Growth of alloyed ZnTe films with Mn leads to degradation of the substructure parameters of ZnTe films. For $Zn_{1-x}Mn_xS$ films obtained at high temperatures, the existence of cubic and wurzite phases is observed, due to the fact that the difference between the formation energies of the sphalerite and wurzite phases is not significant and the formation of each of the phases has the same probability.

Optical studies of $Zn_{1-x}Mn_x(Te, S)$ showed that in $Zn_{1-x}Mn_xS$ films, the bandgap increases with the growth temperature, which corroborated a decrease in the Manganese content. On the contrary, in $Zn_{1-x}Mn_xTe$ films, this value did not change significantly regardless of temperature, which is associated either with the low content of the alloying element or with its complete absence at high growth temperatures.

The results obtained in this work have both a fundamental and an applied significance. The new information about the structure and crystalline substructure, the chemical composition, the film surface morphology, the optical characteristics, depending on the growth conditions and growth methods, should contribute to the development of materials based on the binary compounds of $A_{II}B_{VI}$. In general, this thesis allowed not only an in-deep study of the properties of functional materials depending on the growth conditions but also the acquisition of skills and wide knowledge of different growth and characterization methods.

Related articles

1. **O.V. Klymov** and D.I. Kurbatov. *Effect of Mn doping on the optical properties of chalcogenide compounds ZnS and ZnTe* (book chapter) // Springer Proceedings in Physics, 240 (Microstructure and Properties of Micro- and Nanoscale Materials, Films, and Coatings (NAP 2019)), pp 325-335, Jan. 2020.

DOI: 10.1007/978-981-15-1742-6_31

2. **O. Klymov**, D. Kurbatov and A. Frolov. *Chemical composition and some structural properties of $Zn_{1-x}Mn_xS$ semiconductor films obtained by close-spaced vacuum sublimation* (conference-paper) // 2018 International Conference on Information and Telecommunication Technologies and Radio Electronics (**UkrMiCo 2018**), Proceedings – Sep. 2018

DOI: 10.1109/ukrmico43733.2018.9047597

3. C. Martínez-Tomás, **O. Klymov**, S. Agouram, D. Kurbatov, A. Opanasyuk and V. Muñoz-Sanjosé, *Substructural properties and anisotropic peak broadening in $Zn_{1-x}Mn_xTe$ films determined by a combined methodology based on SEM, HRTEM, XRD, and HRXRD* (journal article) // Metallurgical and Materials Transactions A: Physical Metallurgy and Materials Science, Vol. 47A, No. 12, p. 6645-6654, Sep. 2016.

DOI: 10.1007/s11661-016-3762-6

4. A. Huerta-Barberá, L. Manel Guia, **O. Klymov**, V. Marín-Borrás et. al, *MOCVD growth of CdO very thin films: Problems and ways of solution* (journal article) // Applied Surface Science, 385, p. 209–215, 2016.

DOI: 10.1016/j.apsusc.2016.05.113

5. D.I. Kurbatov, **A.V. Klymov**, A.S. Opanasyuk, A.G. Ponomarev and S.S. Melnik, *Studying the elemental composition and manganese distribution in $Zn_{1-x}Mn_xTe$ and $Zn_{1-x}Mn_xS$ films using the μ -PIXE and EDAX methods* (journal article) // Journal of Surface Investigation: X-Ray, Synchrotron and Neutron Techniques, Vol. 8, No. 2, p. 259-262, Mar. 2014.

DOI: 10.1134/S1027451014020177

6. **O. Klymov**, D. Kurbatov, O. Levchenko, *Some optical properties of $Zn_{1-x}Mn_xTe$ semi-magnetic films Levchenko* (conference paper) // 6th International Conference On Advanced Optoelectronics And Lasers (**CAOL 2013**), p.376-377, Sep. 2013.

DOI: 10.1109/CAOL.2013.6657643

7. D.I. Kurbatov, **O.V. Klymov**, A.S. Opanasyuk, A.G. Ponomarev, P.M. Fochuk and H.M. Khlyap, *Structural characteristics of $Zn_{1-x}Mn_xTe$ polycrystalline films* (conference paper) // Proceedings of **SPIE** - The International Society for Optical Engineering, 8507, 85071J, 2012.

DOI: 10.1117/12.928990

8. D.I. Kurbatov, **O.V. Klymov**, A.S. Opanasyuk, S.M. Danilchenko, H.M. Khlyap, *Sub-structural features of $Zn_{1-x}Mn_xTe$ solid solution thin films* (conference paper) // Proceeding of the International Conference, Nanomaterials: Applications and properties (**NAP-2012**)-Vol. 1 - № 3 – P. 03TF23(4), 2012.

Part II: Spanish summary

Chapter 7

Resumen en español

La presentación del trabajo que se somete a consideración para la obtención del título de doctor se ha organizado en seis capítulos, que incluyen la introducción, el desarrollo de la tesis, las conclusiones y las referencias. Algunas de las abreviaturas de los términos utilizados en este resumen no se traducirán del inglés. En algunos casos, esto también se aplicará a la designación de las aleaciones ternarias estudiadas capas ternarias, donde los subíndices se omitirán para simplificar (por ejemplo, CdZnO y ZnMnTe en lugar de $Cd_{1-x}Zn_xO$ y $Zn_{1-x}Mn_xTe$).

En el Capítulo 1 se presenta la motivación, tema de estudio y objetivos de esta tesis:

Desde sus inicios, la humanidad ha buscado oportunidades para inventar herramientas que mejoraran sus condiciones de vida. Un gran salto en el desarrollo instrumental fue la gran revolución industrial de los siglos XVIII-XIX, durante la cual se produjo la transición del trabajo manual al mecanizado. La principal consecuencia fue la transición de una economía predominantemente agraria a la producción industrial. Esto indujo y promovió la invención de nuevos equipos y dispositivos. Los logros técnicos en electricidad y magnetismo y los nuevos avances en química aceleraron el desarrollo de la humanidad y agregaron diversidad en la instrumentación.

Vale la pena señalar que el desarrollo de la tecnología también nos enfrenta a problemas energéticos. Encontrar esta energía y poder minimizar su consumo mientras se mejora la eficiencia se ha convertido en un nuevo desafío para los científicos. Para reemplazar los recursos no renovables como el carbón, el petróleo o el gas natural, se ha utilizado fuentes renovables de agua, viento y radiación solar. Esto obliga a los científicos a desarrollar materiales y estructuras basados en ellos que puedan general transferir energía de manera efectiva.

Para abrir nuevos caminos a las aplicaciones tecnológicas ahora, a principios del siglo XXI, existe una búsqueda activa de materiales que puedan ser complementarios de los pioneros semiconductores como el Silicio o el Germanio. Así, el interés por el estudio de capas mono y policristalinas, así como de nanocristales de diferentes compuestos como, por ejemplo, los de la familia $A_{II}B_{VI}$ ha aumentado significativamente. El interés por esta familia se debe

al enorme potencial que, en diferentes áreas, podrían tener sus materiales como antirreflecentes, absorbentes y ventanas de heterouniones fotovoltaicas, células solares tandem (SC), capas base de fotodetectores, detectores de radiación, LED, sensores de gas, dispositivos piro y piezoelectrónicos, etc.

Entre toda la variedad de materiales II-VI, hay 2 grupos de semiconductores que han atraído un interés particular debido a sus características únicas. El primero incluye óxidos de elementos como zinc y cadmio con una alta transparencia en el rango óptico visible, que se han estudiado ampliamente para su uso en diversas aplicaciones electroópticas, entre otras, como óxidos conductores transparentes (TCO). El otro conjunto está formado por los semiconductores magnéticos diluidos (DMS) de los compuestos II-VI que, además de las propiedades ordinarias de un semiconductor, tienen propiedades magnéticas.

Tanto el óxido de zinc (ZnO) como el óxido de cadmio (CdO) pueden ser TCO con sus fortalezas y debilidades. Para mejorar las propiedades del material es posible utilizar compuestos ternarios, que son una opción para modificar las propiedades de las estructuras binarias, ampliando así el rango de aplicación del material. Esto da como resultado cambios en características tales como los parámetros de red, ancho de banda prohibida, movilidad de portadores o transmitancia. Cabe notar que las propiedades de los compuestos ternarios dependen en gran medida de las técnicas de crecimiento. En particular, los materiales con diferentes parámetros de red o diferentes fases cristalinas (wurtzita o zincblenda en el caso de ZnO y CdO) son difíciles de combinar. Las tensiones y imperfecciones debidas a la baja calidad del cristal pueden dar como resultado propiedades optoelectrónicas inadecuadas. Por tanto, un punto importante será la optimización de las condiciones de crecimiento de los cristales para conseguir una buena calidad cristalina y, en consecuencia, mejores propiedades optoelectrónicas.

La obtención de compuestos ternarios de CdZnO es un reto atractivo ya que la diferencia entre las estructuras cristalinas de los compuestos binarios y las diferencias en los parámetros de red y tamaño de los radios iónicos de Cd^{2+} (0,95 Å) y Zn^{2+} (0,74 Å) hacen augurar la presencia de una miscibilidad restringida y la presencia de mezcla de fases.

Por su parte los semiconductores semi-magnéticos (SMSC) o semiconductores magnéticos diluidos (DMS), combinan elementos de la física de los semiconductores y el magnetismo, lo que constituye una oportunidad única para la investigación y la tecnología.

La inclusión de átomos de Mn en la red II-VI puede mostrar fenómenos como magnetorresistencia negativa, rotación de Faraday gigante y comportamiento de espín. Este elemento (Mn) puede ser parte de diferentes estructuras aleadas, pero nos fijaremos en la aleación de Mn con películas delgadas de ZnS y ZnTe, debido a las propiedades ópticas de estos compuestos binarios.

Por otro lado, el telururo de cadmio (CdTe) es otro semiconductor representativo típico del grupo II-VI. A pesar de la amplia gama de uso de CdTe como semiconductor, continúa

la búsqueda de heterouniones y compuestos basados en él. Debido a sus propiedades optoelectrónicas, se puede utilizar como material tipo p en células solares CdTe/CdS simples y baratas, por esta razón, las heterouniones CdTe/CdS y CdTe/CdSe han sido bien estudiadas. Sin embargo, las heteroestructuras con TCOs, en particular la heterounión p-n de CdTe/CdO ha sido menos estudiado. La complejidad en la formación de esta estructura se debe, entre otros factores, al desajuste de la red entre el parámetro de red de CdO (4,69 Å) y CdTe (6,49 Å). Otra dificultad es el control de la orientación preferencial de la capa al crecer sobre la subyacente, en la que el parámetro de red no coincide ni tampoco sus coeficientes de expansión térmica, estas dificultades hacen que el estudio de la heteroestructura CdTe/CdO sea un atractivo desafío para la investigación fundamental.

En el contexto del interés comentado anteriormente sobre los materiales II-VI el objetivo principal de esta tesis es el estudio del crecimiento cristalino y caracterización de algunos de los materiales de esta gran familia. La obtención de capas de compuestos binarios y ternarios con buena calidad cristalina requiere la elección de un método y parámetros de crecimiento adecuados, pero para ello se debe establecer una correlación entre las condiciones de crecimiento y las propiedades, lo que será desarrollado en esta tesis.

Capítulo 2

El Capítulo 2 muestra las principales propiedades de los materiales utilizados con una descripción detallada de los métodos para la obtención de películas de calcogenuros de $A_{II}MnB_{VI}$ y películas a base de óxidos, así como información general sobre los parámetros de crecimiento y las condiciones para el crecimiento de estos materiales.

La estructura de la wurtzita de ZnO es la más estable en condiciones ambientales y, por tanto, la más extendida. Los parámetros de la red de ZnO con estructura hexagonal son $a \sim 3.250$ Å y $c \sim 5.205$ Å; y su relación $c/a \sim 1.60$ está cerca del valor ideal para la celda hexagonal $c/a = 1.633$. El ZnO tiene un enlace predominantemente iónico, como la mayoría de los semiconductores II-VI. Debido a la amplia banda prohibida ($E_g = 3,37$ eV), el ZnO tiene una alta absorción óptica en la región UV (320-400 nm). Por otro lado, debido a la alta energía de los excitones (60 meV), es posible una generación láser a temperatura ambiente. El ZnO es un semiconductor de conductividad de tipo n debido al exceso de átomos de zinc, lo que resulta en la presencia de defectos inherentes como vacantes de oxígeno (V_O) o intersticiales de zinc (I_{Zn}).

Por su parte el CdO cristaliza en la estructura de sal de roca que consta de una red cúbica centrada en las caras (fcc) con una base de dos átomos, Cd en (0,0,0) y O en (1/2, 1/2, 1/2), con un parámetro de red ~ 4.695 Å. La banda prohibida fundamental de CdO es indirecta a $\sim 0,84$ eV (~ 1480 nm), y esto es demasiado bajo para la transparencia óptica (380 a

740 nm), sin embargo la transmisión del espectro visible se produce debido a la banda prohibida directa de $\sim 2,28$ eV (~ 500 -560 nm). La alta concentración de portadores y al efecto Moss-Burshtein, puede aumentar la banda prohibida a 3,25 eV (~ 380 nm). Esto hace que el CdO sea ópticamente transparente, ya que, usualmente y sin dopar, tiene una alta concentración de portadores ($> 10^{21} \text{ cm}^{-3}$).

Debido a las propiedades de ZnO y CdO, estos semiconductores se pueden utilizar en varios campos. Además, la síntesis de compuestos ternarios basados en estos semiconductores binarios ampliará aún más el alcance de sus aplicaciones. En el caso de CdZnO (compuesto rico en Cd y de estructura cúbica), el gap directo de CdO se extenderá por la presencia de Zn. En ambos casos, las propiedades del compuesto resultante dependerán del contenido del elemento de aleación, pero aparecerán varios problemas debido a la diferencia en la estructura cúbica del CdO y la estructura de la wurtzita del ZnO, dependiendo de este contenido.

El lo que refiere al CdTe con estructura cristalina de zinc blenda (ZB) es un semiconductor con una banda prohibida directa de $\sim 1,49$ eV, que está cerca del intervalo de banda óptimo, teóricamente establecido, para las células solares (1,28 eV) y un alto coeficiente de absorción óptica ($> 5 \times 10^5 \text{ cm}^{-1}$). La conductividad de CdTe se puede cambiar dependiendo de las condiciones de crecimiento. Así el CdTe crecido en condiciones ricas en Cd es de tipo n debido a que el nivel de Fermi está fijado en o cerca del medio de la banda prohibida por el defecto del donante compensador Cd_i^{2+} . Por otro lado, en el límite rico en Te, CdTe tiene conductividad de tipo p , ya que la energía de Fermi está fijada cerca del máximo de la banda de valencia.

En lo que se refiere a los DMS la aleación ZnMnTe, que puede considerarse como una mezcla de sistemas cristalinos entre dos materiales de zinc blenda, ZnTe y MnTe. En este compuesto, los iones Zn^{2+} se reemplazan por iones Mn^{2+} . Y la banda prohibida se puede, en principio controlar mediante la composición. El radio iónico de Zn es 0.88 Å, pero de Mn depende del estado de giro, por lo tanto, puede 0.81 Å para el estado de giro bajo y 0.97 Å para el estado de giro alto. En este sentido, un aumento en la concentración de Mn conducirá a un aumento en el parámetro de red del compuesto ZnMnTe, además de un aumento de la banda prohibida, y la generación de una cierta densidad de vacantes e intersticiales que pueden alterar el parámetro de red. Con respecto a la banda prohibida, cambia entre la banda prohibida de energía de 2.28 eV (ZnTe) a 2.9 eV (zincblenda MnTe), cuando los iones Zn^{2+} son reemplazados por iones Mn^{2+} .

El sulfuro de zinc aleado con manganeso (ZnMnS) es un semiconductor con transparencia en la región visible UV y gap directo ancho ($\sim 3,8$ eV). El ZnS es químicamente estable y se considera un material anfitrión prometedor para los iones Mn^{2+} . Como regla general, las aleaciones ternarias formadas sustituyendo el elemento del grupo II por Mn en la red de $A_{II}B_{VI}$ retienen la estructura cristalina del compuesto de $A_{II}B_{VI}$ "parental". Las excepciones a esta regla son ZnMnS y ZnMnSe, que exhiben la estructura del anfitrión $A_{II}B_{VI}$ cúbica para un

contenido bajo de Mn, pero por encima de un cierto valor de x muestran la estructura de wurtzita. En el caso de ZnMnS, la estructura de ZB se mantiene a una concentración de Mn del 10 % o menos. En la estructura cristalina cúbica de ZnS, las propiedades ópticas son isotrópicas. Se trata la estructura cristalina cúbica centrada en caras con ~ 5.4093 Å. La transición de ZB a la estructura de wurtzita ocurre a 1020 °C. La estructura hexagonal tiene los parámetros de red de $a \sim 3.811$ Å y $c \sim 6.234$ Å.

Para el crecimiento de los materiales estudiados en esta tesis se utilizaron dos métodos de crecimiento, que abarcan dos enfoques de la metodología de crecimiento: un sistema más preciso, multiparámetro el Metal Organic Chemical Vapor Deposition (MOCVD) y, en consecuencia, una metodología costosa, y uno no demasiado costoso y menos parámetro-controlado, como el Close Space Vacuum Sublimation (CSVS) sin renunciar a ofrecer buenas capas para algunas aplicaciones.

El MOCVD se basa en la transferencia en fase gaseosa de elementos constitutivos (generalmente en forma de un precursor) a un sustrato donde reaccionarán. La deposición finalmente ocurre a través de una reacción química en la superficie de un sustrato y generalmente conduce a una deposición de alta calidad de películas delgadas en condiciones de crecimiento optimizadas. Este método es muy adecuado para la producción de capas con una morfología superficial de alta calidad y un control preciso del grosor y la uniformidad utilizados para diferentes tipos de dispositivos.

Por su lado el CSVS permite obtener capas con un grosor de unos pocos angstroms a varias decenas de micrones, por evaluación en vacío. La fase de vapor consta solo de átomos o moléculas que forman la fuente y el cristal y se puede lograr una buena uniformidad y una gran pureza del material, las condiciones de crecimiento de la película se controlan fácilmente y es posible utilizar máscaras para la fabricación de capas de una configuración determinada. El uso de un control de la temperaturas de evaporación (T_e) y la del sustrato (T_s) permite un mejor control del proceso de crecimiento. Este método se ha utilizado para el crecimiento de películas delgadas de ZnMnTe y ZnMnS.

En lo referente a los sustratos, se ha utilizado zafiro cortado en diferentes planos (en el caso de estructuras de ZnO, CdZnO y CdTe/CdO); y vidrio transparente para películas de ZnMnS y ZnMnTe.

Capítulo 3

En el Capítulo 3 se describen los diferentes métodos de caracterización para el estudio de la morfología, propiedades estructurales y subestructurales, características electrónicas y ópticas. Para el estudio morfológico de las muestras se ha empleado la microscopía electrónica de barrido

(SEM) y la microscopía electrónica de transmisión (TEM) combinada con microscopía de fuerza atómica (AFM) para determinar la rugosidad cuadrática media (*rms*) de la superficie.

En el SEM, cuando un haz de electrones primarios incide en el área de la superficie de una muestra, los electrones penetran y se propagan a través del material. La profundidad de la interacción o la disminución de la energía del haz de electrones está relacionada con las propiedades del material. Los elementos ligeros permiten una penetración más profunda del haz, mientras que el volumen de dispersión de los elementos pesados se encuentra más cerca de la superficie. En este proceso, los electrones primarios pueden interactuar de forma inelástica con electrones atómicos o elásticamente con núcleos atómicos y generar varios tipos de señales. Un microscopio de este tipo se utiliza para formar una imagen de una señal de electrones secundarios y electrones retrodispersados. La señal principal, sin embargo, muestra electrones secundarios.

A diferencia de SEM, la información en el TEM se obtiene del haz primario de electrones que incide en la muestra y es transmitido. Debido al alto voltaje, llegando hasta 1 MeV o más en algunos microscopios, se pueden realizar investigaciones con resolución a escala atómica de décimas de nm. En la AFM, el principio de funcionamiento consiste en escanear la superficie de la muestra utilizando un cantilever con la punta con un radio nanométrico y determinar la fuerza resultante de la interacción punta-muestra. Un sistema de realimentación regula el cambio de frecuencia para mantener un valor constante de la frecuencia, lo que permite adquirir la topografía de la superficie de la muestra.

Entre las señales generadas por el SEM, la emisión o las radiaciones de rayos X se pueden utilizar para la determinación de la composición. Esto se llama análisis de rayos X de energía dispersiva (EDX) el cual permite correlacionar la morfología con la composición de la muestra. El voltaje de aceleración de los electrones determina la profundidad del volumen de interacción. Es decir, a más energía en el haz de electrones, más profundo es el volumen de interacción. Otro método para el estudio de la composición es la emisión de rayos X inducida por partículas (PIXE). Cuando una partícula cargada, con suficiente energía (del orden de varios MeV), atraviesa un material, pierde energía debido a la ionización de la capa interna de los átomos por los que pasa. Esto crea rayos X con longitudes de onda características de un elemento en particular. El PIXE es una técnica analítica relativamente simple y multielemental que se puede utilizar para identificar y cuantificar elementos que van de Na a U. En el caso del método EDX, se pueden detectar todos los elementos químicos con un número atómico superior a 4 (Be).

La información sobre las propiedades estructurales y subestructurales de los materiales se obtiene utilizando difracción de rayos X de alta resolución (HRXRD). El método permite realizar un barrido $2\theta - \theta$ en el que se mide la intensidad del haz difractado en función del ángulo de difracción (θ), manteniendo constante esta relación entre los ángulos. A diferencia de un

difractómetro convencional, la capacidad de mover el soporte con muestras a lo largo de los ejes x , y y z permite realizar medidas de muestras en diferentes puntos. De la posición de los picos se puede extraer información del tipo de la estructura, así como de las fases presentes, mientras que de la forma de los picos se puede deducir la calidad cristalina de la muestra. La intensidad de difracción en función de 2θ y la orientación de la muestra dan patrones de difracción que permiten realizar análisis del tamaño de la cristalita/microstress, con gran precisión de alto nivel, por un tiempo de medición más largo.

Las características ópticas de las películas obtenidas se determinaron utilizando espectros de transmitancia y absorbancia mediante espectrofotometría óptica. Este método de caracterización determina qué parte del haz de luz monocromática se absorbe y qué parte se transmite a través de la muestra, dependiendo de la energía del haz de luz incidente. A partir de estos valores se obtendrá la absorción en función de la energía del haz con cuya ayuda se determina la banda prohibida óptica de los compuestos. Los espectros de transmitancia del material se normalizaron de tal forma que su valor máximo de curva correspondiera al 100 % de la transmitancia posible. Esto se hizo para que, al calcular los espectros de absorción a partir de los espectros de transmitancia, las curvas tuvieran un valor mínimo a bajas energías. Las propiedades eléctricas de unas películas se investigaron utilizando los métodos de diferencia de potencial de contacto (CPD) y fotovoltaje de superficie (SPV). Para este propósito, se utilizó Kelvin Probe Force Microscopy (KPFM) para medir la diferencia de potencial de contacto local entre una punta conductiva de AFM y la muestra, mapeando así la función de trabajo del material o el potencial de superficie de la muestra con una alta resolución espacial. En el caso de SPV, para hacer un análisis de los cambios de voltaje superficial provocados por la iluminación se utilizó como fuente de radiación un láser rojo (633 nm). El rayo del láser se enfocó de manera que incidiera en el punto de contacto de la punta de la aguja del microscopio con la superficie de la muestra.

Capítulo 4

El estudio de los óxidos del grupo A_{II} , ZnO y CdO en particular, y su heteroestructura se presentan en el Capítulo 4. En él se muestra la influencia en la morfología de las capas respecto de la temperatura de crecimiento, tiempo de deposición, cantidad de precursores y sustrato utilizado. Se estudia la influencia de la concentración de zinc en las capas de CdZnO, y finalmente, se analiza la heteroestructuras CdTe/CdO.

Estudios del crecimiento cristalino de capas delgadas de ZnO

Con el fin de estudiar la influencia de las condiciones de crecimiento sobre la obtención de capas delgadas de ZnO con morfología plana y mínimo grosor, se ha estudiado la dependencia de la morfología de capas de ZnO crecidas sobre zafiro-*R* en función de la temperatura de crecimiento en el rango de temperaturas de 300-400 °C durante 90 min. Las capas obtenidas a temperaturas más bajas muestran la presencia de una fina capa de transición material/substrato sobre la cual se produce el crecimiento ulterior de cristales de ZnO. A temperaturas más altas, la superficie de las capas presentan una morfología mas plana, especialmente en el rango 350-400 °C. De hecho, a 375 °C, las muestras presentan una morfología de superficie plana. Las películas que estaban más cerca de la entrada al reactor (el grupo *Front*) eran más gruesas y planas que las muestras del grupo *Rear*, donde la temperatura de crecimiento era algo más alta. Al aumentar la temperatura se produce una degradación de la superficie debido a la presencia de agujeros que se puede asociar con un régimen de crecimiento de alta temperatura, en el que la tasa de crecimiento disminuye debido a factores termodinámicos, o la reevaporación de precursores causada por una temperatura más alta.

Para tiempos de crecimiento de 10 min, en los que se obtuvieron superficies planas de ~ 65 nm de espesor a 375 °C, al disminuir el flujo de entrada de precursores de 71,77 y 14,22 $\mu\text{mol/min}$ a 14,35 y 2,85 $\mu\text{mol/min}$ para los precursores de Oxígeno y Zinc, respectivamente, perdimos la planitud/uniformidad y para recuperar esta superficie plana fue necesario un aumento del tiempo de crecimiento a 45 min. Las muestras en las posiciones FC y FR resultaron ser de la más alta calidad. El aumento posterior del flujo de precursores a 43.06/8.54 $\mu\text{mol/min}$ demostró que una cantidad de 800 μmol de precursores totales y 15 min de tiempo de crecimiento, permiten retener una superficie lisa con aproximadamente el mismo grosor de ~ 60 nm. A mayor flujo de material (100,48 y 19,91 $\mu\text{mol/min}$) y un tiempo de crecimiento menor de 5 min, no fue posible obtener una morfología de superficie lisa y uniforme.

Para aumentar el número de puntos de nucleación, se llevó a cabo un tratamiento químico del sustrato de zafiro con una disolución de $H_3PO_4 : H_2SO_4$ en una relación de volumen de 1:3 durante 3 horas a 120 °C. Se encontró que el ataque químico no mejoró significativamente las propiedades morfológicas de las películas de ZnO en el zafiro del plano *R*. Las muestras, que perdió su tersura con un tiempo de crecimiento de solo 5 min a 375 °C, ha reducido su espesor de 42 a 34 nm, pero la superficie no era uniformemente lisa y presentaba algunos agujeros. A modo de comparación, el espesor de la película de ZnO que creció en el zafiro del plano *M* con y sin el tratamiento químico estaba en el rango de 80 nm, mientras que el espesor de la muestra que se creció en la superficie químicamente tratada del zafiro en el plano *A* disminuyó un poco de 60 a 50 nm con el mismo tratamiento. Después del tratamiento químico, las muestras

que estan crecidos en zafiro *M*- y *A*- eran policristalinas, debido al aumento de los puntos de nucleación y la reducción del crecimiento *1D* con aumentando el crecimiento *2D* del material.

Los estudios de AFM han demostrado una disminución en la rugosidad de la superficie *rms* de las películas de ZnO crecidas en zafiro del plano R de 11 a 3 nm con un aumento de temperatura de 325 a 375 °C. A 400 °C, la rugosidad vuelve a 11 nm, por estar trabajando en régimen de alta temperatura. Con una disminución en el tiempo de crecimiento para las muestras obtenidas a 375 °C, la rugosidad rms de la superficie de la capa permaneció prácticamente constante y estuvo dentro del rango de 1.5-2 nm. Con 3 minutos de crecimiento, el material se distribuye a lo largo de los bordes de los escalones del sustrato, y podemos verlos organizados en matrices lineales y paralelas con una rugosidad rms de ~ 3 nm.

Con diferentes parámetros de crecimiento y flujo de precursores en los que es posible obtener películas delgadas y lisas, la rugosidad *rms* de la superficie de las muestras tiene el mismo valor, aproximadamente de 2 nm, y aumentará al disminuir el tiempo de crecimiento. Para muestras con el mismo tiempo de crecimiento pero diferente flujo de precursores, se encontró que un aumento del flujo conduce a una fuerte disminución en la rugosidad de la superficie *rms* de la película en el rango de tiempo de deposición de 5 a 15 min, con una disminución gradual adicional a los 25 min.

La muestra que creció sobre el sustrato después de un tratamiento químico aumentó ligeramente la rugosidad *rms* de su superficie de 2 a 2.8 nm. El aumento en la rugosidad de la superficie debería estar asociado con el aumento del número de puntos de nucleación, lo que afectará la cantidad de material depositado durante el crecimiento.

Estudios del crecimiento cristalino de compuesto ternario de $Cd_{1-x}Zn_xO$

Se ha estudiado la aleación $Cd_{1-x}Zn_xO$ creciendola mediante el método MOCVD sobre sustratos de zafiro-*R* usando DEZn, Dimetil cadmio (DMCd) y TBA como precursores. En las condiciones en las que es posible obtener CdO de alta calidad cristalina, la superficie se vuelve más rugosa cuando se agrega Zn. Sin embargo, el aumento del contenido nominal de Zn en las muestras casi no tuvo efecto sobre su grosor.

El compuesto de CdZnO ternario tiene una estructura cúbica estable (ZB) con un plano (200) de fase cúbica, igual que el CdO binario. El desplazamiento del pico de difracción (200) hacia ángulos más grandes con la incorporación de Zn está asociado con la diferencia de radios atómicos entre Cd y Zn, lo que afecta al parámetro de red del compuesto ternario. No se observó fase hexagonal a valores bajos del contenido nominal de Zn, pero al 20 % del valor nominal de Zn apareció el pico de $CdZnO_{(102)hex}$, lo que indica el inicio la presencia de una mezcla de fases.

Los estudios de difracción de alta resolución (HRXRD) mostraron que a $x < 10 \%$ del contenido de Zn, los compuestos tienen una estructura cúbica monofásica. Con el aumento del contenido de Zn en el rango de $10 \% \leq x \leq 15 \%$, comenzó a surgir la competencia entre la tensión de desajuste y el encogimiento de la red, lo que provoca una inversión de la deformación de la celda de red, que se agranda in-plane y se reduce en out-plane. En $x \approx 15 \%$, la relación entre los parámetros c/a comienza a aumentar, lo que favorecerá la formación de una estructura de wurtzita.

A partir de la ley de Vegard se puede determinar que los contenidos de Zn en las muestras son 3.66, 5.24, 6.44, 5.93 (con N_2 como gas portador) y 9.31 % (con He como gas portador) para 5, 10, 15, 20 (N_2) y 20 % (He) del contenido nominal de Zn, respectivamente. El análisis de EDX mostró que el contenido de Zn era 3.03, 5.91, 7.86, 11.5 (N_2) y 14.7 % (He), respectivamente. Vale la pena señalar que la presencia mezcla de fases hace poco realistas los valores que podría ofrecer la ley de Vegard.

El parámetro de red del compuesto ternario calculado a partir de la posición del pico (200) disminuyó de 4.6955 a 4.6511 Å con el aumento del contenido de Zn de 0 a 20 %. Para la muestra con un 20 % del contenido nominal de Zn, el parámetro de red, obtenido mediante mediciones de XRD, es similar al calculado por la ley de Vegard para un 10 % de la concentración de Zn. Lo que coincide aproximadamente con los valores obtenidos por el método EDX. El tamaño de la cristalita se redujo de 0.76 a 0.33 nm, mientras que la FWHM para el pico (200) se incrementó en el intervalo de 0.2-0.4 grados.

Con respecto a la transmitancia del CdZnO al aumentar el contenido de Zn, se observó un desplazamiento gradual en la pendiente máxima de las curvas de transmitancia hacia la longitud de onda más corta de la luz transmitida. El espectro de absorbancia, se desplaza claramente hacia energías más altas de 2.60 a 2.81 eV con la incorporación de zinc. Pero después del 15 % de contenido de Zinc, la tendencia de aumentar de la banda prohibida disminuye debido a la presencia de fases mixtas. La muestra en la que se utilizó Helio como gas portador tenía un valor más ancho de banda prohibida ($\sim E_g = 2.87$ eV).

Heteroestructuras de CdTe/CdO

Con el fin de optimizar las condiciones de crecimiento de los compuestos binarios para la heteroestructura, se crecieron una serie de muestras de CdTe por el método MOCVD, sobre sustratos de GaAs (100), en el rango de temperatura de 285-380 °C, sobre sustratos de GaAs (100), utilizando diisopropilo de telurio (*DIpTe*) y *DMCd* como precursores. La XRD de estas muestras mostró la presencia de los planos (111), (311) y (511)/(333). Un aumento de la relación entre el flujo de los precursores aumentando el flujo del precursor de *DIpTe* resultó en un aumento en el grosor y la rugosidad de las películas. A temperaturas de 340-360 °C, el

grosor de la muestra disminuyó y la superficie de las películas se volvió más lisa con la formación de estructuras piramidales. La orientación de las películas se cambió a (100).

Con respecto a la heteroestructura de CdTe/CdO, donde la capa inferior [100] de CdO se depositó sobre el sustrato de zafiro del plano R, la capa superior de CdTe se orientó en la dirección [111] o en ambas. Los dos materiales tienen un gran desajuste de red $\sim 38,4 \%$, lo que dificulta el que la orientación del CdO se mantenga en la capa de CdTe. Para atacar este problema se llevó a cabo un proceso de deposición de película de dos pasos con el crecimiento de una capa durante 2,5 min de crecimiento a una temperatura de 295°C en el primer paso, y con el posterior crecimiento de una capa durante 57,5 min a una temperatura en el rango $330\text{-}370^\circ\text{C}$ en el segundo paso. Sin embargo este procedimiento de dos pasos, exitoso en otros casos, no permitió obtener una película superior de CdTe con la orientación de la capa de CdO subyacente. La relación de las intensidades de XRD para los picos de CdTe (400) y CdTe (111) tuvo el valor más alto $R = 0.637$ a 350°C y disminuyó al cambiar la temperatura de crecimiento en el rango de $330\text{-}370^\circ\text{C}$.

Los estudios de diferencia de potencial de contacto (CPD) sugieren que los límites de grano (GB) actúan como centros de recombinación. Aunque las caras pertenecen a la misma familia cristalográfica, no son eléctricamente equivalentes y parte superior de los granos tiene un valor de CPD más alto que las juntas de grano (GB) entre ellos. Se espera que se acumulen huecos en las GB, pero se eliminan los electrones minoritarios, lo que reduce la recombinación en tales defectos de GB.

A 295°C de temperatura de crecimiento y con una disminución del tiempo de crecimiento a 1 min, solo se formaron partículas individuales, el tamaño de las mismas varió dependiendo de la relación entre los precursores de Cd y Te. El uso de un procedimiento de crecimiento de CdTe de dos pasos con 1 min de crecimiento a 250°C y la utilización de solo uno de los precursores durante 6 min a 350°C en el segundo paso de crecimiento, permitió obtener una capa gruesa (utilizando el precursor *DipTe*), o partículas separadas de CdTe (usando *DMCd*), que no cubrieron completamente la capa inferior de CdO. Solo con el crecimiento en un paso durante 3 min con la temperatura de crecimiento de 250°C fue posible obtener una muestra con la película de CdTe relativamente continua de aproximadamente 30 nm de grosor.

La disminución de la potencia de irradiación del láser incidente (633 nm) conduce, como se esperaba, a una disminución del fotovoltaje superficial (SPV). Los resultados de SPV se pudieron dividir en 3 grupos en los que a temperaturas más bajas de crecimiento de $330\text{-}340^\circ\text{C}$ el valor fue negativo, a temperaturas medias su valor fue cercano a cero y a temperaturas altas de 370°C el SPV fue positivo. Un valor negativo podría deberse a una fuerte recombinación de huecos de electrones en la superficie, lo que reduce significativamente el SPV. Además, fotoportadores pueden contribuir a un cambio en la capacitancia de la sonda-muestra, lo que conduce a un posible error sistemático en las mediciones de SPV utilizando métodos KPFM.

Finalmente, la adsorción de oxígeno con formación de óxidos en la superficie de las películas podría conducir a la formación de estados superficiales que afectan las propiedades eléctricas.

El desajuste de la red y las dificultades para optimizar las condiciones de crecimiento no permitieron obtener superficies planas y con orientación preferencial lo que afecta la morfología de la superficie y debido al relieve de la superficie, la distribución del potencial de la superficie fue desigual.

Capítulo 5

En el Capítulo 5 se presenta el crecimiento y propiedades de los calcogenuros ZnTe y ZnS aleados con Mn para bajos contenidos del mismo. Se analiza la morfología, características estructurales, y respuesta óptica con respecto al contenido de Mn.

Estudios de $Zn_{1-x}Mn_xTe$

Las películas delgadas de ZnMnTe con un 5 % del contenido nominal de Mn, fueron obtenidas mediante el método CVD sobre sustratos de vidrio en el rango de temperaturas de crecimiento de 350-650 °C. Se observaron granos de 600 a 800 nm con una densidad de $2 \times 10^{12} - 1 \times 10^{12} \text{ NPs/m}^2$, respectivamente. El tamaño de los granos aumentó con el aumento de la temperatura de crecimiento, lo que conduce a una disminución del contenido de Mn.

En las muestras de ZnMnTe aparece una capa de transición entre el sustrato y el material sobre la que crecen cristales orientados en el plano (111) paralelo al sustrato. A altas temperaturas del sustrato el modo de crecimiento cambió de columnas largas a columnas cortas, lo que provocó una disminución en el espesor de la película en el rango de 2.5–1.9 μm a temperaturas de 350–550 °C.

El patrón XRD es una estructura cúbica con una orientación preferencial (111) para todas las muestras, y su posición corresponde aproximadamente a la del ZnTe puro. A bajas temperaturas del sustrato de 623 K (350 °C), el parámetro de red de las muestras de ZnMnTe es mayor que el de ZnTe, lo que indica la sustitución de iones Mn^{2+} más grandes en los sitios Zn^{2+} , pero con un aumento de temperatura de crecimiento superior a 500 °C, el parámetro de red mostró un valor constante cercano al del ZnTe binario puro, lo que significa la ausencia, o contenido reducido de Mn, en las películas. La alta intensidad de los picos (111) en los patrones de XRD sugiere una orientación preferencial out of plane y los planos cristalográficos dominantes son los (111) para todas las temperaturas de crecimiento.

El valor real del contenido de Mn calculado por EDX disminuye en el rango de 0.7 a 2.05 % con un aumento en la temperatura del sustrato, que está significativamente por debajo del valor nominal (5 %) en la carga. La razón de esto puede ser la re-evaporación del Mn en la

superficie de las muestras o no incorporación en los procesos de transporte y deposición a mayor temperatura. El estudio mediante PIXE mostró que el manganeso está distribuido de manera bastante uniforme en el área de la muestra.

Las figuras de polos de la reflexión 111 mostraron que las muestras de ZnMnTe exhiben un pico ancho con su máximo en un ángulo de inclinación de 0 grados y un anillo ancho en un ángulo de inclinación de ≈ 70 grados, lo que indica una orientación azimutal aleatoria. Esta orientación uniaxial muestra que las películas poseen una orientación preferencial out-plane pero no orientación preferencial en in-plane. El porcentaje de partículas con una orientación (111) dentro de ± 10 grados es de 83-92 %.

Las películas de ZnMnTe en el rango estudiado tienen una clara prevalencia de dislocaciones de tornillo. El tamaño longitudinal medio de los cristalitos aumenta considerablemente con la caída del contenido de Mn en las muestras obtenidas a mayor temperatura. El tamaño transversal medio también aumenta, pero menos. La relación de aspecto D_{long}/D_{transv} va de 3,5 a 5 cuando el contenido de Mn se reduce al aumentar la temperatura del sustrato. Comparando el tamaño transversal con los valores obtenidos por SEM se puede concluir que los granos columnares son policristalinos.

La densidad promedio de dislocaciones es débilmente dependiente de la concentración de Mn a temperaturas del sustrato bajas y medias y disminuye cuando el crecimiento se realiza a una temperatura mayor de 923 K (650 °C). Para las dislocaciones del tornillo (111), el vector de Burger, la línea de dislocación y el eje de la dislocación del tornillo siguen la misma dirección. Las muestras obtenidas a menor temperatura muestran una mayor concentración de dislocaciones, lo que confirma los resultados obtenidos mediante de rayos X.

El valor de CSD disminuye al reducir el contenido de Mn con la temperatura y luego aumenta a 773 K (500 °C) en la dirección del plano (111). El valor máximo existe en el rango de temperatura $T_s = 600-650$ K, donde los valores de contenido de Mn fueron mínimos. Por otro lado, el grado de microestres en esta dirección disminuyó con la reducción de Mn y aumenta ligeramente a temperaturas más altas. Esto puede deberse a un cambio en el modo de crecimiento de columnas largas a cortas. Los valores experimentales de tamaño de CSD y grado de microestres fueron más altos que para las películas de ZnTe depositadas con condiciones de crecimiento similares.

El ensanchamiento de la reflexión de las líneas (111) y (222) indica la presencia de defectos de crecimiento y una mejora en la estabilidad de la fase cúbica con menor contenido de Mn. La concentración media de defectos en las películas de ZnMnTe disminuye con la reducción del contenido de Mn, lo que indica una mejora de la estabilidad de la fase cúbica. Por lo tanto, las películas de ZnTe aleadas con Mn sufren la degradación de los parámetros de la subestructura de las películas de ZnTe, lo que se muestra a medida que aumentan la microdeformación y las CSD, así como la concentración de defectos.

La transmitancia de las películas de ZnMnTe muestra un fuerte aumento en la transmitancia a longitudes de onda > 540 nm, lo que indica una buena cristalinidad de las películas depositadas. A valores altos de la longitud de onda de la radiación incidente, las curvas de transmisión adquieren un carácter oscilatorio de interferencia, cuya distancia entre los picos aumenta con el aumento de la temperatura. Con la reducción del contenido de Mn aumenta el coeficiente R , lo que obviamente está asociado con la aparición de películas con un relieve piramidal pronunciado. Las películas de ZnMnTe con más corto tiempo de crecimiento tienen un coeficiente de reflexión más bajo, y esta dependencia se mantiene al calcular el coeficiente de reflexión especular de este material.

Los cálculos de la banda prohibida se realizaron utilizando el máximo del pico de la derivada de los espectros de absorción del material, mostrando que independientemente de la temperatura de crecimiento, tenían una banda prohibida de aproximadamente $E_g = 2.26\text{--}2.27$ eV, que corrobora la presencia de una concentración de Mn muy baja en las películas o su ausencia total en las obtenidas a mas alta temperatura.

Estudios del crecimiento cristalino de $Zn_{1-x}Mn_xS$

Como en el caso anterior, se obtuvieron, mediante el método CSVS, muestras policristalinas de ZnMnS con un 7 % de contenido nominal de Mn sobre sustratos de vidrio en el rango de temperatura de crecimiento de 100-450 °C. A temperaturas del sustrato < 100 °C se destruye la integridad de las películas debido a la aparición de tensiones superficiales asociadas a la diferencia en el coeficiente de expansión térmica entre capa y sustrato y las condiciones de crecimiento poco favorables a la constitución de una estructura cristalina estable. La presencia de Mn cambia la morfología de la película de ZnS desde una más uniforme a una granular.

Con la reducción del contenido de Mn con el incremento de la temperatura de crecimiento el tamaño de grano aumenta (0,65-3,13 μm), con una reducción de la densidad ($0,18 \times 10^{12}$ - $1,16 \times 10^{12}$ NPs/m^2). El grosor de las películas, por el contrario, disminuyó con el aumento de la T_s , lo que puede ser causado por un cambio en el modo de crecimiento, reevaporación y no incorporación de los átomos de Mn a temperaturas más altas.

Entre todas las reflexiones de los planos cristalográficos a temperaturas de crecimiento más bajas 373-623 K (100-400 °C), la intensidad dominante es el pico (111), que indica la presencia de una textura expresada con una estructura cúbica [111], ya que esta dirección coincide con la dirección de el crecimiento más rápido de las cristalitas. A temperaturas de 673-723 K (400-450 °C), la intensidad del pico (111) disminuye fuertemente y la reflexión desde el plano (200) se vuelve dominante. Los picos de difracción correspondientes al Mn elemental (300) observados a una temperatura más baja $T_s = 373\text{--}623$ K (100-350 °C), desaparecen a temperaturas más

altas [> 623 K (> 350 °C)], lo que puede deberse a la re-evaporación y/o no incorporación de Mn en las muestras.

El material de partida tenía las fases cubica y wurtzita, lo que a altas temperaturas probablemente favorece la formación de la fase de wurtzita en las películas depositadas. La existencia de 2 fases se explica por la ausencia de una diferencia entre la energía de formación de las fases de esfalerita y wurtzita para un compuesto de ZnS puro y su igual posibilidad de existencia. El número de cristalitos con una orientación (200) aumenta con la temperatura de crecimiento y el grado de orientación preferencial sube al reducir el contenido de Mn en temperaturas medias del sustrato de 623-673 K (350-400 °C), pero vuelve a bajar a $T_s > 723$ K (450 °C).

El contenido real de Mn disminuyó con la temperatura de crecimiento. La relación entre la concentración atómica de zinc y manganeso ($C_{(Zn+Mn)}$) y la concentración atómica de azufre (C_s) aumentó y a alta temperatura [$T_s = 723$ K (450 °C)] siendo aproximadamente 1,08, que se acerca a la proporción estequiométrica ideal entre los elementos. El parámetro de red para una serie de muestras de ZnMnS estuvo en el rango de 5,6406-5,6424 Å y disminuyó con el aumento de la temperatura de crecimiento, lo que se puede esperar ya que $a_{ZnS} < a_{MnS}$ y la concentración de Mn tendía a disminuir.

El tamaño de la CSD fue significativamente menor que el tamaño del grano y cambió con el aumento de la temperatura en el rango de 42-84 nm, mientras que en el rango de temperatura $T_s = (500-550)$ K con 2.9 % atómico de Mn, su valor fue máximo. El nivel de microestres en la dirección [111] no es uniforme con la reducción del contenido de Mn. Se registró un aumento monótono, después del cual hubo una disminución en el valor y un segundo aumento a altas temperaturas. Este comportamiento está asociado con un cambio en el modo de crecimiento en $T_s > 623$ K. El tamaño de las CSD es significativamente menor que el tamaño del grano. Podemos suponer que estas dimensiones en la dirección perpendicular a los planos (111) se limitan a las maclas, los defectos y los propios CSD están en la forma cercana al cilíndrico. En este caso, la altura del cilindro $L_{(hhh)}$, es ligeramente menor que su diámetro.

El nivel de microestres varió en el rango $\sigma = (7.04-13.83)$ MPa y se concentran principalmente en los límites del CSD, mientras que el volumen de cristalitos está prácticamente libre de dislocaciones. Con un aumento de temperatura, el valor del nivel de microesfuerzo, determinado a partir de las reflexiones del plano (111) - (222) disminuye, alcanzando su mínimo en ~ 2.9 % atómico en el rango de crecimiento $T_s = 500-600$ K, después de lo cual el valor aumenta gradualmente. Con la reducción del contenido de Mn, aumenta la estabilidad del componente cúbico de la película, disminuye la probabilidad de violación del orden de alternancia de los planos (111) y, en consecuencia, disminuye la concentración de los defectos. La baja energía interfacial durante la transición de la fase cúbica a la de wurtzita y los pequeños cambios de energía en la red cristalina en los cambios de fase conducirán a una alta probabilidad de errores

en la alternancia de planos compactos y la formación de defectos, que afectarán la estructura y características subestructurales de las películas.

La transmitancia de las películas de ZnMnS aumenta al alcanzar el "borde rojo" a 340-350 nm, Con la reducción del contenido de Mn aumenta el coeficiente R , lo que obviamente está asociado con la aparición de películas con un relieve piramidal pronunciado. Los cálculos de la banda prohibida muestran que esta se desplaza hacia energías más altas desde 3.569 eV (para 373 K [100 °C]) a 3.642 eV (para 723 K [450 °C]) con el aumento de la temperatura del sustrato, lo que indica, de nuevo, una disminución en el contenido de Mn en las muestras. Para temperaturas medias de 623-673 K (350-400 °C), la posición del máximo es casi similar, lo que apunta a una incorporación de Mn similar.

Capítulo 6

Finalmente, en el Capítulo 6 hemos resumido las principales conclusiones resultantes de este trabajo, parte de las cuales ya han sido descritas con anterioridad y ahora sintetizamos brevemente.

El trabajo realizado en esta tesis ha contribuido al estudio del crecimiento y caracterización de los óxidos binarios de zinc y cadmio, la aleación ternaria asociada y la heteroestructura CdTe/CdO, así como los DMS, ZnMnTe y ZnMnS.

Se ha analizado el efecto de la temperatura y los parámetros de crecimiento sobre las propiedades estructurales de películas delgadas de ZnO y el compuesto ternario CdZnO cúbico del que también se ha estudiado su respuesta óptica. Las dificultades para obtener heteroestructuras de alta calidad basadas en CdTe/CdO están asociadas con un gran desajuste de sus parámetros de red, como resultado de lo cual el CdTe no reproduce fielmente las propiedades de la capa de CdO, dificultando el procesamiento de la heteroestructura. De hecho debido a la compleja morfología, el potencial de contacto superficial no se distribuye uniformemente sobre la superficie de las muestras.

Se encontró que en materiales funcionales ZnMn (Te,S) obtenidos con el método CSVS sobre vidrio, el contenido de Mn disminuyó con el aumento de la temperatura de crecimiento como resultado de su re-evaporación o no incorporación en los procesos de transporte y deposición a mayor temperatura. Para las películas de ZnMnTe, se observó una orientación preferencial *out-plane* con un claro predominio de las dislocaciones de tornillo. La incorporación de Mn induce una degradación en las películas de ZnTe. Para películas de ZnMnS obtenidas a altas temperaturas, se observa la existencia de fases cúbica y wurzita. debido a que la diferencia entre las energías de formación de las fases de esfalerita y wurzita no es significativa y la formación de cada una de las fases tiene la misma probabilidad.

Los estudios ópticos de los estos DMS mostraron que en las películas de ZnMnS la banda prohibida aumentó con la temperatura de crecimiento, lo que corrobora una disminución en el contenido de Manganeso. Por el contrario, en las películas de ZnMnTe este valor no cambió significativamente independientemente de la temperatura, la cual está asociada o con el bajo contenido del elemento de aleación o con su completa ausencia a temperaturas más altas.

Los resultados obtenidos en este trabajo tienen un significado tanto fundamental como aplicado. La nueva información sobre las condiciones de crecimiento, la estructura y subestructura cristalina, la composición química, la morfología de la superficie de la película, sus características ópticas, dependiendo de las condiciones físicas y tecnológicas de crecimiento, debe contribuir al desarrollo de materiales basados en los compuestos binarios de $A_{II}B_{VI}$. En general, esta tesis permitió no solo un estudio en profundidad de las propiedades de los materiales funcionales en función de las condiciones de crecimiento, sino también la adquisición de habilidades y un amplio conocimiento de los diferentes métodos de crecimiento y caracterización.

Bibliography

- [1] D. Bell, *The Coming of Post-Industrial Society: A Venture in Social Forecasting*. New York: Basic Books, 1999. (Cited on page [3](#).)
- [2] J. Poortmans and V. Arkhipov, *Thin Film Solar Cells: Fabrication, Characterization and Applications*. Wiley Series in Materials for Electronic & Optoelectronic Applications, Leuven, Belgium: Wiley & Sons, 2006. (Cited on page [4](#).)
- [3] A. Farenbrook and R. Bub, *Solar cells. Theory and experiment*. Moscow: Energoatomizdat, 1987. (In Russian). (Cited on page [4](#).)
- [4] P. Mahawela, G. Sivaraman, S. Jeedigunta, J. Gaduputi, and et al., “II–VI compounds as the top absorbers in tandem solar cell structures,” *Materials Science and Engineering: B*, vol. 116, no. 3, pp. 283–291, 2005. (Cited on page [4](#).)
- [5] A. Georgobiani, “ A_2B_6 wide-gap semiconductors and prospects for their use,” *Physics-Uspekhi*, vol. 113, no. 1, pp. 129–155, 1974. (Cited on page [4](#).)
- [6] S. Kasap and P. C. (eds.), *Springer Handbook of Electronic and Photonic Materials*. Springer Handbooks, Springer International Publishing, 2017. (Cited on page [4](#).)
- [7] A. Owens and A. Peacock, “Compound semiconductor radiation detectors,” *Nuclear Instruments and Methods in Physics Research. Section A: Accelerators, Spectrometers, Detectors and Associated Equipment*, vol. 531, no. 1, pp. 18–37, 2004. (Cited on page [4](#).)
- [8] B. Grinev, V. Ryzhikov, and V. Seminozhenko, *Scintillation detectors and radiation monitoring systems based on them*. Kyiv: Naukova Dumka, 2007. (In Russian). (Cited on page [4](#).)
- [9] L. Kolodziejski, R. L. Gunshor, and A. Nurmikko, “Wide-bandgap II–VI heterostructures for blue/green optical sources,” *Annu. Rev. Mater. Sci.*, vol. 25, pp. 711–753, 1995. (Cited on page [4](#).)

Bibliography

- [10] P. Barquinha, R. Martins, L. Pereira, and E. F. (auth.), *Transparent Oxide Electronics From Materials to Devices*. J. Wiley & Sons, Ltd. Singapore, 2012. (Cited on page 5.)
- [11] F. Streintz, “Ueber die elektrische leitfähigkeit von gepressten pulvern,” *Ann. Phys.*, vol. 314, no. 12, pp. 854–885, 1902. (Cited on page 5.)
- [12] K. Bädeker, “Über die elektrische leitfähigkeit und die thermoelektrische kraft einiger schwermetallverbindungen,” *Annalen der Physik*, vol. 327, no. 4, pp. 749–766, 1907. (Cited on page 5.)
- [13] J. D. P. David S. Ginley, *Handbook of Transparent Conductors*. Springer US, 2011. (Cited on page 5 and 15.)
- [14] M. Burbano, D. O. Scanlon, and G. W. Watson, “Sources of conductivity and doping limits in CdO from hybrid density functional theory,” *Journal of the American Chemical Society*, vol. 133, no. 38, pp. 15065–15072, 2011. (Cited on page 5.)
- [15] D. Kammler, B. Harder, N. Hrabe, N. McDonald, and et al., “Subsolidus phase relations and transparent conductors in the Cadmium-Indium-Tin Oxide system,” *J. Am. Ceram. Soc.*, vol. 85, pp. 2345–2352, 2002. (Cited on page 5.)
- [16] Z. Zhao, D. Morel, and C. Ferekides, “Electrical and optical properties of tin-doped CdO films deposited by atmospheric metalorganic chemical vapor deposition,” *Thin Solid Films*, vol. 413, no. 1, pp. 203–211, 2002. (Cited on page 5.)
- [17] Wikipedia, “II-VI semiconductor compound — Wikipedia, the free encyclopedia.” [Online; accessed 09- February -2021]. (Cited on page 5.)
- [18] U. K. and B. A.R., “Structural, optical, and electrical properties of Zn-doped CdO thin films fabricated by a simplified spray pyrolysis technique,” *Acta Metall. Sin. (Engl. Lett.)*, vol. 28, pp. 64–71, 2015. (Cited on page 5, 6, 16, 17 and 130.)
- [19] A. Dakhel, “Structural and optoelectronic properties of Zn-incorporated CdO films prepared by sol–gel method,” *Journal of Alloys and Compounds*, vol. 539, pp. 26–31, 2012. (Cited on page 5.)
- [20] G. Alarcon-Flores, B. Vasquez-Perez, A. Pelaez-Rodriguez, and et al., “Electrical and structural characteristics of spray deposited $(ZnO)_x-(CdO)_{1-x}$ thin films,” *Revista Mexicana de Fisica*, vol. 59, no. 5, pp. 403–411, 2013. (Cited on page 6 and 17.)
- [21] J. Yu, J. Kim, D. S. Park, T. Jeong, C. J. Youn, and K. Hong, “Effect of rapid thermal annealing on $Zn_{1-x}Cd_xO$ layers grown by radio-frequency magnetron co-sputtering,” *Crystal Research and Technology*, vol. 45, pp. 1050–1056, 2010. (Cited on page 6.)

-
- [22] W. F. Yang, B. Liu, R. Chen, L. M. Wong, and et al., “Pulsed laser deposition of high-quality ZnCdO epilayers and ZnCdO/ZnO single quantum well on sapphire substrate,” *Applied Physics Letters*, vol. 97, no. 6, p. 061911, 2010. (Cited on page 6 and 17.)
- [23] J. R. Bakke, C. Hägglund, H. J. Jung, and et al., “Atomic layer deposition of CdO and $Cd_xZn_{1-x}O$ films,” *Materials Chemistry and Physics*, vol. 140, no. 2-3, pp. 465–471, 2013. (Cited on page 6 and 17.)
- [24] V. Venkatachalapathy, A. Galeckas, M. Trunk, T. Zhang, and et al., “Understanding phase separation in ZnCdO by a combination of structural and optical analysis,” *Phys. Rev. B*, vol. 83, p. 125315, 2011. (Cited on page 6 and 17.)
- [25] H.-W. Lei, D.-W. Yan, H. Zhang, X.-M. Wang, and et al., “Temperature dependence of surface and structure properties of ZnCdO film,” *Chinese Physics B*, vol. 23, no. 12, p. 126104, 2014. (Cited on page 6.)
- [26] S. T., D. K. Pandya, and R. Singh, “Growth of CdO and ZnCdO-based novel nanostructures using electrochemical deposition,” *International Journal of Nanoscience*, vol. 10, no. 04n05, pp. 827–831, 2011. (Cited on page 6.)
- [27] A. Thompson, C. Boutwell, J. Mares, W. Schoenfeld, and et al., “Thermal stability of CdZnO/ZnO multi-quantum-wells,” *Applied Physics Letters*, vol. 91, no. 20, p. 201921, 2007. (Cited on page 6.)
- [28] J. H. Yu, J. H. Kim, T. S. Jeong, M. S. Akhtar, and et al., “Study on the structural and optical properties of $Cd_{1-x}Zn_xO$ layers enhanced by rapid thermal annealing,” *Electronic Materials Letters*, vol. 7, pp. 215–220, 2011. (Cited on page 6 and 122.)
- [29] J. Tamayo-Arriola, A. Huerta-Barberà, M. M. Bajo, E. Muñoz, V. Muñoz-Sanjosé, and A. Hierro, “Rock-salt CdZnO as a transparent conductive oxide,” *Applied Physics Letters*, vol. 113, 2018. (Cited on page 6, 16, 122 and 131.)
- [30] Y. Sui, Y. Yue, Y. Song, Y. Cao, and et al., “Effects of Cd concentration on microstructure and optical properties of the ternary $Zn_{1-x}Cd_xO$ alloy thin films synthesized by magnetron sputtering,” *Materials Research Bulletin*, vol. 70, pp. 348–353, 2015. (Cited on page 6 and 122.)
- [31] H. Tabet-Derraz, N. Benramdane, D. Nacer, A. Bouzidi, and M. Medles, “Investigations on $Zn_xCd_{1-x}O$ thin films obtained by spray pyrolysis,” *Solar energy materials and solar cells*, vol. 73, no. 3, pp. 249–259, 2002. (Cited on page 6, 16 and 122.)

Bibliography

- [32] N. M. Rao, R. Vijayalakshmi, D. R. Reddy, and B. Reddy, “EPR and susceptibility studies on $(ZnS)_{1-x}(MnTe)_x$ powders,” *Spectrochimica Acta Part A: Molecular and Biomolecular Spectroscopy*, vol. 69, no. 2, pp. 688–691, 2008. (Cited on page 6.)
- [33] O. Goede and W. Heimbrodt, “Optical properties of (Zn, Mn) and (Cd, Mn) chalcogenide mixed crystals and superlattices,” *Phys. stat. sol. (b)*, vol. 146, no. 1, pp. 11–62, 1988. (Cited on page 6.)
- [34] H. Y. Lü, Q. Mu, L. Zhang, Y. J. Lü, and et al., “Photoluminescence characteristics of ZnTe bulk crystal and ZnTe epilayer grown on GaAs substrate by MOVPE,” *Chinese Physics B*, vol. 24, 2015. (Cited on page 7.)
- [35] J. K. Jan A. Gaj, *Introduction to the Physics of Diluted Magnetic Semiconductors*. Springer Series in materials science, Warsaw:Springer US, 2010. (Cited on page 7.)
- [36] A. Avdonin, “Properties of ZnMnTe alloy doped with oxygen and chromium,” *PhD Thesis, Institute of Physics, Polish Academy of Sciences, Warsaw*, 2010. (Cited on page 7.)
- [37] T.-R. Yang, C.-C. Lu, M. M. Dvoynenko, and W.-C. Chou, “The photoluminescence investigation of $Zn_xMn_{1-x}Te$ films,” *Physica B: Condensed Matter*, vol. 329, pp. 928–929, 2003. (Cited on page 7.)
- [38] D. S. Reddy, B. Kang, S. Yu, K. Gunasekhar, and P. S. Reddy, “Synthesis and characterization of $Zn_{1-x}Mn_xS$ nanocrystalline films prepared on glass substrates,” *Applied Physics A*, vol. 91, no. 4, pp. 627–630, 2008. (Cited on page 7 and 25.)
- [39] S. Shaari, M. S. A. Rahman, and N. A. A. M. Arif, “Effect of fabrication parameters on luminescent properties of ZnS:Mn nanocrystals,” in *Proceedings, Optoelectronic Materials and Devices IV*, vol. 7631, p. 76310U, SPIE-OSA-IEEE, 2009. (Cited on page 7.)
- [40] W. Hollerman, S. Goedeke, N. Bergeron, R. Moore, S. Allison, and L. Lewis, “Emission spectra from ZnS:Mn due to low velocity impacts,” in *Proceedings, Photonics for Space Environments X*, vol. 5897, p. 58970F, Proc. of SPIE, 2012. (Cited on page 7.)
- [41] A. Zozime, M. Seibt, J. Ertel, A. Tromson-Carli, and et al., “Influence of a ZnMnTe buffer layer on the growth of ZnTe on (001)GaAs by MOVPE,” *Journal of Crystal Growth*, vol. 249, no. 1, pp. 15–22, 2003. (Cited on page 7 and 23.)
- [42] E. Dynowska and E. Przeździecka, “The crystallographic structure of thin Mn-rich ZnMnTe layers grown by molecular beam epitaxy,” *Journal of Alloys and Compounds*, vol. 401, no. 1, pp. 265–271, 2005. (Cited on page 7, 23 and 154.)

-
- [43] H. Masterson, J. Lunney, and J. Coey, "Investigation into the magnetic properties of $Zn_{1-x}Mn_xTe$ thin films by the Faraday effect," *Journal of Applied Physics*, vol. 81, no. 2, pp. 799–805, 1997. (Cited on page 7 and 23.)
- [44] R. Sahraei, A. Daneshfar, A. Goudarzi, S. Abbasi, M. H. Ara, M., and F. Rahimi, "Optical properties of nanocrystalline ZnS:Mn thin films prepared by chemical bath deposition method," *Journal of Materials Science: Materials in Electronics*, vol. 24, no. 1, pp. 260–266, 2013. (Cited on page 7 and 25.)
- [45] G. Boutaud, W. Cranton, D. Koutsogeorgis, R. Ranson, and et al., "Growth optimisation of ZnS:Mn thin film phosphors for high intensity miniature electroluminescent displays," *Materials Science and Engineering: B*, vol. 165, no. 3, pp. 202–206, 2009. (Cited on page 7, 24 and 25.)
- [46] S. G. Kumar and K. S. R. K. Rao, "Physics and chemistry of CdTe/CdS thin film heterojunction photovoltaic devices: fundamental and critical aspects," *Energy Environ. Sci.*, vol. 7, pp. 45–102, 2014. (Cited on page 7 and 8.)
- [47] F. Lisco, N. Goffin, A. Abbas, G. Claudio, and et al., "Laser annealing of thin film CdTe solar cells using a 808 nm diode laser," in *IEEE 43rd Photovoltaic Specialists Conference (PVSC)*, pp. 2811–2816, Portland, OR, 2016. (Cited on page 7 and 19.)
- [48] A. Romeo, M. Terheggen, D. Abou-Ras, and et al., "Development of thin-film $Cu(In,Ga)Se_2$ and CdTe solar cells," *Progress in Photovoltaics: Research and Applications*, vol. 12, no. 2-3, pp. 93–111, 2004. (Cited on page 7.)
- [49] Wikipedia, "Cadmium telluride photovoltaics — Wikipedia, the free encyclopedia." [Online; accessed 09- February -2021]. (Cited on page 8.)
- [50] Greentechmedia.com, "First solar hits record 22.1 % conversion efficiency for CdTe solar cell." [Online; accessed 09-February-2021]. (Cited on page 8.)
- [51] D. Dorfs, T. Franzl, R. Osovsky, M. Brumer, and et al., "Type-I and type-II nanoscale heterostructures based on CdTe nanocrystals: a comparative study," *Small*, vol. 4 8, pp. 1148–52, 2008. (Cited on page 8.)
- [52] C. Sravani, K. Reddy, and P. Jayarama Reddy, "Preparation and properties of CdO/CdTe thin film solar cells," *Journal of Alloys and Compounds*, vol. 215, no. 1, pp. 239–243, 1994. (Cited on page 8.)

Bibliography

- [53] J. Santos-Cruz, G. Torres-Delgado, R. Castanedo-Pérez, S. Jiménez-Sandoval, and et al., “Influence of the growth parameters of p-CdTe thin films on the performance of Au–Cu/p-CdTe/n-CdO type solar cells,” *Solar Energy*, vol. 80, no. 2, pp. 142–147, 2006. (Cited on page [8](#).)
- [54] X. Zhang, X. ping Zhou, S. yu Ni, G. liang Dai, and Y. sheng Wang, “Preparation and optical properties of CdTe/*CdOnH₂O* core/shell nano-composites in aqueous solution,” *Chinese Journal of Chemical Physics*, vol. 20, no. 6, pp. 779–783, 2007. (Cited on page [8](#).)
- [55] I. Kalinkin, V. Aleskovsky, and A. Simashkevich, *Epitaxial films of A^{II}B^{VI} compounds*. Leningrad: Leningrad State University Publishing House, 1978. (In Russian). (Cited on page [9](#), [46](#) and [47](#).)
- [56] Y. Bubnov, M. Lurie, and F. S. et al., *Vacuum deposition of films in quasi-closed volume*. Moscow: Soviet Radio, 1975. (In Russian). (Cited on page [9](#).)
- [57] A. Lopez-Otero, “Hot wall epitaxy,” *Thin Solid Films*, vol. 49, no. 1, pp. 3–57, 1978. (Cited on page [9](#).)
- [58] J. Zúñiga-Pérez, “Crecimiento de CdTe sobre zafiro: Metodo MOCVD,” *Master’s thesis, Facultat de Fisica, Universitat de Valencia*, 2003. (Cited on page [9](#), [26](#) and [38](#).)
- [59] I. Mora-Seró, “Crecimiento de compuestos II-VI mediante la tecnica MOCVD: Aplicacion al crecimiento de CdTe, HgTe y *Hg_{1-x}Cd_xTe*,” *PhD thesis, Facultat de Fisica, Universitat de Valencia*, 2004. (Cited on page [9](#), [19](#), [35](#), [40](#), [41](#) and [135](#).)
- [60] E. Fortunato, D. Ginley, H. Hosono, and D. C. Paine, “Transparent conducting oxides for photovoltaics,” *MRS bulletin*, vol. 32, no. 3, pp. 242–247, 2007. (Cited on page [11](#).)
- [61] O. Madelung, *Semiconductors—basic data (2nd Edition)*. Springer Science & Business Media, 1996. (Cited on page [12](#).)
- [62] A. A. Ashrafi, A. Ueta, A. Avramescu, H. Kumano, I. Suemune, Y.-W. Ok, and T.-Y. Seong, “Growth and characterization of hypothetical zinc-blende ZnO films on GaAs (001) substrates with *zns* buffer layers,” *Applied Physics Letters*, vol. 76, no. 5, pp. 550–552, 2000. (Cited on page [12](#).)
- [63] F. Decremps, J. Pellicer-Porres, F. Datchi, J. Itié, A. Polian, F. Baudalet, and J. Jiang, “Trapping of cubic ZnO nanocrystallites at ambient conditions,” *Applied physics letters*, vol. 81, no. 25, pp. 4820–4822, 2002. (Cited on page [12](#).)

-
- [64] H. Morkoç and Ü. Özgür, *Zinc oxide: fundamentals, materials and device technology*. John Wiley & Sons, 2009. (Cited on page 12.)
- [65] U. Rössler *et al.*, “Landolt-börnstein, new series, group iii, vols. 17b, 22, 41b,” 1999. (Cited on page 12.)
- [66] V. Karpina, V. Lazorenko, C. Lashkarev, and V. e. a. Dobrowolski, “Zinc oxide—analogue of GaN with new perspective possibilities,” *Crystal Research and Technology: Journal of Experimental and Industrial Crystallography*, vol. 39, no. 11, pp. 980–992, 2004. (Cited on page 13.)
- [67] L. L. Yang, “Synthesis and characterization of ZnO nanostructures,” *PhD thesis, Department of Science and Technology, Linköping University, Sweden*, 2010. (Cited on page 13.)
- [68] A. Umar, N. University, and S. Arabia, *Metal Oxide Nanostructures and their Applications, Vol 5. Ch. 4 (ZnO Nanoparticles: Growth, Properties, and Applications)*. American Scientific Publishers, CA, USA, 2009. (Cited on page 13.)
- [69] H. Morkoç and Ü. Özgür, *Zinc oxide: fundamentals, materials and device technology*. John Wiley & Sons, 2009. (Cited on page 12 and 100.)
- [70] Y. Zhang, T. R. Nayak, H. Hong, and W. Cai, “Biomedical applications of zinc oxide nanomaterials,” *Current molecular medicine*, vol. 13, no. 10, pp. 1633–1645, 2013. (Cited on page 13.)
- [71] D. C. Look, “Recent advances in ZnO materials and devices,” *Materials Science and Engineering: B*, vol. 80, no. 1-3, pp. 383–387, 2001. (Cited on page 13.)
- [72] X.-L. Guo, J.-H. Choi, H. Tabata, and T. Kawai, “Fabrication and optoelectronic properties of a transparent ZnO homostructural light-emitting diode,” *Japanese Journal of Applied Physics*, vol. 40, no. 3A, p. L177, 2001. (Cited on page 13.)
- [73] Y. Qin, X. Wang, and Z. L. Wang, “Microfibre–nanowire hybrid structure for energy scavenging,” *nature*, vol. 451, no. 7180, pp. 809–813, 2008. (Cited on page 13.)
- [74] X. Zheng, G. Shen, C. Wang, Y. Li, D. Dunphy, T. Hasan, C. J. Brinker, and B.-L. Su, “Bio-inspired murray materials for mass transfer and activity,” *Nature communications*, vol. 8, no. 1, pp. 1–9, 2017. (Cited on page 13.)
- [75] J. Kong, “Development of ZnO based light emitting diodes and laser diodes,” *PhD thesis, University of California, US*, 2012. (Cited on page 13.)

Bibliography

- [76] S. Pearton, W. Lim, J. Wright, L. Tien, and et al., “ZnO and related materials for sensors and light-emitting diodes,” *Journal of Electronic Materials*, vol. 37, no. 9, pp. 1426–1432, 2008. (Cited on page [13](#).)
- [77] M. Arafat, B. Dinan, S. A. Akbar, and A. Haseeb, “Gas sensors based on one dimensional nanostructured metal-oxides: a review,” *Sensors*, vol. 12, no. 6, pp. 7207–7258, 2012. (Cited on page [13](#).)
- [78] A. Wei, L. Pan, and W. Huang, “Recent progress in the ZnO nanostructure-based sensors,” *Materials Science and Engineering: B*, vol. 176, no. 18, pp. 1409–1421, 2011. (Cited on page [13](#).)
- [79] Z. L. Wang, “Zinc oxide nanostructures: growth, properties and applications,” *Journal of physics: condensed matter*, vol. 16, no. 25, p. R829, 2004. (Cited on page [13](#).)
- [80] A. Janotti and C. G. Van de Walle, “Fundamentals of zinc oxide as a semiconductor,” *Reports on progress in physics*, vol. 72, no. 12, p. 126501, 2009. (Cited on page [13](#) and [26](#).)
- [81] J. Tang, L. Deng, C. Tay, X. Zhang, and et al., “Determination of carrier concentration dependent electron effective mass and scattering time of n-ZnO thin film by terahertz time domain spectroscopy,” *Journal of Applied Physics*, vol. 115, no. 3, p. 033111, 2014. (Cited on page [13](#).)
- [82] S. Mehmood, M. A. Rehman, H. Ismail, B. Mirza, and A. S. Bhatti, “Significance of post-growth processing of ZnO nanostructures on antibacterial activity against gram-positive and gram-negative bacteria,” *International journal of nanomedicine*, vol. 10, p. 4521, 2015. (Cited on page [14](#).)
- [83] J. Zúñiga-Pérez, C. Munuera, C. Ocal, and V. Muñoz-Sanjosé, “Structural analysis of CdO layers grown on r-plane sapphire (01 $\bar{1}$ 2) by metalorganic vapor-phase epitaxy,” *Journal of crystal growth*, vol. 271, no. 1-2, pp. 223–228, 2004. (Cited on page [14](#), [15](#) and [124](#).)
- [84] M. Burbano, D. O. Scanlon, and G. W. Watson, “Sources of conductivity and doping limits in CdO from hybrid density functional theory,” *Journal of the American Chemical Society*, vol. 133, no. 38, pp. 15065–15072, 2011. (Cited on page [14](#).)
- [85] O. Madelung, *Semiconductors: data handbook*. Springer Science & Business Media, 2004. (Cited on page [14](#), [15](#), [18](#) and [19](#).)
- [86] A. Segura, J. Sánchez-Royo, B. García-Domene, and G. Almonacid, “Current underestimation of the optical gap and Burstein-Moss shift in CdO thin films: A consequence of

- extended misuse of α -versus- $h\nu$ plots,” *Applied Physics Letters*, vol. 99, no. 15, p. 151907, 2011. (Cited on page 14.)
- [87] K. M. Yu, M. A. Mayer, D. T. Speaks, H. He, and et al., “Ideal transparent conductors for full spectrum photovoltaics,” *Journal of Applied Physics*, vol. 111, no. 12, p. 123505, 2012. (Cited on page 14.)
- [88] N. Rajesh, J. Kannan, S. Leonardi, G. Neri, and T. Krishnakumar, “Investigation of CdO nanostructures synthesized by microwave assisted irradiation technique for NO_2 gas detection,” *Journal of alloys and compounds*, vol. 607, pp. 54–60, 2014. (Cited on page 14.)
- [89] P. Dhivya, A. K. Prasad, and M. Sridharan, “Nanostructured cadmium oxide thin films for hydrogen sensor,” *International journal of hydrogen energy*, vol. 37, no. 23, pp. 18575–18578, 2012. (Cited on page 14.)
- [90] R. A. Ismail and O. A. Abdulrazaq, “A new route for fabricating CdO/c-Si heterojunction solar cells,” *Solar energy materials and solar cells*, vol. 91, no. 10, pp. 903–907, 2007. (Cited on page 14.)
- [91] M. Ortega, G. Santana, and A. Morales-Acevedo, “Optoelectronic properties of CdO/Si photodetectors,” *Solid-State Electronics*, vol. 44, no. 10, pp. 1765–1769, 2000. (Cited on page 14.)
- [92] M. Zaïen, N. M. Ahmed, and H. Zainuriah, “Structural and optical properties of nanocrystalline CdO thin film growth by solid-vapor deposition,” in *Advanced Materials Research*, vol. 620, pp. 241–245, Trans Tech Publ, 2013. (Cited on page 14.)
- [93] R. Gupta, K. Ghosh, R. Patel, S. Mishra, and P. Kahol, “Structural, optical and electrical properties of In doped CdO thin films for optoelectronic applications,” *Materials Letters*, vol. 62, no. 19, pp. 3373–3375, 2008. (Cited on page 14.)
- [94] P. Sakthivel, R. Murugan, S. Asaithambi, M. Karuppaiah, S. Rajendran, and G. Ravi, “Radio frequency magnetron sputtered CdO thin films for optoelectronic applications,” *Journal of Physics and Chemistry of Solids*, vol. 126, pp. 1–10, 2019. (Cited on page 14.)
- [95] P. Jefferson, S. Hatfield, T. Veal, P. King, C. McConville, J. Zúñiga-Pérez, and V. Muñoz-Sanjosé, “Bandgap and effective mass of epitaxial cadmium oxide,” *Applied Physics Letters*, vol. 92, no. 2, p. 022101, 2008. (Cited on page 14 and 15.)

- [96] D. İskenderoğlu, “Mg doped CdO thin films grown on glass substrate by spray pyrolysis method,” *Materials Research Express*, vol. 6, no. 2, p. 026423, 2018. (Cited on page 14.)
- [97] M. Zaien, N. Ahmed, and Z. Hassan, “Effects of annealing on the optical and electrical properties of CdO thin films prepared by thermal evaporation,” *Materials Letters*, vol. 105, pp. 84–86, 2013. (Cited on page 14.)
- [98] M. Amini, “First-principles study of defects in transparent conducting oxide materials,” *Phd thesis, Faculteit Wetenschappen, Universiteit Antwerpen, Belgium*, 2014. (Cited on page 15.)
- [99] J. Zúñiga-Pérez, C. Martínez-Tomás, and V. Muñoz-Sanjose, “X-ray characterization of CdO thin films grown on a-, c-, r-and m-plane sapphire by metalorganic vapour phase-epitaxy,” *physica status solidi (c)*, vol. 2, no. 3, pp. 1233–1238, 2005. (Cited on page 15, 122 and 124.)
- [100] A. Huerta-Barberà, L. M. Guia, O. Klymov, and et al., “MOCVD growth of CdO very thin films: Problems and ways of solution,” *Applied Surface Science*, vol. 385, pp. 209–215, 2016. (Cited on page 15, 41 and 125.)
- [101] A. H. i Barberà, “Creixement cristal·lí mitjançant la tècnica MOCVD i caracterització morfològica i estructural dels òxids de cadmi i zinc,” *PhD thesis, Facultat de Física, Universitat de Valencia*, 2019. (Cited on page 15, 17, 37 and 122.)
- [102] A. B. Khatibani, S. Rozati, and Z. Hallaj, “Synthesis and characterization of nanostructure CdO:Zn thin films deposited by spray pyrolysis technique: Molarity and heat treatment effects,” *Materials science in semiconductor processing*, vol. 16, no. 3, pp. 980–986, 2013. (Cited on page 16 and 17.)
- [103] O. Vigil, L. Vaillant, F. Cruz, G. Santana, A. Morales-Acevedo, and G. Contreras-Puente, “Spray pyrolysis deposition of cadmium–zinc oxide thin films,” *Thin Solid Films*, vol. 361, pp. 53–55, 2000. (Cited on page 16.)
- [104] F. Liu, Y. Lai, J. Liu, B. Wang, and et al., “Characterization of chemical bath deposited CdS thin films at different deposition temperature,” *Journal of alloys and compounds*, vol. 493, no. 1-2, pp. 305–308, 2010. (Cited on page 16.)
- [105] L. Hong-Wen, Y. Da-Wei, Z. Hong, W. Xue-Min, and et al., “Temperature dependence of surface and structure properties of *znco* film,” *Chinese Physics B*, vol. 23, no. 12, p. 126104, 2014. (Cited on page 17.)

-
- [106] T. Liu, D. Wang, F. Guo, S. Jiao, and et al., “Effect of annealing temperature on the optical property of high Cd content CdZnO films,” *Superlattices and Microstructures*, vol. 97, pp. 569–574, 2016. (Cited on page 17.)
- [107] X. Zhang, M. Guo, W. Li, and C. Liu, “First-principles study of electronic and optical properties in wurtzite $Zn_{1-x}Cd_xO$,” *Journal of Applied Physics*, vol. 103, no. 6, p. 063721, 2008. (Cited on page 17.)
- [108] S. S. Li, *Semiconductor physical electronics*. Springer Science & Business Media, 2012. (Cited on page 18.)
- [109] S. Hossain, N. Amin, M. Martin, M. M. Aliyu, and et al., “A numerical study on the prospects of high efficiency ultra thin $Zn_xCd_{1-x}S/CdTe$ solar cell,” *Chalcogenide Letters*, vol. 8, no. 4, 2011. (Cited on page 18.)
- [110] J. Donegan and Y. Rakovich, *Cadmium telluride quantum dots: advances and applications*. CRC Press, 2013. (Cited on page 19.)
- [111] University of reading, “Cadmium telluride (CdTe) — infrared multilayer laboratory.” [Online; accessed 11- February -2021]. (Cited on page 19.)
- [112] D. Bonnet and P. Meyers, “Cadmium-telluride—material for thin film solar cells,” *Journal of Materials Research*, vol. 13, no. 10, pp. 2740–2753, 1998. (Cited on page 19.)
- [113] J. D. Poplawsky, “Cadmium telluride solar cells: Record-breaking voltages,” *Nature Energy*, vol. 1, no. 3, pp. 1–2, 2016. (Cited on page 19.)
- [114] W. Chen, D. Grouquist, and J. Roark, “Voltage tunable electroluminescence of CdTe nanoparticle light-emitting diodes,” *Journal of Nanoscience and Nanotechnology*, vol. 2, no. 1, pp. 47–53, 2002. (Cited on page 19.)
- [115] C. M. Courtney, S. M. Goodman, J. A. McDaniel, N. E. Madinger, and et al., “Photoexcited quantum dots for killing multidrug-resistant bacteria,” *Nature materials*, vol. 15, no. 5, pp. 529–534, 2016. (Cited on page 19.)
- [116] T. Du, K. Cai, H. Han, L. Fang, and et al., “Probing the interactions of CdTe quantum dots with pseudorabies virus,” *Scientific reports*, vol. 5, no. 1, pp. 1–10, 2015. (Cited on page 19.)
- [117] Y. Eisen, A. Shor, and I. Mardor, “CdTe and CdZnTe x-ray and gamma-ray detectors for imaging systems,” *IEEE Transactions on Nuclear Science*, vol. 51, no. 3, pp. 1191–1198, 2004. (Cited on page 19.)

Bibliography

- [118] A. Rogalski, “HgCdTe infrared detector material: history, status and outlook,” *Reports on Progress in Physics*, vol. 68, no. 10, p. 2267, 2005. (Cited on page 19.)
- [119] C. Szeles, “CdZnTe and CdTe materials for X-ray and gamma ray radiation detector applications,” *physica status solidi (b)*, vol. 241, no. 3, pp. 783–790, 2004. (Cited on page 19.)
- [120] J. Gao, W. Jie, Y. Yuan, T. Wang, G. Zha, and J. Tong, “Dependence of film texture on substrate and growth conditions for CdTe films deposited by close-spaced sublimation,” *Journal of Vacuum Science & Technology A: Vacuum, Surfaces, and Films*, vol. 29, no. 5, p. 051507, 2011. (Cited on page 19.)
- [121] K. Diwate, A. Pawbake, S. Rondiya, R. Kulkarni, and et al., “Substrate temperature dependent studies on properties of chemical spray pyrolysis deposited cds thin films for solar cell applications,” *Journal of Semiconductors*, vol. 38, no. 2, p. 023001, 2017. (Cited on page 19.)
- [122] S. Deivanayaki, P. Jayamurugan, R. Mariappan, and V. Ponnuswamy, “Optical and structural characterization of CdTe thin films by chemical bath deposition technique,” *Chalcogenide Letters*, vol. 7, no. 3, pp. 159–163, 2010. (Cited on page 19.)
- [123] V. Barrioz, D. A. Lamb, E. W. Jones, and S. Irvine, “Suitability of atmospheric-pressure MOCVD CdTe solar cells for inline production scale,” *MRS Online Proceedings Library Archive*, vol. 1165, 2009. (Cited on page 19.)
- [124] S. Chander and M. Dhaka, “Optimization of physical properties of vacuum evaporated CdTe thin films with the application of thermal treatment for solar cells,” *Materials Science in Semiconductor Processing*, vol. 40, pp. 708–712, 2015. (Cited on page 19.)
- [125] A. Pidluzhna, K. Ivaniuk, P. Stakhina, and Z. e. a. Hotra, “Multi-channel electroluminescence of CdTe/CdS core-shell quantum dots implemented into a QLED device,” *Dyes and pigments*, vol. 162, pp. 647–653, 2019. (Cited on page 19.)
- [126] B. Ghosh, S. Hussain, D. Ghosh, R. Bhar, and A. Pal, “Studies on CdTe films deposited by pulsed laser deposition technique,” *Physica B: Condensed Matter*, vol. 407, no. 21, pp. 4214–4220, 2012. (Cited on page 19.)
- [127] M. K. Khalaf, B. A. ALhilli, A. I. Khudiar, and A. Abd Alzahra, “Influence of nanocrystalline size on optical band gap in CdSe thin films prepared by dc sputtering,” *Photonics and Nanostructures-Fundamentals and Applications*, vol. 18, pp. 59–66, 2016. (Cited on page 19.)

-
- [128] R. Bhattacharya and K. Rajeshwar, “Electrodeposition of CdTe thin films,” *Journal of the Electrochemical Society*, vol. 131, no. 9, p. 2032, 1984. (Cited on page [19](#).)
 - [129] S.-H. Kim, J.-Y. Lee, W.-K. Han, and J.-H. Lee, “Electrochemical deposition of CdSe/CdTe multilayer nanorods for hybrid solar cell,” *Thin Solid Films*, vol. 518, no. 24, pp. 7222–7224, 2010. (Cited on page [19](#).)
 - [130] Z. Zhao, V. Komin, V. Viswanathan, D. Morel, and C. Ferekides, “Application of tin-doped cadmium oxide films in CdTe/CdS solar cells,” in *Conference Record of the Twenty-Eighth IEEE Photovoltaic Specialists Conference-2000 (Cat. No. 00CH37036)*, pp. 662–665, IEEE, 2000. (Cited on page [19](#).)
 - [131] S. Irvine, D. Lamb, V. Barrioz, A. Clayton, and et al., “The role of transparent conducting oxides in metal organic chemical vapour deposition of CdTe/CdS photovoltaic solar cells,” *Thin Solid Films*, vol. 520, no. 4, pp. 1167–1173, 2011. (Cited on page [19](#).)
 - [132] H. Munekata, H. Ohno, S. Von Molnar, A. Segmüller, L. Chang, and L. Esaki, “Diluted magnetic III-V semiconductors,” *Physical Review Letters*, vol. 63, no. 17, p. 1849, 1989. (Cited on page [21](#).)
 - [133] Warwick. Department of Physics, “Dilute magnetic semiconductors — III-V compound semiconductors (DMS).” [Online; accessed 11- February -2021]. (Cited on page [21](#).)
 - [134] J. K. Furdyna and J. Kossut, *Diluted magnetic semiconductors*. Academic Press (Series: Semiconductors and Semimetals 25), 1988. (Cited on page [21](#), [22](#) and [23](#).)
 - [135] M. Hamedoun, Z. Elachheb, H. Bakrim, A. Hourmatallah, and et al., “Electronic and magnetic properties of diluted magnetic semiconductors $A_{1-x}Mn_xTe$ ($A = \text{Cd}, \text{Zn}$) ($0 \leq x \leq 1$),” *physica status solidi (b)*, vol. 236, no. 3, pp. 661–667, 2003. (Cited on page [22](#).)
 - [136] C. Martinez-Tomas, O. Klymov, S. Agouram, D. Kurbatov, A. Opanasyuk, and V. Munoz-Sanjose, “Substructural properties and anisotropic peak broadening in $Zn_{1-x}Mn_xTe$ films determined by a combined methodology based on SEM, HRTEM, XRD, and HRXRD,” *Metallurgical and Materials Transactions A*, vol. 47, no. 12, pp. 6645–6654, 2016. (Cited on page [22](#).)
 - [137] P. Zhukovskii, Y. Partyka, P. Vengerek, Y. V. Sidorenko, and et al., “Optical band gap of $Cd_{1-x}Mn_xTe$ and $Zn_{1-x}Mn_xTe$ semiconductors,” *Semiconductors*, vol. 35, no. 8, pp. 900–903, 2001. (Cited on page [22](#).)

Bibliography

- [138] S. Touat, F. Litimein, A. Tadjer, and B. Bouhafs, “The spin effect in zinc-blende $Cd_{0.5}Mn_{0.5}Te$ and $Zn_{0.5}Mn_{0.5}Te$ diluted magnetic semiconductors: FP-LAPW study,” *Physica B: Condensed Matter*, vol. 405, no. 2, pp. 625–631, 2010. (Cited on page 22.)
- [139] M. Imamura, A. Okada, and T. Yamaguchi, “Magneto-optical properties of wider gap II-VI $ZnMnTe$ and $ZnMnCoTe$ films,” *Journal of applied physics*, vol. 99, no. 8, p. 08M706, 2006. (Cited on page 22 and 189.)
- [140] Y.-M. Yu, O. Byungsung, M.-Y. Yoon, and et al., “Effect of Mn concentration on photoluminescence characteristics of $Zn_{1-x}Mn_xTe$ epilayers,” *Thin Solid Films*, vol. 426, no. 1-2, pp. 265–270, 2003. (Cited on page 22 and 23.)
- [141] Y.-M. Yu, J. Park, M. Hyun, S. Nam, and et al., “Structural and optical properties of $Zn_{1-x}Mn_xTe$ epilayers as diluted magnetic II–VI semiconductors,” *Journal of crystal growth*, vol. 237, pp. 1589–1593, 2002. (Cited on page 22.)
- [142] K. Yu, W. Walukiewicz, J. Wu, and W. a. a. Shan, “Diluted II-VI oxide semiconductors with multiple band gaps,” *Physical Review Letters*, vol. 91, no. 24, p. 246403, 2003. (Cited on page 23.)
- [143] J.-H. Lee, J. Wu, and J. C. Grossman, “Enhancing the thermoelectric power factor with highly mismatched isoelectronic doping,” *Physical review letters*, vol. 104, no. 1, p. 016602, 2010. (Cited on page 23.)
- [144] U. Hömmerich, J. Seo, A. Bluiett, M. Turner, and et al., “Mid-infrared laser development based on transition metal doped cadmium manganese telluride,” *Journal of Luminescence*, vol. 87, pp. 1143–1145, 2000. (Cited on page 23.)
- [145] W. Khan, S. Azam, I. Ullah, M. Rani, and et al., “Insight into the optoelectronic and thermoelectric properties of Mn doped $ZnTe$ from first principles calculation,” *Crystals*, vol. 9, no. 5, p. 247, 2019. (Cited on page 23.)
- [146] S.-W. Han, H.-S. Kang, B.-Z. Jiang, S.-Y. Seo, and et al., “Structural and magnetic properties of $ZnMnTe$ semiconductor,” *Journal of magnetism and magnetic materials*, vol. 310, no. 2, pp. 2114–2116, 2007. (Cited on page 23.)
- [147] Y. R. Do, Y.-C. Kim, D.-H. Park, and Y.-D. Huh, “Effects of 2D SiO_2 nanorod-modified substrates on the morphology and CL properties of $ZnS:Mn$ particle-like thin-film phosphors,” *Journal of the Electrochemical Society*, vol. 152, no. 4, p. H48, 2005. (Cited on page 24.)

-
- [148] X. Fang, T. Zhai, U. K. Gautam, L. Li, and et al., “ZnS nanostructures: from synthesis to applications,” *Progress in Materials Science*, vol. 56, no. 2, pp. 175–287, 2011. (Cited on page 24.)
 - [149] A. K. Rath, S. Bhaumik, and A. J. Pal, “Mn-doped nanocrystals in light-emitting diodes: Energy-transfer to obtain electroluminescence from quantum dots,” *Applied Physics Letters*, vol. 97, no. 11, p. 113502, 2010. (Cited on page 24.)
 - [150] N. Gurin and O. Y. Sabitov, “Relaxation of parameters of thin-film electroluminescent ZnS:Mn-based structures when turned off,” *Semiconductors*, vol. 42, no. 6, pp. 675–688, 2008. (Cited on page 24.)
 - [151] M. Chattopadhyay, P. Kumbhakar, R. Sarkar, and A. Mitra, “Enhanced three-photon absorption and nonlinear refraction in ZnS and Mn^{2+} doped ZnS quantum dots,” *Applied physics letters*, vol. 95, no. 16, p. 163115, 2009. (Cited on page 24.)
 - [152] C. Sombuthawee, S. Bonsall, and F. Hummel, “Phase equilibria in the systems ZnS-MnS, ZnS- $CuInS_2$, and MnS- $CuInS_2$,” *Journal of Solid State Chemistry*, vol. 25, no. 4, pp. 391–399, 1978. (Cited on page 24.)
 - [153] M. S. Khan, L. Shi, X. Yang, S. Ali, and et al., “Optoelectronic and magnetic properties of Mn-doped and Mn-C co-doped wurtzite ZnS: a first-principles study,” *Journal of Physics: Condensed Matter*, vol. 31, no. 39, p. 395702, 2019. (Cited on page 24.)
 - [154] T. Schuler, R. Stern, R. McNorton, S. Willoughby, and et al., “Electronic structure of the dilute magnetic semiconductor $Zn_{0.90}Mn_{0.10}S$ obtained by soft x-ray spectroscopy and first-principles calculations,” *Physical Review B*, vol. 72, no. 4, p. 045211, 2005. (Cited on page 25.)
 - [155] M. Sebastian and P. Krishna, “Stacking faults and structural transformations in $Zn_xMn_{1-x}S$ single crystals grown from vapour,” *Journal of crystal growth*, vol. 66, no. 3, pp. 586–592, 1984. (Cited on page 25.)
 - [156] A. Divya, B. Reddy, S. Sambasivam, K. S. Kumar, and P. S. Reddy, “Structural and optical characterization of ZnS nanoparticles co-doped with Mn and Te,” *Physica E: Low-dimensional Systems and Nanostructures*, vol. 44, no. 3, pp. 541–545, 2011. (Cited on page 25.)
 - [157] D. Son, D.-R. Jung, J. Kim, T. Moon, and et al., “Synthesis and photoluminescence of Mn-doped zinc sulfide nanoparticles,” *Applied Physics Letters*, vol. 90, no. 10, p. 101910, 2007. (Cited on page 25 and 169.)

Bibliography

- [158] S. Schön, M. Chaichimansour, W. Park, T. Yang, B. Wagner, and C. Summers, “Homogeneous and δ -doped ZnS:Mn grown by MBE,” *Journal of crystal growth*, vol. 175, pp. 598–602, 1997. (Cited on page 25.)
- [159] M. Migita, O. Kanehisa, M. Shiiki, and H. Yamamoto, “The preparation of ZnS:Mn electroluminescent layers by mocvd using new manganese sources,” *Journal of Crystal Growth*, vol. 93, no. 1-4, pp. 686–691, 1988. (Cited on page 25.)
- [160] Z. Ren, H. Yang, L. Shen, and S. Do Han, “Hydrothermal preparation and properties of nanocrystalline ZnS:Mn,” *Journal of Materials Science: Materials in Electronics*, vol. 19, no. 1, pp. 1–4, 2008. (Cited on page 25.)
- [161] N. Karar, S. Raj, and F. Singh, “Properties of nanocrystalline ZnS:Mn,” *Journal of crystal growth*, vol. 268, no. 3-4, pp. 585–589, 2004. (Cited on page 25.)
- [162] E. Monakhov, A. Y. Kuznetsov, and B. Svensson, “Zinc oxide: bulk growth, role of hydrogen and Schottky diodes,” *Journal of Physics D: Applied Physics*, vol. 42, no. 15, p. 153001, 2009. (Cited on page 26.)
- [163] S. Pearton, W. Lim, J. Wright, L. Tien, H. Kim, D. Norton, H. Wang, B. Kang, F. Ren, J. Jun, *et al.*, “ZnO and related materials for sensors and light-emitting diodes,” *Journal of Electronic Materials*, vol. 37, no. 9, pp. 1426–1432, 2008. (Cited on page 26.)
- [164] D. W. Shaw, “Mechanisms in vapour epitaxy of semiconductors,” in *Crystal Growth*, pp. 1–48, Springer, 1974. (Cited on page 27 and 28.)
- [165] A. C. Jones and M. L. Hitchman, *Chemical vapour deposition: precursors, processes and applications*. Royal society of chemistry, 2009. (Cited on page 27, 28 and 37.)
- [166] L. M. Guia, “Creixement del MgCdO: un nou aliatge ternari d’oxids II –VI,” *PhD thesis, Facultat de Fisica, Universitat de Valencia*, 2017. (Cited on page 29.)
- [167] FCON CO, “What is a mass flow controller? – Principle and sturacture of mass flow controllers..” [Online; accessed 11- February -2021]. (Cited on page 31 and 32.)
- [168] K. Seshan, *Handbook of thin film deposition processes and techniques (Second Edition)*. William Andrew, 2002. (Cited on page 35 and 37.)
- [169] M. A. Herman, W. Richter, and H. Sitter, *Epitaxy: physical principles and technical implementation*, vol. 62. Springer Science & Business Media, 2013. (Cited on page 35.)
- [170] R. J. Betsch, “Parametric analysis of control parameters in MOCVD,” *Journal of Crystal Growth*, vol. 77, no. 1-3, pp. 210–218, 1986. (Cited on page 36.)

-
- [171] G. B. Stringfellow, *Organometallic vapor-phase epitaxy: theory and practice*. Elsevier. Academic Press, 1999. (Cited on page 37 and 102.)
- [172] Americal Elements, “Diisopropyl telluride (DIPTe).” [Online; accessed 11- February -2021]. (Cited on page 37.)
- [173] Wikipedia, “Diethylzinc — Wikipedia, the free encyclopedia.” [Online; accessed 11- February -2021]. (Cited on page 37.)
- [174] Wikipedia, “Dimethylcadmium — Wikipedia, the free encyclopedia.” [Online; accessed 11- February -2021]. (Cited on page 37.)
- [175] Wikipedia, “Tert-butanol — Wikipedia, the free encyclopedia.” [Online; accessed 11- February -2021]. (Cited on page 37.)
- [176] Aston Chemical, “Diisopropyl telluride.” [Online; accessed 11- February -2021]. (Cited on page 37.)
- [177] MolPort.com, “Dimethylcadmium.” [Online; accessed 11- February -2021]. (Cited on page 37.)
- [178] Sigmaaldrich.com, “Tert-butanol — Merck.” [Online; accessed 11- February -2021]. (Cited on page 37.)
- [179] Wikipedia, “Atmospheric pressure — Wikipedia, the free encyclopedia.” [Online; accessed 11- February -2021]. (Cited on page 37.)
- [180] J. Z. Pérez, “Crystal growth and characterization of II-VI oxides thin films,” *PhD thesis, Facultat de Fisica, Universitat de Valencia*, 2005. (Cited on page 38, 41, 110, 111, 115 and 135.)
- [181] Roditi.com, “Sapphire properties.” [Online; accessed 11- February -2021]. (Cited on page 39.)
- [182] PmOptics.com, “Sapphire.” [Online; accessed 01- February -2021]. (Cited on page 39.)
- [183] Wikipedia, “Gallium arsenide — Wikipedia, the free encyclopedia.” [Online; accessed 11- February -2021]. (Cited on page 39.)
- [184] O. Madelung, *Semiconductors: group IV elements and III-V compounds (Group III, Vol. 41A1a)*. Springer Science & Business Media, 1991. (Cited on page 39.)
- [185] E. R. Dobrovinskaya, L. A. Lytvynov, and V. Pishchik, “Properties of sapphire,” in *Sapphire*, pp. 55–176, Springer, 2009. (Cited on page 39 and 130.)

Bibliography

- [186] Hyperphysics, “Semiconductor band gaps.” [Online; accessed 11- February -2021]. (Cited on page [39](#).)
- [187] Janis.com, “Gallium arsenide (GaAs) transmission curve datasheet.” [Online; accessed 11- February -2021]. (Cited on page [39](#).)
- [188] Clipartmax.com, “Trigonal crystal structure of sapphire.” [Online; accessed 17- July - 2021]. (Cited on page [39](#).)
- [189] Y. A. Du, S. Sakong, and P. Kratzer, “As vacancies, Ga antisites, and Au impurities in zinc blende and wurtzite GaAs nanowire segments from first principles,” *Physical Review B*, vol. 87, no. 7, p. 075308, 2013. (Cited on page [39](#).)
- [190] F. Cuccureddu, S. Murphy, I. Shvets, M. Porcu, and et al., “Surface morphology of c-plane sapphire (α -alumina) produced by high temperature anneal,” *Surface Science*, vol. 604, no. 15-16, pp. 1294–1299, 2010. (Cited on page [40](#).)
- [191] S. Vasheghani Farahani, V. Muñoz-Sanjosé, J. Zúñiga-Pérez, C. McConville, and T. Veal, “Temperature dependence of the direct bandgap and transport properties of CdO,” *Applied Physics Letters*, vol. 102, no. 2, p. 022102, 2013. (Cited on page [41](#).)
- [192] I. A. Sluchinskaya, *Fundamentals of Materials Science and Semiconductor Technology*. Moscow: Mir, 2002. [In Russian]. (Cited on page [43](#), [44](#) and [46](#).)
- [193] B. R. Pamplin, *Crystal growth (2nd edition)*. Pergamon press, 1980. (Cited on page [44](#).)
- [194] P. Capper, *Crystal Growth Technology: From Fundamentals and Simulation to Large-scale Production*. Wiley-VCH, 2008. (Cited on page [44](#), [45](#) and [46](#).)
- [195] J. C. B. at el., *Ullmann’s Encyclopedia of Industrial Chemistry (chapter "Crystal Growth")*. Wiley-VCH, 2007. (Cited on page [45](#).)
- [196] Owen.ru, “TRM10 PID-controller with universal input.” [In Russian. Online; accessed 11- February -2021]. (Cited on page [48](#) and [49](#).)
- [197] M. Kolesnyk, “Structural, electrophysical and optical properties of ZnTe films and ZnTe/CdTe heterojunctions,” *PhD thesis, Faculty of Electronics and Information Technologies, Sumy State University*, 2010. (In Ukrainian). (Cited on page [49](#), [53](#) and [54](#).)
- [198] Owen.ru, “CUTT control unit thyristors and simisters.” [In Russian. Online; accessed 11- February -2021]. (Cited on page [50](#).)

-
- [199] Koppglass.com, “3 common glass types: Properties and applications.” [Online; accessed 11- February -2021]. (Cited on page 51, 52 and 53.)
- [200] S. Irvine and P. Capper, *Metalorganic Vapor Phase Epitaxy (MOVPE)*. Wiley Online Library, 2019. (Cited on page 51.)
- [201] M. I. Ojovan, W. E. Lee, and S. N. Kalmykov, *An introduction to nuclear waste immobilisation*. Elsevier, 2005. (Cited on page 51.)
- [202] Britannica.com, “Properties of glass — Industrial glass.” [Online; accessed 11- February -2021]. (Cited on page 51 and 52.)
- [203] Obgonay.ru, “Crystalline and amorphous substances.” [In Russian. Online; accessed 11- February -2021]. (Cited on page 52.)
- [204] D. Kurbatov, “Structural, optical and electrophysical properties of ZnS film and n-ZnS/p-CdTe heterojunctions,” *PhD thesis, Faculty of Electronics and Information Technologies, Sumy State University*, 2010. [In Ukrainian]. (Cited on page 54.)
- [205] W. Zhou and Z. L. Wang, *Scanning microscopy for nanotechnology: techniques and applications*. Springer science & business media, 2007. (Cited on page 56.)
- [206] S. Hofmann, *Auger-and X-ray photoelectron spectroscopy in materials science: a user-oriented guide*, vol. 49. Springer Science & Business Media, 2012. (Cited on page 56.)
- [207] Wikipedia, “Scanning electron microscope — Wikipedia, the free encyclopedia.” [Online; accessed 17- February -2021]. (Cited on page 57.)
- [208] The university of Utah, “Electron microscopy tutorial — Advanced microscopy.” [Online; accessed 17- February -2021]. (Cited on page 57.)
- [209] D. B. Williams, C. B. Carter, and D. B. Williams, *Transmission Electron Microscopy: A Textbook for Materials Science (2nd Edition)*. Springer Science & Business Media, 2009. (Cited on page 58, 62 and 63.)
- [210] Encyclopaedia Britannica, “The components of a scanning electron microscope (SEM).” [Online; accessed 26-May-2021]. (Cited on page 59.)
- [211] R. A. Haight, F. M. Ross, and J. B. Hannon, *Handbook Of Instrumentation And Techniques For Semiconductor Nanostructure Characterization (In 2 Volumes)*, vol. 2. World Scientific, 2011. (Cited on page 59.)

Bibliography

- [212] P. Echlin, C. Fiori, J. Goldstein, D. C. Joy, and D. E. Newbury, *Advanced scanning electron microscopy and X-ray microanalysis*. Springer Science & Business Media, 2013. (Cited on page [60](#).)
- [213] B. Fultz and J. M. Howe, *Transmission electron microscopy and diffractometry of materials*. Springer Science & Business Media, 2012. (Cited on page [62](#) and [65](#).)
- [214] D. N. M. Martínez, “Crecimiento cristalino de nano y microestructuras de ZnO mediante PVD y MOCVD,” *PhD thesis, Facultat de Fisica, Universitat de Valencia*, 2013. (Cited on page [63](#) and [64](#).)
- [215] C. R. Brundle, C. A. Evans, L. Wilson, S. Wilson, and G. Wilson, *Encyclopedia of materials characterization: surfaces, interfaces, thin films*. Gulf Professional Publishing, 1992. (Cited on page [65](#) and [71](#).)
- [216] B. K. Agarwal, *X-ray spectroscopy: an introduction*, vol. 15. Springer, 1991. (Cited on page [65](#).)
- [217] J. C. Russ, M. A. Frs, R. Kiessling, and J. Charles., *Fundamentals of Energy Dispersive X-ray Analysis*. Elsevier Ltd., 1984. (Cited on page [65](#).)
- [218] K. Ishii, “PIXE and its applications to elemental analysis,” *Quantum Beam Science*, vol. 3, no. 2, p. 12, 2019. (Cited on page [67](#).)
- [219] Ruder Bošković Institute, “PIXE, RBS and PIGE spectroscopies.” [Online; accessed 17-February -2021]. (Cited on page [67](#) and [68](#).)
- [220] Wikipedia, “Particle-induced X-ray emission — Wikipedia, the free encyclopedia.” [Online; accessed 17- February -2021]. (Cited on page [68](#).)
- [221] L. C. Wagner, *Failure analysis of integrated circuits: tools and techniques*, vol. 494. Springer Science & Business Media, 1999. (Cited on page [68](#).)
- [222] S. A. Johansson, J. L. Campbell, and K. G. Malmqvist, *Particle-induced X-ray emission spectrometry (PIXE)*, vol. 133. Wiley New York, 1995. (Cited on page [70](#).)
- [223] D. Magilin, A. Ponomarev, V. Rebrov, N. Sayko, and et al., “Performance of the sumy nuclear microprobe with the integrated probe-forming system,” *Nuclear Instruments and Methods in Physics Research Section B: Beam Interactions with Materials and Atoms*, vol. 267, no. 12-13, pp. 2046–2049, 2009. (Cited on page [70](#).)
- [224] Wikipedia, “Miller index — Wikipedia, the free encyclopedia.” [Online; accessed 27-May-2021]. (Cited on page [72](#).)

-
- [225] M. Birkholz, *Thin film analysis by X-ray scattering*. John Wiley & Sons, 2006. (Cited on page 73.)
- [226] B. D. Cullity, *Elements of X-ray Diffraction*. Addison-Wesley Publishing, 1956. (Cited on page 73.)
- [227] Wikipedia, “Bragg’s law — Wikipedia, the free encyclopedia.” [Online; accessed 17- February -2021]. (Cited on page 73.)
- [228] Q.-J. Xu, B. Liu, S.-Y. Zhang, T. Tao, and et al., “Structural characterization of $Al_{0.55}Ga_{0.45}N$ epitaxial layer determined by high resolution x-ray diffraction and transmission electron microscopy,” *Chinese Physics B*, vol. 26, no. 4, p. 047801, 2017. (Cited on page 74.)
- [229] W. D. Callister Jr and D. G. Rethwisch, *Fundamentals of materials science and engineering: an integrated approach*. John Wiley & Sons, 2015. (Cited on page 75.)
- [230] G. Williamson and W. Hall, “X-ray line broadening from filed aluminium and wolfram,” *Acta metallurgica*, vol. 1, no. 1, pp. 22–31, 1953. (Cited on page 76.)
- [231] G. Kumar, S. Sarmash, L. Obulapathi, and et al., “Structural, optical and electrical properties of heavy ion irradiated CdZnO thin films,” *Thin Solid Films*, vol. 605, pp. 102–107, 2016. (Cited on page 76.)
- [232] E. J. Mittemeijer and U. Welzel, “The “state of the art” of the diffraction analysis of crystallite size and lattice strain,” *Zeitschrift für Kristallographie International journal for structural, physical, and chemical aspects of crystalline materials*, vol. 223, no. 9, pp. 552–560, 2008. (Cited on page 76.)
- [233] M. A. Krivoglaz, *Theory of X-ray and Thermal-Neutron scattering by real crystals*. Springer, 1969. (Cited on page 76.)
- [234] T. Ungár, S. Ott, P. Sanders, A. Borbély, and J. Weertman, “Dislocations, grain size and planar faults in nanostructured copper determined by high resolution X-ray diffraction and a new procedure of peak profile analysis,” *Acta materialia*, vol. 46, no. 10, pp. 3693–3699, 1998. (Cited on page 76.)
- [235] T. Ungár, “Strain broadening caused by dislocations,” in *Materials Science Forum*, vol. 278, pp. 151–157, Trans Tech Publ, 1998. (Cited on page 76.)

Bibliography

- [236] T. Ungár, I. Dragomir-Cernatescu, D. Louër, and N. Audebrand, “Dislocations and crystallite size distribution in nanocrystalline CeO_2 obtained from an ammonium cerium (IV)-nitrate solution,” *Journal of Physics and Chemistry of Solids*, vol. 62, no. 11, pp. 1935–1941, 2001. (Cited on page [76](#).)
- [237] Y. Wang, S. L. I. Chan, R. Amal, Y. R. Shen, and K. Kiatkittipong, “XRD anisotropic broadening of nano-crystallites,” *Powder Diffr*, vol. 25, pp. 217–217, 2010. (Cited on page [76](#).)
- [238] A. U. A.S. Kagan, L.M. Shishlyannikova, “Application of triple convolution in the method of approximating the shape of profiles of x-ray diffraction lines [In Russian],” *Factory laboratory. Diagnostics of materials*, vol. 46, no. 10, pp. 903–906, 1980. (Cited on page [77](#).)
- [239] L. Palatnik, M. Y. Fuks, and V. Kosevich, *Formation Mechanism and Substructure of Condensed Films*. Nauka, Moscow, 1972. in Russian. (Cited on page [77](#), [78](#), [178](#) and [181](#).)
- [240] D. Kurbatov, V. Kosyak, M. Kolesnyk, A. Opanasyuk, and S. Danilchenko, “Morfological and structural characteristics of II–VI semiconductor thin films (ZnTe, CdTe, ZnS),” *Integrated Ferroelectrics*, vol. 103, no. 1, pp. 32–40, 2008. (Cited on page [77](#) and [78](#).)
- [241] T. Mahalingam, V. John, G. Ravi, and P. Sebastian, “Microstructural characterization of electrosynthesized ZnTe thin films,” *Crystal Research and Technology: Journal of Experimental and Industrial Crystallography*, vol. 37, no. 4, pp. 329–339, 2002. (Cited on page [78](#), [164](#) and [178](#).)
- [242] K. Nagao and E. Kagami, “X-ray thin film measurement techniques. VII. pole figure measurement,” *Rigaku J*, vol. 27, no. 2, pp. 6–14, 2011. (Cited on page [79](#).)
- [243] L. Vegard, “Die konstitution der mischkristalle und die raumfüllung der atome,” *Zeitschrift für Physik*, vol. 5, no. 1, pp. 17–26, 1921. (Cited on page [79](#).)
- [244] L. Vegard, “XV. die röntgenstrahlen im dienste der erforschung der materie,” *Zeitschrift für Kristallographie-Crystalline Materials*, vol. 67, no. 1-6, pp. 239–259, 1928. (Cited on page [79](#).)
- [245] Wikipedia, “Vegard’s law — Wikipedia, the free encyclopedia.” [Online; accessed 17-February -2021]. (Cited on page [80](#).)
- [246] Southeast university. Shool of materials science and enginreering, “D8 X-ray diffractometer Vol. I.” [Online; accessed 26-May-2021]. (Cited on page [81](#).)

-
- [247] D. K. Bowen and B. K. Tanner, *X-ray metrology in semiconductor manufacturing*. CRC Press, 2006. (Cited on page [81](#).)
- [248] S. Danilchenko, O. Kukharenko, C. Moseke, and et al., “Determination of the bone mineral crystallite size and lattice strain from diffraction line broadening,” *Crystal Research and Technology: Journal of Experimental and Industrial Crystallography*, vol. 37, no. 11, pp. 1234–1240, 2002. (Cited on page [81](#) and [161](#).)
- [249] Kirensky Institute of Physics, “X-ray diffractometer dron-4-07— Scientific equipment.” [Online; accessed 17- February -2021]. (Cited on page [82](#).)
- [250] Wikipedia, “Absorbance — Wikipedia, the free encyclopedia.” [Online; accessed 17- February -2021]. (Cited on page [85](#).)
- [251] F. Atay, I. Akyuz, S. Kose, E. Ketenci, and V. Bilgin, “Optical, structural and surface characterization of CdO:Mg films,” *Journal of Materials Science: Materials in Electronics*, vol. 22, no. 5, pp. 492–498, 2011. (Cited on page [86](#).)
- [252] K. V. Shalímová and A. Grdiam, *Física de los Semiconductores*. Mir: Moscu, 1975. (Cited on page [86](#).)
- [253] W. Melitz, J. Shen, A. C. Kummel, and S. Lee, “Kelvin probe force microscopy and its application,” *Surface science reports*, vol. 66, no. 1, pp. 1–27, 2011. (Cited on page [90](#), [91](#), [92](#) and [93](#).)
- [254] A. M. Baró and R. G. Reifengerger, *Atomic force microscopy in liquid: biological applications*. John Wiley & Sons, 2012. (Cited on page [90](#).)
- [255] G. Binnig, C. F. Quate, and C. Gerber, “Atomic force microscope,” *Physical review letters*, vol. 56, no. 9, p. 930, 1986. (Cited on page [90](#), [92](#) and [93](#).)
- [256] Wikipedia, “Hooke’s law — Wikipedia, the free encyclopedia.” [Online; accessed 17- February -2021]. (Cited on page [91](#).)
- [257] E. de Prado Fernández, “Crystal growth and characterization of $Zn_{1-x}Mg_xO$ advanced micro- and nanostructures,” *PhD thesis, Facultat de Fisica, Universitat de Valencia*, 2018. (Cited on page [92](#).)
- [258] J. Xu, Y. Wu, W. Li, and J. Xu, “Surface potential modeling and reconstruction in Kelvin probe force microscopy,” *Nanotechnology*, vol. 28, no. 36, p. 365705, 2017. (Cited on page [94](#).)

Bibliography

- [259] C. Lotze, “Fundamental processes in single molecule junctions: Interplay of forces and electronic effects,” *PhD thesis, Fachbereich Physik der Freien Universität Berlin, Germany*, 2014. (Cited on page [94](#).)
- [260] H. Seo, D. Goo, and G. Jung, “How to obtain sample potential data for KPFM measurement.” [Online; accessed 26-May-2021]. (Cited on page [95](#).)
- [261] W. H. Brattain and J. Bardeen, “Surface properties of germanium,” *The Bell System Technical Journal*, vol. 32, no. 1, pp. 1–41, 1953. (Cited on page [95](#).)
- [262] L. Kronik and Y. Shapira, “Surface photovoltage spectroscopy of semiconductor structures: at the crossroads of physics, chemistry and electrical engineering,” *Surface and Interface Analysis: An International Journal devoted to the development and application of techniques for the analysis of surfaces, interfaces and thin films*, vol. 31, no. 10, pp. 954–965, 2001. (Cited on page [95](#).)
- [263] L. Kronik and Y. Shapira, “Surface photovoltage phenomena: theory, experiment, and applications,” *Surface science reports*, vol. 37, no. 1-5, pp. 1–206, 1999. (Cited on page [95](#) and [96](#).)
- [264] D. Cavalcoli and A. Cavallini, “Surface photovoltage spectroscopy-method and applications,” *physica status solidi c*, vol. 7, no. 5, pp. 1293–1300, 2010. (Cited on page [95](#) and [96](#).)
- [265] A. Minj, A. Cros, N. Garro, J. Colchero, and et al., “Assessment of polarity in GaN self-assembled nanowires by electrical force microscopy,” *Nano letters*, vol. 15, no. 10, pp. 6770–6776, 2015. (Cited on page [97](#).)
- [266] D. Wang, Y. Qiu, W. Li, H. Zhang, and et al., “Interface-induced d^0 ferromagnetism in undoped ZnO thin films grown on different oriented sapphire substrates,” *Journal of Materials Science: Materials in Electronics*, vol. 30, no. 12, pp. 11086–11093, 2019. (Cited on page [100](#) and [109](#).)
- [267] K. Ogata, K. Maejima, S. Fujita, and S. Fujita, “Growth mode control of ZnO toward nanorod structures or high-quality layered structures by metal-organic vapor phase epitaxy,” *Journal of Crystal Growth*, vol. 248, pp. 25–30, 2003. (Cited on page [102](#).)
- [268] P. Souletie and B. Wessels, “Growth kinetics of ZnO prepared by organometallic chemical vapor deposition,” *Journal of Materials Research*, vol. 3, no. 4, pp. 740–744, 1988. (Cited on page [105](#).)

-
- [269] S. R. Achary, S. Agouram, J. F. Sánchez-Royo, and et al., “One-step growth of isolated CdO nanoparticles on r-sapphire substrates by using the spray pyrolysis methodology,” *RSC Advances*, vol. 4, no. 44, pp. 23137–23144, 2014. (Cited on page 108 and 112.)
- [270] X. Fan, H. Sun, Z. Shen, J.-L. Kuo, and Y. Lu, “A first-principle analysis on the phase stabilities, chemical bonds and band gaps of wurtzite structure $A_xZn_{1-x}O$ alloys ($A = \text{Ca, Cd, Mg}$),” *Journal of Physics: Condensed Matter*, vol. 20, no. 23, p. 235221, 2008. (Cited on page 122 and 128.)
- [271] J. Ishihara, A. Nakamura, S. Shigemori, and et al., “ $Zn_{1-x}Cd_xO$ systems with visible band gaps,” *Applied physics letters*, vol. 89, no. 9, p. 091914, 2006. (Cited on page 122 and 127.)
- [272] J. Yu, J. Kim, T. Jeong, M. S. Akhtar, and et al., “Study on the structural and optical properties of $Cd_{1-x}Zn_xO$ layers enhanced by rapid thermal annealing,” *Electronic Materials Letters*, vol. 7, no. 3, pp. 215–220, 2011. (Cited on page 122 and 132.)
- [273] M. del Carmen Martínez-Tomás, A. Huerta-Barberà, S. Agouram, and V. Muñoz-Sanjosé, “Induced crystallographic changes in $Cd_{1-x}Zn_xO$ films grown on r-sapphire by AP-MOCVD: the effects of the Zn content when $x \leq 0.5$,” *CrystEngComm*, vol. 22, no. 1, pp. 74–84, 2020. (Cited on page 123, 124, 126 and 127.)
- [274] D. M. Detert, K. B. Tom, C. Battaglia, and et al., “Fermi level stabilization and band edge energies in $Cd_{1-x}Zn_xO$ alloys,” *Journal of Applied Physics*, vol. 115, no. 23, p. 233708, 2014. (Cited on page 127.)
- [275] K. W. Böer, *Handbook of the physics of thin-film solar cells*. Springer Science & Business, 2014. (Cited on page 127.)
- [276] T. Murata, M. Ohtsuka, K. Hotta, and M. Fujisawa, “Conversion from helium to nitrogen as a TEOS carrier gas in sub-atmospheric chemical vapor deposition,” in *2013 e-Manufacturing & Design Collaboration Symposium (eMDC)*, pp. 1–4, IEEE, 2013. (Cited on page 130.)
- [277] H. C. Jang, K. Saito, Q. Guo, K. M. Yu, W. Walukiewicz, and T. Tanaka, “Realization of rocksalt $Zn_{1-x}Cd_xO$ thin films with an optical band gap above 3.0 eV by molecular beam epitaxy,” *CrystEngComm*, vol. 22, no. 16, pp. 2781–2787, 2020. (Cited on page 131.)
- [278] S. Kalogirou, *McEvoy’s handbook of photovoltaics: fundamentals and applications*. Academic Press, 2017. (Cited on page 135.)

Bibliography

- [279] J. Santos-Cruz, G. Torres-Delgado, R. Castanedo-Pérez, S. Jiménez-Sandoval, J. Márquez-Marín, and O. Zelaya-Angel, “Au–Cu/p–CdTe/n–CdO/glass-type solar cells,” *Solar energy materials and solar cells*, vol. 90, no. 15, pp. 2272–2279, 2006. (Cited on page 135.)
- [280] E. M. Tennyson, J. L. Garrett, J. A. Frantz, and et al., “Nanoimaging of open-circuit voltage in photovoltaic devices,” *Advanced Energy Materials*, vol. 5, no. 23, p. 1501142, 2015. (Cited on page 142.)
- [281] I. Visoly-Fisher, S. R. Cohen, K. Gartsman, and et al., “Understanding the beneficial role of grain boundaries in polycrystalline solar cells from single-grain-boundary scanning probe microscopy,” *Advanced Functional Materials*, vol. 16, no. 5, pp. 649–660, 2006. (Cited on page 143.)
- [282] A. Cavallini, A. Castaldini, D. Cavalcoli, and B. Fraboni, “Photocurrent and surface photovoltage spectroscopy investigations of cdte-based compounds,” *IEEE Transactions on Nuclear Science*, vol. 54, no. 5, pp. 1719–1722, 2007. (Cited on page 148.)
- [283] Z. Schumacher, Y. Miyahara, A. Spielhofer, and P. Grutter, “Measurement of surface photovoltage by atomic force microscopy under pulsed illumination,” *Physical Review Applied*, vol. 5, no. 4, p. 044018, 2016. (Cited on page 149.)
- [284] M. El-Dessouki and V. Attia, “Surface photovoltage spectroscopy for real n-and p-type (110) CdTe surfaces in the visible and near infra-red spectral range,” *Applied physics. A, Solids and surfaces*, vol. 45, no. 2, pp. 175–178, 1988. (Cited on page 149.)
- [285] P. F. Fewster, “X-ray analysis of thin films and multilayers,” *Reports on Progress in Physics*, vol. 59, no. 11, p. 1339, 1996. (Cited on page 153.)
- [286] M. Imamura and T. Yamaguchi, “Crystallographic and optical properties of Mn-substituted II-VI based magnetic semiconductor films,” *Journal of Physics: Conference Series*, vol. 200, no. 6, p. 062009, 2010. (Cited on page 153.)
- [287] R. D. Shannon, “Revised effective ionic radii and systematic studies of interatomic distances in halides and chalcogenides,” *Acta crystallographica section A: crystal physics, diffraction, theoretical and general crystallography*, vol. 32, no. 5, pp. 751–767, 1976. (Cited on page 153.)
- [288] A. Avdonin, L. Van Khoi, and W. e. a. Pacuski, “Preparation and optical properties of $Zn_{1-x}Mn_xTe_{1-y}O_y$ highly mismatched alloy,” *Acta Physica Polonica A*, vol. 2, no. 112, pp. 407–414, 2007. (Cited on page 153.)

-
- [289] E. Janik, E. Dynowska, J. Bak-Misiuk, and et al., “Structural properties of cubic MnTe layers grown by MBE,” *Thin Solid Films*, vol. 267, no. 1-2, pp. 74–78, 1995. (Cited on page [154](#).)
- [290] P. Djemia, Y. Roussigné, A. Stashkevich, and et al., “Elastic properties of zinc blende MnTe,” *Acta Physica Polonica-Series A General Physics*, vol. 106, no. 2, pp. 239–248, 2004. (Cited on page [154](#).)
- [291] D. Kurbatov, A. Opanasyuk, S. Duvanov, and et al., “Growth kinetics and stoichiometry of zns films obtained by close-spaced vacuum sublimation technique,” *Solid state sciences*, vol. 13, no. 5, pp. 1068–1071, 2011. (Cited on page [154](#).)
- [292] B. Hafner, “Energy dispersive spectroscopy on the sem: a primer,” *Characterization Facility, University of Minnesota*, pp. 1–26, 2006. (Cited on page [155](#).)
- [293] D. Kurbatov, A. Klymov, A. Opanasyuk, and et al., “Studying the elemental composition and manganese distribution in $Zn_{1-x}Mn_xTe$ and $Zn_{1-x}Mn_xTe$ films using the μ -PIXE and EDAX methods,” *Journal of Surface Investigation. X-ray, Synchrotron and Neutron Techniques*, vol. 8, no. 2, pp. 259–262, 2014. (Cited on page [155](#).)
- [294] G. Harris, “X. Quantitative measurement of preferred orientation in rolled uranium bars,” *The London, Edinburgh, and Dublin Philosophical Magazine and Journal of Science*, vol. 43, no. 336, pp. 113–123, 1952. (Cited on page [157](#).)
- [295] W. Mahmood and N. A. Shah, “Effects of metal doping on the physical properties of ZnTe thin films,” *Current Applied Physics*, vol. 14, no. 3, pp. 282–286, 2014. (Cited on page [157](#).)
- [296] C. V. Thompson and R. Carel, “Texture development in polycrystalline thin films,” *Materials Science and Engineering: B*, vol. 32, no. 3, pp. 211–219, 1995. (Cited on page [159](#).)
- [297] O. V. Klymov, D. Kurbatov, A. S. Opanasiuk, and et al., “Substructural features of $Zn_{1-x}Mn_xTe$ solid solution thin films,” *Proc. of the International Conference, Nanomaterials: Applications and Properties*, vol. 1, no. 3, p. 03TF23(4pp), 2012. (Cited on page [161](#) and [163](#).)
- [298] M. Kolesnyk, D. Kurbatov, A. Opanasyuk, and V. Loboda, “The substructural and optical characteristics of ZnTe thin films,” *Semiconductor Physics, Quantum Electronics & Optoelectronics*, vol. 12, no. 1, pp. 35–41, 2009. (Cited on page [161](#), [162](#), [163](#) and [164](#).)

Bibliography

- [299] M. Kolesnyk, S. Danilchenko, A. Opanasyuk, and N. Opanasyuk, “Substructure of ZnTe thin films,” *Vesnik Sumy State University. Series: Physics, Mathematics, Mechanics*, vol. 2, pp. 91–101, 2008. in Ukrainian. (Cited on page [163](#) and [164](#).)
- [300] V. Kosyak, A. Opanasyuk, P. Bukivskij, and Y. P. Gnatenko, “Study of the structural and photoluminescence properties of CdTe polycrystalline films deposited by close-spaced vacuum sublimation,” *Journal of Crystal Growth*, vol. 312, no. 10, pp. 1726–1730, 2010. (Cited on page [163](#).)
- [301] D. Kurbatov, A. Opanasyuk, and H. Khlyap, “Substrate-temperature effect on the microstructural and optical properties of ZnS thin films obtained by close-spaced vacuum sublimation,” *physica status solidi (a)*, vol. 206, no. 7, pp. 1549–1557, 2009. (Cited on page [163](#), [170](#) and [180](#).)
- [302] T. Ungár and A. Borbély, “The effect of dislocation contrast on x-ray line broadening: a new approach to line profile analysis,” *Applied Physics Letters*, vol. 69, no. 21, pp. 3173–3175, 1996. (Cited on page [164](#).)
- [303] B. Lee, “Elastic constants of ZnTe and ZnSe between 77–300 K,” *Journal of Applied Physics*, vol. 41, no. 7, pp. 2984–2987, 1970. (Cited on page [165](#).)
- [304] Y. Nishi and R. Doering, *Handbook of semiconductor manufacturing technology (2nd ed)*. CRC press, 2007. (Cited on page [165](#).)
- [305] T. Ungár, I. Dragomir, Á. Révész, and A. Borbély, “The contrast factors of dislocations in cubic crystals: the dislocation model of strain anisotropy in practice,” *Journal of applied crystallography*, vol. 32, no. 5, pp. 992–1002, 1999. (Cited on page [165](#).)
- [306] M. Kalita, K. Deka, J. Das, and et al., “X-ray diffraction line profile analysis of chemically synthesized lead sulphide nanocrystals,” *Materials Letters*, vol. 87, pp. 84–86, 2012. (Cited on page [165](#).)
- [307] Á. Révész, T. Ungár, A. Borbély, and J. Lendvai, “Dislocations and grain size in ball-milled iron powder,” *Nanostructured materials*, vol. 7, no. 7, pp. 779–788, 1996. (Cited on page [165](#).)
- [308] C. Qin, H. Qimin, and a. e. Wu, Lili, “Direct growth of ZnTe on Si (100) and Si (111) substrate by molecular beam epitaxy,” *Materials Research Express*, vol. 6, no. 7, p. 076425, 2019. (Cited on page [167](#).)
- [309] C. Panchal, A. S. Opanasiuk, V. V. Kosyak, and et al., “Structural and substructural properties of the zinc and cadmium chalcogenides thin films (a review),” *Journal of Nano*

- and Electronic Physics*, vol. 3, no. 1, pp. 274–301, 2011. (Cited on page [168](#), [170](#), [176](#), [179](#) and [181](#).)
- [310] D. H. Hwang, J. H. Ahn, K. N. Hui, and et al., “Structural and optical properties of ZnS thin films deposited by RF magnetron sputtering,” *Nanoscale research letters*, vol. 7:26, no. 1, pp. 1–7, 2012. (Cited on page [169](#), [172](#) and [189](#).)
- [311] D. Kurbatov, A. Opanasiuk, V. Denisenko, and et al., “Investigations of surface morphology and chemical composition of Ag/ZnS/glass ceramic thin-film structure,” *Semiconductor Physics, Quantum Electronics & Optoelectronics*, vol. 11, no. 3, pp. 252–256, 2008. (Cited on page [169](#).)
- [312] Y. Dieckmann, H. Cölfen, H. Hofmann, and A. Petri-Fink, “Particle size distribution measurements of manganese-doped ZnS nanoparticles,” *Analytical chemistry*, vol. 81, no. 10, pp. 3889–3895, 2009. (Cited on page [169](#).)
- [313] V. Mote, Y. Purushotham, and B. Dole, “Structural, morphological and optical properties of Mn doped ZnS nanocrystals,” *Cerâmica*, vol. 59, no. 352, pp. 614–619, 2013. (Cited on page [169](#).)
- [314] Y. Yan, M. Al-Jassim, K. Jones, and et al., “Observation and first-principles calculation of buried wurtzite phases in zinc-blende CdTe thin films,” *Applied Physics Letters*, vol. 77, no. 10, pp. 1461–1463, 2000. (Cited on page [170](#).)
- [315] V. Dimitrova and J. Tate, “Synthesis and characterization of some ZnS-based thin film phosphors for electroluminescent device applications,” *Thin solid films*, vol. 365, no. 1, pp. 134–138, 2000. (Cited on page [170](#).)
- [316] R. Sahraei, A. Daneshfar, A. Goudarzi, and et al., “Optical properties of nanocrystalline ZnS:Mn thin films prepared by chemical bath deposition method,” *Journal of Materials Science: Materials in Electronics*, vol. 24, no. 1, pp. 260–266, 2013. (Cited on page [171](#).)
- [317] A. Goudarzi, G. M. Aval, S. S. Park, and et al., “Low-temperature growth of nanocrystalline Mn-doped ZnS thin films prepared by chemical bath deposition and optical properties,” *Chemistry of Materials*, vol. 21, no. 12, pp. 2375–2385, 2009. (Cited on page [171](#).)
- [318] S. Kumar, H. Jeon, T. Kang, and et al., “Structural and optical properties of silica capped ZnS:Mn quantum dots,” *Journal of Materials Science: Materials in Electronics*, vol. 26, no. 6, pp. 3939–3946, 2015. (Cited on page [171](#).)

Bibliography

- [319] K. Bindu and E. Anila, “Structural and optical properties of white light emitting $ZnS : Mn^{2+}$ nanoparticles at different synthesis temperatures,” *Journal of fluorescence*, vol. 25, no. 4, pp. 795–801, 2015. (Cited on page [171](#).)
- [320] F. Weinberg, *Instruments and Methods for Physical Metallography*, [Russian translation]. Mir, Moscow, 1973. (Cited on page [171](#).)
- [321] J. S. Umanskij, J. A. Skakov, A. Ivanov, and L. Rastorgujev, *Crystallography, X-ray graph and electron microscopy*. Metallurgy, Moskow, 1982. in Russian. (Cited on page [173](#) and [181](#).)
- [322] A. Opanasiuk, M. Kurbatov, D.I. and Ivashchenko, and et al., “Properties of the window layers for the CZTSe and CZTS based solar cells,” *J. Nano- Electron. Phys*, vol. 4, no. 1, p. 01024(3pp), 2012. (Cited on page [174](#).)
- [323] N. Karar, F. Singh, and B. Mehta, “Structure and photoluminescence studies on $ZnS:Mn$ nanoparticles,” *Journal of Applied Physics*, vol. 95, no. 2, pp. 656–660, 2004. (Cited on page [174](#).)
- [324] A. K. Aqili, Z. Ali, and A. Maqsood, “Optical and structural properties of two-sourced evaporated $ZnTe$ thin films,” *Applied Surface Science*, vol. 167, no. 1-2, pp. 1–11, 2000. (Cited on page [183](#).)
- [325] F. Ozutok, K. Erturk, and V. Bilgin, “Growth, electrical, and optical study of $ZnS:Mn$ thin films.,” *Acta Physica Polonica, A.*, vol. 121, no. 1, pp. 221–223, 2012. (Cited on page [186](#).)
- [326] S. H. Chaki, S. M. Chauhan, J. P. Tailor, and et al., “Synthesis of manganese sulfide (MnS) thin films by chemical bath deposition and their characterization,” *Journal of materials research and technology*, vol. 6, no. 2, pp. 123–128, 2017. (Cited on page [189](#).)
- [327] D. Vij and N. Singh, *Luminescence and related properties of II-VI semiconductors. (Zinc Sulphide section)*. Nova Publishers, 1998. (Cited on page [189](#).)
- [328] P. Ghosh, S. F. Ahmed, S. Jana, and K. Chattopadhyay, “Photoluminescence and field emission properties of $ZnS:Mn$ nanoparticles synthesized by rf-magnetron sputtering technique,” *Optical Materials*, vol. 29, no. 12, pp. 1584–1590, 2007. (Cited on page [189](#).)
- [329] O. Klymov, D. Kurbatov, and O. Levchenko, “Some optical properties of $Zn_{1-x}Mn_xTe$ semimagnetic films,” in *2013 International Conference on Advanced Optoelectronics and Lasers (CAOL 2013)*, pp. 376–377, IEEE, 2013. (Cited on page [189](#).)

- [330] R. Amutha, A. Subbarayan, and R. Sathyamoorthy, “Influence of substrate temperature on microcrystalline structure and optical properties of ZnTe thin films,” *Crystal Research and Technology: Journal of Experimental and Industrial Crystallography*, vol. 41, no. 12, pp. 1174–1179, 2006. (Cited on page [189](#).)
- [331] G. Rusu, P. Prepelita, R. Rusu, and et al., “On the structural and optical characteristics of zinc telluride thin films,” *Journal of Optoelectronics and Advanced Materials*, vol. 8, no. 3, p. 922, 2006. (Cited on page [189](#).)